8-23-2017

Computational Design of Multifunctional Nanodielectrics

John Mangeri
University of Connecticut - Storrs, john.mangeri@uconn.edu

Computational Design of Multifunctional Nanodielectrics

John Mangeri, PhD

University of Connecticut, 2017

In this dissertation, a mesoscale modeling approach is developed aimed at simulating the properties of dielectric nano/microstructures with coupled polar, elastic, and thermal degrees of freedom, as well as the dependence of these properties on the structure size, shape, morphology and applied conditions. The versatility of this computational method to predict functional behavior is exemplified in the following systems:

(i) Zn-ZnO and ZnO-TiO2 semiconducting core-shell nanoparticles and the influence of their size, anisotropy, microstructure and applied pressure on their optical properties;

(ii) Ferroelectric PbTiO3 and BaTiO3 nanoparticles embedded in a dielectric medium, and the dependence on their polarization-field topology and transitions on particle shape and size, dielectric medium strength, applied electric field, as well as other factors;

(iii) Artificial layered-oxide material exhibiting polar Goldstone-like (or phason) excitations and its electrocaloric properties that are tuneable under a wide range of applied conditions.

The results of these investigations highlight the great promise of functional nano/microstructures for a variety of advanced engineering applications, including electrothermal energy conversion, non-volatile multibit memories, opto and low-power electronics, as well as metamaterials by design. They also detail the utility of mesoscale "control dials," I.e., manipulation of size, shape and microstructure, for fine-tuning the useful properties and operational response of functional nano/microstructures. Finally, we demonstrate that the development of predictive-grade mesoscale-level simulation techniques that accurately underpin complex physical phenomena occurring at this length scale is paramount for deeper understanding of the behavior of functional dielectrics and other related materials.

Computational Design of Multifunctional Nanodielectrics

John Mangeri

B.Sc. Embry-Riddle Aeronautical University, 2012

A Dissertation

Submitted in Partial Fulfillment of the

Requirements for the Degree of

Doctor of Philosophy

at the

University of Connecticut

2017

APPROVAL PAGE

Doctor of Philosophy Dissertation

Computational Design of Multifunctional Nanodielectrics

Presented by

John Mangeri B.Sc.

Major Advisor _____

Serge Nakhmanson

Associate Advisor _____

Jason Hancock

Associate Advisor _____

S. Pamir Alpay

University of Connecticut

2017

To my grandfather.

Acknowledgments

First, I would like to thank my advisor Dr. Serge Nakhmanson for his great wisdom and consistent support throughout this work. Serge provided invaluable guidance with my writing and important insight in creative discussions that I hope to that carry with me for the rest of my career. I also would like to acknowledge my mentors Dr. Olle Heinonen and Dr. S. Pamir Alpay who shared their professional advice and scientific knowledge which helped formulate new developments that moved forward this work. Of course, thanks should be extended to the MOOSE team at Idaho National Laboratory (INL) for providing an exceptional computational tool to the scientific community.

This dissertation would not have been possible without the funding extended from the U.S. Department of Energy, Office of Science, Office of Workforce Development for Teachers and Scientists, Office of Science Graduate Student Research (SCGSR) award (under contract number DE-SC0014664) and also INL through their summer internship program. I am also grateful for the internship opportunity at the Mathematics and Computer Science Division at Argonne National Laboratory (ANL) with Dr. Dmitry Karpeyev that helped lay much of the initial groundwork for this research. Additionally, the gracious computational resources provided on Blues, operated by the Laboratory Computing Resource Center at ANL, and on Hornet, hosted by the Taylor L. Booth Engineering Center for Advanced Technology, located at the University of Connecticut are acknowledged as integral to completing this work.

I have immense gratitude and deep thanks to my family: my mother, Elsie, father, Michael, and sister, Lauren, who have always been caring, loving, and supportive through this long journey. Finally, my dearest Izzy, who moved half-way across the country with me to start graduate school, deserves recognition for her unconditional devotion, friendship, and finding the best dank spicy memes.

TABLE OF CONTENTS

Chapter 1

Introduction

Miniaturization of conventional dielectric materials into microscopic and nanoscopic structures of various shapes and morphologies, including thin films, wires, core-shell particles and other composites, can lead to new and unexpected properties that may be useful for a wide range of different applications [67, 216, 93, 85, 130]. Moreover, an ability to control these properties with externally applied fields allows for additional functionalities and/or greatly enhanced performance to be engineered into devices. Extensive efforts aimed at better understanding the physical interplay between dielectric nanostructures geometries, properties and operation, involving both basic and applied research initiatives, are indicating broad applicability of such material systems in the areas of electronics, photonics and optics [10], energy storage and conversion [130, 260], computing [18, 32], and national security [165].

Conducive to facilitating transformative changes in all of these areas, theoretical and computational methods of materials science have to evolve accordingly to become capable of accurately predicting the properties and performance of nano- and microscale dielectric architectures possessing complicated shapes, non-trivial structural inhomogeneities and multiple — but interconnected — material attributes, including polar, magnetic, thermal and mechanical 'degrees of freedom.' Since individual device components or complete

functional heterostructures can range from a few nm to hundreds of μm in size, a number of different theoretical tools may be needed to capture their behavior. For instance, quantum mechanical theories, that have access to information about electronic wavefunctions and their interactions with crystal lattice, are very successful in predicting structural, elastic, dielectric, vibrational and electronic properties of basic material 'units,' represented by small (few nm in size, containing from a few dozen to around a hundred atoms) crystallographic cells. However, most generic quantum mechanical methods, such as the widely popular density functional theory (DFT) approach that is available to the field practitioners in a variety of different flavors, cannot effectively reproduce the properties of certain complex systems, e.g., 'strongly correlated' ones, that instead have to be treated by exceedingly expensive computational techniques. Another complication stems from great difficulties — and prohibitive computational costs — encountered in *ab initio* analysis of finite-temperature, non-equilibrium and long time-scale phenomena, especially those that may be related to realistic device operation.

Empirical methods describing interatomic interactions with simple potential functions provide huge performance boost for materials simulations making them capable of handling a few million atoms on modern supercomputers. However, this increase in efficiency comes at a price of abandoning all information about electronic degrees of freedom that are a hallmark of quantum mechanical modeling approaches. Still, on the road to simulating the behavior of even larger structures, such as nano- and microscopic device components, even more drastic coarse-graining of materials properties is necessary, as realized in a variety of so-called *continuum* approximations, where atomistic-level material structure is replaced by statistically averaged field variables representing aggregate responses of large assemblies of atoms. Although this dissolution of the atomistic-based description of materials results in yet another substantial improvement in computational efficiency (and thus the size of systems that can be probed with such techniques) it carries its own serious limitations that have to be

recognized and respected, especially when considering the complex *multiphysics* problems that involve multiple material attributes that may be connected across different length and time scales.

Predicting the behavior of multifunctional dielectric heterostructures possessing complicated shapes and morphologies with continuum theory certainly does qualify as such a problem. Due to the large size of the simulated domains and the complexity of processes that may be occurring within them, numerous difficulties of both mathematical and physical nature have to be resolved before truly useful and flexible computational tools could be created. For example, the most generic mathematical roadblocks to be overcome for such simulations involve uniform treatment of fully and partially periodic, as well as aperiodic structures, proper localization of material properties to surfaces and interfaces, balancing out widely different time scales of various relaxation processes in the system, and other numerical/computational issues related to algorithm parallelization and solver techniques. On the physical side, most careful attention has to be paid to development of robust models representing the energetics of competing polar, elastic, thermal and other interactions, needed to accurately describe the evolution of the dielectric material towards the state of equilibrium.

In this regard, ferroelectric thin films may already serve as a great example highlighting the involved complexities that have to be carefully accounted for in modeling multifunctional behavior of ferroic dielectrics at nanoscale. These films are usually made up of perovskite-oxide compounds, such as $BaTiO_3$, $PbTiO_3$, or solid solutions of x-$PbZrO_3$-$(1-x)$-$PbTiO_3$, or x-$Pb(Mg_{1/3}Nb_{2/3})O_3$-$(1-x)PbTiO_3$. They can be grown on a substrate in a layer-by-layer fashion with a number of different synthetic techniques [271, 263, 273, 216]. The choice of the substrate geometry, including the type of the exposed surface and the lattice mismatch with the film, can drastically alter the mechanical properties of the latter, with misfit-strain induced elastic distortions penetrating tens of nanometers deep into the film. Even stronger influence on the behavior of the dielectric films can be imposed by altering

the conductivity or resistivity of the substrate, as well as any additional layers that may be grown on top of the film, such as a top electrode. Good or poor conductivity of components in contact with the film triggers completely different mechanisms for screening of its surface charges, which in turn produce vividly dissimilar polarization patterns inside the film and their responses to external stimuli, e.g., polar domain structure formation and dynamics of domain-wall motion in applied electric field. Finally, these films may also be strongly sensitive to thermal fluctuations (i.e., exhibit pyroelectric [169] behavior), which may give rise to a variety of interesting effects when the presence of a varying electric field induces reorientation of the polar dipole moments and, as a result, adiabatic changes in the system entropy leading to heating or cooling of the film [12].

Nonetheless, despite the complexity of functional behavior, the saving grace of thin film systems is in simplicity of their geometry. This is, however, not the case for a wide variety of other dielectric nanostructures that could be produced by advanced synthesis techniques. Such structures — that can be fabricated from perovskites, binary oxides, or other materials, and may be attached to a substrate or other supports, or freestanding — include wires, islands, ridges, pores, mesas, as well as particles of all kinds of shapes, e.g., spherical, cubic, elliptic, tetrahedral or octahedral. Naturally, computational techniques developed specifically for simulating the properties of bulk materials and 'slabs,' and thus heavily relying on spatial periodicity (for example, spectral Fourier methods), will *not* be effective in treating these sorts of systems.

Although the field of computer modeling of functional dielectrics at the mesoscale has seen dramatic progress in the past few decades, spearheaded by developments in effective Hamiltonian [334, 305, 240] and phenomenological approaches [128, 55, 188, 189, 185, 292, 319], and has been very successful although lacking popular, standardized, flexible and widely accessible (e.g., open source) computational tools. This situation is unusual, compared to most other areas of computer materials simulations, where widely popular

modeling tools exist (both open-source and commercial), such as, e.g., Quantum Espresso [98], VASP [113], and Gaussian [91] codes based on *ab initio* approaches, LAMMPS package for classical molecular-dynamics calculations [256], and finite element method (FEM) based materials-engineering suites like ANSYS [70], COMSOL [262] and etc. The main goal of this dissertation lies in development of such a tool (actually, a complete tool-chain that extends from conceptualizing the material model all the way through to visualizing the results of computations) for prediction of properties and the functional response of complex dielectric materials and nano/microstructures. This tool is then applied to the studies of a number of different dielectric systems to evaluate its predictive power, performance and possible deficiencies. Our modeling approach is based on the MOOSE (**M**ultiphysics-**O**bject-**O**riented-**S**imulation-**E**nvironment)[95] finite element framework, which is an open-source programming environment for defining, solving and analyzing complex multiphysics problems with coupled system variables. The remainder of this dissertation is structured as follows:

- Chapter 2: theoretical background and derivation of continuum-level equations governing polar, elastic, and thermal properties in a dielectric structure, as well as a review of ferroelectric materials and related functionalities and phenomena.

- Chapter 3: a partial review of the FEM and specific MOOSE coding procedures used in the development of our computational modeling approach.

- Chapter 4: a test case of a purely elastic systems with *ab initio* fitted postprocessing of electronic properties: investigation of an electronic band gap dependence of Zn/ZnO and ZnO/TiO_2 spherical core-shell nanoparticles on their size, microstructure, material choice and applied mechanical boundary conditions [210].

- Chapter 5: a test case of a coupled polar-elastic system: a study of equilibrium polarization patterns, phase transformations and field response in spherical ferroelectric nanoparticles [209].

- Chapter 6: a test case of a polar-elastic-thermal system with unusual excitations: an investigation of electrothermal properties of a simple quasi-two-dimensional model, inspired by a Ruddlesden-Popper type layered-oxide material that possesses polar Goldstone-like excitations [211].

- Chapter 7: conclusions and future outlook.

Chapter 2

Continuum thermodynamic models of dielectric materials

Within this Chapter, a time-dependent Landau-Ginzburg-Devonshire model will be developed to evaluate the properties of a ferroelectric material that has elastic, polar, and thermal state variables. We begin the chapter with deriving the equations of linear elasticity for the elastic degrees of freedom. This is followed by the discussion of the equations governing the electrostatics and thermodynamics of a dielectric material. Properties of the ferroelectric phase are described next, including spatial polarization-field inhomogeneities, also known as ferroelectric domains and domain walls. Finally, the formalism of the Landau theory of phase transformations as applied to ferroelectric structures is derived along with mathematical formulations for all of the relevant energy terms. Possible interactions (or 'couplings') between the different state variables are also introduced as needed and include discussions of piezoelectric, electrostrictive, and electrocaloric effects.

2.1 The theory of linear elasticity

2.1.1 Elastic displacement and strain

The concept of a continuum (or continuous medium) involves defining a *measure* of a material that must be constant throughout. For an elastic continuum, this measure is the mass density. The mass density is formally defined within some small volume ΔV containing mass ΔM as,

$$\beta = \lim_{\Delta V \to 0} \frac{\Delta M}{\Delta V} \geq 0. \tag{2.1}$$

For an infinitesimally small mass dm, confined within volume dV, the constraint that a relationship $dm = \beta dV$ holds at all spatial coordinates of the medium makes the theory continuous[1].

For an *homogeneous* material, which has the same chemical formula throughout, the following thought experiment can be conducted: If one takes a large number of small volumes, ΔV, and calculates β for each piece, then if β plotted vs. the size of ΔV is not constant, then likely the classical continuum theory is not a good mathematical approximation. This is seen in Fig. 2.1 if $\Delta V > \Delta V^*$ where ΔV^* is a large enough volume such that β is approximately constant no matter *where* this volume is chosen in the material. This consideration is important for developing mesoscale models as they do not take into account molecular-level granularity of the material, instead introducing interactions over larger volumes where such granularity is erased or averaged out. The same 'continuous theory measure' argument is applicable to the electric charge density, as will be discussed in a later section.

Now, consider a body with an initial volume V_i and surface S_i, and final volume V_f and surface S_f, as shown in Fig. 2.2. A linear transformation $\mathbf{T}$ relates these two states and

[1]The variable β is used here for the mass density instead of the usual ρ, which is introduced later as the charge density. Typically, $\beta = MZ/N_0V$ where Z is the number of molecules per unit cell, M molecular weight, N_0 Avogadro's number, and V is the unit cell volume [242].

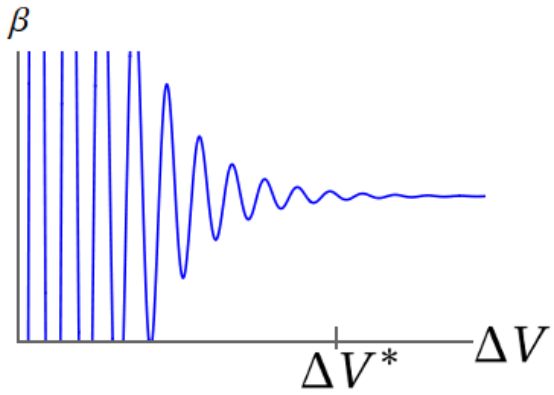

Fig. 2.1 Material mass density plotted as a function of small volumes ΔV. As the volume $\Delta V > \Delta V^*$, the continuum approximation is valid.

can account for any changes in body volume and/or shape, as well as any possible body *translations* in space. The position of the mass *dm* in the *initial* state is described by position vector

$$\mathbf{r} = x_j \hat{e}_j, \tag{2.2}$$

where x_j denotes an orthonormal coordinate system measured from the origin O and $\hat{e}_j$ is a unit vector of the coordinate system ($j = 1,2,3$). Here, Einstein notation is used[2], in which the repeated index is summed over (in this case j). A corresponding position of the mass from the origin O in the *final* state is given by

$$\mathbf{R} = X_j \hat{e}_j, \tag{2.3}$$

where $X_j = X_j(\mathbf{x})$ is a function of the coordinates $\mathbf{x}$. The difference

$$\mathbf{u}(\mathbf{x}) = \mathbf{r} - \mathbf{R} = \left(x_j - X_j\right) \hat{e}_j, \tag{2.4}$$

[2]Occasionally, the summation is explicitly stated, but unless noted, the Einstein convention is used throughout this dissertation.

defines the material *displacement vector*. One important detail is that this vector **u** does

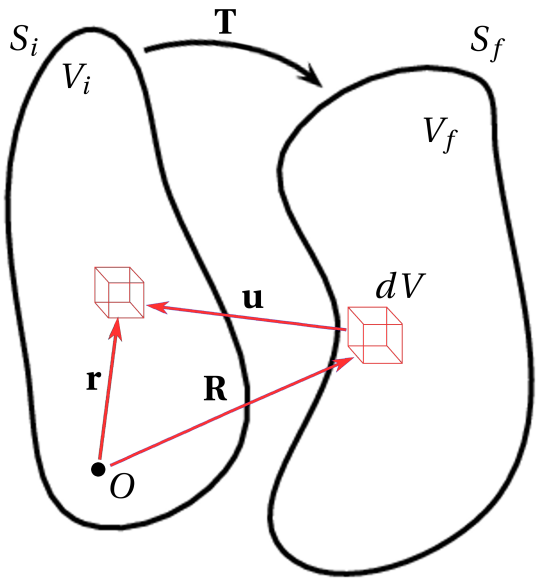

Fig. 2.2 A transformation **T** relates the arbitrary volume V_i to the final volume V_f. Displacements of infinitesimal volume dV can be described by a displacement vector $\mathbf{u} = \mathbf{r} - \mathbf{R}$ which is a vector valued function of the global coordinates x_j.

not necessarily describe a change in shape or volume, as it could also apply to a rigid-body translation or rotation. For example, $\mathbf{u} = u_0 \hat{e}_1$, with u_0 being a constant, describes a translation along $\hat{e}_1$, while $\mathbf{u} = \langle -\omega, \omega, 0 \rangle$ describes a rigid-body rotation about $\hat{e}_3$.

When the body is transformed, the distance between its volume elements may change. For example, consider two volume elements who are initially a distance dl apart in space. This distance is

$$dl^2 = dx_j dx_j \text{ and } (dl')^2 = dX_j dX_j = \left(dx_j + du_j\right)^2 \tag{2.5}$$

before and after (dl') the transformation respectively. But, rewriting the differential of $du_j = \frac{\partial u_j}{\partial x_k} dx_k$, we then have

$$\begin{aligned}(dl')^2 &= dl^2 + 2\frac{\partial u_j}{\partial x_k} dx_j dx_k + \frac{\partial u_j}{\partial x_k}\frac{\partial u_j}{\partial x_l} dx_k dx_l \\ &= dl^2 + 2\left[\frac{1}{2}\left(\frac{\partial u_j}{\partial x_k} + \frac{\partial u_k}{\partial x_j} + \frac{\partial u_j}{\partial x_k}\frac{\partial u_k}{\partial x_j}\right)\right] dx_j dx_k.\end{aligned} \tag{2.6}$$

The quantity in brackets is known as the *elastic strain tensor*[3], $\varepsilon_{jk} = \varepsilon_{jk}(\mathbf{x})$, which is symmetric upon change of the index $\left(\varepsilon_{jk} = \varepsilon_{kj}\right)$.

2.1.2 Mechanical equilibrium of the continuum under arbitrary load

Consider again our differential volume dV. Let $\mathbf{f}$ be the total force density acting within (and on) dV. Therefore, the following integrated relation holds for the total force on an arbitrary volume V enclosed by the surface S,

$$\mathbf{F} = \iiint_V \mathbf{f}\, dV \tag{2.7}$$

This total force can be decomposed into two contributions, one being a body force $\mathbf{b}$ acting at every point within V, and the other a surface force, which is described by a surface integral over forces $\mathbf{t}$ acting on each differential surface element dS. Thus,

$$\mathbf{F} = \iiint_V \mathbf{b}\, dV + \oiint_S \mathbf{t}\, dS. \tag{2.8}$$

[3] In the linear theory, the term $\partial u_j/\partial x_k \partial u_k/\partial x_j$ is always considered to be very small and is thus neglected, hence the familiar result.

It is convention to align the action of the surface force $\mathbf{t}$ with the direction of the outward facing normal unit vector $\hat{\mathbf{n}}$, i.e.,

$$\mathbf{F} = \iiint_V \mathbf{b}\, dV + \oiint_S \mathbf{T}\cdot\mathbf{n} dS. \tag{2.9}$$

In order for Eq. 2.9 to be satisfied covariantly[84], the object $\mathbf{T}\cdot\hat{\mathbf{n}}$ must be a vector, which in turn implies that $\mathbf{T}$ is a tensor quantity of rank two. This quantity is known as the *stress tensor* field and is usually denoted as σ_{jk}. In index notation, Eq. (2.9) is written as

$$F_j = \iiint_V b_j\, dV + \oiint_S \sigma_{jk}\hat{n}_k\, dS. \tag{2.10}$$

Applying the divergence theorem [4] to Eq. (2.10), allows us to recast the surface integral as a volume integral:

$$F_j = \iiint_V b_j\, dV + \iiint_V \frac{\partial \sigma_{jk}}{\partial x_k}\, dV. \tag{2.11}$$

In static equilibrium, the total force is zero. Since the integration is carried over an arbitrary V,

$$\frac{\partial \sigma_{jk}}{\partial x_k} + b_j = 0, \tag{2.12}$$

which is known as Cauchy's first law of linear momentum — also commonly referred to as the stress divergence equation — and a condition for the static mechanical equilibrium.

[4] The divergence theorem allows for equivalence between surface and volume integrals. The general form is $\int_{\partial\Omega}\mathbf{A}\cdot d(\partial\Omega) = \int_\Omega \nabla\cdot\mathbf{A} d\Omega$ for arbitrary vector field $\mathbf{A}$ within a volume Ω enclosed by a surface $\partial\Omega$ provided that components of $\mathbf{A}$ have continuous first derivatives.

2.1.3 Symmetry of the stress tensor and Hooke's law

It is important to discuss the symmetry relations that have to be satisfied by the elastic stress (and strain) tensors. Eq. (2.12) does not describe any equilibrium conditions for torques, i.e., rotational forces applied to the body, but we can write one down [41]

$$\iiint_V \mathbf{x} \times \mathbf{b}\, dV + \oiint_S \mathbf{x} \times \boldsymbol{\sigma} : \hat{\mathbf{n}}\, dS = 0, \tag{2.13}$$

which is known as Cauchy's second law of angular momentum balance. Rewriting Eq. (2.13) in index notation, one finds

$$\iiint_V \epsilon_{ijk} x_j b_k\, dV + \oiint_S \epsilon_{ijk} x_j \sigma_{kl} \hat{n}_l\, dS = 0, \tag{2.14}$$

where ϵ_{ijk} is the pseudo-tensor (Levi-Civita) density[5] Applying the divergence theorem once again, we get

$$\iiint_V \epsilon_{ijk} x_j b_k\, dV + \iiint_V \frac{\partial}{\partial x_l} \left(\epsilon_{ijk} x_j \sigma_{kl}\right)\, dV = 0. \tag{2.15}$$

Noting that $\frac{\partial x_j}{\partial x_l} = \delta_{jl}$, where δ_{jl} is the Kroenecker delta symbol[6], we obtain

$$\iiint_V \epsilon_{ijk} x_j b_k\, dV + \iiint_V \left[\epsilon_{ijk} \delta_{jl} \sigma_{kl} + x_j \frac{\partial \sigma_{kl}}{\partial x_l}\right]\, dV = 0. \tag{2.16}$$

[5]The Levi-Civita pseudo-tensor of rank three is defined as a coordinate-free invariant, $\epsilon_{ijk} = \hat{e}_i \cdot (\hat{e}_j \times \hat{e}_k)$, from any complete set of orthogonal unit vectors.

[6]The Kroenecker product, δ_{ij}, is equal to unity if $i = j$ and zero otherwise.

Removing integration over an arbitrary volume, same as before, and rearranging Eq. (2.16) one finds that

$$\epsilon_{ijk}\delta_{jl}\sigma_{kl} = -\epsilon_{ijk}x_j\left(\frac{\partial\sigma_{kl}}{\partial x_l} + b_k\right) = 0, \tag{2.17}$$

where the quantity in parenthesis must vanish due to Eq. (2.12). Then[7]

$$\begin{aligned}\epsilon_{ijk}\delta_{jl}\sigma_{kl} = 0 &\Rightarrow \epsilon_{ijk}\sigma_{kj} = 0 \\ &\Rightarrow \epsilon_{imn}\epsilon_{ijk}\sigma_{jk} = 0 \\ &\Rightarrow \left(\delta_{jm}\delta_{kn} - \delta_{mk}\delta_{nj}\right)\sigma_{jk} = 0\end{aligned} \tag{2.18}$$

which implies

$$\sigma_{jk} = \sigma_{kj}. \tag{2.19}$$

Therefore, the stress tensor must be symmetric under interchange of the indices. Now consider a Taylor series expansion of σ_{ij} as a function of the elastic strain ε_{kl} as in Ref. [84],

$$\sigma_{ij} = \sigma_{ij}\left(\varepsilon_{kl} = 0\right) + \left(\frac{\partial\sigma_{ij}}{\partial\varepsilon_{kl}}\right)_{\varepsilon_{kl}=0}\varepsilon_{kl} + \ldots \tag{2.20}$$

Since ε_{kl} is considered to be small, we can disregard all of the non-linear terms in this decomposition. Furthermore, as the absence of strain produces zero stress, Eq. (2.20) becomes

$$\sigma_{ij} \simeq \left(\frac{\partial\sigma_{ij}}{\partial\varepsilon_{kl}}\right)_{\varepsilon_{kl}=0}\varepsilon_{kl}. \tag{2.21}$$

[7] In general, $\epsilon_{ijk}\epsilon_{lmn} = \delta_{il}\delta_{jm}\delta_{kn} + \delta_{im}\delta_{jn}\delta_{kl} + \delta_{in}\delta_{jl}\delta_{km} - \delta_{il}\delta_{jn}\delta_{km} - \delta_{in}\delta_{jm}\delta_{kl} - \delta_{im}\delta_{jl}\delta_{kn}$. This can be shown to be reduced to the form used in Eq. (2.18) by letting $l \to i$ and noting that $\delta_{rr} = 1$ for all r.

which is known as the generalized Hooke's law. Interchange of the indices for both the strain and stress tensors shows that the quantity (which is a tensor of rank four)

$$C_{ijkl} = \left(\frac{\partial \sigma_{ij}}{\partial \varepsilon_{kl}}\right)_{\varepsilon_{kl}=0}$$

must satisfy $C_{ijkl} = C_{klij}, C_{ijkl} = C_{jikl}, C_{ijkl} = C_{ijlk}$ symmetry. This means that, at most, there could be 21 independent components of C_{ijkl}[8]. Since under the assumptions of linear elasticity, the *elastic stiffness tensor*, C_{ijkl}, does not depend on any external influences, such as an externally applied force, or is a consequence of the linear transformation from whence the elastic displacements arise, this object must be a material property similar to the mass density β defined earlier in this Chapter.

2.1.4 Work done on the deformed medium

The work, W, required to deform V by some infinitesimal displacement $\delta\mathbf{u}$, can be written as a sum of the body and surface work [168],

$$W = \iiint_V \delta W dV = \iiint_V \mathbf{b}\cdot\delta\mathbf{u} dV + \oiint_S (\sigma : \hat{\mathbf{n}})\cdot\delta\mathbf{u} dS. \tag{2.22}$$

Using the divergence theorem,

$$\begin{aligned} W = \iiint_V \delta W dV &= \iiint_V \mathbf{b}\cdot\delta\mathbf{u} dV + \iiint_V \nabla\cdot[\sigma : \delta\mathbf{u}]\, dV. \\ &= \iiint_V \mathbf{b}\cdot\delta\mathbf{u} dV + \iiint_V (\nabla : \sigma)\cdot\delta\mathbf{u}\, dV + \iiint_V \sigma : \delta(\nabla\cdot\mathbf{u})\, dV. \\ &= \iiint_V [\mathbf{b} + \nabla : \sigma]\cdot\delta\mathbf{u}\, dV + \iiint_V \sigma : \delta(\nabla\cdot\mathbf{u})\, dV. \end{aligned} \tag{2.23}$$

[8] Similarly, the elastic strain can be expanded in terms of the stress fields and it is found that $\varepsilon_{kl} = s_{klij}\sigma_{ij}$ where s_{klij} is the elastic compliance tensor (of rank four). It can be shown that $C_{ijkl}s_{klij} = 1$. In other words, $s = C^{-1}$.

With the first term vanishing due to Eq. (2.12) at mechanical equilibrium, this can be reduced to the following expression

$$\delta W = \boldsymbol{\sigma} : \delta \left(\nabla \cdot \mathbf{u} \right). \tag{2.24}$$

In index notation Eq. (2.24) is,

$$\delta W = \sigma_{ij} \delta \left(\frac{1}{2} \left[\frac{\partial u_i}{\partial x_j} + \frac{\partial u_j}{\partial x_i} \right] \right) = \sigma_{ij} \delta \varepsilon_{ij}, \tag{2.25}$$

due to the symmetry properties of the stress tensor [see Eq. (2.19)]. $\delta \varepsilon_{ij}$ is an infinitesimal strain.

2.1.5 Thermodynamics of the elastic medium

Now we consider elementary thermodynamics of the elastic medium, connecting in the thermal system variables. The internal energy, dU, of a material is equivalent to the sum of the heat, dQ, flowing into the volume and the work done dW,

$$dU = dW + dQ. \tag{2.26}$$

Under a reversible change, the second law of thermodynamics states that

$$dQ = T dS, \tag{2.27}$$

where T is the temperature and dS is differential change of the entropy. Therefore, combining the energy terms from Eqs. (2.25) and (2.27), the internal energy of an elastic material can

be recast as

$$dU = \sigma_{ij} d\varepsilon_{ij} + T dS. \tag{2.28}$$

If we consider a new definition of energy (from Gibbs, see Ref. [245]),

$$dG = d\left(U + \sigma_{ij}\varepsilon_{ij} - TS\right), \tag{2.29}$$

it follows that,

$$dG = dU + \varepsilon_{ij} d\sigma_{ij} + \sigma_{ij} d\varepsilon_{ij} - T dS - S dT.$$

But, $dU = \sigma_{ij} d\varepsilon_{ij} + T dS$ by Eq. (2.28), so

$$dG = \sigma_{ij} d\varepsilon_{ij} - S dT. \tag{2.30}$$

Therefore,

$$\sigma_{ij} = \left(\frac{dG}{d\varepsilon_{ij}}\right)_T \text{ and } S = -\left(\frac{dG}{dT}\right)_{\sigma_{ij}}. \tag{2.31}$$

The first of these relations can be turned into an integral form:

$$G(T) = \int_V \sigma_{ij}\varepsilon_{ij} dV, \tag{2.32}$$

which defines the *elastic free energy*. Using Eq. (2.21), it can be rewritten as

$$G(T) = \frac{1}{2}\int_V C_{ijkl}\varepsilon_{ij}\varepsilon_{kl} dV, \tag{2.33}$$

where C_{ijkl} may be a function of T.

2.1.6 Surface contributions to the elastic energy

Elastic equilibrium state of a continuous material with a *free* surface may be different from the bulk. From a simplified atomistic description, atoms at the surface have fewer bonds than those within the structure. Therefore, they may rearrange themselves into a new structure or phase that is different from that of the bulk and could have its own distinct symmetry [74, 140]. By default, this distinct surface phase will not be in elastic equilibrium with the bulk phase underneath, which should give rise to a residual stress field at the surface. An effective approach to treating the influence of a free surface on the mechanical properties of the elastic body has been put forward by Gurtin and Murdoch [111]. This approach treats the surface as a thin boundary layer attached to the material bulk that possesses its own elastic stiffness parameters [283, 75, 56].

For the surface stress tensor $\sigma^S_{\alpha\beta}$, we can write the following expression:

$$\sigma^S_{\alpha\beta} = \tau^0 \delta_{\alpha\beta} + \frac{\partial F^S}{\partial \varepsilon^S_{\alpha\beta}}, \tag{2.34}$$

where τ^0 is the intrinsic residual surface tension, $\varepsilon^S_{\alpha\beta}$ is the surface strain tensor and F^S is the surface elastic energy. The Greek indices α, β denote directions tangent to the surface. The same thermodynamical arguments hold for the reversible work done on the surface as they do in the bulk. Therefore,

$$F^S = \frac{1}{2} \oiint_S dS C^S_{\alpha\beta\delta\gamma} \varepsilon^S_{\alpha\beta} \varepsilon^S_{\delta\gamma}. \tag{2.35}$$

Since the tensors $\sigma^S_{\alpha\beta}, \varepsilon^S_{\alpha\beta}$, and $C^S_{\alpha\beta\delta\gamma}$, which uniquely define the mechanical equilibrium, are only defined on the surface, they must be properly projected onto it, which implies

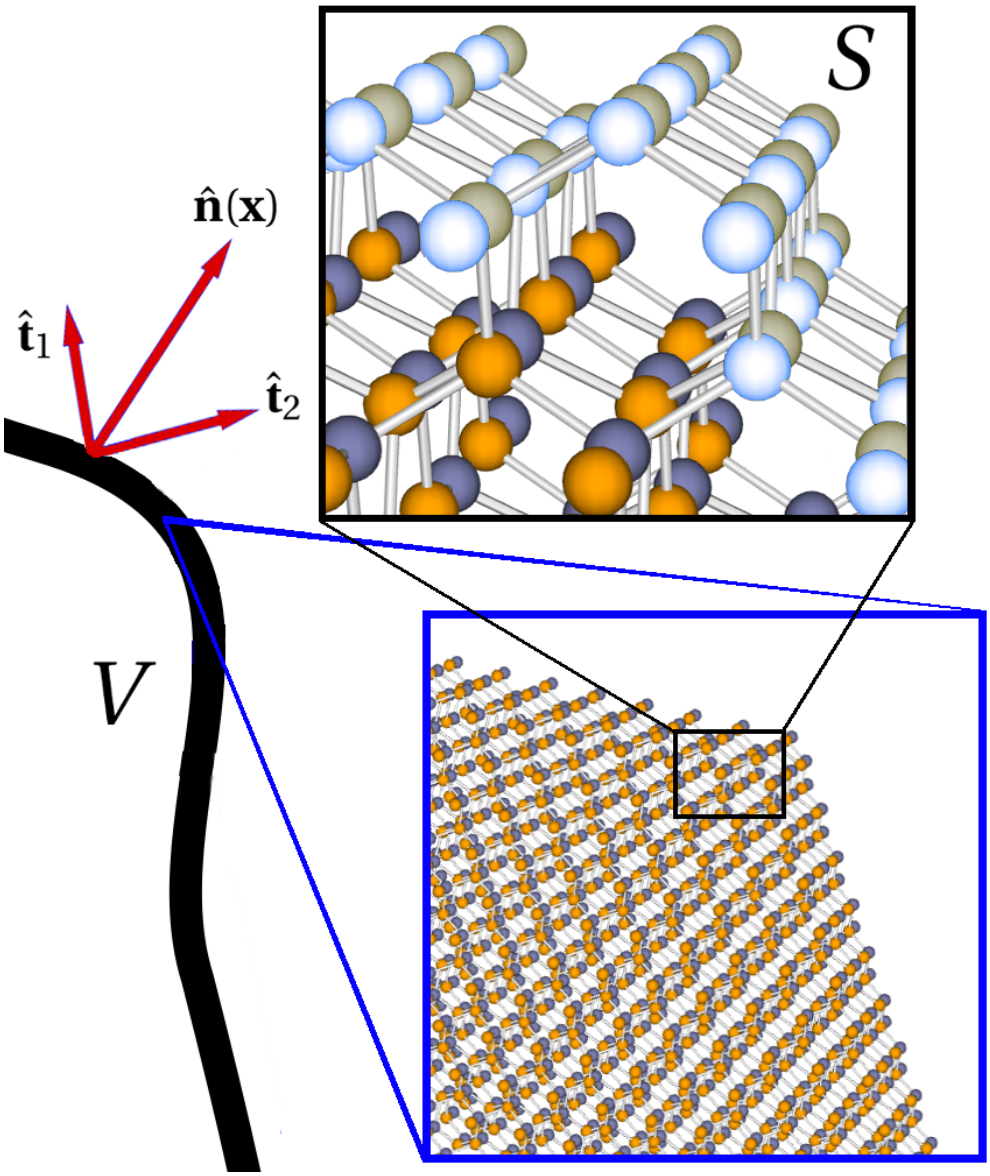

Fig. 2.3 Continuum based approach to surface elasticity, after Gurtin and Murtoch [111]. A projection operator is constructed from the normal vector $\hat{\mathbf{n}}(\mathbf{x})$ and the surface tangent vectors $\hat{\mathbf{t}}_k$ (note $\hat{\mathbf{t}}_k \perp \hat{\mathbf{n}}$ for $k = 1,2$) for a thin near-surface region indicated by the black curve. The insets show an example of ZnS atoms arranged in the zinc blende structure where outer surface atoms, colored in blue and gray, have fewer bonds than their inner neighbors. The near-surface area can be considered as a distinct phase different from the bulk, which has its own elastic stiffnesses C^s_{ijkl} and consequently an additional surface elastic energy F^S.

reducing their dimensionality by one, compared to their bulk counterparts. An appropriate projection operator, $\mathbb{P}$, can be constructed from the outward-facing normal unit vector $\hat{\mathbf{n}}$ as

$$\mathbb{P} = \mathbb{1} - \hat{\mathbf{n}} \otimes \hat{\mathbf{n}}, \tag{2.36}$$

with $\mathbb{1}$ being the identity operator. A surface projection of a tensor quantity A then may be defined as

$$A^S_{ij} = P_{ik} A_{kl} P_{lj} \tag{2.37}$$

and

$$A^S_{ijkl} = P_{im} P_{jn} A_{mnrs} P_{rk} P_{sl}, \tag{2.38}$$

for the rank two and four tensors, respectively. It can be shown that the minor symmetries $C^S_{ijkl} = C^S_{jikl} = C_{ijlk} = C^S_{klij}$ are preserved under this operation. Therefore, if one solves Eq. 2.12 along with

$$\frac{\partial \sigma^S_{\alpha\beta}}{\partial x_i} = 0, \tag{2.39}$$

then mechanical equilibrium is satisfied for the continuous elastic body enclosed by a free surface. The presence of the surface tension, τ^0, will cause residual stress fields within the otherwise stress-free structure. It should be noted that the surface elastic strain can be defined in the usual fashion as

$$\varepsilon^S_{\alpha\beta} = \frac{1}{2}\left(\frac{\partial u_\alpha}{\partial x_\beta} + \frac{\partial u_\beta}{\partial x_\alpha}\right). \tag{2.40}$$

with α, β being the tangent directions of the surface.

2.2 Electrostatic equations of state

2.2.1 Governing equations of microscopic/macroscopic electrostatics

Analogous to the mass density being a *measure* of the continuous elastic theory, electric charge density ρ may become a similar measure for dielectric materials treated at continuum level. Once again, we introduce a formal definition of the material measure,

$$\rho = \lim_{\Delta V \to 0} \frac{\Delta Q}{\Delta V} \lesseqgtr 0 \tag{2.41}$$

where ρ may be positive or negative. Within the volume V enclosed by S, the total volume and surface charge density, σ, can be decomposed into free and bound charges,

$$\rho(\mathbf{x}) = \rho_f(\mathbf{x}) + \rho_b(\mathbf{x}) \tag{2.42}$$

and

$$\sigma(\mathbf{x}) = \sigma_f(\mathbf{x}) + \sigma_b(\mathbf{x}). \tag{2.43}$$

The electrostatic potential created by this system of charges is [137],

$$\Phi(\mathbf{x}) = \iiint_V dV' \frac{\rho(\mathbf{x}')}{|\mathbf{x}-\mathbf{x}'|} + \oiint_S dS' \frac{\sigma(\mathbf{x}')}{|\mathbf{x}-\mathbf{x}'|}, \tag{2.44}$$

where the integration is taken over primed coordinates. The curl-less electric field condition,

$$\nabla \times \mathbf{E}(\mathbf{x}) = 0, \tag{2.45}$$

implies

$$\mathbf{E}(\mathbf{x}) = -\nabla\Phi(\mathbf{x}). \tag{2.46}$$

Therefore, we have

$$\nabla\cdot\mathbf{E}(\mathbf{x}) = \nabla^2\Phi(\mathbf{x}). \tag{2.47}$$

which is the Poisson equation. For a dielectric material, it is beneficial to reduce it to a form that depends on the material polarization, which is done as follows. We consider the dielectric medium as a collection of dipoles $\mathbf{p}_k$. Its total polarization density then is

$$\mathbf{P}(\mathbf{x}) = \frac{1}{V}\sum_k \mathbf{p}_k$$

. The associated electrostatic potential is[1]

$$\Phi^{\text{polar}}(\mathbf{x}) = \iiint_V dV'\mathbf{P}(\mathbf{x}')\nabla'\left(\frac{1}{|\mathbf{x}-\mathbf{x}'|}\right). \tag{2.48}$$

The integrand in Eq. (2.48) can be rewritten as

$$\mathbf{P}(\mathbf{x}')\nabla'\left(\frac{1}{|\mathbf{x}-\mathbf{x}'|}\right) = \nabla'\left(\frac{\mathbf{P}(\mathbf{x})}{|\mathbf{x}-\mathbf{x}'|}\right) - \frac{1}{|\mathbf{x}-\mathbf{x}'|}\nabla'\cdot\mathbf{P}(\mathbf{x}'). \tag{2.49}$$

[1]The potential due to one dipole sitting at the origin $\mathbf{x}' = 0$ is (after Ref. [137]),

$$\Phi^{\text{dipole}} \sim \frac{\mathbf{p}\cdot\mathbf{x}}{|\mathbf{x}|^3} = \mathbf{p}\cdot\nabla\left(\frac{1}{\mathbf{x}}\right)$$

Inserting Eq. (2.49) into Eq. (2.48) and applying the divergence theorem to the first term we get

$$\Phi^{\text{polar}}(\mathbf{x}) = \oiint_S dS' \left(\frac{\mathbf{P}(\mathbf{x})}{|\mathbf{x}-\mathbf{x}'|} \right) \cdot \hat{\mathbf{n}} - \iiint_V dV' \frac{1}{|\mathbf{x}-\mathbf{x}'|} \nabla' \cdot \mathbf{P}(\mathbf{x}'). \tag{2.50}$$

In the absence of free volume and surface charges, the comparison of Eqs. (2.50) and (2.44) produces

$$\rho_b(\mathbf{x}) = -\nabla \cdot \mathbf{P}(\mathbf{x}) \text{ and } \sigma_b(\mathbf{x}) = \mathbf{P}(\mathbf{x}) \cdot \hat{\mathbf{n}}. \tag{2.51}$$

The Poisson equation [Eq. (2.47)] becomes

$$\nabla^2 \Phi(\mathbf{x}) = \frac{\rho}{\epsilon_0} = \nabla \cdot \mathbf{E}(\mathbf{x}) = \frac{1}{\epsilon_0} \left(\rho_f - \nabla \cdot \mathbf{P} \right). \tag{2.52}$$

where $\epsilon_0 = 8.85 \times 10^{-12}$ F/m is vacuum permitivity. Here, a new quantity can be introduced,

$$\mathbf{D} = \epsilon_0 \mathbf{E} + \mathbf{P} \tag{2.53}$$

which is an electric *displacement* vector. If the medium does not have any polarization, then $\rho_b = \sigma_b = 0$. However, an applied electric field can still polarize it, with induced polarization being linearly proportional to the field:

$$P_i = \chi_{ij} E_j. \tag{2.54}$$

with χ_{ij} being the dielectric susceptibility.

2.3 Constitutive relationships for the dielectric media

In the previous discussion, the temperature is assumed to be constant, which allows for analytic definitions of the elastic energy for the given temperature. Simultaneously, a connection between the elastic fields σ_{ij} and ε_{ij} through the temperature dependent material tensor C_{ijkl} can be obtained by simple force balancing considerations. On the other hand, the relationship between bound charge density, $\rho_b = -\nabla \cdot \mathbf{P}$, its electric displacement field, $\mathbf{D} = \epsilon_0 \mathbf{E} + \mathbf{P}$, and the total electric field is established as $\mathbf{D} = \epsilon \mathbf{E}$. The electrostatic field is also shown to obey the Poisson equation.

As demonstrated by Jacques and Pierre Curie in an experiment in 1880 [65], an additional relation may exist in some materials, connecting elastic strains or stresses with electrostatic fields and polarization (at fixed temperature). This connection is called a *piezoelectric* effect, with the *direct* effect involving an emergence of an electric field in response to the deformation of the material. The same researchers also demonstrated that with the application of an electric field, the shape of the crystal can deform. This was formally defined as the *converse* piezoelectric effect[9].

Similar observations has been made for the connections between elasticity and temperature, i.e., the changes in elastic fields can alter the temperature, and, conversely, temperature changes can produce elastic distortions[245]. Furthermore, it has long been known (since as far back as the 4th century BC) that a temperature change can cause an attractive force to appear — which was recognized by Thomson and Lord Kelvin as an electrostatic force [169]). Heckmann [245] was the first to devise a famous diagram that visualizes multiple couplings existing in dielectric materials. In a similar fashion, magnetic materials can also display a number of analogous phenomena, such as pyromagnetic, magnetostrictive, and piezomagnetic effects, that can be assembled in an appropriate Heckmann diagram. Finally, in some materials direct couplings may exist between magnetic and electric state variables,

[9] Discovery of this useful reversible phenomena led to the development of sonar by Rutherford and Langevin [150] near the end of World War I.

giving rise to a *magnetoelectric* effect. In that case, a three-dimensional Heckmann diagram can be constructed for a system that has both electric and magnetic degrees of freedom. Other Heckmann diagrams exist that relate cross-coupled transport phenomena, such as thermoelectricity, electrolysis, and thermal diffusion [242]. An example of this diagram is in Fig. 2.4.

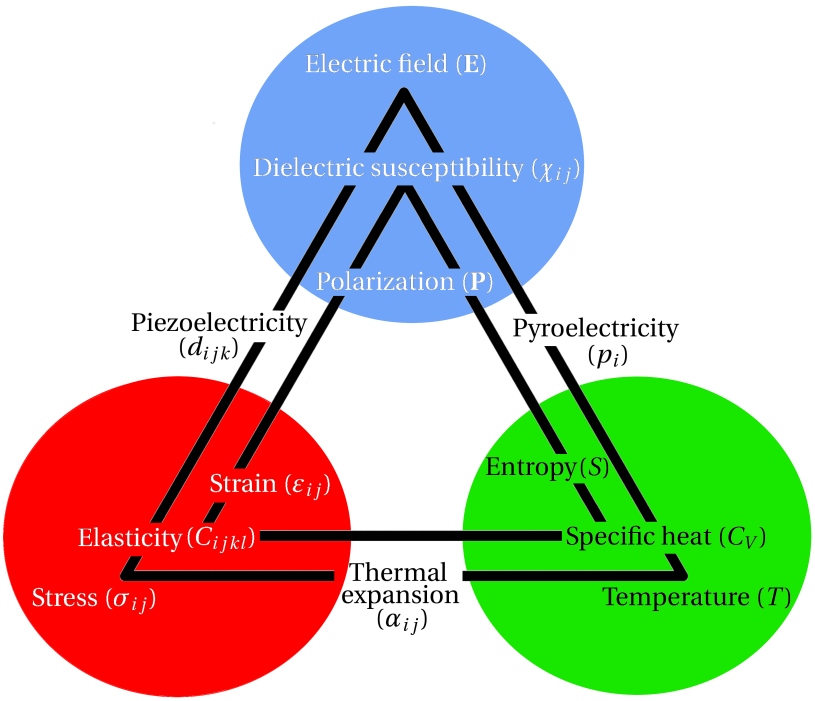

Fig. 2.4 Heckmann diagram showing the cross-coupling between elastic, thermal, and electric state variables. The lines between the variables describe a certain physical process implying a linear connection between them. The inner triangle shows an equivalent relationship between secondary variables.

Ferroelectric materials have long been known [146, 195, 67, 12, 216] to exhibit strong connections between their elastic, polar, and thermal degrees of freedom. Therefore, any continuum-level theories and computational tools developed for such materials need to accurately capture the physical nature of these connections, as well as account for any relevant spatial inhomogeneities of the state variables. In the following sections, we discuss basic thermodynamic relations for a uniform polar-elastic dielectric and derive the expressions for

its piezo- and pyroelectric constants. Then, we discuss the symmetry of the different material tensors (or compliances) that are necessary for the treatment of ferroelectric compounds.

2.3.1 Thermodynamics

The internal energy of the polar-elastic dielectric crystal may be written as

$$dU = \sigma_{ij} d\varepsilon_{ij} + E_i dD_i + T dS \tag{2.55}$$

where $\mathbf{D}$, S, and ε_{ij} are the electric displacement, entropy, and strain, respectively. These fields have linear (physical) relations to the electric, temperature, and stress variables, as derived in the previous sections. Therefore, one could write

$$dU = \varepsilon_{ij} d\sigma_{ij} + D_i dE_i + S dT \tag{2.56}$$

as an equivalent expression for independent fields σ_{ij}, E_i, and T. The Gibbs free energy is

$$G = U - \sigma_{ij} d\varepsilon_{ij} + E_i dD_i + T dS, \tag{2.57}$$

whose differential

$$dG = -\varepsilon_{ij} d\sigma_{ij} - D_i dE_i - S dT, \tag{2.58}$$

can be obtained with the help of Eq. (2.55). The so-called Maxwell relations can be extracted from this differential as

$$dG = \left(\frac{\partial G}{\partial \sigma_{ij}}\right)_{\mathbf{E},T} d\sigma_{ij} + \left(\frac{\partial G}{\partial E_i}\right)_{\sigma,T} dE_i + \left(\frac{\partial G}{\partial T}\right)_{\sigma,\mathbf{E}} dT, \tag{2.59}$$

so that

$$\varepsilon_{ij} = -\left(\frac{\partial G}{\partial \sigma_{ij}}\right)_{\mathbf{E},T}, \; D_i = -\left(\frac{\partial G}{\partial E_i}\right)_{\sigma,T}, \text{ and } S = -\left(\frac{\partial G}{\partial T}\right)_{\sigma,\mathbf{E}}. \tag{2.60}$$

by comparison with Eq. (2.58). Three more relations can be obtained by taking the second derivative of G,

$$d_{ijk}^{T} = -\left(\frac{\partial^2 G}{\partial \sigma_{ij}\partial E_k}\right)_{T}, \; \alpha_{ij}^{\mathbf{E}} = -\left(\frac{\partial^2 G}{\partial \sigma_{ij}\partial T}\right)_{\mathbf{E}}, \text{ and } p_i^{\sigma} = -\left(\frac{\partial^2 G}{\partial E_i \partial T}\right)_{\sigma}. \tag{2.61}$$

which yields the piezoelectric (d_{ijk}), thermal expansion α_{ij}, and pyroelectric (p_i) material constants (compliances) at constant temperature, electric, and stress field respectively. Therefore, one can write after integration [245],

$$\begin{aligned} \varepsilon_{ij} &= s_{ijkl}^{\mathbf{E},T}\sigma_{kl} + d_{kij}^{T}E_k + \alpha_{ij}^{\mathbf{E}}\Delta T \\ D_i &= d_{ijk}^{T}\sigma_{jk} + \epsilon_{ij}^{\sigma,T}E_j + p_i^{\sigma}\Delta T \\ \Delta S &= \alpha_{ij}^{\mathbf{E}}\sigma_{ij} + f_i^{\sigma}E_i + \left(\frac{C_V^{\sigma,\mathbf{E}}}{T}\right)\Delta T, \end{aligned} \tag{2.62}$$

where the superscripts indicate compliances at constant field. The specific heat C_V is taken at constant volume (and constant electromechanical boundary conditions) and relates the changes in entropy to the change in the temperature.

2.3.2 Material tensor symmetries

The inherent symmetries of the material must be reflected in the *measured* physical properties of the crystal. Formulated as Neumann's principle, this statement postulates that *if* the lattice is invariant with respect to certain symmetry elements, then the observable

physical properties must also be invariant with respect to the same symmetry elements. Mathematically, this powerful principle can be used to drastically simplify a variety of different calculations. In our case, we utilize symmetrized compliance tensors for all the calculations reported in Chapters 4, 5, and 6. In order to identify what elements of a material tensor are zeroed out by virtue of a certain symmetry being present in the crystal, one needs to employ a simple linear relationship,

$$T'_{ijkl\ldots} = a_{i\alpha}a_{j\beta}a_{k\gamma}a_{l\delta}T_{\alpha\beta\gamma\delta\ldots}, \tag{2.63}$$

where a is the corresponding symmetry operation. I.e., if the crystal possesses this symmetry element, then the material tensor must be left unchanged by it:

$$T'_{ijkl\ldots} = T_{ijk\ldots}, \tag{2.64}$$

Symmetry operation a is usually uniquely represented by an appropriate direction cosine matrix [78]. For example, let's consider a coordinate system denoted by $\{\hat{e}_1, \hat{e}_2, \hat{e}_3\}$ that will be transformed into $\{\hat{e}'_1, \hat{e}'_2, \hat{e}'_3\}$. The symmetry operation can rotate, reflect, and invert, and its representation matrix a_{ij} obeys $a_{ik}a_{kj} = \delta_{ij}$ and $a^{-1} = a_{ji} = a^T_{ij}$, where T denotes the transpose operation. Therefore, the relation

$$\hat{e}'_i = a_{ij}\hat{e}_j, \tag{2.65}$$

must hold.

Rotations of a material tensor

The directions of local crystallographic axes within a material may not always coincide with those of the cartesian axes of some global coordinate system. For example, in polycrys-

talline films, individual crystalline grain orientations are likely to be different from that of the global 'measurement' coordinate axis. Therefore, all the local materials tensors of individual grains must be rotated to align with the global coordinate system. These rotations are done with the help of Euler rotation matrices that are constructed from special rotation operators, which can capture any orientation of a crystallographic axis in space. Consider the following rotations

$$R(\theta)_{\hat{x}} = \begin{pmatrix} \cos\theta & \sin\theta & 0 \\ -\sin\theta & \cos\theta & 0 \\ 0 & 0 & 1 \end{pmatrix}, \tag{2.66}$$

$$R(\theta)_{\hat{y}} = \begin{pmatrix} \cos\theta & 0 & \sin\theta \\ 0 & 1 & 0 \\ -\sin\theta & 0 & \cos\theta \end{pmatrix},$$

$$R(\theta)_{\hat{z}} = \begin{pmatrix} 1 & 0 & 0 \\ 0 & \cos\theta & \sin\theta \\ 0 & -\sin\theta & \cos\theta \end{pmatrix},$$

which constitute rotations by angle θ about the cartesian axes $\hat{e}_1 = \hat{x}$, $\hat{e}_2 = \hat{y}$, and $\hat{e}_3 = \hat{z}$ (indicated by subscripts) respectively. The Bunge [45] sequence performs rotations in $\mathbf{Z}(\theta)\mathbf{X}(\phi)\mathbf{Z}(\psi)$ order, i.e., as three successive transformations $\{\hat{e}_k\} \rightarrow \{\hat{e}'_k\} \rightarrow \{\hat{e}''_k\}$. Specifically, the first rotation is by angle Ψ about the $\hat{z}$ axis, the second is by angle ϕ about the new $\hat{x}'$ axis and the third is by angle θ about the new $\hat{z}''$ axis. This transformation sequence can be compactly represented as

$$R_{\alpha\beta} = R_{\alpha j}(\theta)_{\hat{z}''} R_{jk}(\phi)_{\hat{x}'} R_{k\beta}(\Psi)_{\hat{z}} \tag{2.67}$$

where $R_{\alpha\beta}$ is the Euler rotation matrix. In expanded form

$$R_{\alpha\beta}(\theta,\phi,\Psi) \tag{2.68}$$
$$= \begin{pmatrix} \cos\theta\cos\Psi - \cos\phi\sin\theta\sin\Psi & -\cos\theta\sin\Psi - \cos\phi\cos\Psi\sin\theta & \sin\theta\sin\phi \\ \cos\Psi\sin\theta + \cos\theta\cos\phi\sin\Psi & \cos\theta\cos\phi\cos\Psi - \sin\theta\sin\Psi & -\cos\theta\sin\phi \\ \sin\phi\sin\Psi & \cos\Psi\sin\phi & \cos\phi \end{pmatrix}$$

2.4 Ferroelectric materials

Depending on the underlying symmetry of the dielectric crystal, it can be assigned to one or another material class, with the members of the same class exhibiting certain unique aspects of dielectric behavior. Out of 32 crystallographic point groups, 11 groups are *centrosymmetric*, i.e., contain an 'inversion center' symmetry operation that is incompatible with any vectorial material property. In such crystals, ionic and electronic charge distributions in the unit cell are arranged centrosymmetrically and their charge centers coincide. Therefore, these crystals cannot exhibit any intrinsic polar properties (e.g., piezo- or pyroelectricity) and are also called *nonpolar*.

The remaining 21 crystallographic point groups can be further partitioned into 10 *polar* and 11 *polar-neutral* groups (according to the classification of Zheludev [333] that does not explicitly discuss the issue of *chirality*). In the *polar-neutral* crystals, the positive/negative charge centers still coincide, however, the charges themselves are no longer arranged centrosymmetrically within the unit cell. Therefore, such positive and negative charge distributions will react differently to applied elastic distortions or electric fields, and the associated materials will possess *piezoelectric* properties. In the *polar* crystals, even the positive/negative charge centers in the unit cell no longer coincide, which is equivalent to the presence of at least one 'special' symmetry axis along which a dipole moment can formally develop (which may be large or small, as symmetry arguments alone cannot determine its magnitude). Such

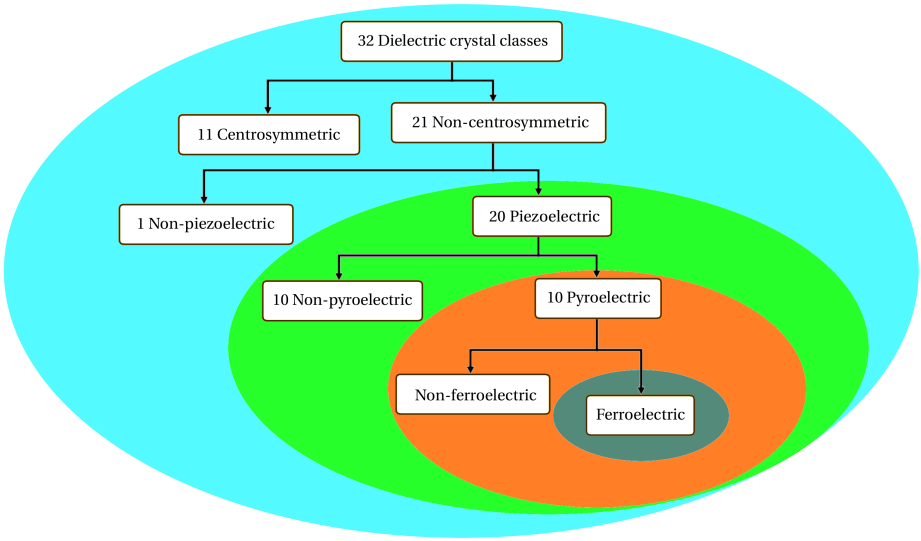

Fig. 2.5 Partitioning of dielectric materials into piezoelectric, pyroelectric and ferroelectric classes according to their symmetry.

polar crystals possess *spontaneous polarization* and are also called *pyroelectric*, although the presence of polarization in them is a consequence of their symmetry and is not connected to any thermal effects. By default, all *pyroelectric* crystals are also *piezoelectric*.

Finally, *ferroelectric* crystals are defined as those *pyroelectric* crystals where spontaneous polarization can be developed along multiple (i.e., two or more) symmetrically equivalent special axes. It is also implied that it should be possible to switch the polarization from one special direction to another by application of a strong enough electric field. By default, all *ferroelectric* crystals are also both *pyroelectric* and *piezoelectric*. Also, at rising temperatures most ferroelectric crystals become nonpolar or polar-neutral, i.e., lose their spontaneous polarization, before melting or decomposing. The associated phase transformation, which may be quite complex in its nature, is called *ferroelectric to paraelectric* and the critical temperature at which it happens is called the Curie temperature, or T_C. A graphical diagram representing the relations between the different dielectric material classes is presented in Fig. 2.5. Occasionally throughout the rest of the thesis, the material symmetry may be discussed in terms of the 32 crystallographic point groups presented here, in either Hermann-

Mauguin (international) or Schoenflies notations. All of the crystallographic point groups together with their associated intrinsic polar properties are shown in Table 2.1.

	International	Schoenflies	Polar	Piezoelectric
Triclinic	1	C_1	✓	✓
	$\bar{1}$	C_i		
Tetragonal	4	C_4	✓	✓
	$\bar{4}$	S_4		✓
	$4/m$	C_{4h}		
	422	D_4		✓
	$4mm$	C_{4v}	✓	✓
	$\bar{4}2m$	D_{2d}		✓
	$4/mmm$	D_{2h}		
Hexagonal	6	C_6	✓	✓
	$\bar{6}$	C_{3h}		✓
	$6/m$	C_{6h}		
	622	D_6		✓
	$6mm$	C_{6v}	✓	✓
	$\bar{6}m2$	D_{3h}		✓
	$6/mmm$	D_{6h}		
Monoclinic	2	C_2	✓	✓
	m	C_8	✓	✓
	$2/m$	C_{2h}		
Orthorhombic	222	D_2		✓
	$mm2$	C_{2v}	✓	✓
	mmm	D_{2h}		
Trigonal	3	C_3	✓	✓
	$\bar{3}$	S_6		
	32	D_3		✓
	$3m$	C_{3v}	✓	✓
	$\bar{3}m$	D_{3d}		
Cubic	23	T		✓
	$m3$	T_h		
	432	O		
	$\bar{4}3m$	T_d		✓
	$m3m$	O_h		

Table 2.1 The 32 crystallographic point groups in both Hermann-Mauguin (international) and Schoenflies notation, along with their intrinsic polar properties (after Ref. [103]).

2.4.1 Ferroelectricity

Since its discovery in the Rochelle salts in 1922 by Valasek [300], a number of scientists have endeavored to understand the *microscopic* origins of ferroelectricity as well as their *macroscopic* manifestations. The first theories from Ginzburg [99] and Devonshire [72, 73] proposed a model that did not consider any microscopic mechanisms, instead describing ferroelectric behavior and the associated phase transformations on the phenomenological level. This model was well-matched with the experimental observations of Merz [224] and others [304, 315], who studied a prototypical ABO_3 perovskite-ferroelectric oxide, $BaTiO_3$.

Merz was able to show that the measured dielectric constant obeys a Curie-Weiss law,

$$\epsilon = \frac{C}{T - T_C} \tag{2.69}$$

where C is a material constant. Note that Eq. (2.69) is valid above T_C, where a similar expression exists for temperatures below the transition point. As shown in Fig. 2.6, the system dielectric constant ϵ, *diverges* at $T \simeq T_C$. At around the same time, other ferroelectric

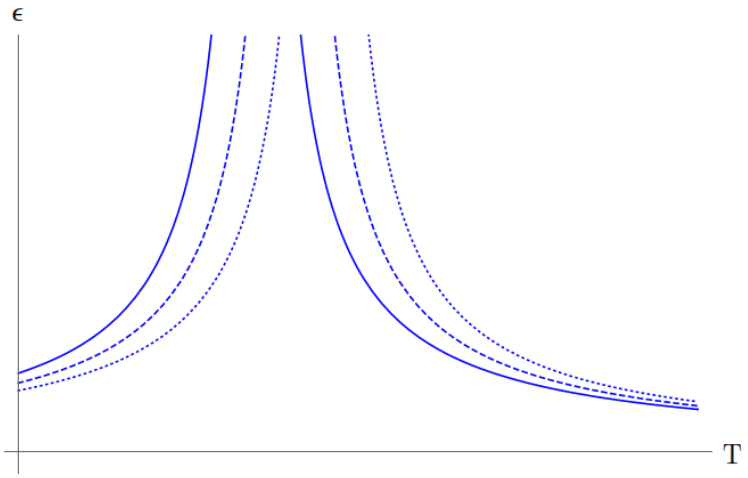

Fig. 2.6 Illustration of the Curie-Weiss temperature dependence, [Eq. (2.69)], near the phase transition point for different T_C.

systems such as tri-glycine sulfate $[(NH_2CH_2COOH)_3 \cdot H_2SO_4]$ (TGS) [218], tri-glycine fluoberyllate $[(CH_2NH_2COOH)_3 \cdot H_2BeF_4]$ (TGFB) [125] and also di-hydrogen phosphate $[KH_2PO_4]$ (KDP) were studied. A similar, i.e., divergent near T_C, dielectric constant behavior was observed in all of these ferroelectric systems [146], however, a microscopic level understanding of physical mechanisms underpinning the emergence of polarization in these materials was not well developed at the time.

The early theories that could explain the divergence of the dielectric constant utilized formalism developed by Landau, that involved expanding the crystal free energy into symmetrically irreducible monomials containing powers of the relevant system variable, or the

so-called *order parameter* based upon it (the latter is usually introduced as having nonzero values below the phase transition temperature that vanish above it). Devonshire's choice for the order parameter was macroscopic polarization, and the developed theory explained both measured ferroelastic effects and the divergent dielectric constant near the phase transition point in $BaTiO_3$ [72, 73]. However, this effort did not answer the question as to what atomistic-level mechanism was responsible for the macroscopic polarization in BTO.

It was hypothesized that below the Curie temperature, the structure of BTO changes from point group $m3m$ (cubic) to $4mm$ (tetragonal) with one of the cube faces elongating along the direction of the polar axis, as shown in Fig. 2.7. Two more phases were observed

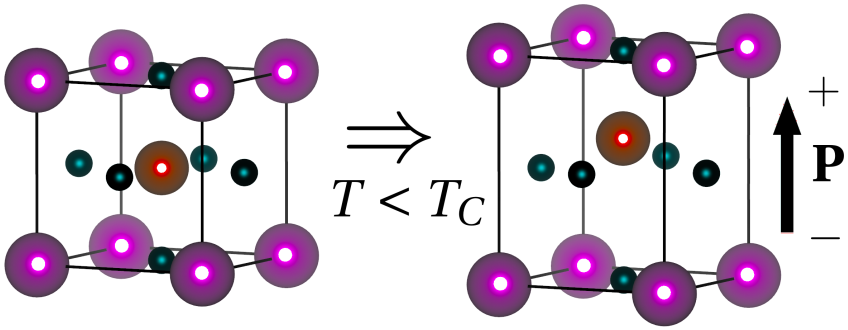

Fig. 2.7 $BaTiO_3$ perovskite unit cell pictured in both cubic (left) and tetragonal (right) symmetry. The tetragonal phase is characterized by an off-centering of the Ti center ion. Here, Ba atoms are shown in purple, Ti atoms in brown and O atoms in black colors.

at temperatures below T_C having (*i*) an *mm* orthorhombic symmetry where the **P** vector is pointing along one of the $\langle 110 \rangle$ directions, which are cubic cell side diagonals, and (*ii*) a $3m$ rhombohedral symmetry where **P** points along one of the $\langle 111 \rangle$ (pseudo-cubic) directions, which are cubic cell space diagonals. At each successive phase transition, the crystal also exhibited large dielectric response.

Early attempts by Slater [288] to illuminate the microscopic origins of ferroelectricity involved a hypothesis that the unit cell tetragonality was not strongly affecting the polarization, with the bulk of the effect being due to off-centering of the Ti ion inside the octahedral oxygen cage. The equation of motion of the Ti ion inside cage under a time-dependent harmonic

electric field applied along the polar direction [$x = x(t)$], is

$$m\frac{d^2x}{dt^2} + \gamma\frac{dx}{dt} + (K_S - K_L + B\cdot T)\,x = eE_0e^{i\omega t}, \tag{2.70}$$

where K_S and K_L are short-range and long-range (electrostatic) resorting force constants. Slater included the linear $B\cdot T$ term to account for possible lowest-order anharmonic restoring forces due to nonzero temperature. Defining the polarization as

$$P(t) = Nex(t) = \chi E_0\, e^{i\omega t}, \tag{2.71}$$

and then solving Eq. (2.70) for x, gives

$$\chi(\omega) = \frac{Ne^2/m}{\bar{\omega}^2 - \omega^2 + i\omega\gamma/m}, \tag{2.72}$$

where

$$\bar{\omega}^2 = (BT - K_L + K_S)/m = \frac{B}{m}\left(T - \frac{K_L - K_S}{B}\right). \tag{2.73}$$

is a *soft-mode* frequency. Clearly if $\omega = 0$, then

$$\chi(0) = \frac{Ne^2/m}{\bar{\omega}^2} = \frac{C}{T - \frac{K_L - K_S}{B}} \tag{2.74}$$

which is a Curie-Weiss law for $T_C = (K_L - K_S)/B$.

The idea of a soft-mode is important for understanding microscopic mechanisms underpinning the ferroelectric behavior. As noted by Cochran [59], as T approaches T_C from above, $\bar{\omega} \to 0$ and the lattice distortion induced by this vibrational mode becomes 'frozen' into the paraelectric crystal structure, effectively breaking its symmetry. The specific symmetry of the emergent polar phase below T_C is then determined by the symmetry of the 'frozen in'

vibrational mode eigenvector, or a combination thereof, if multiple modes are slowing down simultaneously. Such *displacive* phonon mode softening in $BaTiO_3$[11] was observed in early inelastic neutron scattering data [286, 277]. But this scenario was challenged by electron paramagnetic resonance [233], diffuse X-ray scattering [62], and nuclear magnetic resonance (NMR) experiments [324, 325].

In the low-temperature NMR data, the potential energy surface for the Ti ion was shown to have eight off-center minima corresponding to the equivalent [111] faces of the octahedral cage. This lead to a different idea, first noted by Bersuker [35], that above T_C polar off-centerings of the Ti ions may be (statically or dynamically) disordered among these eight possible directions, which would produce a non-polar symmetry when Ti displacements are averaged out over all the directions . The other polar-to-polar phase transformations occurring below T_C in $BaTiO_3$ were then explained as well, utilizing the same arguments. Therefore, one could say that experimental signatures of both order-disorder and displacive transitions are seen in $BaTiO_3$, which are important for understanding of its macroscopic polar behavior.

Now we return to the discussion of Devonshire's theory with better understanding of the molecular, or unit-cell level phenomena that may be behind the emergence of macroscopic ferroelectricity. As one of the simplest cases of this theory, we can consider a system free energy expansion, up to sixth monomial order, in powers of the one-dimensional order parameter P, which is spatially uniform and cannot vary with the change of position vector $\mathbf{x}$:

$$F_p = \frac{1}{2}a_0(T - T_C)P^2 + \frac{1}{4}bP^4 + \frac{1}{6}cP^6 - EP. \tag{2.75}$$

[11] This transition — from cubic ($Pm\bar{3}m$) to tetragonal ($P4mm$) structure — in $BaTiO_3$ involves freezing in of a Brillouin-zone-center vibrational mode, which leads to macroscopic polarization (since the frozen in distortion is the same in each unit cell). Other transformations are possible, such as, e.g., in $SrTiO_3$, where the transition from cubic ($Pm\bar{3}m$) to tetragonal ($I4/mcm$) happens by freezing in of a vibrational mode that belongs to the Brillouin-zone boundary. The latter is an antiferrodistortive transition accompanied by doubling of the unit cell at $T = 110$ K [282].

In the paraelectric system state at $T > T_C$, this function produces a quadratic dependence on the polarization at zero electric field, with F_p having a minimum at $P = 0$. When the electric field is nonzero, the location of this parabolic energy minimum is shifted, as shown in Fig. 2.8 **(a)**. This behavior is representative of that of a linear dielectric under applied electric field. On the other hand, for $T < T_C$ and $E = 0$, F_p adopts a well-known 'double well' form, with both symmetrically equivalent energy minima occurring at $P \neq 0$. The presence of a nonzero electric field breaks this symmetry, favoring one energy minimum over the other, as shown in Fig. 2.8 **(b)**. Obtaining the minima of this function by taking

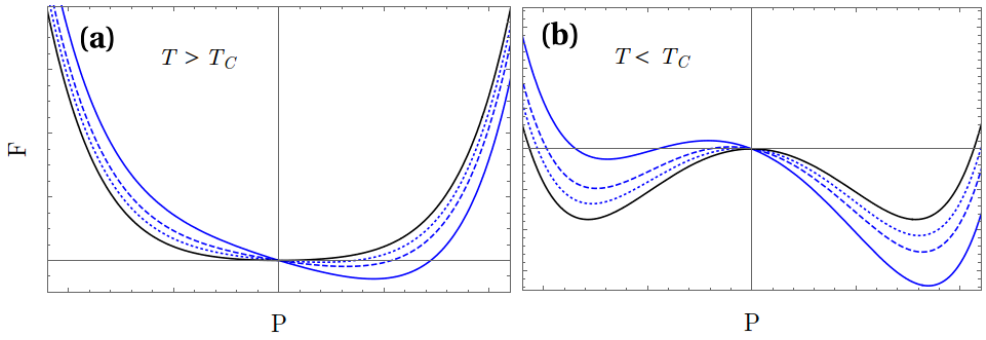

Fig. 2.8 **(a)** Paraelectric ($T > T_C$) and **(b)** ferroelectric ($T < T_C$) F_p distributions for zero-field (black) and under successively stronger electric fields (blue), which bias the energy wells along the $+P$ direction.

$$\frac{dF_p}{dP} = 0, \tag{2.76}$$

leads to the following expressions for the electric field

$$E = a_0(T - T_C)P + bP^3 + cP^4, \tag{2.77}$$

and dielectric susceptibility χ

$$\chi \approx \frac{P}{E} = \frac{P}{a_0(T - T_C)P + bP^3 + cP^4}, \tag{2.78}$$

which again captures the Curie-Weiss behavior shown in Fig. 2.6.

It is instructive to highlight the dependence of the system polarization on the applied electric field for both the paraelectric $T > T_C$ and ferroelectric $T < T_C$ cases. The former case, corresponding to the typical behavior of a linear dielectric, is visualized in Fig. 2.9 **(a)**. However, below T_C, ferroelectric polarization switches in a highly nonlinear fashion — or exhibits a so-called *hysteretic* behavior — as shown in two examples are in Fig. 2.9 **(b)** and **(c)**. This nonlinear behavior arises due to two primary factors:

- The electric field needs to be sufficiently large to switch the polarization from one symmetry equivalent direction to another *over the zero field energy barrier*.
- The presence of ferroelectric domains in the sample (the origins of domains will be discussed in the following section).

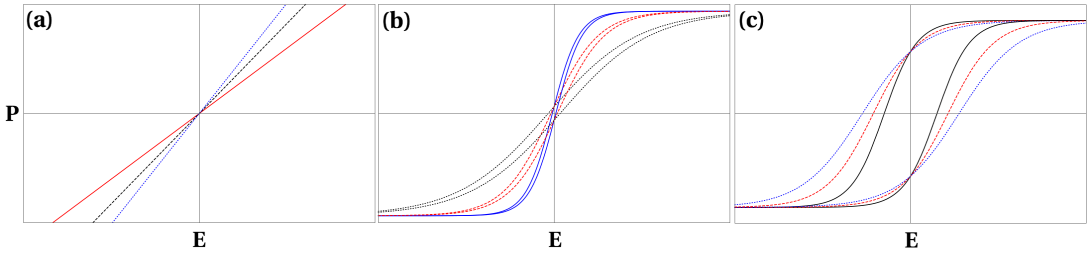

Fig. 2.9 Linear **(a)**, nonlinear lossless **(b)**, and nonlinear lossy **(c)** ferroelectric polarization switching.

The lateral width of the hysteresis loop (or equivalently, the value of *coercive* electric field needed to de-polarize the sample to zero polarization) is known to be strongly dependent on a variety of different factors, including absence or presence of any defects in the sample, as well as their concentration, frequency of the applied electric field, absence or presence of any distortions of the sample shape and etc. For more information on the applications of the Landau theory for the studies of ferroelectric behavior, the reader is referred to comprehensive discussions found in the texts by Jona and Shirane [146], and Lines and Glass [195].

2.4.2 Ferroelectric domains and their structure

A distinct feature of ferroelectric materials is their ability to form polar domains under certain conditions. As the material is cooled down below the Curie temperature, its local polarization evolves towards thermodynamic equilibrium. In the absence of an applied field (or some other ordering influence), the stationary state of the polarization distribution throughout the material is usually a complex equilibrium pattern[12] pattern, known as the *domain structure*. Locally, individual unit-cell polar distortions tend to point along energetically favorable directions (i.e., 'easy' polarization axes set by the symmetry and electronic properties of a given material), will these directions being correlated among multiple unit cells within the same finite spatial region. However, since in a ferroelectric there are multiple symmetrically equivalent 'easy' polarization directions to choose from, under no applied bias different spatial regions may develop differently oriented local polarizations. For example, in the tetragonal (*P*4*mm*) phase of an ABO_3 perovskite ferroelectric there are six symmetrically equivalent directions along which the B cation can off-center towards one of the oxygens comprising the octahedral cage that surrounds it, thus inducing a unit-cell dipole moment in the same direction. When spatial regions (or domains) possessing differently oriented polarizations meet, a boundary — or domain wall — separating individual domains is formed. If within the domain the polarization may be nearly constant, it has to vary quite strongly both in magnitude and in direction within the domain wall area, and thus the latter may be considered as a special boundary phase that is symmetrically distinct from those of the neighboring domains.

For example, in the above simple case of a tetragonal ferroelectric, a mating of differently oriented 'polar variants' usually results in polarization rotating by either 180° or 90°, which can be used for classification of the emerging domain-wall patterns[13]. An example of a 180°

[12] Which is not the true global energy minimum of the system, but rather a local metastable energy minimum [128].

[13] The latter could be "charge-neutral" with head-to-tail arrangement, or be a "charged" domain wall with tail-to-tail or head-to-head configuration.

or "stripe" domain-wall pattern is shown in Fig. 2.10 and is characteristic for a variety of thin perovskite-ferroelectric films grown on supporting substrates with compressive elastic misfit epitaxy (to be discussed shortly).

For such thin-film geometries (i.e., structures that can be considered quasi-infinite in the substrate plane and finite along the perpendicular/growth direction), it has been observed in early work from Landau [166] and Kittel [159] that the "stripe" domain periodicity or, equivalently, the spacing between adjacent domain walls w has a proportional simple dependence on the film thickness h:

$$w \propto \sqrt{h}, \tag{2.79}$$

which, remarkably, remains valid for many different types of ferroelectric materials.

However, this law breaks down for some nanoscale structures with characteristic sizes of 10 nm to a few μm. For example, Son *et al.* [289] fabricated $PbTiO_3$ nanoislands and found that a non-ferroelectric surface layer can form due to a lateral-size effect which modifies the Kittel scaling law quite dramatically,

$$w = \sqrt{\frac{h}{cP_0^2}\left[a\left(\frac{n-1}{n}\right)+b\frac{1}{n}\right]}, \tag{2.80}$$

where a, b, c, P_0 are island material parameters and n is the number of "stripes" supported by the island. In a limit of low n where $a > b$, Eq. (2.80) produces a different scaling law, compared to that of Eq. (2.79), suggesting that inhomogeneous phases, such as nonferroelectric dead layers and etc., can radically alter materials behavior at small length scales.

We should point out that in addition to simple "stripe" patterns, much more complicated domain wall arrangements are possible, depending on the underlying symmetry of the particular polar phase of the ferroelectric material (e.g. in $BiFeO_3$ [142, 318]). Ferroelectric domains are typically 10 nm to a few μm in size [146, 195]. Their presence in a material

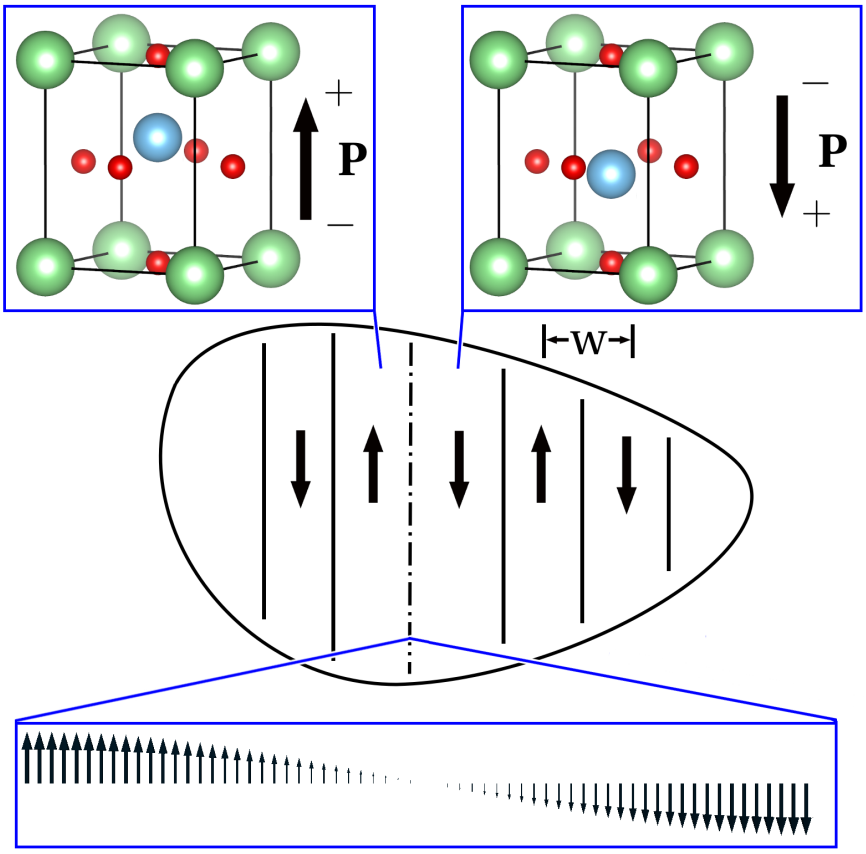

Fig. 2.10 Unit-cell off-centerings of Ti^{4+} ions in tetragonal $BaTiO_3$ leading to an emergence of a simple 180° "stripe" domain-wall pattern with Ising domain walls. Such wall type is characterized by shrinking of the polarization magnitude and absence of polarization vector rotations as the domain wall is traversed.

or nanostructure can be determined by a number of different experimental techniques, such as electron microscopy, second-harmonic generation, optical birefringence measurements, x-ray diffraction, or ultraviolet photoemission [195].

Domain wall types and topological defects

In addition to the already mentioned Ising domain-wall type, there are other basic types, such as Bloch and Neél, as well as 'hybrid' walls that simultaneously exhibit behavior characteristic of two different basic types, for example, Ising-Neél or Ising-Bloch. Illustrations of some of domain-wall types are presented in Fig. 2.11 **(a)** and **(b)**. Recent experimental and theoretical data suggest that most domain-wall configurations encountered in ferroelectric systems are actually *hybrid* walls, where both polarization vector magnitude and direction change substantially as the wall area is traversed [173, 53, 291], although there is a debate whether rotational, i.e., Bloch-type walls could occur in tetragonal ABO_3 systems [122].

It is clear that the combination of system variables, such as strain and polarization, within the domain-wall region must be energetically unfavorable, compared that of inside the domain, and thus any kind of 'domain-wall energy' terms must come as a penalty to the system free energy. For example, while traversing the Ising domain wall, polarization has to shrink to zero see Fig. 2.11 **(a)**]. This corresponds to establishing a paraelectric state below the Curie temperature, which has much higher energy, compared to the ferroelectric phase. On the other hand, in walls with rotational character [see Fig. 2.11 **(b)**], polarization can point along elastically sub-optimal directions, such as, e.g., compressed, rather than elongated unit-cell sides, which also carries a steep energy penalty.

In our previous discussion, we considered an example where multiple polar regions (domains) may form in different areas of the sample, with their orientations chosen randomly among the possible 'easy' axis orientations, which would eventually lead to the formation of domain walls separating these regions. However, if the presence of domain walls in

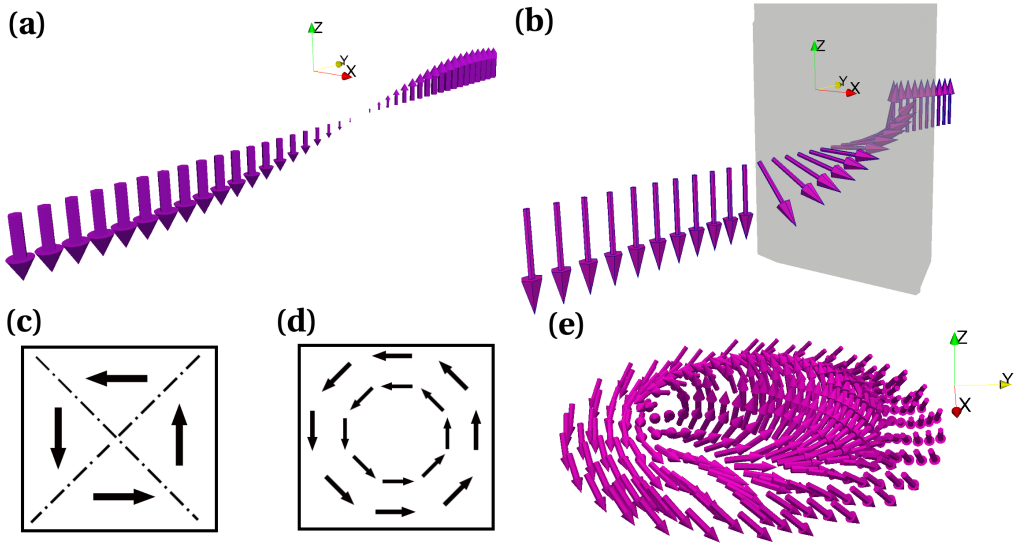

Fig. 2.11 Some topological defects possible in ferroic systems. **(a)** An Ising domain wall, where the magnitude of the polarization decreases and then grows again across the domain wall and **(b)** a Bloch domain wall, where the polarization magnitude is fixed, while its direction rotates in the $\hat{\mathbf{x}}$-$\hat{\mathbf{z}}$ plane across the domain wall region. Two possible domain states, a flux-closure pattern of 90° (correlated) domains **(c)** and a vortex-like (circular) phase **(d)** are **(e)** A skyrmion is a collection of vectors that produce a 360° axially symmetric twist in both the $\hat{\mathbf{x}}$-$\hat{\mathbf{y}}$ and $\hat{\mathbf{x}}$-$\hat{\mathbf{z}}$ planes.

the sample is energetically unfavorable, we are left with the question how a multidomain configuration could ever be realized over a monodomain one (assuming that the system always have enough time to evolve towards the true ground state by moving all the domain walls out of the sample)? The answer to this question comes from considering possible electrostatic boundary conditions for the *surface* of the ferroelectric sample. For example, in a thin-film sample, pictured in Fig. 2.12 **(a)**, the electric displacement field normal to the interface of the free surface must be zero, i.e.,

$$D_z = 0 = \epsilon_0 \left(\mathbf{E}_{\text{dep}} \cdot \hat{\mathbf{z}}\right) + \alpha P_z \Rightarrow P_z = -\frac{\epsilon_0}{\alpha} \left(\mathbf{E}_{\text{dep}} \cdot \hat{\mathbf{z}}\right),$$

where $\mathbf{E}_{\text{dep}}$ is the so-called depolarizing field. The solution of the Poisson equation will minimize surface charges, represented by the $\mathbf{P} \cdot \hat{\mathbf{z}}$ term, so that for the 'open-circuit' boundary condition, shown in Fig. 2.12 **(a)**, formation of a normal P_z component will be energetically unfavorable and an in-plane monodomain (or multidomain) will form instead. However, this consideration is true only for a sample that is free to distort in order to accommodate any polarization orientation. If instead the sample is elastically clamped to an *insulating* substrate that strongly encourages normal polarization direction (e.g., by squeezing the lateral planes of the perovskite unit cells), optimizing the system energy by pointing the polarization vector in-plane will be impossible. In that particular case, an optimal polarization field $\mathbf{P}(\mathbf{r})$ configuration is a stripe domain pattern with P_z components alternating between positive and negative directions in neighboring domains. And it is clear that, although such a domain pattern does not result in a surface that is charge neutral in any *local* area, it does create a surface that that is charge neutral *globally*, since alternating regions of positive and negative surface charge will average out over the whole surface, thus eliminating the global depolarizing field. This is exactly the configuration that gets realized in many perovskite ferroelectric thin films that are grown pseudomophically on *compressive* non- or poorly-conductive substrates. However, if a highly conductive substrate and a top electrode are used

instead, i.e., a ferroelectric capacitor is formed, as shown in Fig. 2.12 **(b)**, then all the the surface charges are screened and the monodomain polarization configuration is the lowest energy state.

Rich behavior that can be realized in ferroelectric systems with domains can lead to variety of interesting phenomena of practical importance. For example, unusual transport properties have been observed for certain domain-wall configurations [281, 206, 280, 221] and in the case of $BiFeO_3$ systems, strong conductivity enhancement was detected for some domain-wall types [24]. Also, domain configurations as the one shown in Fig. 2.11 **(c)** include flux-closure points that emerge at intersections of four 90° domain walls. Recent work has shown that flux-closure polarization motifs interact rather weakly with one another (in $BaTiO_3$) and that they can be manipulated independently by external electric fields [220], which may open up new avenues for applications of such systems for nonvolatile memory applications. It has also been predicted (by Kittel [159]), that a circular ordering of spins

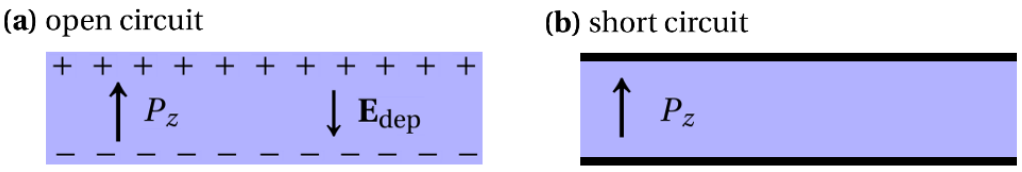

Fig. 2.12 **(a)** Open-circuit and **(b)** short-circuit boundary conditions for the ferroelectric thin-film sample.

in magnetic nanostructures, such as the one shown in Fig. 2.11 **(d)**, can form when system size is reduced. Such vector patterns must possess *toroidal* degrees of freedom, i.e., toroidal moment

$$\mathbf{G} = \frac{1}{V}\left[\sum_k \mathbf{P}_k \times \mathbf{R}_k\right], \tag{2.81}$$

where index k enumerates unit cells located at $\mathbf{R}_k$ that are enclosed by volume V. Simulations utilizing effective hamiltonian techniques had suggested that such 'electric-dipole vortex

states' can be stabilized under certain boundary conditions [240, 241] and may be useful for integrating new functionalities into electronic devices.

In ferroelectric $(PbTiO_3)_n/(SrTiO_3)_m$ superlattices, polarization-vortex phases were observed in $(PbTiO_3)$ layers. Stabilization of the vortex states was found to be strongly dependent on the thickness (in the number of unit cells n, m) of the $(PbTiO_3)$ and $(SrTiO_3)$ superlattice component layers [319]. Furthermore, vortex-core lines were seen to develop long-range ordering, spanning a few *microns* in the material, which could also potentially be exploited for memory applications.

Very similar topological defects incorporating domains and domain walls are also encountered in ferromagnets, where the relevant system variable is a fixed-magnitude magnetization field. Experimental observations of a skyrmion state, namely a 360° axially symmetric twist in two planes [see, e.g., Fig. 2.11 **(e)**], in chiral ferromagnets (such as MnSi [232] or FeGe [322]) have determined that the canting of the magnetic moments is due to Dzyaloshinski-Moriya interactions [77, 230]. Also, by nanopatterning trilayer magnetic composites of Ta (5 nm) / $Co_{20}Fe_{60}B_{20}$ (1.1 nm) / TaO_x (2 nm) grown with magnetron sputtering, Jiang *et al.* [141] were able to show that under applied current, the moving domain walls in the heterostructure form enclosed skyrmionic regions (or bubbles). This work highlights a dynamic approach to generating skyrmions,[14] which could lead to useful insights for novel spintronic applications.

There are a number of works attempting to induce the skyrmion polarization texture in ferroelectric materials by using external electric fields. For instance, in an effective hamiltonian simulation it was shown that a stable skyrmion could exist at the 90° domain-wall flux-closure points in a cylindrical BTO sample embedded in a $Ba_{0.15}Sr_{0.85}TiO_3$ matrix [236] after thermal annealing under an electric field. Quite recently, a simulation of an intersection of two oppositely-helical (180°) Ising domain walls in $BaTiO_3$ predicted that a

[14] It should be noted that in addition to ferroic crystals, skyrmions have been also observed in chiral nematic liquid crystals [92, 109], superconductors [175, 160, 94], and Bose-Einstein condensates [176, 154, 31].

skyrmion-like texture can be realized [291], suggesting that such quasi-particles may already exist in inhomogeneous ferroelectric systems.

One possible use of topologically protected objects, such as skyrmions, is for new types of memory applications. Under a strong applied electric field, any types of topological defects will move, reorient and eventually disappear in favor of a homogeneous polarization distribution aligned with the field direction.

Understanding and controlling the domain wall (or other topological defect) dynamics during switching is very important for possible memory applications. The switching process depends strongly on the spatial distribution of **P**, and in "exotic" ferroelectric systems that can support vortex-like phases, the generic (hysteretic) process of polarization switching can be engineered to proceed in multiple steps [174, 285]. This behavior was observed experimentally by Gruverman *et al*. in $Pb_xZr_{1-x}Ti_3$ disks [105] and also predicted theoretically (using the Landau formalism) by Martelli *et al.* in 180° domain structures in disks of $NaNO_2$.

If the new multistate switching can be efficiently implemented in real applications, then density of stored information can increase tremendously [278, 17]. Furthermore, ferroelectric systems usually have correlation lengths that are about an order of magnitude lower than those of their magnetic counterparts [195, 132]. This favorable reduction in length scale should allow packing more bits into a smaller area.

An applied voltage is not the only available "dial" to dynamically control the behavior of ferroelectric topological defects and domain structure, as well as the resulting material properties. In the last two decades, a considerable progress has been made in the art of growing highly-coherent epitaxial thin films of perovskite oxides on a variety of different substrates [273], introducing lattice misfit strain between substrate and thin film as another functional "dial." Since most of the substrates useful for perovskite phases growth have to provide exactly or approximately square in-plane patterns, static misfit strain (for the stress-free substrate) is biaxially symmetric, so that $\varepsilon = \varepsilon_{xx} = \varepsilon_{yy}$, with the $\hat{\mathbf{z}}$ axis corresponding to the

direction of the film growth. By reasonable pairings of films and substrates, which ensures that ε is not too large (usually below $\pm 2\%$), coherently strained films without significant deprecating defect formation can be produced [326]. The most apparent manifestation of the misfit strain influence on ferroelectric properties is the shifting of the material T_C away from its bulk value. This behavior can be explained by the competition of coupled polar and elastic interactions within the film, where the presence of additional strain (such as uniform biaxial compression or tension) can force the formation of *particular* domain structures [253], which would in turn affect ferroelectric switching. Although being a rather simple phenomenological model, the Landau theory has proven to be remarkably successful in reproducing the prominent features of the $\varepsilon - T$ phase diagrams for $BaTiO_3$ [185], $SrTiO_3$ [186] and $PbTiO_3$ [188], as well as for other oxide materials under various mechanical and electrical boundary conditions. Yet another important parameter that can control ferroelectric behavior is (usually nano- or microscopic) film thickness. Both, thickness-strain and thickness-temperature phase diagrams have also been constructed with the help of Landau theory, for example, for lead zirconate and lead titanate thin films [264].

It is also well known that the misfit strain can gradually relax (diminish in magnitude) away from the substrate-film interface, or be released completely by formation of different crystallographic defects, such as dislocations, when film thickness grows beyond a certain critical value. In the former case, large strain gradients (up to $10^5 m^{-1}$ [216]) may emerge in the film as a result, altering its thermodynamic and ferroelectric behavior. Furthermore, strain gradients may be intentionally engineered into thin films, for example, by compositional grading. In Refs. [208, 207], it was shown that a compositionally graded film [from $PbZr_{0.2}Ti_{0.8}O_3$ to $PbZr_{0.8}Ti_{0.2}O_3$] could exhibit strain gradients that induce tetragonal lattice distortions close to the substrate/film interface and rhombohedral distortions far away from the interface. The low-field dielectric constant obtained for this film was equivalent to that of a monodomain film, despite the presence of domain structure.

Strain-gradient related energy contributions are represented by the *flexoelectric* energy term [5],

$$f_{\text{flexo}} = \frac{F_{ijkl}}{2}\left(\frac{\partial P_k}{\partial x_l}\sigma_{ij} - \frac{\partial \sigma_{ij}}{\partial x_l}P_k\right) \tag{2.82}$$

where F_{ijkl} is the flexoelectric coupling tensor. It was recently demonstrated that in a ferroelectric thin film subjected to a lattice misfit strain, the minimization of the total free energy with the inclusion of this energy term leads to the formation of rotational Bloch- and Neél-type domain walls [107], which may suggest new pathways for engineering skyrmion- or vortex-like polarization configurations into ferroelectric media.

2.4.3 Gradient-flow approach

An important technical question, that was originally highlighted by Hu and Chen [128, 188], is how one can predict the equilibrium inhomogeneous ferroelectric microstructure — or the 'shape' of the polarization field $\mathbf{P}(\mathbf{r})$ — while making no particular assumptions about its initial state? Cao and Cross [48] conducted analytical calculations for highly simplified quasi-one and -two dimensional systems, utilizing homogeneous elastic fields. Nevertheless, important insights were gained from such simple models concerning the energetics and geometry of 90° and 180° (twin) domain walls. Furthermore, this work also validated some assumptions about the form of inhomogeneous elastic fields whose presence is required for thermodynamic stability of the domain walls, as seen in experiments.

Following the work of Su and Landis [292] and starting from the elementary second law of thermodynamics[15], one can derive a time-dependent equation describing the evolution of

[15]The second law states that the total entropy of an isolated system can only increase in time. Mathematically, it can be written as

$$dS > dQ/T$$

for entropy S, temperature T, and heat Q. Implicit within this statement is that the process is irreversible, which is the case of the domain structure formation as ferroic material is cooled below T_C.

$\mathbf{P}(\mathbf{r})$ that has the form of the celebrated Allen-Cahn equation [52, 167, 11]. This equation is known as the time-dependent Landau-Ginzburg-Devonshire equation (TDLGD) and can be used to predict, with some general assumptions about initial conditions, the equilibrium polar domain structure within a ferroelectric system at a given temperature and elastic/electric boundary conditions.

In previous sections, we have established that the ferroelectric polarization field $\mathbf{P}(\mathbf{r})$ can serve as an order parameter describing the polar phase transition within the system. Local polar dipole moments, comprising $\mathbf{P}(\mathbf{r})$, are considered to be immovable ("glued" to the lattice), but also *stretchable* and *rotatable*. One can consider the forces and amount of work needed to reorient these dipoles to form a domain. Fried and Gurtin [88, 89, 110] first introduced such a microforce in continuum-level theory of thermally induced phase transitions. Let ζ_{ij} be a conjugate microforce tensor, such that $\zeta_{ij}\hat{n}_j\frac{\partial P_i}{\partial t}$ is a power density expended across some surface (with usual outward-facing normal $\hat{\mathbf{n}}$) by adjacent distributions of polar dipoles $\mathbf{P}$.

Along with the microforce across a surface, an internal volume microforce π_i exists, such that $\pi_i\frac{\partial P_i}{\partial t}$ is a power density within a given volume. We have to make a distinction between internal and external microforces γ_i that also can influence the state of the polar medium and thus must be taken into account during the force balancing,

$$\oiint_S \zeta_{ij}\hat{n}_j dS + \iiint_V \pi_i dV + \iiint_V \gamma_i dV = 0. \tag{2.83}$$

Applying the divergence theorem to the surface integral and realizing that the volume integration is conducted over an arbitrary volume, we get

$$\frac{\partial \zeta_{ij}}{\partial x_j} + \pi_i + \gamma_i = 0. \tag{2.84}$$

For an *isothermal* process below the Curie temperature, the second law of thermodynamics can be presented in the form of the Clausius-Duhem inequality [298, 147, 292]. In terms of the polar-elastic material variables at constant temperature,

$$\iiint_V \frac{d\mathcal{F}}{dt}dV + \frac{1}{2}\beta\frac{d}{dt}\iiint_V \left(\frac{du_k}{dt}\cdot\frac{du_k}{dt}\right)dV \leq \iiint_V \left(b_k\frac{du_k}{dt} + \Phi\frac{d\rho}{dt} + \gamma_i\frac{\partial P_i}{\partial t}\right)dV \\ + \oiint_S \left(\sigma_{kj}\hat{n}_j\frac{du_k}{dt} - \Phi\frac{\partial\left(D_i\hat{n}_i\right)}{\partial t} + \zeta_{ij}n_j\frac{\partial P_i}{\partial t}\right)dS, \tag{2.85}$$

with ρ the charge density and $\mathbf{u}$ the material elastic displacement vectors. This inequality states that the rate of change of the free energy added to the rate of change of kinetic energy of the elastic medium (with mass density β) must be less than or equal to energy dissipation out of the system (i.e., the energy leaving volume V across surface S) due to the action of the external forces. It is important to note that the internal microforce does not contribute to the power expended [292]. Now, by utilizing the Cauchy's linear momentum equation, which is a version of Eq. (2.12), we can reorganize the second term on the left hand side:

$$\frac{1}{2}\beta\frac{d}{dt}\iiint_V \left(\frac{du_k}{dt}\cdot\frac{du_k}{dt}\right)dV = \beta\iiint_V dV\left(\frac{d^2u_k}{dt^2}\right)\frac{\partial u_k}{\partial t} = \iiint_V dV\left(\frac{\partial\sigma_{kj}}{\partial x_j} + b_k\right)\cdot\frac{du_k}{dt}, \tag{2.86}$$

while one of the surface integrals can again be processed with the help of the divergence theorem:

$$\oiint_S dS\,\sigma_{kj}\hat{n}_j\frac{du_k}{dt} = \iiint_V dV\,\sigma_{ij}\frac{d\varepsilon_{ij}}{dt} + \iiint_V dV\,\frac{\partial\sigma_{ij}}{\partial x_j}\frac{du_i}{dt}. \tag{2.87}$$

By inserting Eqs. (2.86) and (2.87) into Eq. (2.85) we have,

$$\iiint_V \frac{d\mathcal{F}}{dt} dV \leq \iiint_V \left(\sigma_{ij} \frac{\partial \varepsilon_{ij}}{\partial t} + \Phi \frac{d\rho}{dt} + \gamma_i \frac{\partial P_i}{\partial t} \right) dV + \oiint_S \left(-\Phi \frac{\partial \left(D_i \hat{n}_i \right)}{\partial t} + \zeta_{ij} n_j \frac{\partial P_i}{\partial t} \right) dS. \tag{2.88}$$

Then, using the microforce balancing Eq. (2.84) and the divergence theorem for the surface integral involving $\zeta_{ij} n_j$ in Eq. (2.88) we have,

$$\iiint_V \frac{d\mathcal{F}}{dt} dV \leq \iiint_V \left(\sigma_{ij} \frac{\partial \varepsilon_{ij}}{\partial t} + \Phi \frac{d\rho}{dt} - \pi_i \frac{\partial P_i}{\partial t} + \zeta_{ij} \frac{\partial \left(\frac{\partial P_i}{\partial x_j} \right)}{\partial t} \right) dV + \oiint_S \left(-\Phi \frac{\partial \left(D_i \hat{n}_i \right)}{\partial t} \right) dS. \tag{2.89}$$

The next step is to utilize,

$$\frac{\partial}{\partial t} \left(\frac{\partial D_i}{\partial x_i} \right) = \frac{\partial}{\partial t} \rho \tag{2.90}$$

via Eq. (2.52) and rearranging the last term on the right hand side in Eq. (2.89)

$$\oiint_S dS \left(\Phi \frac{dD_i}{dt} \hat{n}_i \right) = \iiint_V dV \left(\frac{\partial \Phi}{\partial x_i} \frac{\partial D_i}{\partial t} + \Phi \frac{\partial^2 D_i}{\partial x_i \partial t} \right), \tag{2.91}$$

we arrive at

$$\iiint_V \frac{d\mathcal{F}}{dt} dV \leq \iiint_V dV \left(\sigma_{ij} \frac{\partial \varepsilon_{ij}}{\partial t} - \frac{\partial \Phi}{\partial x_i} \frac{\partial D_i}{dt} - \pi_i \frac{\partial P_i}{\partial t} + \zeta_{ij} \frac{\partial \left(\frac{\partial P_i}{\partial x_j} \right)}{\partial t} \right). \tag{2.92}$$

It is now assumed without any loss of generality, that the free energy $\mathcal{F}$ can explicitly depend on a number of different system variables, i.e.,

$$\mathcal{F} = \mathcal{F}\left(\varepsilon_{ij}, D_i, P_i, \frac{\partial P_i}{\partial x_j}, \frac{\partial P_i}{\partial t}, \frac{\partial^2 P_i}{\partial t^2}\right). \tag{2.93}$$

Then taking the differential of $\mathcal{F}$ gives

$$\frac{d\mathcal{F}}{dt} = \frac{d\mathcal{F}}{d\varepsilon_{ij}}\frac{d\varepsilon_{ij}}{dt} + \frac{d\mathcal{F}}{dD_k}\frac{dD_k}{dt} + \frac{d\mathcal{F}}{dP_k}\frac{dP_k}{dt} + \frac{d\mathcal{F}}{d\left(\frac{\partial P_i}{\partial x_j}\right)}\frac{d\left(\frac{\partial P_i}{\partial x_j}\right)}{dt} + \frac{\partial\mathcal{F}}{\partial\left(\frac{\partial P_i}{\partial t}\right)}\frac{\partial^2 P_i}{\partial t^2}. \tag{2.94}$$

Noting that

$$\frac{\partial\mathcal{F}}{\partial\varepsilon_{ij}} = \sigma_{ij}, \text{ and } \frac{\partial\mathcal{F}}{\partial D_i} = E_i = \frac{\partial\Phi}{\partial x_i}, \tag{2.95}$$

and then substituting Eq. (2.94) into Eq. (2.92), we get

$$\begin{aligned}\iiint_V \left(\frac{\partial\mathcal{F}}{\partial P_k}\frac{\partial P_k}{\partial t} + \frac{d\mathcal{F}}{d\left(\frac{\partial P_i}{\partial x_j}\right)}\frac{\partial\left(\frac{\partial P_i}{\partial x_j}\right)}{\partial t} + \frac{\partial\mathcal{F}}{\partial\left(\frac{\partial P_i}{\partial t}\right)}\frac{\partial^2 P_i}{\partial t^2}\right) dV \\ \leq -\iiint_V dV\left(\pi_i\frac{\partial P_i}{\partial t} + \zeta_{ij}\frac{\partial\left(\frac{\partial P_i}{\partial x_j}\right)}{\partial t}\right).\end{aligned} \tag{2.96}$$

Since the right hand side of Eq. (2.96) has no second time derivatives, it is implied that

$$\frac{\partial\mathcal{F}}{\partial\left(\frac{\partial P_i}{\partial t}\right)} = 0.$$

By comparing the terms on the left and right hand sides of Eq. (2.96), one can identify the following relationships for the *equality* case:

$$\zeta_{ij} = \frac{\partial \mathcal{F}}{\partial \left(\frac{\partial P_i}{\partial x_j}\right)}, \qquad \pi_i = \frac{\partial \mathcal{F}}{\partial P_k}. \tag{2.97}$$

However, this setup does not satisfy the *inequality*. We can then assume that

$$\eta_i = \frac{\partial \mathcal{F}}{\partial P_k}, \tag{2.98}$$

which implies [292]

$$(\pi_i + \eta_i)\frac{\partial P_i}{\partial t} \leq 0 \text{ and } \pi_i = -\eta_i - \Gamma_{ij}\frac{\partial P_j}{\partial t}, \tag{2.99}$$

where Γ_{ij} is an inverse mobility tensor that is positive definite. For the high-symmetry cubic phase, $\Gamma_{ij} = \Gamma\delta_{ij}$, with δ_{ij} being the Kroenecker product. Substitution of Eq. (2.97) into Eq. (2.84) gives,

$$-\left[\frac{\partial \mathcal{F}}{\partial P_i} - \frac{\partial}{\partial x_j}\left(\frac{\partial \mathcal{F}}{\partial \left(\frac{\partial P_i}{\partial x_j}\right)}\right)\right] + \gamma_i = \Gamma\delta_{ij}\frac{\partial P_j}{\partial t}. \tag{2.100}$$

Identifying the term in brackets as a variational derivative [16] with respect to P_i, we get

$$\frac{\partial P_i}{\partial t} = -\Gamma \frac{\delta}{\delta P_i}\left(\mathcal{F}[P_i,]\right) - \gamma_i \text{ for } i = 1,2,3, \tag{2.101}$$

which is the desired time-dependent Landau-Ginzburg-Devonshire equation.

The value of Γ that has to be adopted for generic ferroelectric materials is still a subject of an extensive debate. Some researchers have suggested that Γ can depend on the strength of the applied electric field during hysteretic switching [223]. Reasonable assumptions about Γ for certain poling scenarios have produced good agreement with experimental results, such as the coercive field magnitudes and relaxation times of the polar field [87, 121]. In fact, Hlinka showed that it is possible to calculate the precise value of Γ, if the plasma frequency and also the damping parameter of the soft mode are known, which are both strongly temperature dependent [121]. Another complication is that a simple expression for Γ does not exist in the presence of defects, and therefore system relaxation times are likely to vary from one local region to the next, depending on the defect concentration, within the same sample. Taking $\Gamma \to 1$ limit in Eq. (2.101) rescales the system evolution time, effectively making it *arbitrary*. This scaled time is still useful for realistic simulation if one is not interested in the system evolution specifics, as the polarization field follows the gradient descent towards the nearest energy minimum.

In real ceramics, there are number of other relaxation processes present that require some brief discussion. Free charges may be present in the sample, but since their mobilities in

[16] Variational derivative (sometimes called functional derivative) relates a change in a functional to a change in the function that functional depends on. Let

$$J[f] = \int L[x, f, f']dx,$$

where J is a functional of L that depends on $f = f(x)$, with f' being the derivative of f with respect to x. Then

$$\frac{\delta J}{\delta f} = \frac{\partial L}{\partial f} - \frac{d}{dx}\frac{\partial L}{\partial f'}.$$

This is also known as the Euler-Lagrange equation, if equated to zero [96].

oxides are usually very large [162], their relaxation (to some metastable energy minimum) should be fast compared to the ionic motions that are connected to the evolution of the polarization field. This consideration justifies solving the Poisson equation at every time step of the polarization field evolution. It has also been suggested that elastic strain fields usually relax much faster than the polarization field [184], which means that solving the stress divergence equation at every time step of the system evolution can be also be considered a good approximation in most cases.

2.4.4 Energetics of competing interactions in the ferroelectric state

As is customary in phase-field simulation approaches, the initial form of $\mathcal{F}$ may be postulated as a polynomial expansion over the relevant system order parameters. In the case of a proper ferroelectric, polarization is considered to be the primary order parameter and elastic strains as *secondary* in order parameter space[188]. We then have to expand $\mathcal{F}$ in terms of $\mathbf{P}$ and ε_{ij}, as well as their gradients in three dimensions ($i,j,k,... = 1,2,3$). The total free energy of the ferroelectric is then represented by a sum of the following energy terms that will be throughly discussed below:

$$\begin{aligned}\mathcal{F} &= F_{\text{bulk}}[\mathbf{P}(\mathbf{x})] + F_{\text{elastic}}[\mathbf{u}(\mathbf{x})] + F_{\text{coupled}}[\mathbf{P}(\mathbf{x}),\mathbf{u}(\mathbf{x})] + F_{\text{wall}}[\mathbf{P}(\mathbf{x})] + F_{\text{elec}}[\mathbf{P}(\mathbf{x}),\mathbf{E}(\mathbf{x})] \\ &= \iiint_V dV \left\{ f_{\text{bulk}}[\mathbf{P}(\mathbf{x})] + f_{\text{elastic}}[\mathbf{u}(\mathbf{x})] + f_{\text{coupled}}[\mathbf{P}(\mathbf{x}),\mathbf{u}(\mathbf{x})] + f_{\text{wall}}[\mathbf{P}(\mathbf{x})] + f_{\text{elec}}[\mathbf{P}(\mathbf{x}),\mathbf{E}(\mathbf{x})] \right\}.\end{aligned} \tag{2.102}$$

The first energy term f_{bulk} is the bulk energy of the ferroelectric that can be represented by an expansion

$$f_{\text{bulk}}[\mathbf{P}(\mathbf{x})] = \alpha_i P_i + \alpha_{ij} P_i P_j + \alpha_{ijk} P_i P_j P_k + \alpha_{ijkl} P_i P_j P_k P_l + \alpha_{ijklm} P_i P_j P_k P_l P_m + ... \tag{2.103}$$

Group theoretical arguments [6, 47] can be used to reduce Eq. (2.103) to a less formidable form by considering the group-subgroup relationship between the nonpolar and polar phases that are connected by the proper ferroelectric phase transition. One of the simplest cases for such a transition is perovskite $PbTiO_3$, that transforms from the nonpolar cubic phase (point group O_h) to a polar tetragonal phase (point group C_{4v}) [see also Table 2.1]. Applying the O_h symmetry operations to the general form of f_{bulk}, one finds

$$\begin{aligned} f_{\text{bulk}} = {} & \alpha_1(T-T_C)\left(P_x^2+P_y^2+P_z^2\right)+\alpha_{11}\left(P_x^4+P_y^4+P_z^4\right) \\ & +\alpha_{12}\left(P_x^2P_2^2+P_y^2P_z^2+P_x^2P_z^2\right)+\alpha_{111}\left(P_x^6+P_y^6+P_z^6\right) \\ & +\alpha_{112}\left[P_x^4\left(P_y^2+P_z^2\right)+P_y^4\left(P_x^2+P_z^2\right)+P_z^4\left(P_x^2+P_y^2\right)\right] \\ & +\alpha_{123}\left(P_x^2P_y^2P_z^2\right). \end{aligned} \tag{2.104}$$

Note that the expression above already includes an explicit dependence on temperature, which is present only in the first term for $PbTiO_3$, but may be more complicated for other materials (in principle, all of the α coefficients may be temperature dependent). The set of minima of f_{bulk} determines the preferred directions and magnitudes of $\mathbf{P}$ in the unit cell at a given temperature T below T_C. For example, in the $PbTiO_3$ case, the energy minima are found for $\mathbf{P}$ pointing along the $\pm\hat{x}, \pm\hat{y}$, or $\pm\hat{z}$ directions at all temperatures below T_C.

The general form of the elastic energy term f_{elastic} expanded in terms of elastic strains is

$$f_{\text{elastic}}[\mathbf{u}(\mathbf{x})] = A_{ij}\varepsilon_{ij} + A_{ijkl}\varepsilon_{ij}\varepsilon_{kl} + A_{ijklmn}\varepsilon_{ij}\varepsilon_{kl}\varepsilon_{mn} + \ldots \tag{2.105}$$

However, as already discussed above, elastic energy must be invariant with respect to an interchange of symmetric strain components. Therefore, $A_{ij}=0, A_{ijkl}=C_{ijkl}$, and $A_{ijklmn}=0$ (i.e., higher order strain energy terms are discarded), and the resulting form of Eq. (2.105) agrees with Eq. (2.33) presented earlier.

The coupled energy term includes monomials made up of combinations of different powers of the polarization and strain order parameters. For most ferroelectrics, only one monomial is usually considered, representing a linear-quadratic coupling between the strain and polarization, i.e., the ferroelectric self-strain [73, 195, 188],

$$\varepsilon^0_{ij} = Q_{ijkl} P_k P_l \tag{2.106}$$

where Q_{ijkl} is the electrostrictive tensor (which has the symmetry of the parent nonpolar phase). Therefore,

$$f_{\text{coupled}}[\mathbf{P}(\mathbf{x}), \mathbf{u}(\mathbf{x})] = -\frac{1}{2} C_{ijkl} Q_{klmn} \varepsilon_{ij} P_m P_n. \tag{2.107}$$

Note that some authors [188, 189] prefer to combine f_{elastic} and f_{coupled} into one term. Here, we have chosen to separate them out due to the fact that the result of the variational differentiation (with respect to $\mathbf{P}$) in Eq. (2.101) is nonzero only for terms that explicitly depend on $\mathbf{P}$.

The domain-wall or polarization-gradient energy term f_{wall} represents the energy contributions arising from *local* gradients of the polarization field. For example, for $PbTiO_3$,

$$\begin{aligned} f_{\text{wall}} = {} & \frac{1}{2} G_{11} \left[\left(\frac{\partial P_x}{\partial x} \right)^2 + \left(\frac{\partial P_y}{\partial y} \right)^2 + \left(\frac{\partial P_z}{\partial z} \right)^2 \right] \\ & + G_{12} \left[\frac{\partial P_x}{\partial x} \frac{\partial P_y}{\partial y} + \frac{\partial P_y}{\partial y} \frac{\partial P_z}{\partial z} + \frac{\partial P_x}{\partial x} \frac{\partial P_z}{\partial z} \right] \\ & + \frac{1}{2} G_{44} \left[\left(\frac{\partial P_x}{\partial y} + \frac{\partial P_y}{\partial x} \right)^2 + \left(\frac{\partial P_y}{\partial z} + \frac{\partial P_z}{\partial y} \right)^2 + \left(\frac{\partial P_x}{\partial z} + \frac{\partial P_z}{\partial x} \right)^2 \right] \\ & + \frac{1}{2} G'_{44} \left[\left(\frac{\partial P_x}{\partial x_2} - \frac{\partial P_y}{\partial x} \right)^2 + \left(\frac{\partial P_y}{\partial z} - \frac{\partial P_z}{\partial y} \right)^2 + \left(\frac{\partial P_x}{\partial z} - \frac{\partial P_z}{\partial x} \right)^2 \right]. \end{aligned} \tag{2.108}$$

Finally, the last energy term in Eq. (2.102) represents energy contributions stemming from the system interactions with internal and external electric fields:

$$f_{\text{elec}} = -\mathbf{P} \cdot \nabla \Phi,$$

where $\Phi(\mathbf{x})$ is the spatially dependent electrostatic potential that also obeys the Poisson equation.

It is usually extremely difficult to accurately determine — either with the help of theory or experiments — the values of all the coefficients present in such a complicated parameterization. For a small number of ferroelectric materials (that have been actively studied for many decades!) such parameterizations do exist, which includes $PbTiO_3$ [188], $PbZrTiO_3$ **fix**, $BaTiO_3$ [123], $Sr_{0.8}Bi_{2.2}Ta_2O_9$ [295], $LiNbO_3$, $LiTaO_3$ [279] and a number of others. However, for such other popular ferroelectric materials as $BiFeO_3$, Landau-type energy expressions had not been developed until this year (2017) [217].

It should be noted that the gradient terms in Eq. (2.108) can be approximated from the curvatures of the polar soft-mode band dispersions in the Brillouin zone, and therefore they can be extracted from *ab initio* calculations [46, 123]. Alternatively, these coefficients can be extracted from inelastic neutron scattering data [116]. Still, for many ferroelectric materials, and especially for solid solutions, gradient energy terms are not known. Landau theory expansion parameters for $BaTiO_3$ and $PbTiO_3$, i.e., materials used extensively in our simulations that will be presented in the following chapters, are assembled in Table 2.3.

2.5 The electrocaloric effect

As discussed in detail in above, in a ferroelectric material below the Curie temperature T_C, contributions from the spontaneous polarization and the applied electric field produce the

	$PbTiO_3$	Ref.	$BaTiO_3$	Ref.	Units
α_1	$3.8(T-752)\times 10^5$	[188]	$3.34(T-381)\times 10^5$	[187]	$C^{-2}m^2N$
α_{11}	-0.73×10^8	-	$[4.69(T-393)-202]\times 10^6$	-	$C^{-4}m^6N$
α_{12}	7.5×10^8	-	3.23×10^8	-	$C^{-4}m^6N$
α_{111}	2.6×10^8	-	$[-5.52(T-120)+276]\times 10^7$	-	$C^{-6}m^{10}N$
α_{112}	6.1×10^8	-	4.47×10^9	-	$C^{-6}m^{10}N$
α_{123}	-3.7×10^9	-	4.919×10^9	-	$C^{-6}m^{10}N$
ϵ_b	10		8	[123]	ϵ_r
Q_{11}	0.089	[188]	0.11	[187]	$C^{-2}m^4$
Q_{12}	-0.026	-	-0.045	-	-
Q_{33}	0.034	-	0.059	-	-
C_{11}	281	[138], [68]	116	[138], [68]	GPa
C_{12}	116	-	104	-	-
C_{33}	97	-	120	-	-

Table 2.3 Ferroelectric material parameters used in this dissertation for $PbTiO_3$ and $BaTiO_3$. Elastic stiffness and electrostrictive tensor coefficients are given in Voight notation[245]. Sixth order expansions of the bulk free energy are used for both materials. All coefficients are given in SI units.

following electric displacement field,

$$\mathbf{D} = \epsilon_0 \mathbf{E} + \mathbf{P}.$$

Noting that in Eq. (2.60), $\mathbf{D}$ is also defined as

$$D_i = -\left(\frac{\partial G}{\partial E_i}\right)_{\sigma_{kl},T} = -\left(\frac{\partial S}{\partial E_i}\right)_{\sigma_{kl},T}, \tag{2.109}$$

and also utilizing Eq. (2.61),

$$p_i^{\sigma} = -\left(\frac{\partial^2 G}{\partial E_i \partial T}\right)_{\sigma}. \tag{2.110}$$

we arrive at a *dual* relation defining the material pyroelectric constant:

$$p_i^{\sigma} = -\left(\frac{\partial^2 G}{\partial E_i \partial T}\right)_{\sigma_{kl}} = \left(\frac{\partial D_i}{\partial T}\right)_{\sigma_{kl}} = \left(\frac{\partial S}{\partial E_i}\right)_{\sigma_{kl}}. \tag{2.111}$$

In other words, this relation equates changes in entropy due to changing electric field to changes in electric displacement due to changes in temperature. Thus, a variation of the dielectric material entropy as a function of the electric field at a given temperature, will result in an adiabatic temperature change, which is the definition of the electrocaloric effect (ECE). Analogous effects have been seen in magnetic systems (magnetocalorics).

To obtain the ECE induced temperature shift ΔT due to an electric field change $\Delta \mathbf{E}$ at some operating temperature T, one can use the following expression [7]:

$$\Delta T = -T \int_{\Delta \mathbf{E}} d\mathbf{E} \cdot \left(\frac{1}{C_{\text{total}}(T, \mathbf{E})} \frac{\partial \mathbf{P}^0}{\partial T}\right). \tag{2.112}$$

Here, $C_{\text{total}}(T, \mathbf{E})$ is the total system heat capacity C_V *plus* the excess heat capacity ΔC^{excess} contributed by the polar-nonpolar phase transformation. The former can be obtained from the system phonon density of states (PDOS) and therefore is easily extracted from *ab initio* calculations [212, 238]. The latter can be calculated in straightforward fashion as [7],

$$\Delta C^{\text{excess}} = T^2 \left(\frac{\partial G^0}{\partial T}\right)_{\mathbf{E}, \sigma_{kl}}, \tag{2.113}$$

where G^0 is the equilibrium free energy.

2.5.1 Example: electrocaloric effect in $BaTiO_3$ thin films

As discussed at length above, ferroelectric thin films are particularly important as potential components for integration into a variety of electronic and electromechanical devices. Here, we borrow a simple Landau-type energy parameterization for a $BaTiO_3$ thin film from

Ref. [7]. This parameterization is expanded only in terms of one-dimensional polarization that points out of the plane of the film. Possible domain structure formation in not taken into account, while a lattice misfit strain between the film and substrate is included in the standard fashion, therefore,

$$G = G_0 + \alpha_1 P^2 + \alpha_{11} P^4 + \alpha_{111} P^6 - EP + \widetilde{C}\left(\varepsilon_m - Q_{12} P^2\right)^2 \tag{2.114}$$

where $\varepsilon_m = (a_{\text{substrate}} - a_{\text{film}})/a_{\text{substrate}}$ is the lattice misfit in terms of lattice constants, G_0 is the paraelectric state energy, and $\widetilde{C}$ is an effective elastic stiffness modulus[1]. Electric field E is also assumed to be one-dimensional and can applied only parallel to P. Q_{ij} is the electrostrictive tensor with coefficients written in in Voight (reduced) notation.

Eq. (2.111) is strictly valid at thermodynamic equilibrium, which requires,

$$\left(\frac{dG}{dP}\right)_{T,E,\varepsilon_m} = 0, \text{ and } \left(\frac{d^2G}{dP^2}\right)_{T,E,\varepsilon_m} > 0. \tag{2.115}$$

for a given T, E and ε_m. By solving for P that fulfills this constraint, we can find the equilibrium polarization $P^0(T,E)$ at the energy minimum. A plot of $P^0 = P^0(T,E)$ for different electric fields at zero applied ε_m is presented in Fig. 2.13. Under no applied electric field, the phase transition is near-first order, as the derivative of the polarization with respect to temperature is not defined when $T = T_C$. When non-zero electric field is applied, the slope of the curve is smoothed out (the derivative of the polarization with respect to temperature now exists everywhere) and the temperature at which the polarization vanishes is increased.

[1] The effective modulus is an averaged quantity,

$$\widetilde{C} = C_{11} + C_{12} - \frac{2C_{12}^2}{C_{11}},$$

in Voight notation. Reduced Voight notation, originally introduced by German physicist Woldemar Voight in 1910 [302], simiplifies discussions involving C_{ijkl} by mapping the indices of the rank four tensor to only two ($ijkl \to mn$) for use in matrix algebra. Explicitly, this follows $11 \to 1$, $22 \to 2$, $33 \to 3$, $23, 32 \to 4$, $31, 13 \to 5$, $12, 21 \to 6$.

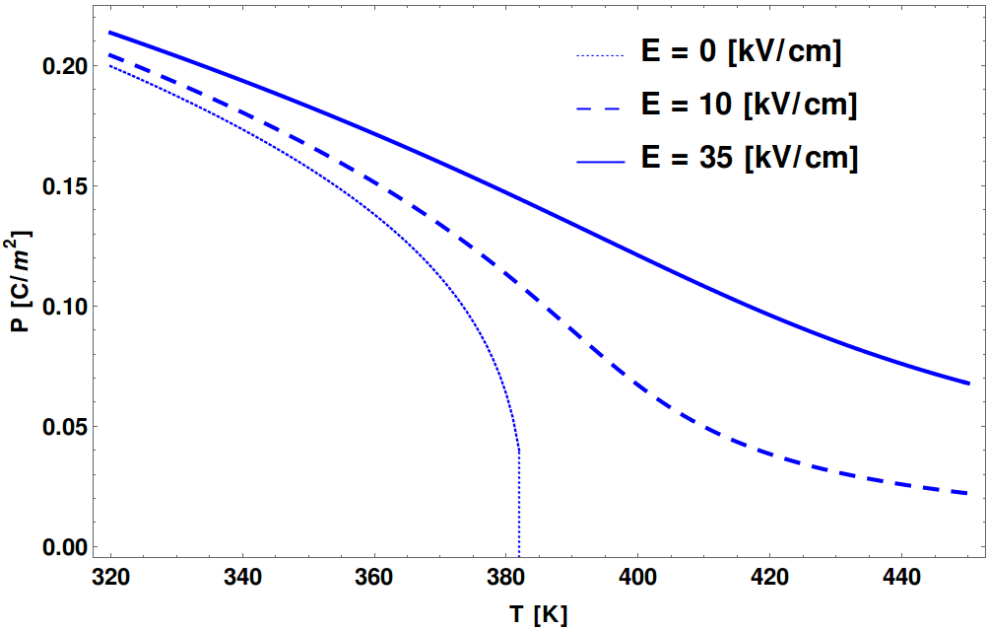

Fig. 2.13 $BaTiO_3$ thin-film polarization as a function of temperature in the vicinity of $T_C = 383$ K for different electric fields. The transition at zero field is near-first order. When an electric field is applied, this phase transition is smoothed out.

On the next step, we can substitute the values of the equilibrium polarization back into the free energy expression, Eq. (2.114), to find the equilibrium free energy $G^0 = G(T,E,P^0(T,E))$ at a given temperature and electric field. We can also write down Maxwell relations for the excess entropy and heat capacity[1]:

$$S^{\text{excess}} = -T\left(\frac{\partial G^0}{\partial T}\right)_{E,\varepsilon_m}, \tag{2.117}$$

[1]To compute S^{excess} and ΔC^{excess} using Eq. (2.115), the finite difference approximation of the derivatives needs to be utilized, i.e.,

$$\frac{df}{dx} \approx \frac{f(x_n) - f(x_{n-1})}{\Delta x}, \tag{2.116}$$

where Δx is the grid size (temperature grid size was chosen to be $\Delta T = 1$ K for this computation).

and

$$\Delta C^{\text{excess}} = T^2 \left(\frac{\partial G^0}{\partial T} \right)_{E,\varepsilon_m}, \tag{2.118}$$

The excess entropy is presented in Fig. 2.14. The negative sign of S^{excess} is physically mean-

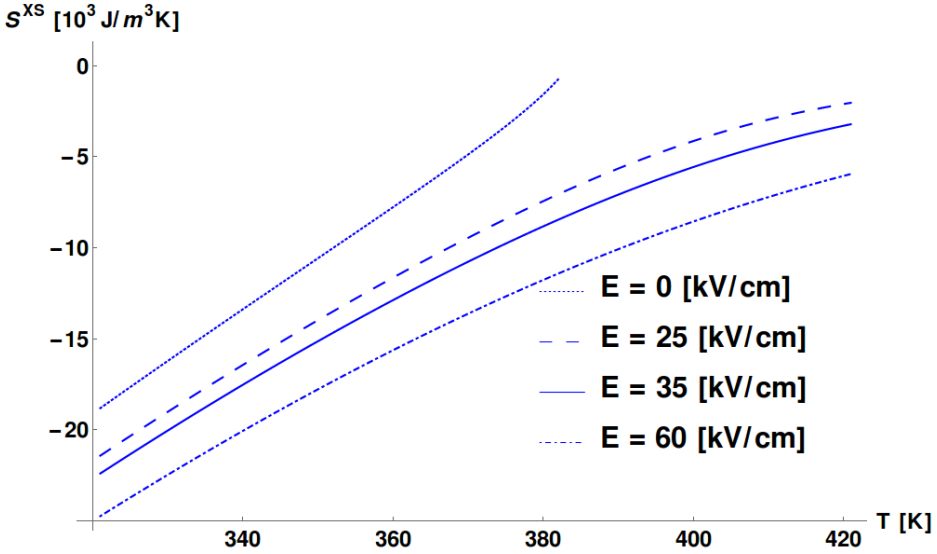

Fig. 2.14 Excess entropy of the $BaTiO_3$ thin film for different applied electric fields at zero misfit strain. The contributions to the total entropy are negative below the phase transition due to the ordering of the system.

ingful and indicates that the system is being transferred to a more ordered state, compared to the paraelectric state above T_C. The excess heat capacity is plotted in Fig. 2.15 that shows divergent behavior of the zero-field polarization in the near first-order phase transition. For one-dimensional P and E, the adiabatic temperature change given by Eq. (2.112) reduces to

$$\Delta T = -T \int_{\Delta E} \frac{1}{C_V + \Delta C^{\text{excess}}} \left(\frac{\partial P^0}{\partial T} \right)_E, \tag{2.119}$$

This expression can be thought of as two contributions to the overall ΔT – one from ΔC^{excess} and the other from the pyroelectric response. The free energy minimum is found for a grid

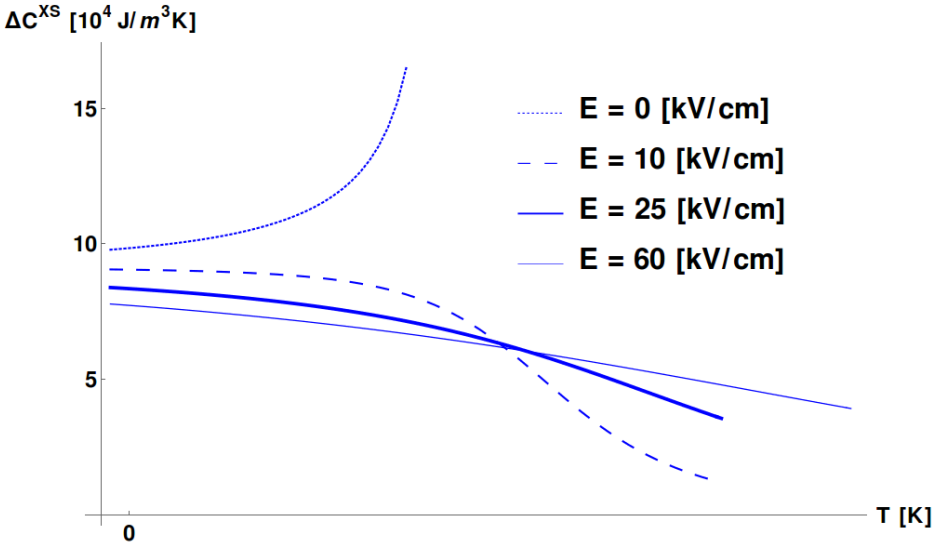

Fig. 2.15 Excess heat capacity of the $BaTiO_3$ thin film for different applied electric fields at zero misfit strain. The divergent behavior for $E = 0$ kV/cm indicates the near first-order phase transition.

of electric fields, operating temperatures, and strains then Eq. (2.119) is computed which is presented in Fig. 2.16

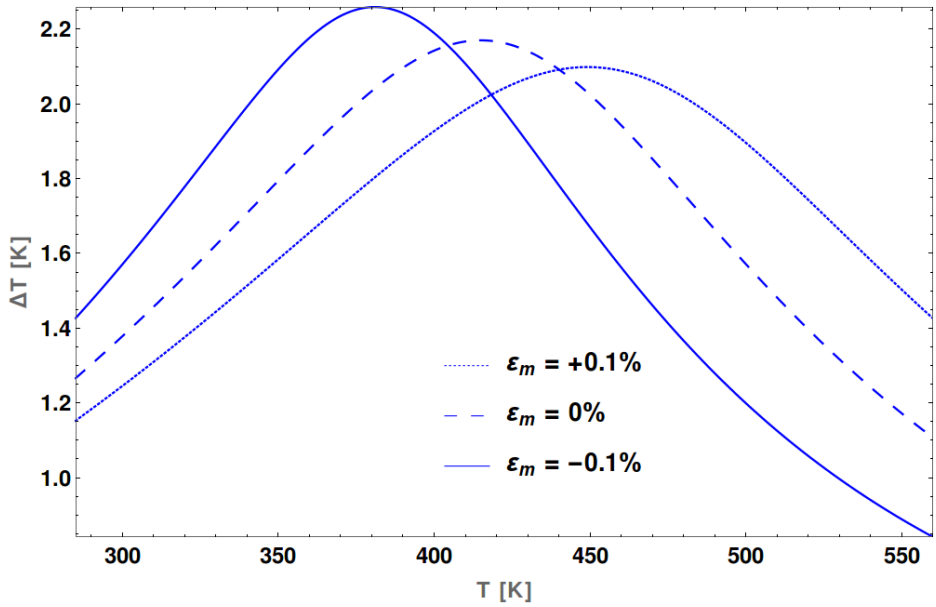

Fig. 2.16 ECE temperature change in the $BaTiO_3$ thin film under an electric field sweep $\Delta E = 100$ kV/cm, computed for various operating temperatures and misfit strains ε_m.

These results (summarized in detail in Ref. [7]) show that compressive misfit strain $\varepsilon_m < 0\%$ lowers the ΔT maximum but broadens the curve across the operating temperature. Applied electric fields smooth out the first-order phase transition and can allow polarization to persist at much higher temperatures than T_C. The misfit strain shifts T_C to higher temperatures when $\varepsilon_m < 0$ and lower temperatures when $\varepsilon_m > 0$, as shown in Fig. 2.16. The peaks in the ΔT vs. T curves stem from the temperature dependence of $\partial P^0/\partial T$ (i.e., the pyroelectric coefficient) that becomes large around T_C, when the *magnitude* of the system polarization changes abruptly with changing temperature [see Fig. 2.13]. Such variation of the polarization vector magnitude, as its direction is fixed, is called an *amplitudon*, and therefore we can claim that normal ECE, illustrated in this example, is due to an *amplitudon* excitation of the system polarization, which is most pronounced around T_C. In Chapter 6, we will carefully analyze the behavior of a more interesting system, where ECE contributions are possible not only from polarization magnitude changes, but also from polarization rotations.

Chapter 3

Computational approach: the finite element method

3.1 A finite element approach

To solve a set of nonlinear partial differential equations, it can be advantageous to use the *finite element method* (FEM). The finite element method is a numerical approach that involves discretizing a computational domain of interest in order to solve a boundary value problem where the analytical solution is very difficult or impossible to obtain. Computational domains with irregular geometries or problems with complicated material properties and governing equation sets are especially suited for FEM.

It is difficult to pin down the exact date of the first use of FEM. Complex elastic and structural analysis problems through the 1940s, '50s, and '60s were tackled using variations of the same approach by a number of independent researchers. The pioneering work of Courant, Argyris, Oganesyan, and Clough [63, 13, 247, 58] appear to be the first formal attempts to develop the approach, but a number of other scientists and engineers made contributions to the general methodology. An early success of FEM was its application to fluid mechanics problems in the 1960s by Hess and Smith [119] to solve the Navier-Stokes equations. This

allowed computational analysis of fluid flow around airfoils in order to optimize the design of aircraft. Since then, FEM has seen continuous, extensive use in physics, nuclear sciences [95, 310, 297, 144], geology [272, 14, 64], materials science [274, 157, 128, 188, 117] and chemical [66, 37], civil [120, 194, 42], and aerospace engineering [119, 133, 290, 237] for nearly six decades. The reader is referred to texts by Carey [33] and Bathe [30] for comprehensive background on the method.

In the last two decades, FEM has extended into the realm of microstructure prediction for materials systems. Within the FEM framework, novel methods were developed to predict dendritic growth [274, 157], spinodal decomposition [27, 145], grain growth [297], and ferromagnetic (micromagnetics) [275, 117, 136] and ferroelectric domain formation [128, 188, 189, 243]. These processes typically happen at length scales smaller than those investigated with aforementioned FEM studies (e.g., fluid flow or elastic deformations of large structures). Certain complications can arise, such as the need to spatially resolve sharp interfacial regions (between phases, domains, or different materials), which can be computationally expensive and where analytical solutions are typically not available. Similarly, the governing equations can be complex, as coupling between many different physical (and chemical) phenomena at this scale can be influential in determining an accurate solution of the problem. To aid in solving these complicated problems, special formulations of FEM have been developed (such as *hp* adaptivity [20, 222, 237, 276], XFEM [227, 34, 90], mesh-free [178, 332, 196], or discontinuous Galerkin [15, 22, 60]) to tackle these problems.

As shown in work by Li [188, 189], Huber and Su [131, 292] and Völker *et al* [303], simulating the evolution of the ferroelectric phase is well-suited for the finite element method. To accomplish the research goals of this Thesis, namely to predict the complex microstructural evolution of arbitrary ferroelectric nanostructures, a code package was developed within the multi-physics finite element framework MOOSE (**M**ultiphysics-**O**bject-**O**riented-**S**imulation-**E**nvironment)[95].

3.1.1 The MOOSE code and its herd of animals

MOOSE is conceptualized as a user-friendly interface to sophisticated and well-maintained finite element method libraries[1] and numerical routines[2] for the scalable solutions of partial differential equations. The MOOSE system is an open-source toolset offered to the scientific community and is primarily developed at Idaho National Laboratory. Its strength, as a code framework, is seen in one of its primary (and current) use-cases for predicting nuclear fuel failure within light-water reactors. This is a difficult problem, due to highly coupled and nonlinear physical interactions across many different length scales within the reactor. Neutronic, thermal-hydraulic, thermo-mechanic, irradiation, and material microstructural processes all needed to be captured effectively [95, 310, 297]. The modular scheme of MOOSE is essential here; individual domain-scientists (e.g. those familiar with one specific area of the nuclear physics) developed and tested their own application that would be coupled across the standardized (and flexible) MOOSE system. This effort eventually led to a "herd" of applications (see Fig. 3.1) that all utilize the same basic functionalities of the framework but each study specific physical problems.

MOOSE has a large number of modules which may be called when developing your own application. To briefly describe a few: The `Kernels` system implements the nonlinear partial differential equation terms. The `Materials` system handles materials properties which are defined across the entire mesh (or a subset) such as elastic stiffness and electrostrictive tensors, thermal conductivity, and mobilities. The `AuxKernel` class allows user-defined spatially dependent computations (fields) that are auxilliary to the PDE being solved. The `Postprocessor` systems outputs single scalar or vector quantity that is computed (integrated,

[1] One library is LIBMESH [158], which brings the capability to implement the a number of different finite element methods on arbitrary geometric mesh (structured or unstructured) configurations along with efficient MPI parallelization.

[2] The framework also interfaces to the well-known library, PETSc (**P**ortable, **E**xtensible **T**oolkit for **S**cientific **c**omputation) [23]. PETSc has been in development at the Mathematics and Computing Science Division at Argonne National Laboratory for over twenty years and has transformed scientific computing. It has been integrated into numerical simulations as wide-ranging as cardiac blood flow [61] to high-fidelity aircraft design optimization [151] the inspiral dynamics of binary black holes [293].

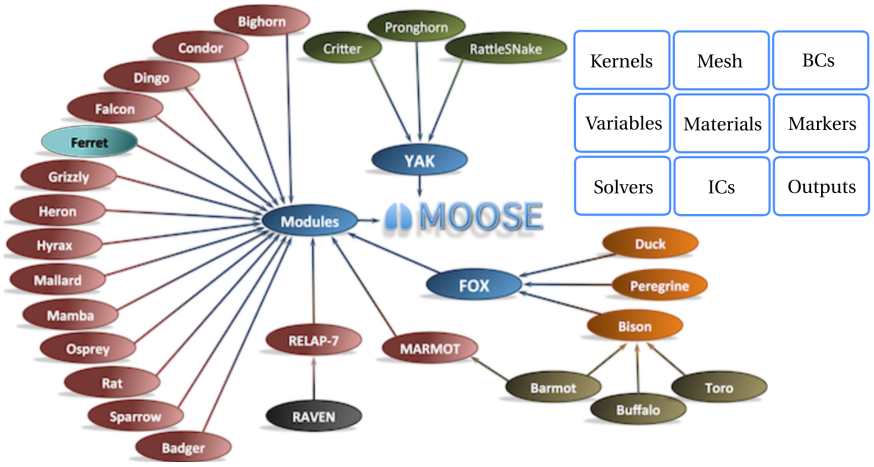

Fig. 3.1 The MOOSE ecosystem pictured on the left. The individual animal names correspond to applications developed by domain scientists. Modules pictured on the left are generally independent from one another while modules on the bottom right deal with predictive simulations in nuclear reactors. For example, the application Bison deals with thermomechanics and species diffusion in light-water reactor fuel rods. The nine panels on the top right highlight some of the MOOSE objects available to the user/developer when working within the framework. Figure is adapted from Ref. [4] with permission from publishing authority.

summed, or averaged) from the full mesh (or sub-domains). A MOOSE-based simulation requires an input file to run; this input file selects which `Kernels`, `Materials`,`AuxKernels`, `Postprocessors`, and others will be used in a given simulation (and also supplies parameterizations for these objects). This relatively simple input file can easily be parsed and scripted with high-level codes such as python or R.

This compartmentalized structure of the package that is accessed via an input file leads to many advantages for a developer. The "on-off" nature of the input file allows for ease of debugging and testing of a given application. One can turn off entire sectors of problems to identify possible issues (or explore coupled-physical connections). The object-oriented design of the package enables one to use significantly fewer lines of code when developing new applications by being able to 'inherit' already existing classes and procedures, with little or no code duplication. This is an important advantage, as no extra time has to be spent re-developing methods or debugging.

The MOOSE team also has implemented a dedicated and automated continuous testing system (CIVET), which independently compiles and tests each application whenever any code is changed.This feature is integral for large-scale scientific projects such as MOOSE, as it effortlessly allows independent researchers to remain up-to-date on code deprecation, implementation changes, and updates. Most importantly, MOOSE has a large user-base and permanent developer team who continue to implement new features, improve MOOSE, and provide support. Detailed instructions for installing the MOOSE code are found at http://mooseframework.org, and its source code available on GitHub at http://github.com/idaholab/moose.

3.1.2 Ferret: overview

The particular module developed by the author for simulating the properties of **ferr**oic nanostructures is called FERRET. It is an open-source code-base under GNU licensing and is available on BitBucket[3]. This package installs seamlessly on top of the MOOSE distribution. The primary capability of FERRET is the solution of the coupled nonlinear time-dependent equation, Eq. (2.101), along with the auxiliary stress divergence, Eq. (2.12), and Poisson, Eq. (2.52), equations at every step in the time evolution. Each of the terms in Eq. (2.101), Eq. (2.12), and Eq. (2.52) are linearized and coded into the `Kernels`.

The `Materials` class used primarily in FERRET inherits from the `tensor_mechanics` module (initially developed by Heinonen and Jokisaari [143]). This module enables tensorial algebraic operations involving the elastic tensors, for example, calculation of $\sigma_{ij}(\mathbf{x})$ at arbitrary position $\mathbf{x}$ in the mesh, thus properly accounting for any crystallographic anisotropies related to elasticity. This module also allows to freely choose the orientation of the elastic stiffness tensor C_{ijkl} within each spatial region by using Euler rotations (as detailed in Chapter 2). The coupling of polar and elastic variables in the ferroelectric system is represented by

[3]The FERRET code-repository is available at https://bitbucket.org/mesoscience/ferret

an electrostrictive tensor $Q_{ijkl} = Q_{ijkl}(\mathbf{x})$, which is also present as a class in FERRET. The values of individual components of C_{ijkl}, Q_{ijkl}, as well as any other relevant tensors may be chosen as spatially dependent, which allows the user to define multiple different ferroelectric materials in separate regions of the same mesh, or a spatially dependent variation of properties of the same material. Finally, FERRET is equipped with `AuxKernels` and `Postprocessors` that compute different energy densities, boundary charges, fringing (or internal) electric fields, refractive indices (and birefingence), and topological winding numbers during the evolution of the system, following Eq. (2.101). Below we summarize the most important capabilities of FERRET, as well as the relevant general features of the finite element method.

3.1.3 Discretization of the computational domain

Central to the finite element methodology is the discretization of a computational domain, including both volume V and surface S, into individual pieces called *elements*. Conventionally, the discretization of a volume, V, and its surface, S, is V_h and S_h respectively. The subscript h typically indicates that a finite mesh "size" is used. The volume V_h is the union of all elements such that $V \approx V_h$ within some discretization error ($|V - V_h|$). Formally, we write,

$$V \approx V_h = \bigcup_{e=1}^{M} V_h^e,$$

for M total number of elements and V_h^e is the volume a single element. The element defined by the volume V_h^e and surface (or bounding curve) S_e may be polygonal (flat n-gon, in the case of a 2D mesh) or polyhedral (3-dimensional object with n-sides). The vertices that define the faces (or edges) of each element are known as *nodes* and they are shared by connected elements[4].

The set of all elements M and nodes N is defined as the *finite element mesh* [33]. An example of three such finite element discretizations of a 2D circle are presented in Fig.

[4]It should be noted that in higher order methods, nodes can be placed at the interior of elements as well.

3.2 for different average triangular element sizes. As the element size is made smaller

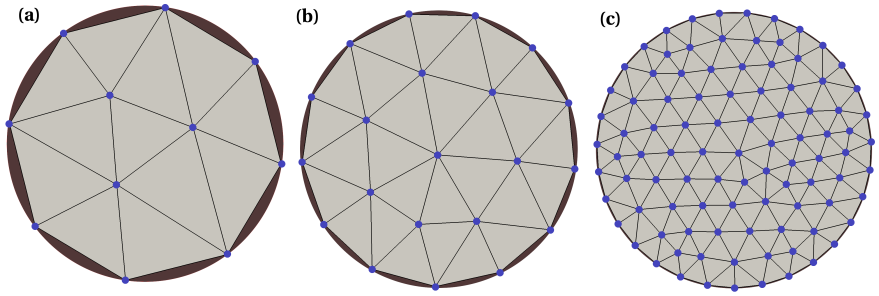

Fig. 3.2 The circle with area $V = \pi$ is discretized into three different sized element sets **(a)**, **(b)**, **(c)**. Nodes are denoted as blue circles at the vertices of the elements. If the average element area is made large, the error $|V - V_h|$ is large, as highlighted by the dark gray area.

(from left to right), the curvature of the circle is successively better approximated, leading to smaller discretization error. If each node is located at a *unique* coordinate such that $\left(x_i, y_j, z_k\right) = (i\,dx, j\,dy, k\,dz)$ where dx, dy, dz are fixed and $i, j, k \in \mathbb{Z}$, that is, the spatial relationship of the nodes is assumed *a priori*, then we say the finite element mesh is *structured*. If the list of all nodes in the mesh do not follow this definition, then the mesh is *unstructured*. Meshes of irregular shapes (such as those in Fig. 3.2) are almost always unstructured, but meshes of regular shapes may also be unstructured. In Fig. 3.3 an example of two structured hexahedral meshes **(c)**, **(d)** and one unstructured tetrahedral mesh **(e)** for the same volume is shown. One clear advantage, however, to using an unstructured mesh, is that it allows for an arbitrarily fine grid near cracks, curves, joints, or voids, which can improve convergence (or greatly lower the discretization error). However, unstructured meshes have some disadvantages. The unique integer set mapping of nodes of the structured mesh allow for additional mathematical tricks (e.g. periodic boundary condition enforcement) that are difficult to implement on the unstructured mesh (but perhaps important for the physical problem studied). The unstructured node grid also makes it difficult to find points or nodes as there is no predefined spatial relationship which can lead to additional computer operations in the algorithm.

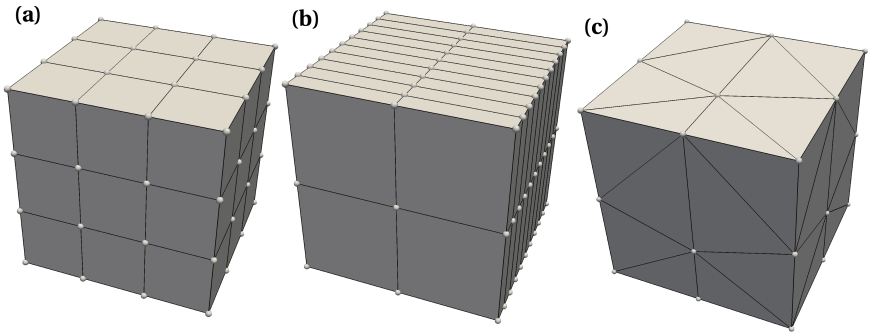

Fig. 3.3 Structured **(a)**, $dx = dy = dz$, **(b)**, $dx = dz \neq dy$, and unstructured **(c)** mesh for the same computational domain (a cube volume). These three FEM meshes are examples of zero discretization error, since $V = V_h$ due to the regular shape of V.

3.2 FEM formulation of the Poisson equation

The goal of this section is to show the reader the general approach for the FEM applied to problems of one variable. Specifically, the focus will be on the governing equation for electrostatics with some discussion of how it relates to FERRET and how the MOOSE framework uniquely handles the FEM. The potential field, $\Phi = \Phi(\mathbf{x})$, in some volume V due to a charge distribution ρ, satisfies the following PDE,

$$\frac{\partial}{\partial x_i}\left(\epsilon_b(\mathbf{x})\frac{\partial \Phi(\mathbf{x})}{\partial x_i}\right) = \frac{\partial P_j(\mathbf{x})}{\partial x_j}, \tag{3.1}$$

where the charge distribution is solely comprised of bound charges $\rho_b = -\nabla \cdot \mathbf{P}$, with polarization field $\mathbf{P}$ that could be zero, fixed, or vary in space. We again employ Einstein's summation convention for repeated indices. The dielectric constant, $\epsilon_b(\mathbf{x})$, is assumed to be a scalar function of space (no anisotropy).

Eq. (3.1) is a boundary value problem that is only solvable when the value of Φ is defined upon some boundary. This PDE is a so-called *strong* problem statement that must be converted into a *weak* form. This is done as follows by constructing a *residual* statement of

this boundary-value problem,

$$r(\mathbf{x}) = \frac{\partial}{\partial x_i}\left(\epsilon_b(\mathbf{x})\frac{\partial \Phi(\mathbf{x})}{\partial x_i}\right) - \frac{\partial P_j(\mathbf{x})}{\partial x_j} = 0. \tag{3.2}$$

We "test" this residual over arbitrary subregions by multiplying it by a sufficiently smooth test function $v(\mathbf{x})$. The residual is then integrated over the domain V,[5] i.e.,

$$\mathcal{R} = \iiint_V d^3\mathbf{x}\, v(\mathbf{x})\, \frac{\partial}{\partial x_i}\left(\epsilon_b(\mathbf{x})\frac{\partial \Phi(\mathbf{x})}{\partial x_i}\right) - \iiint_V d^3\mathbf{x}\, v(\mathbf{x})\, \frac{\partial P_j(\mathbf{x})}{\partial x_j} = 0. \tag{3.3}$$

Integration by parts allows us to obtain an expression with terms only containing first derivatives of Φ and $\mathbf{P}$,

$$\mathcal{R} = \iiint_V d^3\mathbf{x}\, \frac{\partial v(\mathbf{x})}{\partial x_i}\, \epsilon_b(\mathbf{x})\, \frac{\partial \Phi(\mathbf{x})}{\partial x_i} - \iiint_V d^3\mathbf{x}\, v(\mathbf{x})\, \frac{\partial P_j(\mathbf{x})}{\partial x_j} - \oiint_S d^2\mathbf{x}\left[\epsilon_b(\mathbf{x})\frac{\partial \Phi}{\partial x_i}\hat{n}_i v(\mathbf{x})\right] = 0, \tag{3.4}$$

where we have transformed the second volume integral (over Φ) to a surface integral (with outward-facing surface normal $\hat{\mathbf{n}}$) by using the divergence theorem. The term involving $\mathbf{P}$ can also be processed in the same fashion,

$$\begin{aligned}\mathcal{R} = &\iiint_V d^3\mathbf{x}\, \frac{\partial v(\mathbf{x})}{\partial x_i}\, \epsilon_b(\mathbf{x})\, \frac{\partial \Phi(\mathbf{x})}{\partial x_i} - \iiint_V d^3\mathbf{x}\, \frac{\partial v(\mathbf{x})}{\partial x_j}\, P_j(\mathbf{x}) \\ &- \oiint_S d^2\mathbf{x}\left[\epsilon_b(\mathbf{x})\frac{\partial \Phi}{\partial x_i}\hat{n}_i v(\mathbf{x})\right] + \oiint_S d^2\mathbf{x}\left[P_k \hat{n}_k v(\mathbf{x})\right] \\ &= 0,\end{aligned} \tag{3.5}$$

[5] The L2 space of v must be smooth enough to be square integrable over the volume, or $\int_V \left\{[\nabla v(\mathbf{x})]^2 + v(\mathbf{x})^2\right\} dV < \infty$. We call these class of functions $H^1(V)$ where the 1 denotes that the first derivative is square integrable.

Eq. (3.5) contains both volume and boundary terms. As mentioned before, the boundary-value problem requires well-defined boundary conditions in order to be solved. Now, note that if

$$\frac{\partial A(\mathbf{x})}{\partial x_k}\hat{n}_k = g(\mathbf{x}) \text{ on } S_1 \subseteq S, \tag{3.6}$$

where $g(\mathbf{x})$ is some nonzero function, $A(\mathbf{x})$ is the variable we are solving for, and $S_1 \cup S_2 = S$ is the boundary where this is satisfied then Eq. (3.6) represents a *Neumann boundary condition*. If such a boundary condition is present for Φ on S_1 then Eq. (3.5) becomes,

$$\begin{aligned}\mathcal{R} = &\iiint_V d^3\mathbf{x}\,\frac{\partial v(\mathbf{x})}{\partial x_i}\,\epsilon_b(\mathbf{x})\,\frac{\partial \Phi(\mathbf{x})}{\partial x_i} - \iiint_V d^3\mathbf{x}\,\frac{\partial v(\mathbf{x})}{\partial x_j}\,P_j(\mathbf{x}) \\ &- \oiint_{S_2} d^2\mathbf{x}\,\left[\epsilon_b(\mathbf{x})\frac{\partial \Phi}{\partial x_i}\hat{n}_i v(\mathbf{x})\right] + \oiint_{S_2} d^2\mathbf{x}\,\left[P_k\hat{n}_k v(\mathbf{x})\right] \\ &- \oiint_{S_1} d^2\mathbf{x}\,\left[\epsilon_b(\mathbf{x})\,g(\mathbf{x})\,v(\mathbf{x})\right] \\ &= 0,\end{aligned} \tag{3.7}$$

where the integration over the surface has been split into regions S_1 and S_2 to emphasize the application of the Neumann boundary condition. The "natural" boundary condition, applied to region S_2 where the value of $\frac{\partial A(\mathbf{x})}{\partial x_k}\hat{n}_k$ is unspecified but still contributes to the residual value *to be minimized*, is a special case of the Neumann boundary condition. In that case, Eq. (3.5) would be unchanged. For the boundary value problem, there is another type of boundary condition that could be specified (Dirichlet) that will be discussed below.

At this stage, the finite element approximation to both v, Φ, S and V is required. The volume V and surface S are discretized as described earlier, such that $V \approx V_h$ and $S \approx S_h$,

with the coordinates of each j^{th} node given by (x_j, y_j, z_j) in Cartesian coordinates[6] for $j = \{1, 2, ...N\}$. The test function v can be expanded as a linear sum of shape (basis) functions $[\phi_j = \phi_j(\mathbf{x})]$ such that

$$v_h(\mathbf{x}) = \sum_{j=1}^{N} v_j \phi_j(\mathbf{x}) \tag{3.8}$$

where N is the number of nodes in the mesh and v_j are *unknown*[7] expansion coefficients. Many different choices for $\phi_j(\mathbf{x})$ exist. Shape or basis functions could be piecewise-linear, quadratic, cubic, or even higher order [33]. The optimum choice of $\phi_j(\mathbf{x})$ typically depends on a specific that needs to be solved, including the desired solution accuracy and computational efficiency. In particular, the piecewise linear (Lagrange) ϕ_i on some (unstructured or structured) one-dimensional mesh,

$$\phi_i(x) = \begin{cases} \frac{x - x_j}{x_i - x_j}, & \text{if } x_j < x \leq x_i \\ \frac{x_j - x}{x_j - x_i}, & \text{if } x_i < x \leq x_j, \end{cases} \tag{3.9}$$

Therefore, the following relationship is established,

$$\phi_i(\mathbf{x}_j) = \delta_{ij}, \tag{3.10}$$

which forces the value of the function to unity at the node. For a node located at $\mathbf{x}_i$ then Eq. (3.9) gives $v_h(\mathbf{x}_i) = v_i$ (equal to the i^{th} coefficient). The variable of interest $\Phi_h(\mathbf{x})$ is also

[6] To be sufficiently general, there is nothing that requires that we work in Cartesian coordinates. For example, MOOSE can perform simulations with a range of coordinate systems (and residual construction can be done with coordinate-free operators).

[7] This is an important detail here. The unidentified values of the expansion coefficients are precisely what we solve for in the FEM.

expanded in terms of the same basis functions ϕ_j which gives

$$\Phi_h(\mathbf{x}) = \sum_{j=1}^{N} \Phi_j \phi_j(\mathbf{x}), \tag{3.11}$$

for some unknown coefficients Φ_j[8]. Introducing Eq. (3.8) and Eq. (3.11) into the above Eq. (3.5) that are integrated over V_h enclosed by S_h gives,

$$\begin{aligned}\mathcal{R} = &\sum_{r=1}^{N}\sum_{s=1}^{N}\left(\iiint_{V_h} d^3\mathbf{x}\,\frac{\partial\left[v_r\phi_r(\mathbf{x})\right]}{\partial x_i}\,\epsilon_b(\mathbf{x})\,\frac{\partial\left[\Phi_s\phi_s(\mathbf{x})\right]}{\partial x_i}\right) - \sum_{r=1}^{N}\left(\iiint_{V_h} d^3\mathbf{x}\,\frac{\partial\left(v_r\phi_r(\mathbf{x})\right)}{\partial x_j}\,P_j(\mathbf{x})\right) \\ &- \sum_{r=1}^{N}\sum_{s=1}^{N}\left(\oiint_{S_h} d^2\mathbf{x}\left[\epsilon_b(\mathbf{x})\frac{\partial\left[\Phi_s\phi_s(\mathbf{x})\right]}{\partial x_i}\hat{n}_i v_r\phi_r(\mathbf{x})\right]\right) + \sum_{r=1}^{N}\left(\oiint_{S_h} d^2\mathbf{x}\left[P_j(\mathbf{x})\hat{n}_j v_r\phi_r(\mathbf{x})\right]\right) = 0,\end{aligned} \tag{3.12}$$

where now we searching for an approximate solution to Eq. (3.5). The coefficients v_r, Φ_s do not depend on space, so they can be pulled out of the integrals, giving,

$$\begin{aligned}\mathcal{R} = &\sum_{r=1}^{N}\sum_{s=1}^{N}\left(v_r\Phi_s\iiint_{V_h} d^3\mathbf{x}\,\frac{\partial\phi_r(\mathbf{x})}{\partial x_i}\,\epsilon_b(\mathbf{x})\,\frac{\partial\phi_s(\mathbf{x})}{\partial x_i}\right) - \sum_{r=1}^{N} v_r\left(\iiint_{V_h} d^3\mathbf{x}\,\frac{\partial\phi_r(\mathbf{x})}{\partial x_j}\,P_j(\mathbf{x})\right) \\ &- \sum_{r=1}^{N}\sum_{s=1}^{N}\left(v_r\Phi_s\oiint_{S_h} d^2\mathbf{x}\left[\epsilon_b(\mathbf{x})\frac{\partial\phi_s(\mathbf{x})}{\partial x_i}\hat{n}_i\phi_r(\mathbf{x})\right]\right) + \sum_{r=1}^{N} v_r\left(\oiint_{S_h} d^2\mathbf{x}\left[P_j(\mathbf{x})\hat{n}_j\phi_r(\mathbf{x})\right]\right) = 0.\end{aligned} \tag{3.13}$$

This equation can be rearranged,

$$\sum_{r=1}^{N} v_r\left(\sum_{s=1}^{N} K_{rs}\Phi_s - F_r\right) = 0. \tag{3.14}$$

[8]The quantity **P** for purposes of this discussion can be considered as a constant (nonzero or zero) as mentioned above.

where

$$K_{rs} = \iiint_{V_h} d^3\mathbf{x} \frac{\partial \phi_r(\mathbf{x})}{\partial x_i} \epsilon_b(\mathbf{x}) \frac{\partial \phi_s(\mathbf{x})}{\partial x_i} - \oiint_{S_h} d^2\mathbf{x} \left[\epsilon_b(\mathbf{x}) \frac{\partial \phi_s(\mathbf{x})}{\partial x_i} \hat{n}_i \phi_r(\mathbf{x}) \right] \tag{3.15}$$

and

$$F_r = \iiint_{V_h} d^3\mathbf{x} \frac{\partial \phi_r(\mathbf{x})}{\partial x_j} P_j(\mathbf{x}) - \oiint_{S_h} d^2\mathbf{x} \left[P_j(\mathbf{x}) \hat{n}_j \phi_r(\mathbf{x}) \right], \tag{3.16}$$

are the *stiffness* matrix and *load* vectors, respectively. The problem defined in Eq. (3.14) contains a linear system of equations,

$$\sum_{s=1}^{N} K_{rs}\Phi_s - F_r = 0. \tag{3.17}$$

to be solved for N values of Φ_s (the unknown degrees of freedom of the problem). If $P_j(\mathbf{x}) = 0$ then we have Laplace's problem (a homogeneous system of linear equations). However, if $P_j(\mathbf{x}) \neq 0$ then we have Poisson's problem and the polarization values will be contained within the load vector F_r[9].

Finally, at this point, the Dirichlet boundary condition can be set within the linear system residual statement, Eq. (3.17). The values of the Φ vector are set as $\Phi_{s'} = \widetilde{\Phi}_{s'}$ for every node

[9]Elementary linear algebra states that the solution of such an equation is $\Phi_r = \sum_{s=1}^{N} (K^{-1})_{sr} F_r$. Of course if $F_r = 0 \forall r$, then Eq. (3.17) is a homogeneous system of linear equations with a trivial solution. If a non-trivial solution exists, it can be found by singular value decomposition or other linear algebra approaches.

s' that lives on some boundary $S_{h,1} \in S_h$. For example, in matrix form, this would be

$$\Phi_s = \begin{pmatrix} \Phi_1 \\ \Phi_2 \\ \Phi_3 \\ \vdots \\ \Phi_N \end{pmatrix} \rightarrow \Phi_s = \begin{pmatrix} \Phi_1 \\ \widetilde{\Phi}_2 \\ \widetilde{\Phi}_3 \\ \vdots \\ \Phi_N \end{pmatrix}, \tag{3.18}$$

where nodes $s' = 2$ and $s' = 3$ live on the boundary sideset of $S_{h,1}$ and have Dirichlet boundary conditions. This means that the Dirichlet data for $\Phi_{s'} = \widetilde{\Phi}_{s'}$ reduces the number of degrees of freedom of the problem. Next, the assembly of the stiffness matrix K and load vector F should be discussed. The integrals within Eq. (3.15) and Eq. (3.16) can be decomposed into a sum of integrals over each element (generating the so-called *summability of the stiffness matrix* property of the FEM, a term coined by Carey and Oden [33]), so that

$$K_{rs} = \sum_{e=1}^{E} K_{rs}^e = \sum_{e=1}^{E} \left(\iiint_{V_h^e} d^3\mathbf{x} \frac{\partial \phi_r^e(\mathbf{x})}{\partial x_i} \epsilon_b \frac{\partial \phi_s^e(\mathbf{x})}{\partial x_i} - \oiint_{S_h^e} d^2\mathbf{x} \left[\epsilon_b \frac{\partial \phi_s^e(\mathbf{x})}{\partial x_i} \hat{n}_i \phi_r^e(\mathbf{x}) \right] \right) \tag{3.19}$$

and

$$F_r = \sum_{e=1}^{E} F_r^e = \sum_{e=1}^{E} \left(\iiint_{V_h} d^3\mathbf{x} \frac{\partial \phi_r^e(\mathbf{x})}{\partial x_j} P_j(\mathbf{x}) - \oiint_{S_h^e} d^2\mathbf{x} \left[P_j(\mathbf{x}) \hat{n}_j \phi_r^e(\mathbf{x}) \right] \right), \tag{3.20}$$

where the integration volume and the shape functions ($\phi_s \rightarrow \phi_s^e$) are simply separated element-wise. Such a result is *indispensable* in FEMs as the summability allows each integral to be computed independently of each other. Therefore, this method is parallelizable as each computer processor can compute each integral without needed information about other integrations.

An alternative approach (and the one used in the MOOSE framework) to solving the problem with FEM is to skip computing the stiffness matrix and load vectors altogether. Here, MOOSE constructs the residual statement and then uses a root finding (Newton's) method to search for zeros. Consider the residual statement of the Poisson problem [Eq. (3.13)] *in the element discretized* form,

$$\mathcal{R}(\Phi) = \sum_{e}^{E}\sum_{r,s}^{N}\left(v_r\Phi_s \iiint_{V_h^e} d^3\mathbf{x}\,\frac{\partial\phi_r^e(\mathbf{x})}{\partial x_i}\,\epsilon_b(\mathbf{x})\,\frac{\partial\phi_s^e(\mathbf{x})}{\partial x_i}\right) - \sum_{e}^{E}\sum_{r}^{N} v_r\left(\iiint_{V_h^e} d^3\mathbf{x}\,\frac{\partial\phi_r^e(\mathbf{x})}{\partial x_j}\,P_j(\mathbf{x})\right) \tag{3.21}$$

$$-\sum_{e}^{E}\sum_{r,s}^{N}\left(v_r\Phi_s \oiint_{S_h^e} d^2\mathbf{x}\,\left[\epsilon_b(\mathbf{x})\frac{\partial\phi_s(\mathbf{x})}{\partial x_i}\hat{n}_i\phi_r^e(\mathbf{x})\right]\right) + \sum_{e}^{E}\sum_{r}^{N} v_r\left(\oiint_{S_h^e} d^2\mathbf{x}\,\left[P_j(\mathbf{x})\hat{n}_j\phi_r^e(\mathbf{x})\right]\right)$$

$$= 0.$$

where we have suppressed summation notation over nodal coordinates slightly and volume (and surface) integration is only taken over the e^{th} element V_h^e (or S_h^e). The dependence on $\mathcal{R} = \mathcal{R}(\Phi)$ indicates that this is a residual contribution due to the variable Φ on all of the nodes (Φ_s). Eq. (3.21) is split into the `Kernel` (first two terms) and `BoundaryCondition` (second two terms) classes. The MOOSE framework implements a quadrature summation [259] for integrations over the element volumes and their surfaces,

$$\int_V f(\mathbf{x})\,dV \approx \sum_{\text{qp}} f(\mathbf{x}_{\text{qp}})w_{\text{qp}}, \text{ and } \int_S f(\mathbf{x})\,dS \approx \sum_{\text{qp}} f(\mathbf{x}_{\text{qp}_{\text{face}}})w_{\text{qp}_{\text{face}}}, \tag{3.22}$$

for some arbitrary function $f(\cdot)$, weights w_{qp}, and quadrature points qp[10]. Each type of element (and its bounding faces) will have their own quadrature rules (the rule consists of qp

[10]In some situations, this integration is exact. For example in one dimension, polynomials of order $2v-1$ can be integrated exactly with v quadrature points

points and weights w_{qp} to approximate the shape functions ϕ_j). Therefore,

$$\begin{aligned}\mathcal{R}(\Phi) = \sum_r \mathcal{R}_r(\Phi) = &\sum_{\text{qp}} \sum_e^E \sum_{r,s}^N w_{\text{qp}} \left(v_r \Phi_s \frac{\partial \phi_r(\mathbf{x})}{\partial x_i} \epsilon_b(\mathbf{x}_{\text{qp}}) \frac{\partial \phi_s(\mathbf{x}_{\text{qp}})}{\partial x_i} \right) \\ &- \sum_{\text{qp}} \sum_e^E \sum_r^N w_{\text{qp}} v_r \left(\frac{\partial \phi_r(\mathbf{x}_{\text{qp}})}{\partial x_j} P_j(\mathbf{x}_{\text{qp}}) \right) \\ &- \sum_{\text{qp}_{\text{face}}} \sum_e^E \sum_{r,s}^N w_{\text{qp}_{\text{face}}} \left(v_r \Phi_s \left[\epsilon_b(\mathbf{x}_{\text{qp}_{\text{face}}}) \frac{\partial \phi_s(\mathbf{x}_{\text{qp}_{\text{face}}})}{\partial x_i} \hat{n}_i \phi_r(\mathbf{x}_{\text{qp}_{\text{face}}}) \right] \right) \\ &+ \sum_{\text{qp}_{\text{face}}} \sum_e^E \sum_r^N w_{\text{qp}_{\text{face}}} v_r \left(\left[P_j \hat{n}_j \phi_r(\mathbf{x}_{\text{qp}_{\text{face}}}) \right] \right) \\ &= 0.\end{aligned} \tag{3.23}$$

Now a root-finding method will be used to find the zeros of Eq. (3.23).

3.2.1 Solving the problem with Newton's method

Eq. (3.21) can be solved using Newton's method which will be summarized below. To restate the overall problem, we want to find Φ_s, for every $s = \{1, 2, ..., N\}$, such that

$$\mathcal{R}_r(\Phi) = 0, \tag{3.24}$$

for every $r = \{1, 2, ..., N\}$. We can do this iteratively and update Φ_s sequentially until the residual is sufficiently minimized. By Taylor expanding $\mathcal{R}_r$ around Φ_s^k for the k^{th} update, one finds,

$$0 = \mathcal{R}_r(\Phi^{k+1}) = \mathcal{R}_r(\Phi^k) + \mathcal{J}_{rs}(\Phi^k) \left(\Phi_s^{k+1} - \Phi_s^k \right) + ... \tag{3.25}$$

where

$$\mathcal{J}_{rk} = \frac{\partial \mathcal{R}_r(\Phi)}{\partial \Phi_j} \tag{3.26}$$

is the *jacobian* matrix. Noting that $\partial \Phi_s / \partial \Phi_k = \delta_{sk}$, then applying Eq. (3.26) to Eq. (3.23) gives,

$$\begin{aligned} \mathcal{J}_{rk} = &\sum_{\mathrm{qp}} \sum_{e=1}^{E} w_{\mathrm{qp}} \left(v_r \frac{\partial \phi_r(\mathbf{x}_{\mathrm{qp}})}{\partial x_i} \epsilon_b(\mathbf{x}_{\mathrm{qp}}) \frac{\partial \phi_k(\mathbf{x}_{\mathrm{qp}})}{\partial x_i} \right) \\ &- \sum_{\mathrm{qp}_{\mathrm{face}}} \sum_{e=1}^{E} w_{\mathrm{qp}_{\mathrm{face}}} \left(v_r \left[\epsilon_b(\mathbf{x}_{\mathrm{qp}_{\mathrm{face}}}) \frac{\partial \phi_k(\mathbf{x}_{\mathrm{qp}_{\mathrm{face}}})}{\partial x_i} \hat{n}_i \phi_r(\mathbf{x}_{\mathrm{qp}_{\mathrm{face}}}) \right] \right). \end{aligned} \tag{3.27}$$

Note that the summability property ($\mathcal{J} = \sum_e \mathcal{J}^e$) can be exploited to parallelize computations of both $\mathcal{J}$ (as well as $\mathcal{R}$). Identifying that $\left(\Phi^{k+1} - \Phi^k\right) = \delta\Phi^k$ is the *update*, and zeroing higher order terms in the Taylor expansion, we have

$$\mathcal{J}_{rs}(\Phi^k)\delta\Phi^k = -\mathcal{R}_r(\Phi^k). \tag{3.28}$$

The initial guess $\Phi^0 = \langle \Phi_1^0, \Phi_2^0, ..., \Phi_N^0 \rangle$ is known (it is constructed from the Dirichlet data of the boundary), and then Eq. (3.28) is iterated until,

$$\frac{||\mathcal{R}(\Phi^n)||}{||\mathcal{R}(\Phi^0)||} < \mathrm{tol}_{\mathrm{residual}}, \tag{3.29}$$

at an arbitrary $k = n$ iterative step with the understanding that $||\mathcal{R}(\Phi^0)||$ is the residual norm (norm of all components, $\mathcal{R}_r$, of the residual vector) of the first iteration. This method is quite effective, and shown to have quadratic convergence [69], if the initial guess is relatively

close to the solution. This means that the error between the solution and the iterate guess plus the update is *at least* proportional to the square of the previous error of the last iterate.

Eq. (3.28), the linear problem for determining $\delta\Phi^k$, may be solved directly or iteratively. The solution to Eq. (3.28) is,

$$\delta\Phi^k = -\mathcal{J}^{-1}(\Phi^k)R(\Phi^k) \tag{3.30}$$

after dropping index notation. Inverting $\mathcal{J}$ can be expensive, so decomposition methods could be used. As an example, decomposing the Jacobian matrix into lower triangular (L) or upper triangular (U) matrices, where $\mathcal{J} = LU$ can be effective in solving the linear problem in one step. Therefore,

$$LU\delta\Phi^k = -\mathcal{R}(\Phi^k) \tag{3.31}$$

so first by solving $Ly = -\mathcal{R}$ for unknown y and then solving $U\delta\Phi^k = y$ for Φ^k can be done efficiently ($k = 1$) compared to directly inverting $\mathcal{J}$. One issue is that this procedure is only efficient for small N which means it is very slow for large problems in three dimensions (order N^3 nodes) where parallelization should be used.

In FERRET, the problems solved (especially those presented in Chapter 5) are typically much larger than those suited for the LU factorization. Fortunately, the PETSC library allows implementation of a popular iterative Krylov-subspace method [270]. There are actually quite a few Krylov methods, but the one used in FERRET is the generalized minimum residual (GMRES) with restart. This iterative method allows the residual to decrease monotonically with a number of k iterations. The number of linear k iterations can be decreased (i.e., improving the convergence properties) by *preconditioning* the system. Preconditioning is a common technique used in conjunction with GMRES and solves the following equivalent

problem,

$$\mathcal{J}W^{-1}W\delta\Phi^k = -\mathcal{R}(\Phi^k) \tag{3.32}$$

where W is a preconditioning matrix with the property that $W^{-1}W = \mathbb{1}$. Solving $\mathcal{J}W^{-1}y = -\mathcal{R}$ first and then solving $W\Phi^k = y$ can result in smaller number of solution iterations, compared to the situation when preconditioning is absent. PETSc supplies hundreds of preconditioning options, where the optimum choice of the matrix W (and its method of construction) might differ from problem to problem. Throughout the development of FERRET, the author investigated a number of different preconditioning methods and found that block-Jacobi preconditioning, which only fills diagonal entries of W, is the most efficient method for the polar-elastic/ferroelectric-strain coupled problems (that are investigated extensively in Chapter 5).

However quite usually, the first guess (or $k = 0$ iterate) may be too far from the solution of the problem. Indeed in the FERRET code, a majority of the accessible problems (such as those discussed in Chapter 5) require a random initial condition of the polarization distributed near zero. This paraelectric guess at the solution is needed for microstructural prediction where there is no *a prior* assumption of domain structure. Such a drastic initial guess of the state of the polarization, i.e; for a fixed temperature $T < T_C$, is far from the solution as the ferroelectric crystal requires **P** to be large in order to minimize the total free energy. Therefore, the linear problem *cannot* be solved, so an additional technique must be used. In MOOSE's program calls down to the PETSc solver, the default method activated to improve convergence is known as a globally convergent line search modification [259] to Newton's method[11]. It may be helpful to summarize them: In a line search, a new definition

[11] For the FERRET problems solved in Chapters 4 and 5, the same default line search options are used.

to the variable update is implemented with some scalar $\lambda < 1$ as,

$$\Phi_s^{k+1} = \Phi_s^k + \lambda \delta \Phi_s^k. \tag{3.33}$$

If

$$\mathcal{R}_r(\Phi^k + \lambda \delta \Phi^k) > \mathcal{R}_r(\Phi^k) + \alpha \lambda \mathcal{J}_{rs} \delta \Phi_s^k, \tag{3.34}$$

where $\alpha \in (0, \frac{1}{2})$ is a weighting parameter[12], then one will need to reduce λ. The backtrack parameter λ is found by the following minimization problem

$$\frac{d\hat{m}_q(\lambda)}{d\lambda} = 0. \tag{3.35}$$

where

$$\hat{m}_q(\lambda) = \left[\mathcal{R}_r(\Phi^k + \delta\Phi^k) - \mathcal{R}_r(\Phi^k) - \mathcal{J}_{rs}(\Phi^k)\delta\Phi_s^k\right]\lambda^2 + \mathcal{J}_{rs}(\Phi^k)\delta\Phi_s^k\lambda + \mathcal{R}_r(\Phi^k) = 0. \tag{3.36}$$

Backtracking can be thought of as an algorithmic way of finding a step size in update space in order to minimize the residual. If once again, Eq. (3.34) is satisfied, then a cubic backtrack schema will need to be chosen and so on. Fortunately, in FERRET, the quadratic backtrack is seen to be sufficient, e.g., for the polar-elastic problems presented in Chapter 5 of this dissertation. It is typically used, for example, towards the end of the evolution of Eq. (2.101) when the polar domain structure has already formed but may be moving slightly and causing large elastic penalties.

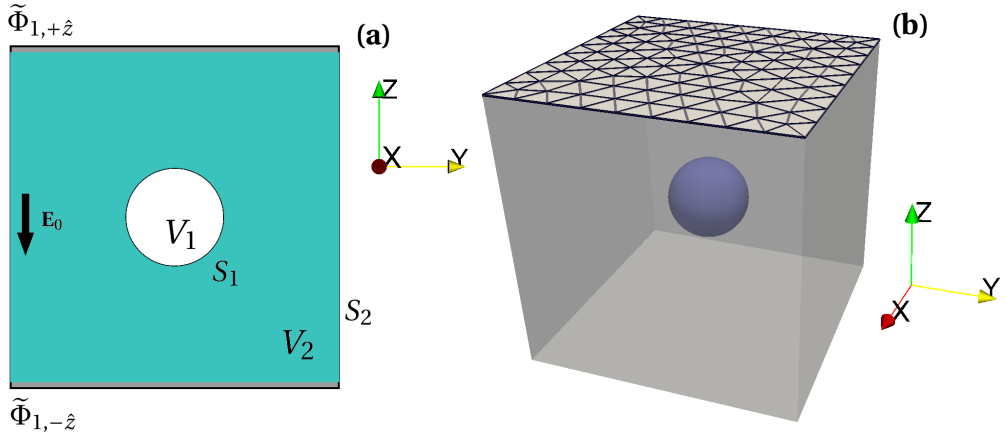

Fig. 3.4 Embedded linearly polarizable sphere in an external electric field. **(a)** The Dirichlet boundary condition sets $\Phi_{1,+\hat{z}}$ and $\Phi_{1,-\hat{z}}$, which gives a *constant* external electric field $\mathbf{E}_0 = -\nabla\Phi = (\Phi_{1,+\hat{z}} - \Phi_{1,-\hat{z}})/V^{1/3}$ with $V = V_1 \cup V_2$. **(b)** 3D representation of the problem. The tetrahedral discretization ($V \approx V_h$) is shown at one boundary. The sphere mesh size is held fixed while the external volume mesh size is relaxed radially away from the sphere (not shown on plot).

3.2.2 Analytical solution of the Laplace equation

The following section compares the analytical and numerical solution found through FERRET/MOOSE's FEM. So far, the governing equations and some of the machinery within the finite element method for arbitrary Poisson kernels have been identified. Now, consider Eq. (3.1) with the geometry shown in in Fig. 3.4. Note that $V_1 \cup V_2 = V$, and that S_2 encloses V_2 at all faces of the cube. Let $\epsilon_b = \epsilon_{b,1}$ in V_1 and $\epsilon_b = \epsilon_{b,2}$ in V_2 with $\epsilon_{b,1} \neq \epsilon_{b,2}$. The sphere, of radius R in the presence of an applied electric field E_0, is going to have zero spontaneous polarization $\mathbf{P} = 0$, which zeroes the right-hand side of Eq. (3.1). This means we are solving Laplace's equation. The subsequent solution will be that of a linearly polarized sphere. The discontinuity in $\epsilon_{b,k}(\mathbf{x})$ at the interface will give rise to a discontinuous radial electric field component at the interface of V_1 and V_2. Of course, such a simple problem with azimuthal symmetry should have analytical solutions which one can find in any elementary text on

[12] In PETSc, this default is $\alpha = 10^{-4}$

electromagnetic theory (the author recommends Jackson [137] who solves a mathematically equivalent problem of a magnetically susceptible sphere).

By using the method of separation of variables in spherical coordinates $\{r, \theta, \phi\}$, the solutions Φ_1 in V_1 and Φ_2 in V_2 are tried

$$\begin{aligned} \Phi_1(r,\theta) &= \sum_{k=0}^{\infty} A_k r^k P_k(\cos\theta) \text{ if } r < R \\ \Phi_2(r,\theta) &= \sum_{k=0}^{\infty} \left(B_k r^k + C_k r^{-k-1} \right) P_k(\cos\theta) \text{ if } r > R, \end{aligned} \tag{3.37}$$

where the coefficients A_k, B_k, C_k are to be determined from the boundary conditions and $P_k(\cdot)$ are the Legendre polynomials as functions of the polar angle. With $\lim_{r\to\infty} \Phi = -E_0 r\cos\theta$, then $B_{k=1} = -E_0$ and $B_{k>2} = 0$. Similarly, we have continuity of Φ at the boundary,

$$\Phi_1(r,\theta)|_{r=R} = \Phi_2(r,\theta)|_{r=R}, \tag{3.38}$$

and the electric displacement field radial component continuity

$$-\epsilon_{b,1} \frac{\partial \Phi_1}{\partial r}|_{r=R} = -\epsilon_{b,2} \frac{\partial \Phi_2}{\partial r}|_{r=R}. \tag{3.39}$$

Eq. (3.38) and (3.39) are special types of boundary conditions that cause the normal component of the electric field to be discontinuous at the interface. By using Eq. (3.38) and (3.39) to find the unknown coefficients, the solution [Eq. (3.37)] reduces to

$$\begin{aligned} \Phi_1(r,\theta) &= -\left(\frac{3}{\epsilon_{b,2}/\epsilon_{b,1} + 2} \right) E_0 r\cos\theta \text{ if } r < R \\ \Phi_2(r,\theta) &= -E_0 r\cos\theta + \left(\frac{\epsilon_{b,2}/\epsilon_{b,1} - 1}{\epsilon_{b,2}/\epsilon_{b,1} + 2} \right) E_0 \left(\frac{R^3}{r^2} \right) \cos\theta \text{ if } r > R, \end{aligned} \tag{3.40}$$

The potential inside the sphere produces a linear (and constant) electric field $\mathbf{E}_1 = -3E_0/(\epsilon_{b,2}/\epsilon_{b,1} + 2)$ and the electric field outside of the sphere is that of a $1/r^3$ dipole close to the sphere, but reproduces a constant field far away.

3.2.3 Numerical solution of the Laplace equation

The residual contributions involve a term of the form,

$$\begin{aligned}\mathcal{R}(\Phi) &= \iiint_V v(\mathbf{x})\,\frac{\partial}{\partial x_i}\left(\epsilon_b(\mathbf{x})\frac{\partial \Phi(\mathbf{x})}{\partial x_i}\right) = 0 \\ &= \iiint_{V_1} v(\mathbf{x})\,\frac{\partial}{\partial x_i}\left(\epsilon_{b,1}\frac{\partial \Phi(\mathbf{x})}{\partial x_i}\right) + \iiint_{V_2} v(\mathbf{x})\,\frac{\partial}{\partial x_i}\left(\epsilon_{b,2}\frac{\partial \Phi(\mathbf{x})}{\partial x_i}\right) = 0,\end{aligned} \tag{3.41}$$

where we have split the volume integration over regions with different dielectric material constants. As described for Eq. (3.21), the problem statement needs to be partitioned into `Kernel` and `BoundaryCondition` classes. In the input file[13] for the Laplace problem, the following blocks are used,

```
[Kernels]
  [./E_Ext_block2]
    type = Electrostatics
    permittivity = 10
    variable = potential
    block = '1'
  [../]
  [./E_Ext_block1]
    type = Electrostatics
    permittivity = 1
    variable = potential
    block = '2'
  [../]
[]
```

which indicates that $\epsilon_{b,1} = 10$ and $\epsilon_{b,1} = 1$. The line `variable = potential` lets the solver know that these two residual contributions are for the Φ variable. The block parameters tell

[13] This linear polarizable sphere in external electric field problem has been implemented as a test for FERRET within the CIVET system. It is located in `/test/tests/electrostatics/dielectric_sphere_test_steady.i`.

the kernels to be separated into sphere (1) and external medium (2) respectively[14]. Finally, the `type = Electrostatics` flag puts this *form* of the Laplace equation as the residual. This defines the actual partial differential equation. In the `Kernel` class `Electrostatics.C` on finds,

```
Real
Electrostatics::computeQpResidual()
{
  return _permittivity*_grad_u[_qp]*_grad_test[_i][_qp];
}
Real
Electrostatics::computeQpJacobian()
{
  return _permittivity*_grad_phi[_j][_qp]*_grad_test[_i][_qp];
}
```

where `test` (i) and `phi` (j) are the basis shape functions from the test function and variable expansions. These two lines pass the correct residual[15], Eq. (3.23), and jacobian, Eq. (3.27), contributions to the solver. The MOOSE system automatically understands that `u` is Φ due to the `variable = potential` passed in the input file.

Next, the boundary conditions are set in the input file,

```
[BCs]
  [./potential_ext_1]
    type = DirichletBC
    variable = potential
    boundary = '1'
    value = 0.25
  [../]
  [./potential_ext_2]
    type = DirichletBC
    variable = potential
    boundary = '2'
    value = -0.25
   [../]
 []
```

[14] The mesh file used must respect the boundary condition that at sufficiently far away from the sphere, the electric field must become constant.

[15] As an important aside, in the previous discussion, the residual is assumed to have contributions from Neumann boundary conditions and some nonzero quantity $\mathbf{P}$. In the case of this specific Laplace problem, this is not the case as $\mathbf{P} = 0$! As such, *only* the first term in Eq. (3.23) is sent to the solver with these lines of code with the distinction that `_test[_i][_qp]` is $(v_i \phi_i)$ and `_phi[_j][_qp]` is simply ϕ_j.

as a `DirichletBC` class, which assigns values of $\Phi = \pm 0.25$ on all nodes that live on `boundary = '1'` and `boundary = '2'` [shown in Fig. 3.4] following conventions of Eq. (3.18).

Furthermore, the input file needs solver options.

```
[Executioner]
  type = Steady
  solve_type = NEWTON
[]
```

Perhaps self-explanatory, the line `type = Steady` indicates that the residual contributions are for a stationary (no time dependence) boundary value problem and `solve_type = NEWTON` calls Newton's method (described above). Results of the MOOSE/Ferret solve are shown as a 2D cut of contours in Fig. 3.5 for Φ **(a)** and $-\nabla\Phi \cdot \hat{z}$ **(b)** in the external region. Also presented in Fig. 3.6 **(b)** is a 3D contour plot of the electric field along $\hat{z}$, which shows the canonical dipole pattern as expected.

It is seen in Fig. 3.6 **(b)** that the agreement between the analytical solution of Eq. (3.40) and the MOOSE results is quite good with the discontinuity appropriately captured.

3.2.4 Comparison of numerical results for the Poisson equation solve

We now consider the following for the situation described in the previous section,

$$\begin{aligned} \Phi &= 0 \text{ on } S_2 \\ \mathbf{P} &\neq 0 \text{ in } V_1 \end{aligned} \tag{3.42}$$

which gives rise to,

$$\sigma = \mathbf{P} \cdot \hat{\mathbf{n}} \neq 0 \text{ on } S_1. \tag{3.43}$$

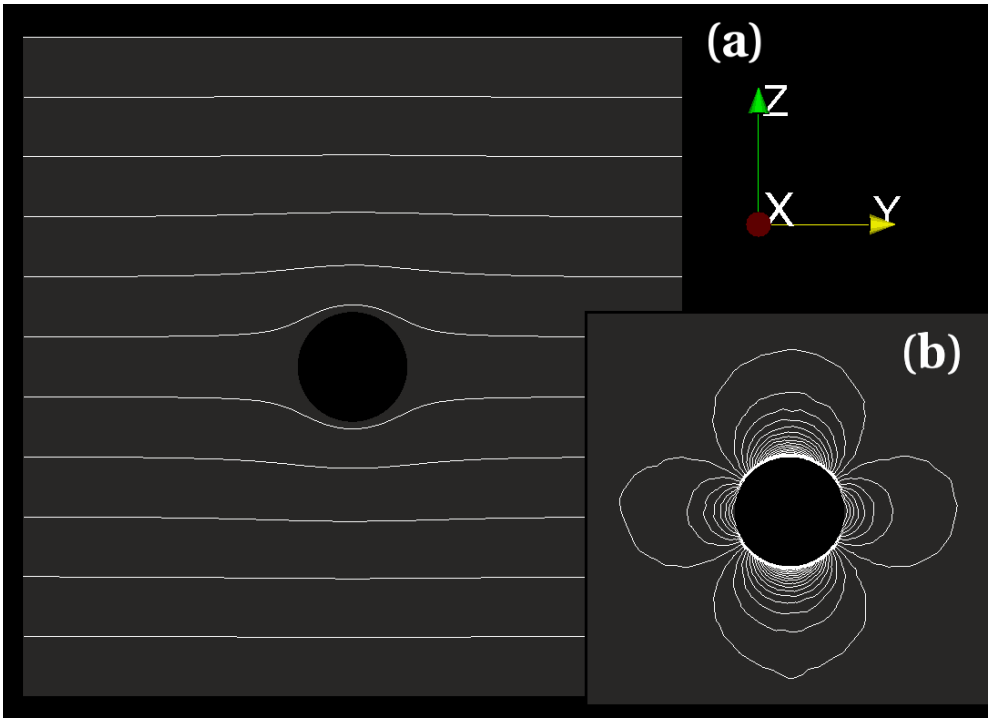

Fig. 3.5 **(a)** 2D contours of the $\Phi(\mathbf{x})$ variable found from MOOSE/FERRET in region V_2 due to an applied electric field. **(b)** Contours of the total electric field component, E_z, outside of the sphere that indicates the induced dipole pattern in the linearly polarizable sphere.

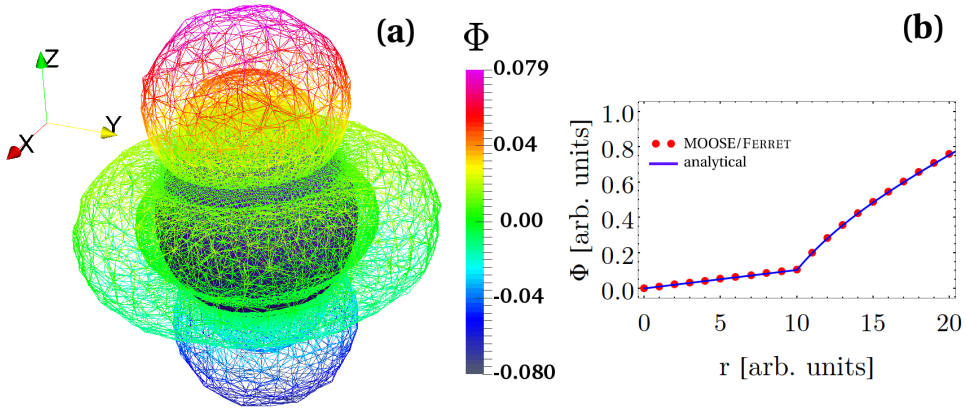

Fig. 3.6 **(a)** 3D contours of the $E_z(\mathbf{x})$ (aux) variable found from MOOSE/FERRET in region V_2. The contours are *colored* by the Φ values. **(b)** Comparison between analytical and numerical results for an arbitrary ($\theta = 0^\circ$) arc length cut from the $R = 10$ sphere.

Now clearly, there are more nonzero terms in Eq. (3.23). To implement a nonzero **P**, we utilize the *coupling* system in MOOSE. This particular MOOSE system is, in a way, hidden from the user or a developer of an application such as FERRET. For this problem[16], **P** could be a `Variable` or a `AuxVariable`:

```
[AuxVariables]
  [./polar_x]
    order = FIRST
    family = LAGRANGE
    block = '1'
    [./InitialCondition]
      type = ConstantIC
      value = 0.0
    [../]
  [../]
  [./polar_y]
    order = FIRST
    family = LAGRANGE
    block = '1'
    [./InitialCondition]
      type = ConstantIC
      value = 0.0
    [../]
  [../]
  [./polar_z]
    order = FIRST
    family = LAGRANGE
    block = '1'
    [./InitialCondition]
      type = ConstantIC
      value = 0.5
    [../]
  [../]
[]
```

where we have chosen to polarize the sphere along the $\hat{\mathbf{z}}$ direction, with $\mathbf{P} = 1/2\,\hat{\mathbf{z}}$ as an `AuxVariable`. The analytical expression for a dipole sitting in space is [137],

$$\mathbf{E}_{\text{dipole}} = \frac{1}{4\pi\epsilon_0}\frac{1}{r^3}\left[3\left(\mathbf{P}\cdot\hat{\mathbf{r}}\right)\hat{\mathbf{r}} - \mathbf{P}\right], \tag{3.44}$$

[16] A test problem solving for $\Phi(\mathbf{x})$ due to the spontaneously polarized sphere is located in `/test/tests/electrostatics/poisson_sphere_test_steady.i`.

where ϵ_0 is a permittivity of space.

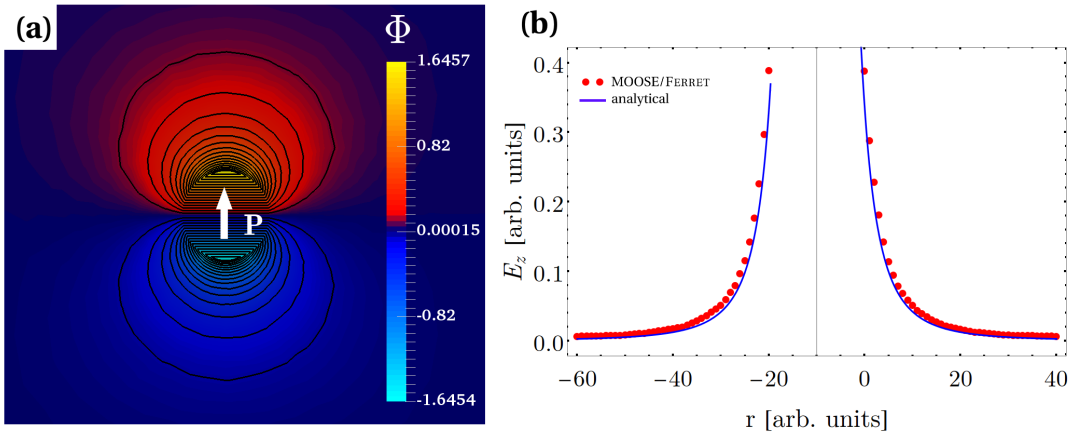

Fig. 3.7 **(a)** Electrostatic potential of a dipole field of $\mathbf{P} = 1/2\hat{\mathbf{z}}$ for a sphere of radius $R = 10$ with $\Phi = 0$ at the boundaries of the computational domain [the sphere is embedded in a box as in Fig. 3.4]. **(b)** Comparison of numerical results from FERRET/MOOSE and Eq. (3.44) along $\theta = 0^\circ$ line.

By looking at Fig. 3.7, one can realize that the agreement with this expression is quite good. A slight numerical discrepancy is noted due to the finite size of the system – the computational boundary where the $\Phi = 0$ Dirichlet boundary condition is applied should be sufficiently far away such that the potential vanishes. Nevertheless, the important physical $1/r^3$ dependence is captured.

3.3 `Kernels` and `Materials` in FERRET

Only some of the `Kernels` and `Materials` are summarized in this dissertation for the sake of brevity [17].

[17] If interested, the FERRET manual located at /ferret/doc/ferret_manual_v2.tex which summarizes all of the MOOSE objects within the FERRET distribution. The author also has prepared a tutorial that includes some basic examples of finding the minimum of free energy of Landau's polynomials under the influence of electrostatic, elastic, or a combination of the two fields found at /ferret/doc/ferret_tutorial_v1.tex. These documents are constantly being improved and updated.

Extensively discussed in the previous chapter is the contribution from different types of competing energies to the ferroelectric microstructure evolution. The master TDLGD equation,

$$\frac{\partial \mathbf{P}}{\partial t} = -\Gamma \frac{\delta \mathcal{F}}{\delta \mathbf{P}}, \tag{3.45}$$

has a right hand side that contains a linear combination of energies under a variation with respect to **P**. The total energy,

$$F = F_{\text{bulk}} + F_{\text{wall}} + F_{\text{elastic}} + F_{\text{elec}} + F_{\text{coupled}}. \tag{3.46}$$

consists of a number of residual contributions. The variation of the cubic-tetragonal bulk crystal energy for example,

$$\begin{aligned}
\frac{\delta F_{\text{bulk}}}{\delta \mathbf{P}} = & \frac{\delta}{\delta \mathbf{P}} \int_V dV \ \left[\alpha_1(T) \left(P_x^2 + P_y^2 + P_z^2 \right) + \alpha_{11} \left(P_x^4 + P_y^4 + P_z^4 \right) \right] \\
& + \frac{\delta}{\delta \mathbf{P}} \int_V dV \ \left[\alpha_{12} \left(P_x^2 P_y^2 + P_y^2 P_z^2 + P_x^2 P_z^2 \right) + \alpha_{111} \left(P_x^6 + P_y^6 + P_z^6 \right) \right] \\
& + \frac{\delta}{\delta \mathbf{P}} \int_V dV \ \left[\alpha_{112} \left[P_x^4 \left(P_y^2 + P_z^2 \right) + P_y^4 \left(P_x^2 + P_z^2 \right) + P_z^4 \left(P_x^2 + P_y^2 \right) \right] + \alpha_{123} \left(P_x^2 P_y^2 P_z^2 \right) \right]
\end{aligned} \tag{3.47}$$

has three terms for each component of **P**. In index notation (repeated indices are *not* summed and it is assumed that $i \neq j \neq k$), Eq. (3.47) is,

$$\frac{\delta F_{\text{bulk}}}{\delta P_k} = \iiint_V d^3\mathbf{x} \left(2\alpha_1(T)P_i + 4\alpha_{11}P_i^3 + 6\alpha_{111}P_i^5 + 2\alpha_{12}P_i\left(P_j^2 + P_k^2\right) + 4\alpha_{112}P_i^3\left(P_j^2 + P_k^2\right)\right) \tag{3.48}$$

$$+ \iiint_V d^3\mathbf{x} \left(2\alpha_{112}P_i\left(P_j^4 + P_k^4\right) + 2\alpha_{123}P_iP_j^2P_k^2\right)$$

Eq. (3.48) is contained in the `Kernel` class called `BulkEnergyDerivativeSixth` in the `computeQpResidual()` member function,

```
const VariableValue & _polar_i = (_component == 0) ?
      _polar_x : (_component == 1) ? _polar_y: _polar_z;
const VariableValue & _polar_j = (_component == 0) ?
      _polar_y : (_component == 1) ? _polar_z: _polar_x;
const VariableValue & _polar_k = (_component == 0) ?
      _polar_z : (_component == 1) ? _polar_x: _polar_y;

return ((2.0 * _alpha1 * _polar_i[_qp]
    + 4.0 * _alpha11 * std::pow(_polar_i[_qp], 3.0)
    + 2.0 * _alpha12 * _polar_i[_qp]*(std::pow(_polar_j[_qp], 2.0)
    + std::pow(_polar_k[_qp], 2.0))
    + 6.0 * _alpha111 * std::pow(_polar_i[_qp], 5.0)
    + 4.0 * _alpha112 * std::pow(_polar_i[_qp], 3.0) * (
      _polar_j[_qp] * _polar_j[_qp]+_polar_k[_qp] * _polar_k[_qp])
    + 2.0 * _alpha112 * _polar_i[_qp]
      *(std::pow(_polar_j[_qp], 4.0) + std::pow(_polar_k[_qp], 4.0))
    + 2.0 * _alpha123 * _polar_i[_qp]*std::pow(_polar_j[_qp], 2.0)
      * std::pow(_polar_k[_qp], 2.0)) * _test[_i][_qp])
      * std::pow(_len_scale, 3.0);
```

where the user choice of `component` determines the Cartesian direction the variation (with respect to P_x, P_y, P_z) is taken. Naturally for a 3D problem, three `Kernel` entries of `type = BulkEnergyDerivativeSixth` are needed in the input file for `component = 0,1,2`. A similar approach exists for the residual contribution from F_{wall} term.

For ferroelectric, the self-strain,

$$\varepsilon_{ij}^{0}(\mathbf{x}) = Q_{ijkl} P_k(\mathbf{x}) P_l(\mathbf{x}) \tag{3.49}$$

is introduced into the total elastic energy as [128, 188]

$$f_{\text{total,elastic}} = \frac{1}{2} C_{ijkl} \left(\varepsilon_{ij} - \varepsilon_{ij}^{0}\right) \left(\varepsilon_{kl} - \varepsilon_{kl}^{0}\right). \tag{3.50}$$

This term can be decomposed into a elastic and polar contribution (zeroing the higher order terms),

$$f_{\text{total,elastic}} = f_{\text{elastic}} + f_{\text{coupled}} = \frac{1}{2} C_{ijkl} \varepsilon_{ij} \varepsilon_{kl} - C_{ijkl} Q_{klmn} \varepsilon_{kl} P_m P_n. \tag{3.51}$$

The `Material` class `ComputeElectrostrictiveTensor` allows the user to input the entries of the Q_{ijkl} and C_{ijkl} and they are filled appropriately for this energy contribution throughout all `Kernels` that use it. This is seen in a typical input file as,

```
type = ComputeElectrostrictiveTensor,
```

```
Q_mnkl = '0.089 -0.026-0.026 0.089 -0.026 0.089 0.03375 0.03375 0.03375'
```

and

```
C_ijkl = '281 115.74 115.74 281 115.74 281 97.18 97.18 97.18',
```

in the [`Materials`] block.

3.4 Multiple variables and time dependence

The full phase-field approach, namely solving Eq. (2.101), along with the auxiliary stress divergence and Poisson equation [Eq. (2.12) and Eq. (2.52) respectively], at every step in the time evolution, involves multiple variables and not just one as described above. A total of seven variables exist in this polar-elastic coupled problem: $\mathbf{P} = \langle P_x, P_y, P_z \rangle$, $\mathbf{u} = \langle u_x, u_y, u_z \rangle$, and Φ. Their time-dependent solutions are found in a Newton-Raphson time-dependent approach [30]. For the sake of brevity of this dissertation, the FEM details of such a formidable equation set are left out.

Chapter 4

Electronic band-gap engineering in semiconducting nanostructures

Theoretical approach used for simulations of ferroelectrics at mesoscale involves coupled interactions between elastic, polar, and thermal variables. The following Chapter details a study that resulted from testing of the purely elastic solver in the FERRET application that was also linked to the electronic properties postprocessor. This solver was developed prior to the coupled polar-elastic-electrostatic solver that will be discussed in the next Chapter.

4.1 Introduction

Composite core-shell nanoparticles (CSNPs) display a diverse range of functional properties, involving combinations of electronic, optical, magnetic, and chemical phenomena that can be altered with respect to the behavior of their bulk-size counterparts. Large surface-to-volume ratios, complex geometries and inherent structural inhomogeneities, characteristic of CSNPs, could all be utilized as useful 'dials' for precise engineering of their functionalities by manipulating the particle size, shape, and microstructure. Possible applications of CSNPs include biomedical imaging[44, 139, 225, 316], catalysis[214, 331, 201], cancer treatment

and drug delivery[57, 51], ecological remediation and detoxification[330, 312, 244], and a variety of electromagnetic radiation sensing, absorption, control, and shielding applications. [108, 336, 309, 54]

Currently, semiconducting particle shells, created from popular oxide materials, such as TiO_2 and ZnO, are a subject of active research aimed at enhancement and fine-tuning of the CSNP optical properties.[54, 148, 199, 191, 193, 182, 299] The expected improvements to the photocatalytic activity and photovoltaic operational efficiency[54, 170, 102] could be extremely useful for a wide range of technological applications. For example, the global demand for catalysis solutions was recently valued at US$33.5 billion [acm] and is only projected to increase in the future.

Modern synthesis routes are capable of fabricating not only spherical particles, but also a variety of different geometrical shapes [328, 327, 329], including cubes, hexagons, disks, rods, tubes, etc. [54] For example, ZnO-based structures have been grown as nanowires[129, 317, 163], nanorods [200, 296], hollow hexagonal nanotubes[314], and nanodisks with a Zn core [93]. In addition, distinct shell morphologies, such as single-crystalline, polycrystalline, or mesoporous were synthesized [93], plus accurate control of core-to-shell thickness ratios was demonstrated [328, 327, 329].

Polymorphic TiO_2 has been investigated[214, 331, 21, 191, 170, 102, 190, 192, 126] as a nanocomposite component for incorporation into solar-cell heterostructures, or as a shell material, e.g., coupled with ZnO and other cores. The improved photoefficiency of the TiO_2 shells was proven to depend strongly on the thickness of the coating [170, 102].

It has also been observed[328, 327, 329, 317, 200, 155] that CSNPs exhibit substantial deviations from corresponding bulk materials in their optical properties, including, e.g., measured values of the electronic band gap E_g. One suggested mechanism that could explain this departure from the bulk behavior involves quantum confinement of the electronic state due to the smallness of the nanostructure. This mechanism is usually activated when the

characteristic particle size d is approximately the same as the de Broglie wavelength of its electronic wavefunctions. However, while quantum confinement effects could be responsible for band-gap shifts in extremely small nanostructures [114, 321], most of the observed discrepancies occurred in structures that are too large for such effects to appreciably affect the location of their electronic bands along the energy axis. It is thus reasonable to assume that some other factors are behind the modulation of E_g in CSNPs.

Specifically, in such particles, complex interactions between their core and shell parts may arise and become tunable by changing the core-to-shell volume ratio, as well as other manipulations of the particle microstructure and geometry. Also, as discussed in Chapter 2, the presence of a free shell surface with its intrinsic surface tension can give rise to additional residual stress fields that may affect the mechanical equilibrium of the composite particle. Furthermore, misfit strains arising between adjacent crystallographically misaligned grains in the polycrystalline shell could also translate into certain modifications of the electronic band structure. In this Chapter, following the work of Ref. [210], a finite-element method based computational approach utilizing parameters fitted from *ab initio* simulations is applied to elucidate a range of factors that could be influencing the band-gap variation in CSNPs and related structures, including their shape, size, geometry and morphology.

4.2 Core-shell nanoparticle models

4.2.1 Mono- and polycrystalline core-shell structures

The models used in this study are created in CUBIT [Cub], which is a CAD and meshing software package developed primarily at Sandia National Laboratories [1]. CUBIT allows for precise user control of finite-element mesh types and sizes. Our construction procedure

[1] Trelis, which is commercial version of the CUBIT software package, was also procured under academic licensing agreements through csimsoft and is available at http://www.csimsoft.com/

for monocrystalline or polycrystalline CSNP structural models can produce particles with spherical or faceted cores as shown in Fig. 4.1 **(a)** and **(b)**.

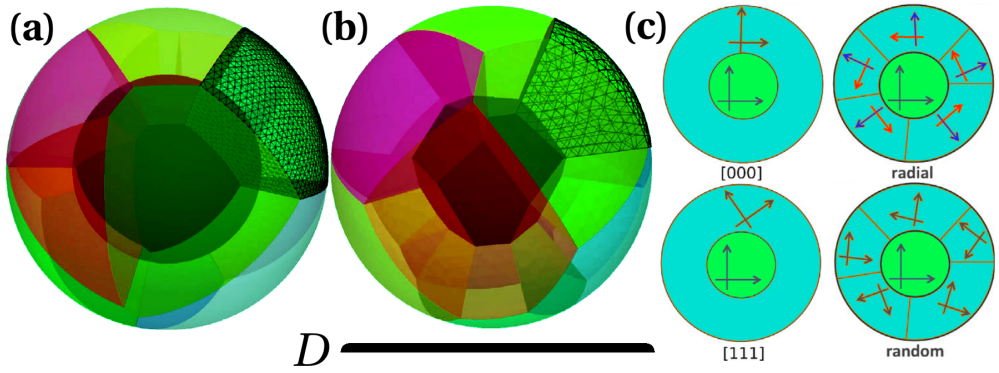

Fig. 4.1 Images of the polycrystalline CSNP models are presented with **(a)** spherical and **(b)** faceted cores. The unstructured finite element mesh is shown as tetrahedron overlay in a sub-block of the shell region. To the right, a diagram **(c)** presents the different arrangements of the elastic stiffness tensor, C_{ijkl}, in the shell, polycrystalline shell, and core. From left to right, and top to bottom, there are [000] uniform collinear, [111] uniform noncollinear, radial, and random orientations. For example, in the radial arrangement, the hexagonal or tetragonal symmetry axis is pointing outward parallel to the surface-normal unit vector, while the axes perpendicular to the radial direction are chosen randomly. Adopted from Ref. [210] with permission from the publisher.

A monocrystalline CSNP model can be built by creating two concentric spheres of different diameters, $\{D_{\text{core}}, D_{\text{shell}}\}$, centered at the origin O with $D_{\text{shell}} > D_{\text{core}}$. The core and shell regions are thus cast as subdomains that can have independently defined material tensors (for example, C_{ijkl} or C^{S}_{ijkl}). Using the Euler rotation method described in Chapter 2, the orientation of crystallographic axes of the elastic stiffness tensor may be adjusted in each subdomain. For the monocrystalline models, the [000] and [111] orientations are shown in Fig. 4.1 **(c)**. The [000] orientation designates a collinear structure with parallel elastic-stiffness tensor axes of both core and shell regions, while in the [111] configuration these axis sets are rotated with respect to one another by an appropriate choice of the Euler angles θ, ϕ, Ψ.

For a polycrystalline CSNP model with a spherical core, a Voronoi construction is carried out with an assistance of the VORO++ package [vor]. In this procedure, the shell volume

defined by $V_{\text{shell}} = \frac{1}{6}\pi\left(D^3_{\text{shell}} - D^3_{\text{core}}\right)$, is subdivided into a N-tuple of Voronoi cells $(G_k)_{k\in N}$. The tessellation of this volume is first carried out by quasi-randomly choosing a set of generating points $P_k = (r_k, \theta_k, \phi_k)$ in spherical coordinates. In order to preserve the spherical surface curvature $\kappa = 2/D_{\text{shell}}$, the value of r_k is chosen to be a constant $(D_{\text{shell}} - D_{\text{core}})/4$, or halfway between core and shell, for all k. Then, the volume subdivision follows the simple mathematical prescription:

$$G_k = \left\{x \in X | d(x, P_k) \leq d(x, P_j) \,\text{for all}\, j \neq k\right\}, \tag{4.1}$$

where d is a distance function in some metric space X, which calculates the Euclidean distance from any point, x, *in* the Voronoi cell to its generating point belonging in V_{shell}. This definition ensures that the k^{th} cell is a region consisting of all points closer to P_k than to all other P_j. It follows then that $\cup_{k\in N} G_k = V_{\text{shell}}$.

In order to create a model with a faceted core (but still preserving spherical surface of the shell), one can introduce small noise into the choice of r_k. Then Eq. 4.1 will no longer produce a spherical surface during the tesselation procedure, however, the external surface of the shell can be restored by cleaving this construction with a perfect sphere. For the models investigated in this section, the number of grains N is chosen to be between 10 and 20, depending on the specific combinations of core and shell sizes. Orientations of the elastic-stiffness tensors within individual grains can also be set by applying Euler rotations, producing, e.g., random or radial arrangements, as shown in Fig. 4.1, or involve more intricate combinations. For the random configuration, the Euler angles θ, ϕ, Ψ are chosen randomly for each grain. For the radial configuration, the Euler angles are chosen such that the high-symmetry axis of the elastic stiffness tensor is aligned along the shell-surface normal $\hat{\mathbf{n}}$ at the Voronoi generator point P_k.

As a final step of the CSNP model construction, the volumes of all subdomains, or 'material blocks,' are discretized with an unstructured grid of tetrahedral elements, which

also includes the appropriate discretization of all the subdomain surfaces, both internal and external.

4.2.2 Materials parameters

As discussed in the previous section, the presence of separate subdomains within the model — monocrystalline or granular shell, and core, in the case of a CSNP — allows the user to 'decorate' these regions with different materials properties, which, in this investigation, are defined solely by the C_{ijkl} tensor. Here, as already outlined in the introduction, metallic Zn, wurtzite (*w*-) ZnO, and rutile (*r*-) TiO_2 are chosen as prospective materials for creating the core/shell materials combinations. The C_{ijkl} values for all of these compounds are presented in Table 4.1 in reduced Voight notation[245].

	Ref.	Crystal Structure	C_{11}	C_{12}	C_{13}	C_{33}	C_{44}	C_{66}
Zn	[171]	hcp ($P6_3/mmc$)	163.0	30.6	48.1	60.3	39.4	65.9
ZnO	[28]	wurtzite ($P6_3mc$)	209.7	121.1	105.1	210.9	42.5	44.3
		isotropic	205.9	118.5			43.7	
TiO_2	[135]	rutile ($P4_2/mnm$)	268.0	174.9	147.4	484.2	123.8	190.2
		isotropic	362.3	136.1			113.1	

Table 4.1 Components of the bulk elastic-stiffness tensor C_{ijkl} for metallic Zn, *w*-ZnO and *r*-TiO_2 in reduced Voigt notation[245] in units of GPa. Averaged components for an isotropic case[245] with $C_{11} = C_{33} = 2\mu + \lambda$, $C_{12} = C_{13} = \lambda$ and $C_{44} = C_{66} = \mu$ are also given for ZnO.

Variants for both fully anisotropic (*a-la* bulk crystal) and averaged isotropic (e.g., amorphous) tensors are included in the Table for both oxide compounds, enabling us to study a variety of different models, including (*i*) an isotropic core, surrounded by an isotropic shell, (*ii*) an isotropic core in an anisotropic shell and etc. E.g., the latter case includes a *w*-ZnO/*r*-TiO_2 core-shell nanoparticle. Although *w*-ZnO formally has hexagonal symmetry, it is nearly isotropic elastically, as is shown by the closeness of the corresponding components of its 'fully anisotropic' and 'averaged' elastic stiffness tensors. Specifically, for *w*-ZnO,

$C_{11} \simeq C_{33}$, $C_{12} \simeq C_{13}$, and $C_{44} \simeq C_{66} \simeq (C_{11} - C_{12})/2$ which approximately satisfies the conditions for elastic isotropy.

Finally, the free surface of the CSNP requires some discussion. Since the surface-to-volume ratio of the CSNP is rather large, the possible influence of surface elasticity is introduced into the model using the Gurtin-Murdoch approach, summarized in Chapter 2. Unlike the bulk elastic-stiffness tensors, the surface elastic parameters $\left\{C^S_{ijkl}, \tau^0\right\}$ are not usually available from experimental measurement. However, with the use of first-principles based numerical calculations, these material constants have been extracted for *w*-ZnO and *r*-TiO_2, as reported in Refs. [323] and [140], respectively. Parameter values used in this Chapter are shown in Table 4.2.

	Reference	C^s_{11}	C^s_{12}	C^s_{66}	C^s_{22}	τ
w-ZnO	[323]	49.1	15.1	13.7	34.9	-1.7
r-TiO_2	[140]	-73.8	-26.3	0.0	-17.7	1.8

Table 4.2 Surface elastic stiffness tensor components in reduced Voight notation [245] and averaged residual stresses τ for the $(10\bar{1}0)$ *w*-ZnO and (110) *r*-TiO_2 surfaces in units of $\mathrm{N/m}$.

In this project, we assume that the surface of the shell is represented only by the lowest-energy surface — i.e., no faceting of the shell is considered, however, this phenomenon can be accounted for in more advanced models if such a need arises. The lowest-energy surfaces are $(10\bar{1}0)$ and (110) for *w*-ZnO and *r*-TiO_2, respectively. The value of the intrinsic surface tension is assumed to be an isotropic average of the tensorial values given in the literature.

4.2.3 Solve

As an aside, the approach to solve for the elastic fields at mechanical equilibrium is summarized. The reader should refer to Chapter 2 for an extensive discussion of the governing

equations of mechanical equilibrium. The following governing equations are solved,

$$\frac{\partial}{\partial x_j}\left(C_{ijkl}\varepsilon_{ij}\right) = 0 \text{ where } i,j,k,l = 1,2,3, \tag{4.2}$$

and the surface problem,

$$\frac{\partial}{\partial x_\beta}\left(C^S_{\alpha\beta\gamma\delta}\varepsilon^S_{\gamma\delta}\right) = 0 \text{ where } \alpha,\beta,\gamma,\delta = 1,2 \tag{4.3}$$

Eqs. 4.2 and 4.3 are cast into a weak-formulation on the finite element mesh and solved concurrently to find the displacement field **u** that satisfies minimization of the residual in the presence of possible surface tension τ^0, or applied hydrostatic pressure. Stationary residual minimization is performed using a preconditioned Jacobi-free Newton-Krylov approach [161] using a block Jacobi preconditioning procedure [269] and the variable residual is converged to below 10^{-10} irrespective of the boundary conditions, or a change of morphology or microstructure of the particle.

4.2.4 Coupling to the electronic band gap

As discussed in the introduction of this Chapter, deviation from bulk behavior in the optical properties of the ZnO and TiO_2 based CSNPs has been observed. It is well-known that electronic band structure depends on the crystal lattice configuration and therefore, if residual strains are strong enough to alter the ionic positions, such properties as the electronic band gap may be influenced by lattice distortions (refer to Fig. 4.2 for an illustration). This effect has been originally calculated with the $\mathbf{k}\cdot\mathbf{p}$ perturbation theory developed by Bardeen and Shockley [25] and further generalized by Herring and Vogt [118], while at present it

can be evaluated by the DFT-based techniques, or even more accurate quantum mechanical approaches. If needed, strain-induced energy shifts can be decomposed into contributions for each of the bands. However, conducting such calculations across the Brillouin Zone can be challenging, as the strain tensor has six independent components ($\varepsilon_{xx}, \varepsilon_{yy}, \varepsilon_{zz}, \varepsilon_{xy}, \varepsilon_{xz}, \varepsilon_{yz}$) and each energy level may behave differently due to the symmetry of the crystal. Further complications can arise if the material has non-trivial spin-orbit coupling, is in the vicinity of a metal-insulator phase transition [16], or has degenerate bands. Another possible complication

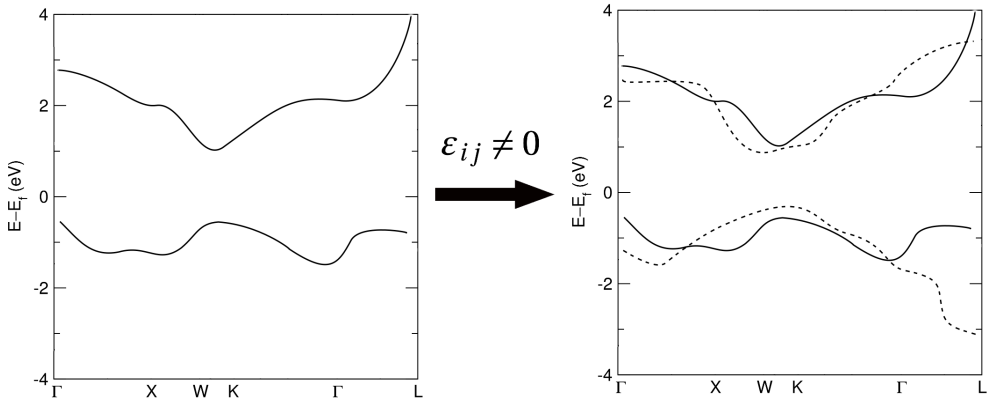

Fig. 4.2 Illustration of the strain-modulated band gap tuning. Here, the changed bands are shown in dashed lines, while stress-free bands are in bold. In general, the presence of an anisotropic elastic strain ε_{ij} will alter the symmetry of the crystal and consequently both the conduction and valence bands across the entire Brillouin zone.

stems from the fact that many past and current electronic structure calculations (such as those based on the DFT formalism) may under/over estimate the band-gap energy, or in general improperly place certain groups of bands on the energy axis. However, in some simple cases, strain-induced modulations of the electronic band gap can be evaluated, for example by decomposing the action of the residual elastic field into contributions from certain highly-symmetric distortions, such as uniaxial tension/compression along a chosen axis, combined with a biaxial tension/compression in a plane perpendicular to that axis.

Such simple decomposition can be carried out for both semiconducting oxide materials considered here. With only linear contributions taken into account, this expression is

$$E_g = E_g^0 + c_u\sigma_u + c_b\sigma_b, \tag{4.4}$$

where E_g^0 is the band-gap energy of a stress-free bulk material. The values of the coefficients for *w*-ZnO and *r*-TiO_2 are presented in Table 4.3. It should be noted that the coefficients c_b and c_u depend on the difference between *specific* conduction and valence bands. No such distinction is made in the coarse-grained model, as it is assumed that many transitions are possible, but the overall average gap is captured by at least one set of these coefficients.

		Stress rate (10^{-1} eV/GPa)	Method and Ref.	E_g^0 (eV)
w-ZnO	c_b	-0.02	HSE + G_0W_0 [306]	3.20
	c_u	-0.32		
r-TiO_2	c_b	-0.07	GGA [320]	3.02
	c_u	0.08		

Table 4.3 Biaxial and uniaxial band-gap stress rates, as well as unstrained band gap energies for *w*-ZnO parameterized from hybrid functional (HSE) and single shot G_0W_0 calculations to correct the band gap, and *r*-TiO_2 using the generalized gradient approximation (GGA).

4.3 Electronic band gap tuning in CSNPs

4.3.1 Residual stress fields

The simultaneous solution of the volume and surface elastic problems for a given CSNP model produces a position-dependent displacement field $\mathbf{u}(\mathbf{x})$, from which all the components of the (nonuniform) stress and strain tensors can be obtained in a standard way. Typical results of such simulations for the $\sigma_{zz} = \sigma_3$ stress-tensor component are presented as three-dimensional maps in Figs. 4.3 (a) and (b) for a particle with a spherical core 15 nm in

diameter and a 5-nm thick monocrystalline shell around it (total diameter 25 nm), kept under a condition of vanishing external pressure.

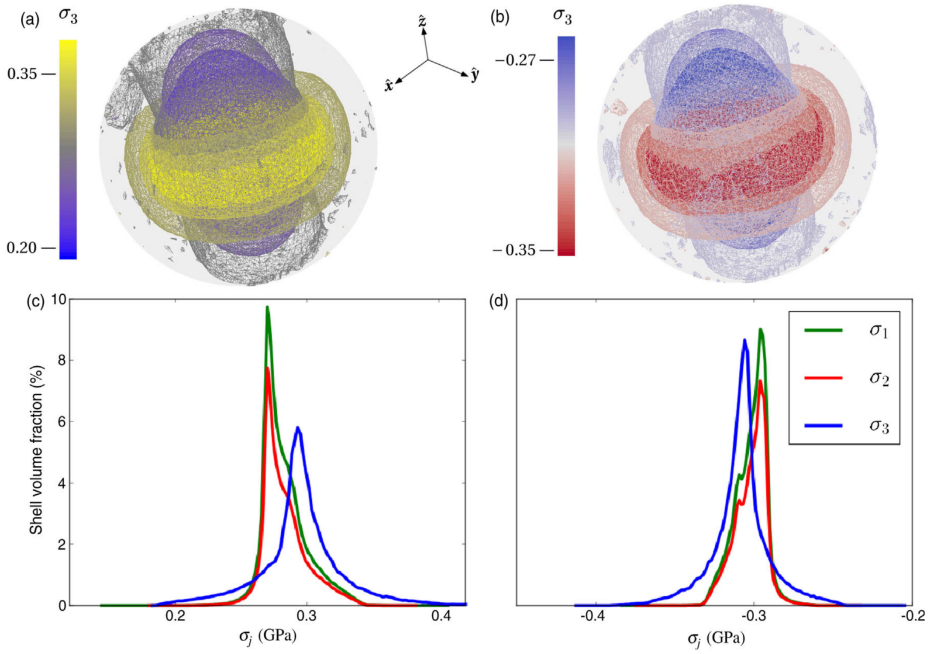

Fig. 4.3 Three-dimensional maps (a),(b) and corresponding shell-volume distribution histograms (c),(d) of the principal stress fields within a CSNP with a spherical core 15 nm in diameter and a 5-nm-thick monocrystalline shell around it (total diameter 25 nm), kept under a condition of vanishing external pressure. (a),(c) Tensile stresses in a Zn/*w*-ZnO particle. (b),(d) Compressive stresses in a *w*-ZnO/*r*-TiO_2 particle. In both cases, the particle core-shell elastic-stiffness tensor axes are collinear and their orientations coincide with those of the global coordinate system, whose axes are shown in the insert. For the sake of clarity, stress fields on the particle surface, or areas close to it, are not shown in (a) and (b). Reprinted from Ref. [210] with permission from the publisher.

These maps are supplemented by histograms in Figs. 4.3(c) and (d), showing how the values of the principal stresses $\sigma_{xx} = \sigma_1$, $\sigma_{yy} = \sigma_2$, σ_3 are distributed throughout the volume of the shell. In the case of a Zn/*w*-ZnO particle [Figs. 4.3(a) and (c)], it is found that its shell expands slightly in order to satisfy the vanishing-external-pressure condition, which results in tensile stresses at the core-shell interface. On the other hand, a *w*-ZnO/*r*-TiO_2 particle [Figs. 4.3(b) and (d)] contracts under the same conditions, which leads to emerging compressive interfacial stresses. In both instances, we observe anisotropic distribution of

stresses throughout the shell volume. Specifically, in the Zn/*w*-ZnO particle oriented as shown in Fig. 4.3(a), the hcp Zn core is stiffer within the *xy* plane and softer along the *z* axis (see Table 4.1), and this elastic anisotropy imprints itself onto the interfacial region of the nearly isotropic *w*-ZnO shell in the form of a varying stress field. Also, as expected from the material symmetry, in both particles, the obtained shell-volume distributions of principal stresses σ_1 and σ_2 are similar to each other, with the one for σ_3 being noticeably different, which is in agreement with the approximation utilized in the fitting of Eq. 4.4. Finally, in both particles, stress fields on or close to the external surface [omitted in Figs. 4.3(a) and (b) for clarity] are found to be smaller, but about the same order of magnitude as the shell-volume stresses discussed above.

Also, in Fig. 4.4, we present line plots of the $\sigma_{zz} = \sigma_3$ principal stress-tensor component along the $\hat{\mathbf{z}}$ and $\hat{\mathbf{y}}$ directions in the simulation cell for a Zn/ZnO CSNP. These curves demonstrate that the stress field is highly inhomogeneous and penetrates into the core region of the particle. The stresses inside the core are lower due to Zn being stiffer than *w*-ZnO. The influence of modification of the intrinsic surface-tension parameter τ can be seen by comparing the dashed and solid lines.

Fig. 4.5 shows variations of the CSNP band gap δE [see Eq. 4.4] throughout the shell volume. These plots are also presented as histograms, similar to those included in Figs. 4.3(c) and (d), for particles with different shell morphologies, but having the same total diameter of 25 nm, as well as the core region of approximately 15 nm in size. Same as before, all of the calculations here are done for the condition of vanishing external pressure. Figs. 4.5(a) and (c) on the left describe the Zn/*w*-ZnO core-shell-material combination, while Figs. 4.5(b) and (d) on the right refer to the w-ZnO/*r*-TiO_2 combination. The top (bottom) panel rows are for the systems with spherical (faceted) cores, respectively. For each specific material and core-geometry configuration, band-gap distributions — obtained from the stress-field calculations with the help of parametrization in Eq. 4.4 — are shown for a number of different

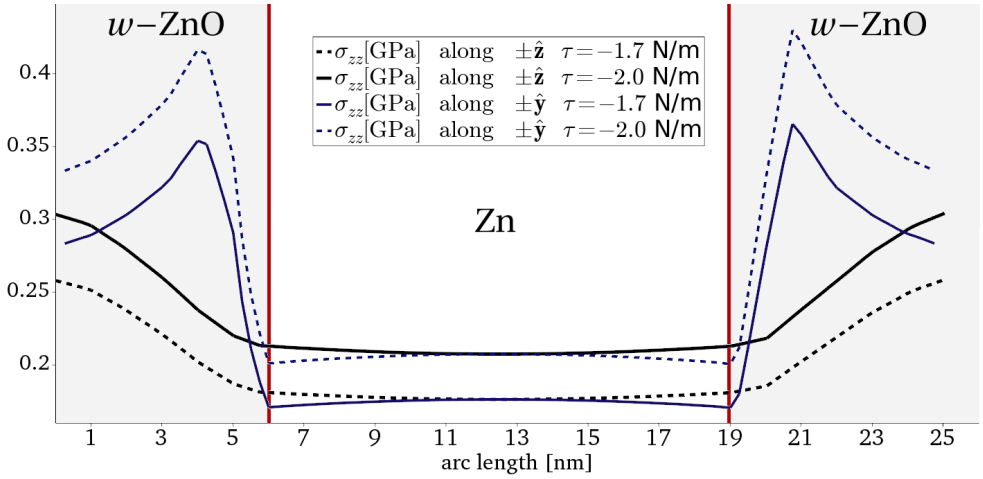

Fig. 4.4 Line plots of the σ_{zz} component of the stress field along the $\hat{\mathbf{z}}$ and $\hat{\mathbf{y}}$ directions in the simulation cell. The stress field is highly inhomogeneous and can penetrate into the core region of the particle. Note that $\tau = -1.7$ N/m is the surface tension chosen from Ref. [323] and used in this Chapter, while the results for $\tau = -2.0$ N/m are also shown here to emphasize the quantitative influence of this parameter on the stress field behavior.

shell structures, as outlined in Fig. 4.1 (c). From the data presented in Fig. 4.5, we can make the following observations. (i) For all of the considered materials and core-geometry combinations, most of the band-gap energies distributed throughout the shell volume are smaller than the bulk value E_g^0. (ii) For both core-shell-material combinations, the distribution curves for spherical and faceted cores look different, with the ones for the spherical core showing a greater range of possible band-gap energies. (iii) For both core-shell-material combinations, shell morphology does not have a strong influence over shaping the form of the band-gap energy distribution curve. Random shell configuration for the *w*-ZnO/*r*-TiO_2 case may be a mild exception here. (iv) In all these cases, the intensity of the remaining elastic stresses within the CSNP that is relaxed to vanishing external pressure can produce only minor shifts in the size of the band gap: 50–60 meV in case of Zn/*w*-ZnO and much smaller for *w*-ZnO/*r*-TiO_2.

In Fig. 4.6, we show the dependence of the band-gap energy distributions throughout the shell volume on the change in particle diameter D at fixed core-to-shell volume ratio

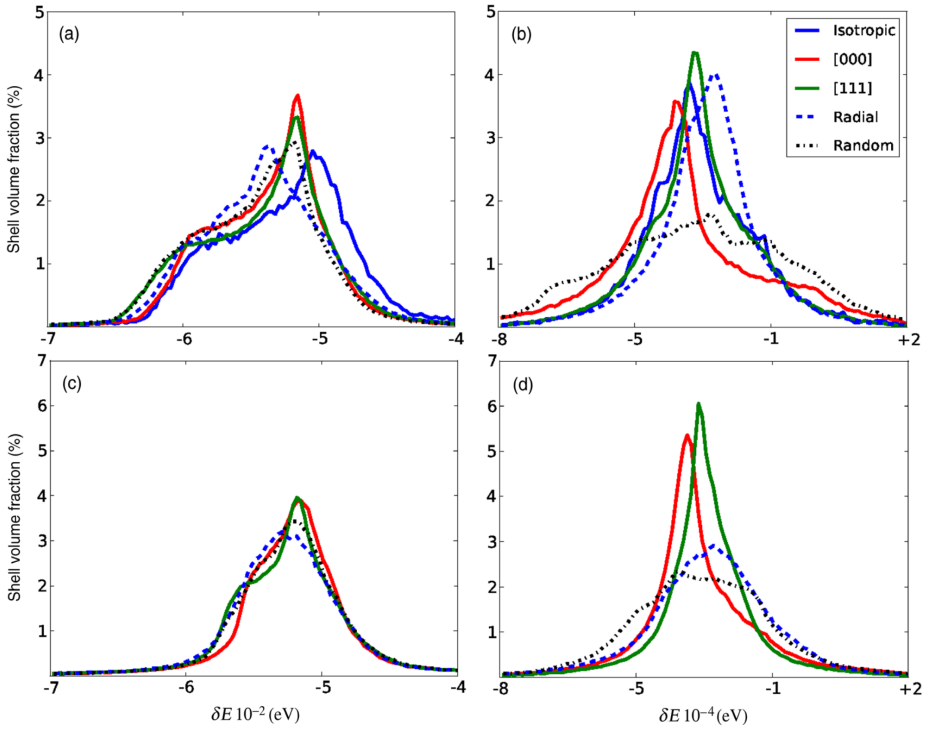

Fig. 4.5 Histogram plots showing distribution of CSNP band-gap energies δE throughout the shell region of the particle for a variety of different shell morphologies at vanishing external pressure. See Fig. 4.1(c) and the accompanying caption for the detailed description of the latter. (a) Zn/*w*-ZnO core-shell-material combination with a spherical core. (b) w-ZnO/*r*-TiO_2 core-shell-material combination with a spherical core. (c) Zn/*w*-ZnO core-shell-material combination with a faceted core. (d) w-ZnO/*r*-TiO_2 core-shell-material combination with a faceted core. Here, isotropic shell morphology refers to a shell material, where the elastic-stiffness tensor components are averaged out to isotropic symmetry. Reprinted from Ref. [210] with permission from the publisher.

(top panels), or the change in core-to-shell volume ratio, expressed through the changing core radius r, at fixed particle diameter (bottom panels). All the particles used in these calculations have spherical cores that are combined with monocrystalline collinear shells and are relaxed under condition of vanishing external pressure. As in the case of the previous

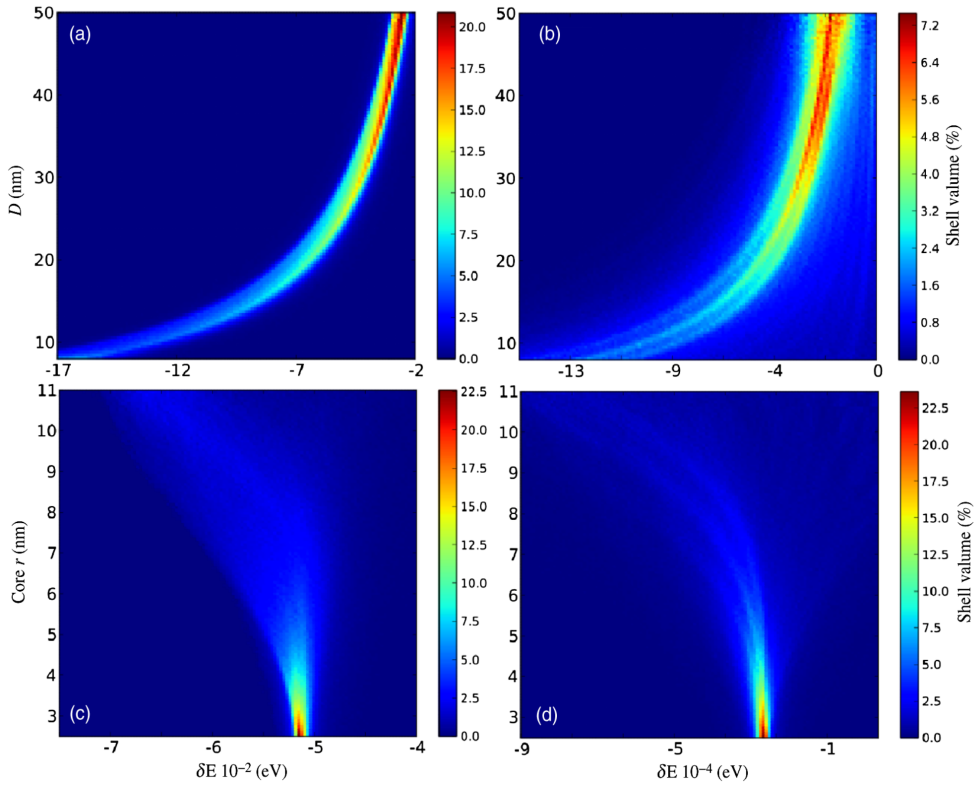

Fig. 4.6 Contour plots showing the dependence of the CSNP band-gap energy distributions throughout the shell volume on particle diameter D at fixed core-to-shell volume ratio (top panels), or core radius r at fixed particle diameter (bottom panels). In the former case, the core-to-shell volume ratio is fixed at 0.276, while in the latter case D = 25 nm. Left panels (a) and (c) refer to the Zn/w-ZnO system; right panels (b) and (d) refer to the w-ZnO/r-TiO_2 system. Combinations of spherical cores and monocrystalline collinear shells are used in all the calculations presented here, with the CSNP shapes relaxed under conditions of vanishing external pressure. Reprinted from Ref. [210] with permission from the publisher.

figure, Figs. 4.6(a) and (c) on the left describe the Zn/w-ZnO core-shell-material combination, while Figs. 4.6(b) and (d) on the right refer to the w-ZnO/r-TiO_2 combination. As can be seen from the top row of panels, the distribution of band-gap energies narrows as D is increased

and its average value shifts closer to that of the bulk band-gap opening E_g^0. On the other hand, reducing D below 25 nm produces wider band-gap energy distributions (compared to those shown in Fig. 4.5) and decreases the average E_g value further, e.g., by up to -0.13 eV in a Zn/*w*-ZnO CSNP that is 10 nm in diameter. However, when the core radius is varied while keeping the particle diameter fixed, a different behavior is observed. For particles with large core radii (narrow shell regions), wide distributions of band-gap variations δE are produced, while for particles with small radii (wide shell regions) rather sharply defined values of $E_g < E_g^0$ are obtained.

In Fig. 4.7, we present the dependence of the variation of the particle-shell band-gap energy δE on the applied hydrostatic pressure p for both the Zn/*w*-ZnO (top) and *w*-ZnO/*r*-TiO_2 (bottom) core-shell-material combinations. These results are obtained for a CSNP model with a 15-nm spherical core and a 5-nm-thick monocrystalline shell (D = 25 nm) that is set up in either a collinear or an isotropic configuration. As can be seen from the data shown, the band gaps change differently under hydrostatic compression in Zn/*w*-ZnO and *w*-ZnO/*r*-TiO_2 CSNPs. In the former system, $\delta E(p) > 0$ and, therefore, the band gap increases and does so quite substantially, e.g., growing by 1 eV for p = 5 GPa. On the other hand, in the latter system, due to canceling out of contributions from uniaxial and biaxial stresses ($cb \simeq -c_u$; see Table 4.3), $\delta E(p)$ is small and negative, i.e., the band gap decreases under pressure, but only by a few meV. We should point out that, under hydrostatic pressures between 8.3 and 9 GPa, ZnO undergoes a phase transition from wurtzite to a rock-salt phase; however, this transformation is not considered here [29, 197, 71].

As shown in Fig. 4.5, our investigation identifies some differences in the shell-volume band-gap energy distributions of monocrystalline collinear [000] and noncollinear (e.g., [111]) mutual arrangements of core-shell elastic-stiffness tensor axes for both of the considered material systems. In Fig. 4.8, we present the changes of the volume-weighted variance of the band-gap energy E_g with respect to all of the symmetrically inequivalent Euler rotations

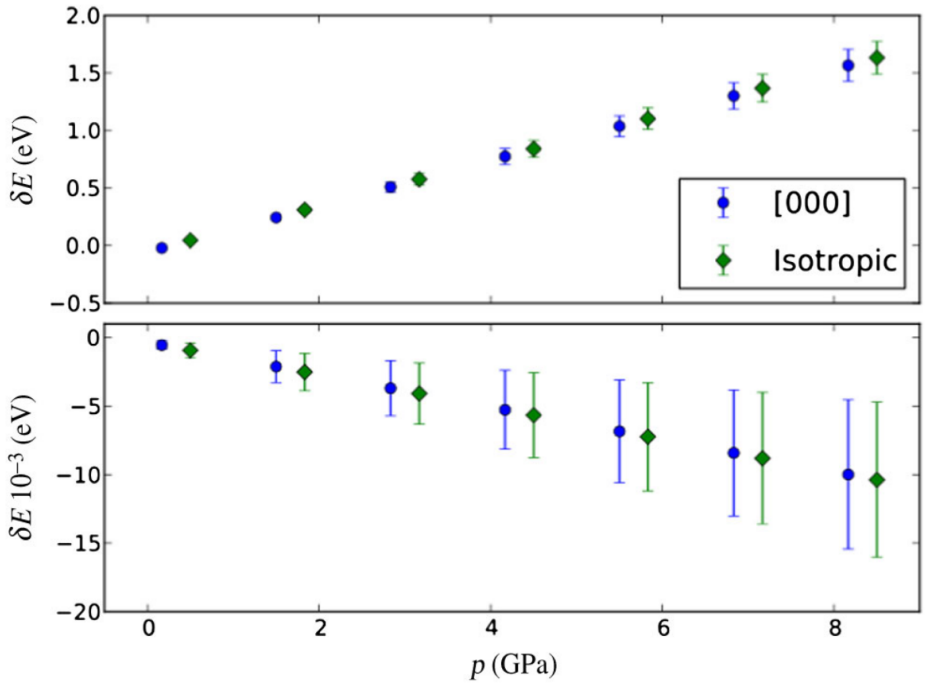

Fig. 4.7 Dependence of the variation of the particle-shell band-gap energy δE on the applied hydrostatic pressure. Top: Zn/*w*-ZnO system. Bottom: *w*-ZnO/*r*-TiO_2 system. In all calculations presented here, a CSNP model with a 15 nm spherical core and a 5-nm-thick monocrystalline shell (D = 25 nm) is used. Results for collinear and isotropic shells are depicted by full circles and diamonds, respectively. Error bars attached to the symbols represent volume-weighted standard δE deviations that show the broadening of the band-gap energy distributions under increasing compressive pressure. Reprinted from Ref. [210] with permission from the publisher.

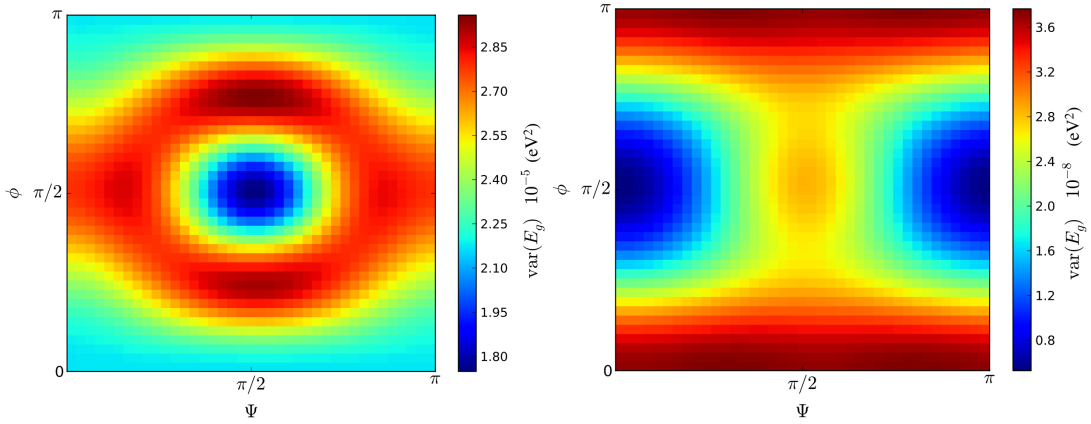

Fig. 4.8 Volume-weighted variance of the band-gap energy E_g with respect to Euler rotations $Z_1(\theta)X_2(\phi)Z_3(\Psi)$ of the orientations of the monocrystalline-shell elastic-stiffness tensor axes away from the directions of the global-coordinate-system axes (which coincide with the orientations of the elastic-stiffness tensor axes within the core region). For example, the [111] orientation of the axes is achieved by setting $\theta = 0^\circ$, $\phi = 54.74^\circ$, and $\Psi = 45^\circ$, which corresponds to the top-right corner of the bottom-left quadrant. This CSNP model has a total diameter of 25 nm, core-shell volume ratio of 0.276, and is relaxed under a condition of vanishing external pressure. The left and right panels contain data for the Zn/*w*-ZnO and *w*-ZnO/*r*-TiO_2 systems, respectively. Reprinted from Ref. [210] with permission from the publisher.

$Z_1X_2Z_3$ the orientations of the shell elastic-stiffness tensor axes. Again, the orientation of the elastic-stiffness tensor axes of the core region is chosen as $\theta, \phi, \Psi = 0$, and the calculations are done for a particle with $D = 25$ nm and core-shell volume ratio of 0.276 at the condition of vanishing external pressure. Although the variance of the band-gap energy is small in both of the considered material systems, the differences in the plot symmetry are quite pronounced between them, with dissimilar combinations of rotation angles ϕ and Ψ required to achieve the largest variance.

4.4 Conclusions

In this investigation, we utilized a finite-element method to study the elastic properties of CSNPs with a variety of different shell morphologies, including mono- and polycrystalline configurations. Two different core types, faceted and spherical, as well as two popular core-shell-material combinations, Zn/*w*-ZnO and *w*-ZnO/*r*-TiO_2, were considered. The connections between the elastic stresses within the particles and their optical properties as reflected in the shell-volume distributions of the band-gap energy values were examined with the help of simple fits obtained for *w*-ZnO and *r*-TiO_2 bulk crystals by quantum-mechanical calculations [306, 320]. Our investigation shows that the band-gap shifts that could be achieved for these two shell materials in the spherical-particle geometry are not large under vanishing external pressure and only weakly depend on the shell morphology. However, in the case of *w*-ZnO, reducing the particle size below 20 nm and/or applying hydrostatic pressure on the order of few GPa can cause substantial changes in the average value of its band gap. In *r*-TiO_2, the band-gap energy changes caused by applied pressure and elastic anisotropy remain uniformly small (on the order of a few meV) for all the considered particle geometries and simulation conditions. In this regard, the anatase TiO_2 polymorph (not studied here) may be a better choice of a shell material for potential photovoltaic applications

because, according to Ref. [320], its E_g should display a much larger variation under applied stress.

Chapter 5

Nanoferroelectric composites

After the test of the elastic solver described in the previous Chapter, a fully coupled polar-elastic-electrostatic model has been developed to study the properites of functional dielectric systems. The associated numerical problems involve obtaining correlated solutions for the elastic displacements, polarization fields and electrostatic potential of a dielectric or ferroelectric system at thermodynamic equilibrium. In this Chapter, the developed approach is applied to the studies of polarization field topology, phase transformations and applied electric field induced response in spherical ferroelectric nanoparticles embedded in a dielectric medium. Nanoparticle properties are evaluated with respect to the particle size and material choice, as well as the choice of the surrounding dielectric medium.

5.1 Introduction and experimental motivations

Reduction of the dielectric device components size, while improving their operation efficiency continues to be a important scientific and engineering problem. Dielectric devices have broad application in electronics, energy interconversion [130, 260], and computing[18, 32]. Composite ferroic systems[130, 49], which consist of one or more ferroic components surrounded by or connected to a permeable or conductive medium, are particularly inter-

esting as potential vehicles for property enhancement or development of new and unusual functionalites. A number of such systems have already been synthesized or predicted, and shown to exhibit useful functional properties, including superparaelectricity [130], interlayer strain-mediated multiferroicity [203], enhanced dielectric, piezoelectric, and pyroelectric response [318, 216], as well as multistage hysteretic switching [32, 209].

A particularly versatile approach for fabricating ferroic composites involves utilization of small ferroelectric particles dispersed within a dielectric matrix [246]. Such particles may be of polymeric[130, 250, 183], ferromagnetic[82] or complex oxide origin[127]. For instance, Huang *et al.* [130] showed that a self-assembled nanoparticle building blocks (based on ferroelectric $BaTiO_3$) can be embedded in a polymer dielectric matrix and exhibit superparaelectric behavior [287].This nanoengineered functionality is extremely useful as it allows an increase in stored energy density of the structure, compared, e.g., to non-composite systems [266]. Another useful property of this sort of a composite system is that it could be mechanically flexible, when a flexible — e.g., polymeric — matrix is used (see, e.g., Ref. [248] for a recent review on flexible microelectronics).

Synthetic chemical-growth routes controlling the formation of ferroelectric nanoparticles can produce a wide variety of shapes, including cuboidal [228, 257, 115, 156, 49], ellipsoidal or spherical [228, 49, 183], and core-shell geometries [250, 183]. These inclusions can be incorporated into the composite in either aggregated, or dispersed, irregular arrangements, providing precise control [49, 183] of the dielectric properties. However, there are limited studies on how the composite properties may be influenced by changing particle size or shape, including identification of the intrinsic critical size for ferroelectric response. There have been extensive studies on critical-size limits for ferroelectricity in bulk ceramics, thin films [284, 164, 67, 85, 134] and multilayers [152, 81, 219, 153], but relatively few [268, 80, 8, 9, 257, 104] investigations dedicated to nanoparticles. Tuning the particle size and the material parameters, as well as those of the surrounding material, directly influences

	$SrTiO_3$	a-SiO_2	vacuum	Ref
C_{11}	319	63	-	[249], [138], [68]
C_{12}	100	6	-	-
C_{44}	110	28	-	-
ϵ_m/ϵ_0	300	2.6	1	[234], [249]

Table 5.1 Elastic and dielectric material parameters used in this work for $SrTiO_3$ and a-SiO_2 at room temperature, $T = 293$ K. The medium dielectric constants are assumed to be isotropic and are given in units of the relative permittivity. Elastic stiffness tensor coefficients are given in Voight notation[245] in units of GPa. Elastic stiffness tensors of the amorphous silica are obtained from averaging data presented in Ref. [249].

the strength of competing interactions within the system, including long-range electrostatics, short-range ferroelectric ordering, and electrostrictive coupling between polar and elastic degrees of freedom. With some or all of these terms being close in magnitude, the system may become highly sensitive to changes in control parameters, so that small external stimuli can generate large responses. As such, understanding these competing interactions is certainly warranted from a scientific standpoint and also for practical applications of these materials.

In this Chapter we report the details of a computational investigation of ferroelectric behavior of nanoparticles consisting of two archetypical ferroelectric materials $PbTiO_3$ (PT) and $BaTiO_3$ (BT) that are surrounded by various dielectric materials. At room temperature, PT has weak electrostrictive coupling between ferroelectric polarization and elastic strain, but a large spontaneous polarization ($P_s^{\mathrm{PT}} = 0.75$ C/m^2). BT, in contrast, has a lower polarization ($P_s^{\mathrm{BT}} = 0.26$ C/m^2) but is much more sensitive to applied strain. Three materials with radically different dielectric and elastic properties are chosen for the external dielectric matrix (characterized by relative permittivity ϵ_m): $SrTiO_3$ (ST, high dielectric permittivity), amorphous silica (a-SiO_2, low dielectric permittivity), and vacuum (described by vacuum permittivity ϵ_0). Their material elastic and dielectric tensor constants are listed in Table 5.1.

The discussion primarily focuses on the topology of polarization fields encountered in spherical FE nanoparticles their resulting dielectric properties. We observe that embedding particles into a high-κ matrix, such as $SrTiO_3$, leads to a polar monodomain state formation

at small particle sizes. However, if instead the matrix has low permittivity, particles of the same sizes can remain completely non-polar. As the particle diameter is increased, we find nontrivial vortex-like polarization patterns emerging. These patterns then transform into polydomain polarization arrangements as the particle size becomes even larger. Interesting switching behavior in the particles is also observed under applied electric fields. While the monodomain polar configuration produces the expected shape of the hysteresis loop with sharp transitions mediated by the coercive field, the vortex-like state does not. At high applied fields, the polarization becomes aligned with the field, however, at intermediate field strengths, vortex-like state can still be present at the particle surface, which can result in a multistage switching of the particle polarization. This interesting functionality can be useful for memory storage applications [105, 215, 38, 39, 32], as it may lead to increase of the information storage density of individual memory elements.

5.2 Energetics of a single ferroelectric particle

In contrast to spectral methods [128, 188, 189, 124, 107, 291] that rely on regular parallelepiped meshes and the numerical solve that is performed in Fourier space, the method utilized in this Chapter implements a real-space approach based on unstructured meshes, which allows one to process irregular geometries (using the LIBMESH library [158]). The evolution of the polarization field, $\mathbf{P} = \mathbf{P}(\mathbf{x},t)$, inside the ferroelectric particle is described by the TDLGD equation,

$$-\gamma\frac{\partial \mathbf{P}}{\partial t} = \frac{\delta}{\delta \mathbf{P}}\int\limits_{V_{\mathrm{FE}}} d^3\mathbf{x}\; f(\mathbf{P}), \tag{5.1}$$

where γ is a time-scaling parameter related to domain-wall mobility [223, 121] and V_{FE} being the volume of the ferroelectric inclusion.

Eq. (5.1) describes the system evolution in scaled time as energy is dissipated out at each consecutive time step. The following mechanical equilibrium condition must be satisfied,

$$\frac{\partial}{\partial x_j}\left[C_{ijkl}\left(\varepsilon_{kl}-Q_{ijmn}P_mP_n\right)\right]=0, \tag{5.2}$$

at each time step of the polarization field evolution, where $Q_{ijmn}P_mP_n$ is the electrostrictive coupling term that gives rise to the ferroelectric self-strain. Furthermore, the evolution of $\mathbf{P}$ is also coupled with that of the local (internal) electrostatic potential Φ by the Poisson equation,

$$\nabla\cdot(\epsilon_b\nabla\Phi)=-\nabla\cdot\mathbf{P}, \tag{5.3}$$

with ϵ_b being the background (optical) dielectric constant of the material [26, 123, 229]. In non-ferroelectric regions representing the elastic, linear-dielectric matrix[1], Eq. (5.2) and Eq. (5.3) are solved at each time-step with $\epsilon_b=\epsilon_m$. The forms of individual energy terms and their material tensors are presented and discussed in Chapter 2 [coefficients and tensor components for BT and PT are summarized in Table 2.3].

The system boundary conditions include vanishing elastic distortions far away from the ferroeelctric inclusion, i.e., Dirichlet $\mathbf{u}=0$ at $\partial\Omega_M$, which is the boundary of the linear-dielectric matrix. A short-circuited boundary condition [189] on the potential Φ is chosen for the pair of opposite sides[2] of the cube Ω_M with plane normals oriented along $[00\pm1]$. Consistency checks were performed to make sure that, as a function of the size of the inclusion sphere, the internal (fringing) electrostatic potential and the strain fields originating from elastic distortions did in fact vanish at the boundaries of the computational domain[3]. A

[1]The same governing equations exist in the vacuum region, except the variable $\mathbf{u}$ is nonexistent.

[2]By adjusting the values of Φ on these two sides, an external electric field can be applied. In the absence of the applied field, the Dirichlet boundary condition $\Phi=0$ is enforced on the boundary planes of Ω_M (which are assumed to be far away from the inclusion).

[3]Larger matrix domains were needed to ensure fringing fields from larger spheres vanished.

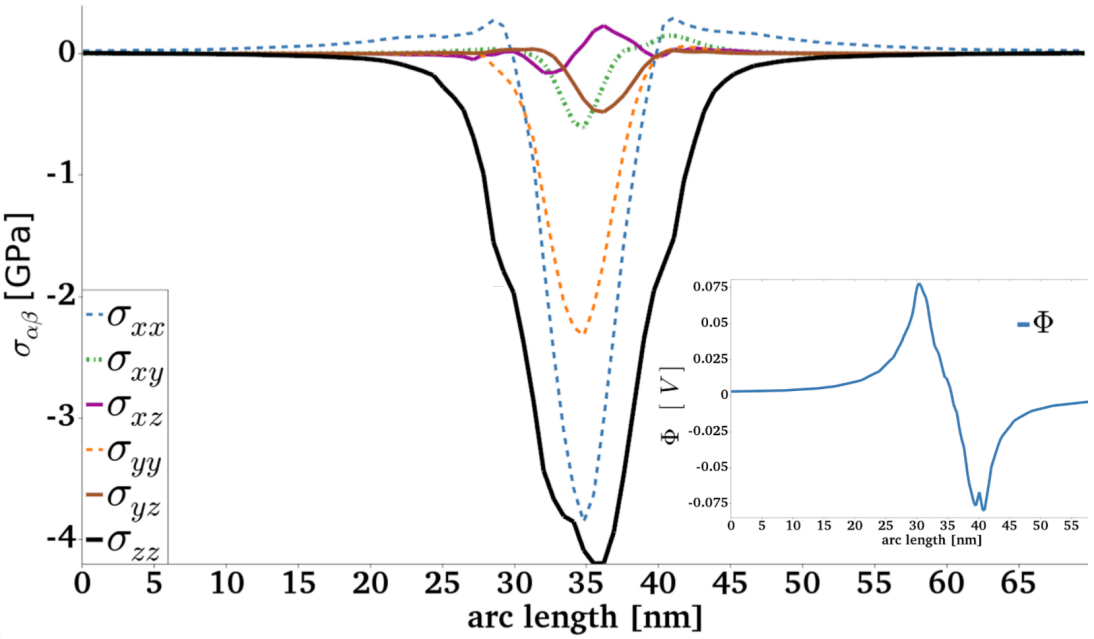

Fig. 5.1 Stress tensor components $\sigma_{\alpha\beta}$ plotted along an arc across the model volume for a 10 nm diameter $PbTiO_3$ particle embedded in $SrTiO_3$ at an arbitrary time step. The inset depicts the electrostatic potential Φ along the same line and for the same time step, showing that it vanishes at the model external boundaries.

typical plot of the spatial variation of the components of the stress field due to these boundary conditions at an arbitrary time step is presented in Fig. 5.1.

Since Eq. (5.1) is a partial differential equation that depends on time, an initial condition for evolving the **P** field must be chosen. For this particular problem, an initial condition was picked that resembles a paraelectric state of the material at some $T > T_C$, which forces **P** to be randomly distributed about a zero (vector) value. The rationale for choosing this random paraelectric initial condition (RPEIC) is to ensure that there is no "memory" bias in the domain structure that forms, as the energy is dissipated out of the system by the gradient-descent algorithm. Such a condition is widely used in phase-field modeling of ferroelectric materials[188, 189]. The temperature is then immediately set below T_C and Eq. (5.1) is evolved — by solving Eq. (5.3) and Eq. (5.2) at each time step — until a (local) energy minimum has been found.

A plot of different energy terms variation with time is presented in Fig. 5.2 for a $d = 10$ nm diameter PT sphere embedded in a ST matrix at room temperature. Here, visualizations of the initial condition **(1)**, intermediate phase **(2)**, and final distribution **(3)** of **P** are shown as figure insets. After forming the domain structure early in the simulation [usually before mark **(2)** on the figure], the gradient-descent algorithm dissipates energy out of the system by growing the magnitudes of the local-polarization vectors. However, the slowest relaxation process in the system involves domain wall motion, which mostly happens between marks **(2)** and **(3)**, as the system approaches equilibrium.

As an important aside before discussing the main results of this study, it is crucial to note that the local surface terminations of the particles may be complicated. For example, as discussed in the previous Chapter, particular surface (or interfacial) cleaving may introduce surface elastic tension, which for a ferroelectric system could strongly influence the polarization [261]. Alternatively, complex oxide surfaces corresponding to PbO, BaO or TiO terminations could be energetically unfavorable due to uncompensated surface charges [101].

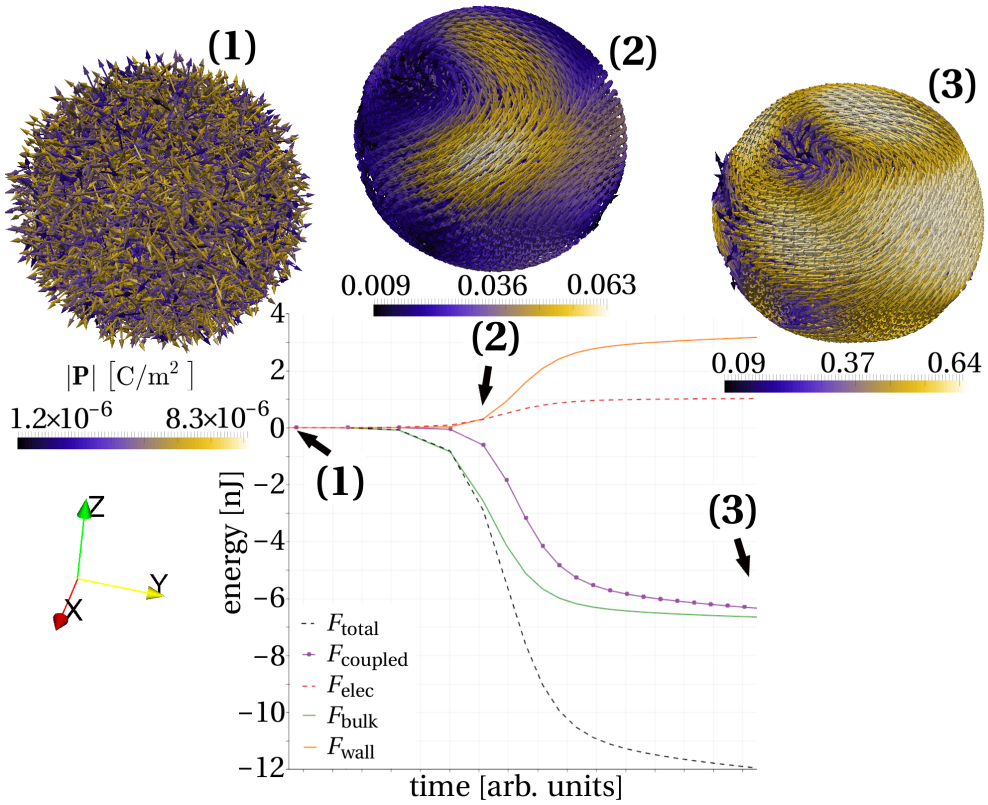

Fig. 5.2 System energies as functions of the scaled time in the TDLGD equation. The insets at **(1)**, **(2)**, and **(3)** visualize the RPEIC, intermediate (metastable) state, and final (local) equilibrium pattern of the polarization for a $d = 10$ nm $PbTiO_3$ sphere at room temperature. The total energy has to decrease monotonically (as shown) during the time-evolution process, while other energy terms could increase in value.

However, particular ionic terminations are likely to vary locally on the surface of the particle, so that the electrostatic and elastic fields arising from them should rapidly average out for large particle sizes. By studying a wide range of dielectric constants of the surrounding matrix, ϵ_m, the aggregate effects of charge compensation at different nanoparticle surface terminations can be effectively captured.

5.3 Paraelectric states at small sizes

After sufficient evolution of the polarization field following Eq. (5.1) the system reaches the state of local equilibrium[4]. In small particles, below a certain critical diameter d_c, the resulting polarization pattern is found to be strongly dependent on the types of ferroelectric material and the surrounding dielectric matrix. For a strong dielectric medium ($\epsilon_m \approx 300$) as in the PT/ST system, nonzero polarization configuration is found in the nanoparticle. Specifically, the polarization field forms a uniform monodomain state, where average polarization is somewhat reduced, compared to the bulk polarization of $|\mathbf{P}_s^{\mathrm{PT}}| \approx 0.8\ \mathrm{C/m^2}$. For lower values of ϵ_m, a paraelectric state ($\mathbf{P} \approx 0$) is found for the PT inclusion, while in the BT system such state persists for all the values of ϵ_m, including one corresponding to the ST matrix.

This behavior is observed for critical diameters $d_c = 2.0$–3.6 nm, which falls within the ranges identified in a number of other studies [257, 9, 8, 85, 80, 104] for a variety of different nanostructures (e.g., thin films). These d_c values are also considerably smaller than the ferroelectric correlation length, estimated to be around $5 - 10$ nm, which is a typical size for supporting a single domain wall. For particles with $d \leq d_c$, the RPEIC, that it introduced at the beginning of the simulation, forces a large contribution of the f_{wall} term to the total energy, compared to other energy terms in the Eq. (5.1), due to the random nature of the polarization field distribution. Therefore, the system evolves towards the monodomain state

[4]The simulation exit criterion is achieved when the difference in the magnitude of the total energy is below 0.1% during the two consecutive time steps.

[shown in Fig. 5.3 **(a)**], to minimize this energy contribution ($f_{\text{wall}} > 0$). The developing monodomain state then produces a nonzero surface-charge density $q_S = \mathrm{P} \cdot \hat{\mathbf{n}}$, where $\hat{\mathbf{n}}$ is the outward-facing surface normal unit vector. The presence of nonzero q_S leads to a sharp increase in the f_{elec} term, unless the dielectric constant of the surrounding matrix is large enough to screen out this uncompensated charge. If the dielectric constant of the surrounding matrix is too small, in order to reduce f_{elec}, the magnitude of $\mathbf{P}$ is uniformly diminished until $\mathbf{P} \approx 0$ within numerical precision of the simulation, resulting in the paraelectric state of the system.

Considering that $|\mathbf{P}_s^{\text{BT}}| < |\mathbf{P}_s^{\text{PT}}|$, the observed behavior of the BT particles is somewhat surprising. Due to the lower bulk spontaneous polarization, the energy penalty arising from f_{elec} for the BT monodomain is lower. However, due to the shallower f_{bulk} energy minimum and energy arising from the stronger electrostrictive coupling f_{coupled}, the f_{elec} term still dominates and the system will reduce its $\mathbf{P}$ to zero.

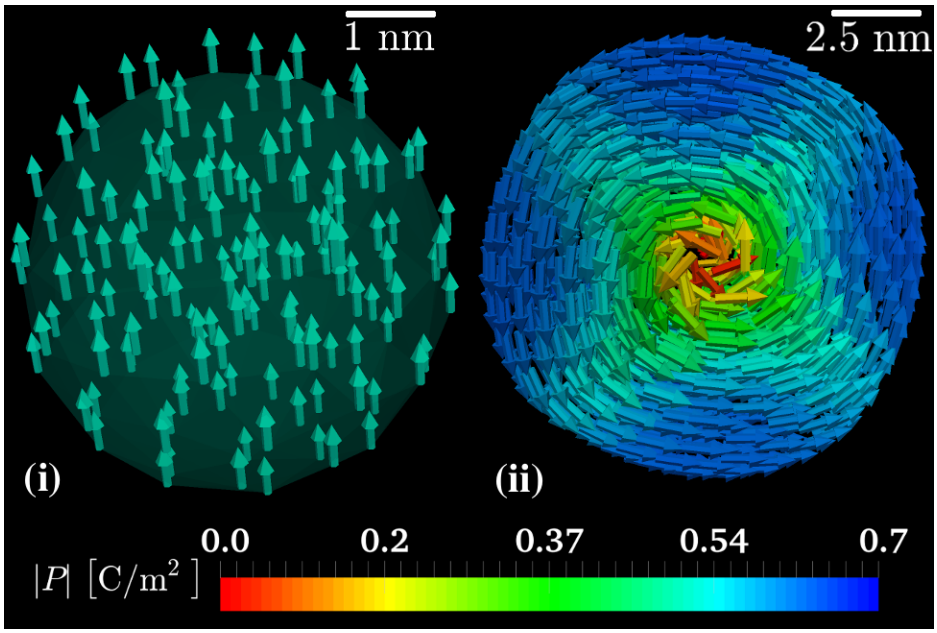

Fig. 5.3 Monodomain **(i)** and vortex-like phases **(ii)** of room temperature $PbTiO_3$ nanoparticles embedded in $SrTiO_3$. Figure is adapted from Ref. [209] with permission from the publisher.

These resulting states (either monodomain or paraelectric) are robust with respect to varying the seed generator[5] within the RPEIC. The influence of the finite element mesh size on these states was also investigated. As long as the interfacial region between the matrix and ferroelctric particle was sufficiently resolved (mesh size h well below a nanometer), then the resulting state would be either monodomain or paraelectric in the $d_c = 2.0$ nm to 3.6 nm range of particle size.

5.4 The vortex-like transition

For particle sizes above d_c, both ferroelectric materials are observed to develop a vortex-like pattern. We should point out that such patterns are not *true topological* vortices and therefore a '-like' suffix is used to describe them. An image of the typical vortex-like polarization field arrangement is shown in Fig. 5.3 **(ii)**, highlighting the behavior of the **P** vector field that "curls" around a central point. The emergence of this vortex-like state in both PT and BT particles can be detected by tracking the dependence of the following expression on d:

$$\widetilde{F}_{\text{bulk}}(d) = \frac{1}{V_{\text{FE}}(d)P_s^3} \int\limits_{V_{\text{FE}}(d)} d^3\mathbf{x}\, f_{\text{bulk}}(\mathbf{x}), \tag{5.4}$$

which is a volume-normalized bulk free energy, as shown in Fig. 5.4 for a particle embedded in the ST matrix. For the PT/ST system, the transition occurs at a critical diameter $d_v \simeq 3.4$ nm and is accompanied by a sharp *increase* of $\widetilde{F}_{\text{bulk}}$, compared to its value in the monodomain state. On the other hand, in the BT/ST system, $\widetilde{F}_{\text{bulk}}$, which is zero by definition in the

[5]Within the MOOSE framework, the random initial condition seeds variables based on the global node identifier assigned by the meshing software. Changing the sizes of the mesh will effectively adjust the global node identifier throughout the mesh. The initial condition uses the Dirichlet boundary condition ($u_s(\mathbf{x}, t = 0) = \hat{u}_s \forall \mathbf{x}$ for some variable u, see Chapter 3.).

paraelectric state, sharply *decreases* upon the formation of the vortex-like state with non-zero polarization at $d_v \equiv d_c \simeq 3.5$ nm.

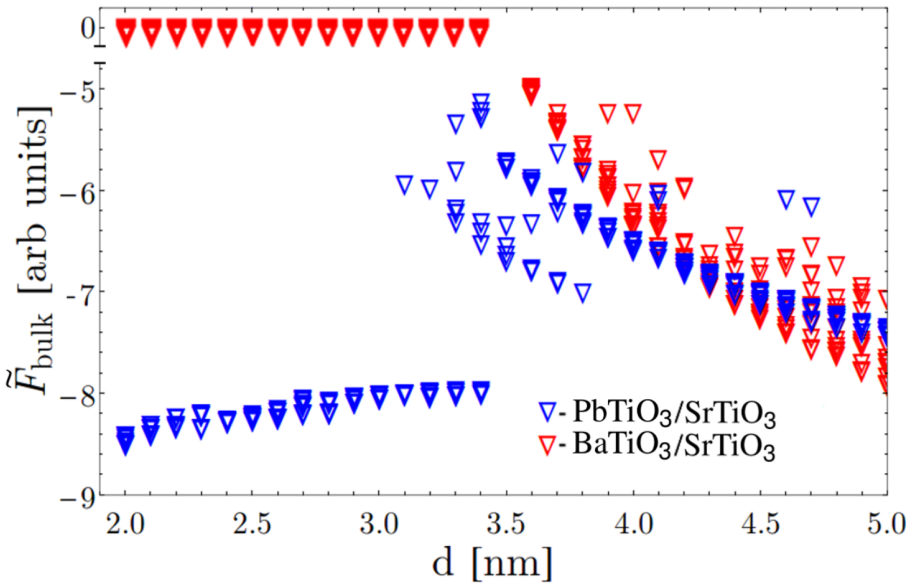

Fig. 5.4 The volume and polarization normalized bulk free energy as a function of particle size d for both PT/ST and BT/ST systems. The downshift of the $\widetilde{F}_{\text{bulk}}$ in BT is due to the onset of ferroelectricity, while the upshift of $\widetilde{F}_{\text{bulk}}$ in PT is due to the paraelectric core formation and nonzero local gradients of **P**. Reprinted from Ref. [209] with permission from the publisher.

While the physics underpinning the energy change in the BT/ST system may be self-evident, understanding the behavior of the PT/ST system requires a detailed examination and comparison of the polarization patterns before and after the transition, i.e., sketches (i) and (ii) depicted in Fig. 5.3. As can be seen from sketch (ii), even though local values of $|\mathbf{P}| \sim P_s^{\text{PT}}$ near the surface of the inclusion, they become strongly suppressed close to its center, forming a weakly polar or even completely paraelectric core region of the vortex. In all of the PT systems, this core region is cylindrical in shape and penetrates the spherical inclusion completely from its northern to southern pole, as shown in Fig. 5.5 **(a)**. In the BT systems, such a region is also present, but its shape may be twisted or bent, as illustrated in Fig. 5.5 **(b)**, and its final conformation exhibits dependence on the RPEIC.

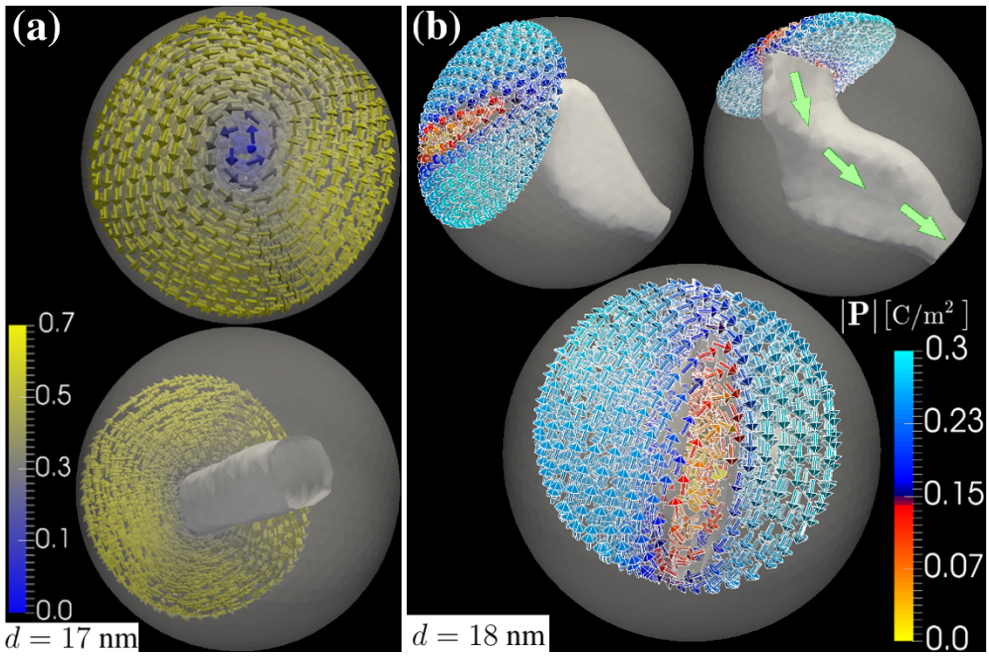

Fig. 5.5 Vortex-core shapes for **(a)** PT/ST and **(b)** BT/ST systems. The gray contour represents cuts through the polarization texture at $|\mathbf{P}| = 0.35$ C/m^2 for **(a)** at zero applied field. In panel **(b)**, the same information is presented for the 18 nm BT/ST inclusion at $|\mathbf{P}| = 0.17$ C/m^2 contour. Adapted from the supplemental of Ref. [209] with permission from the publisher.

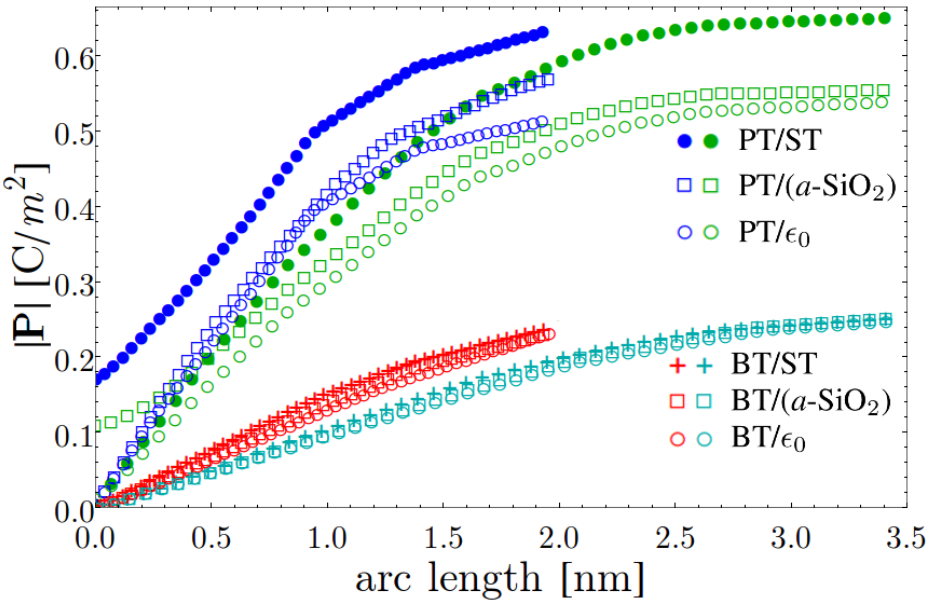

Fig. 5.6 The radial profile of |**P**| along a line perpendicular to the vortex core in 4 and 7 nm wide inclusions with vortex-like polarization textures. In both PT/ST and BT/ST systems, the values of |**P**| in the vortex-like phase are depressed, compared to those in the monodomain phase, or respective $\mathbf{P}_s$. The influence of the dielectric permittivity of the surrounding medium on the polarization values is also presented in the panel, with curves corresponding to different dielectric materials shown for all the considered systems.

The change in the value of $|\mathbf{P}|$ along the direction perpendicular to the vortex core axis is presented in Fig. 5.6 for particles of two different sizes for both PT and BT systems coupled with all the considered dielectric matrices. These data show that $|\mathbf{P}|$ in the core region may be reduced by a factor of 3–5, compared to its surface value (in PT), or even disappear completely (in PT and always in BT). This tendency is mostly unaffected by the dielectric strength of the surrounding matrix. Such behavior is in sharp contrast with that of ferromagnetic vortices, where, at temperatures well below T_C, magnetization density at the core is constrained to a constant magnitude.[172, 335]

Fig. 5.6 also describes the effect of the surrounding matrix on the value of $|\mathbf{P}|$ at the surface of the inclusion. In the PT system, surface polarization is $\sim 20\%$ larger when it is coupled with a high dielectric permittivity medium, such as ST. In contrast, surface polarization of the BT system is not affected by the strength of the dielectric screening provided by the matrix.

Topological features of polarization textures, presented in Figs. 5.3, 5.5 and 5.6, are in general agreement with the analytical work of Levanyuk and Blinc [177] that highlights the sensitivity of the radial polarization distribution on the dielectric strength of the surrounding material. The observed similarities include the dependence of $|\mathbf{P}|$ on the surrounding medium, its suppression at the core of the vortex-like phase, as well as transitory nature of monodomain states in low dielectric permittivity medium. However, the investigation of Levanyuk and Blinc did not consider coupling between ferroelectric and elastic degrees of freedom. Although the results presented here include the effects of electrostrictive coupling, we have also performed a series of simulations with the electrostrictive tensor set to zero in order to examine its influence on the behavior of the system. The resulting polarization textures have sharp 90° domain walls, resembling Landau flux-closure patterns found in some magnetic microstructures.[132, 265] Thus, we conclude that the presence of the electrostrictive coupling is responsible for the softening of the domain walls, which produces

more rounded textures, such as the ones that were observed or predicted in other experimental and theoretical studies.[241, 105, 236] Representative images of polarization textures formed with and without the electrostrictive coupling in a PT/ST system are shown in Fig. 5.7.

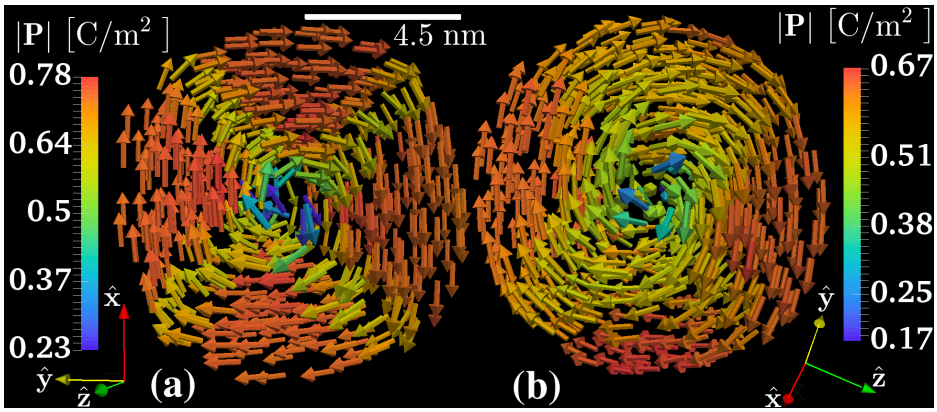

Fig. 5.7 Image slices perpendicular to the vortex core are shown, highlighting the differences between the states with (a) no electrostrictive coupling ($Q_{ijkl} = 0$) and (b) active electrostrictive coupling in a $d = 9$ nm PT particle embedded in the $SrTiO_3$ matrix.

5.5 Vortex-like to multidomain transition

For particle diameters, $d > d_v$, the most important energy term that influences further polarization texture evolution is the normalized gradient energy,

$$\widetilde{F}_{\text{wall}}(d) = \frac{1}{V_{\text{FE}}(d) P_s^3} \int\limits_{V_{\text{FE}}(d)} d^3\mathbf{x}\, f_{\text{wall}}(\mathbf{x}). \tag{5.5}$$

In the case of BT, the well-known parameterization of Hlinka and Marton [123] is used for the material gradient coefficient tensor G_{ijkl}. However, a number of parameterizations exist for G_{ijkl} for PT, such as the three different sets chosen for this study, attributed to the phase-field studies of Li *et al.* [188, 189] (set I), Wang *et al.* [307] (set II), and Hong *et al.* [124] (set III). G_{ijkl} values from all of the parameter sets used here are listed in Table 5.2.

G_{ijkl}	PT set I [188, 189]	PT set II [307]	PT set III [124]	BT [123]
G_{110}	1.73	1.73	1.73	1.0
G_{11}/G_{110}	0.6	1.6	2.0	5.1
G_{12}/G_{110}	0.0	0.0	0.0	0.0
G_{44}/G_{110}	0.3	0.8	1.0	0.2
G'_{44}/G_{110}	0.3	0.8	1.0	0.2

Table 5.2 Different sets of gradient energy parameters, G_{ijkl}, presented in Voigt notation[245] for G_{ij} and G_{110} in units of $10^{-10}\mathrm{C}^{-2}\mathrm{m}^4\mathrm{N}$. We utilize three different sets of parameters from the literature to evaluate how polar properties of PT inclusions are affected by their choice. For BT, only one set of gradient terms due to Hlinka and collaborators is used.

The dependence of $\widetilde{F}_{\mathrm{wall}}$ on d is presented in Fig. 5.8. As expected, the gradient energy is zero in the monodomain phase, but grows rapidly upon transitioning to the vortex-like state. The latter can be regarded as a domain structure consisting of continuous domain wall that has energetically sub-optimal polarization arrangements.

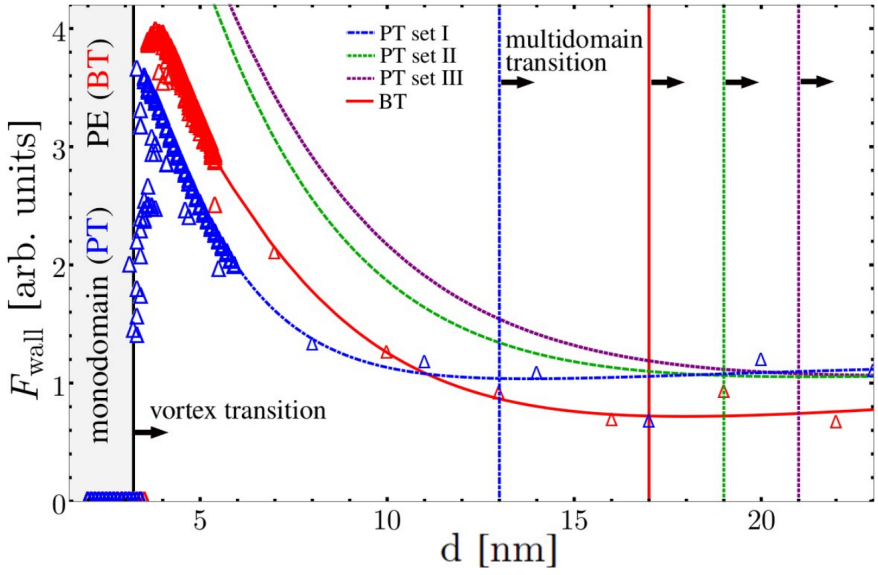

Fig. 5.8 Normalized gradient energy $\widetilde{F}_{\mathrm{wall}}$ as a function of particle size$d$ for the PT/ST and BT/ST systems. $\widetilde{F}_{\mathrm{wall}}$ is zero for $d < d_v$, but increases rapidly in the vortex-like state because of sub-optimal arrangements of the local polarization vectors. It then levels off, i.e., becomes bulk-like, in the multidomain state, with the transition point (marked by vertical lines) depending rather sensitively on the choice of G_{ijkl} parameters for PT.

As the particle size increases beyond d_v (which is, again, the critical diameter for the vortex-like state formation), the volume-normalized $\widetilde{F}_{\text{wall}}$ gradually decreases and levels off to a constant[6] . This saturation of $\widetilde{F}_{\text{wall}}$ is indicative of a "bulk-like" multidomain state. This state contains relatively large areas of correlated polarization divided by domain walls that are similar to the 90° and 180° types.

Defining the critical size for this transformation (into the *multidomain* state) as d_m, we obtain d_m value of 17 nm for the BT/ST system. In the PT/ST system, d_m is sensitive to the G_{ijkl} coefficient choice and covers a range from 13 to 21 nm. However, the equilibrium topologies of multidomain states obtained for PT/ST do not seem to be strongly affected by the choice of G_{ijkl} parameterizations. We *speculate* that by measuring certain experimentally observable quantities linked to this transition — e.g., electric field response that is discussed next — it may be possible to obtain better gradient energy estimates for PT. Images of the polarization field topology for two such multidomain states are presented in Fig. 5.9. The resulting pattern at local equilibrium produces polarization aligned tangential to the surface of the nanoparticle. This distribution minimizes the electrostatic energy arising from the surface charge density $\mathbf{P} \cdot \hat{\mathbf{n}}$.

The non-polar or weakly polar vortex core area becomes unstable at $d > d_m$, developing uniform polarization and eventually splitting into multiple domains. The apparent vorticity of the polarization texture sharply decreases after the transition into the multidomain state, but it does not disappear completely, as localized vortices, marked by largely suppressed $\mathbf{P}$, still remain near some domain walls, which may be characterized as hybrid walls (see discussion in Chapter 2). Due to the curvature of the inclusion surface, the observed domain patterns cannot be directly partitioned into collections of low-energy 90° or 180° variants

[6]One can fit $\widetilde{F}_{\text{wall}} = \widetilde{F}_{\text{wall}}(d)$ using

$$\widetilde{F}_{\text{wall}}(d) = c_1 e^{c_2 d} + \frac{c_3}{d} + c_4.$$

It is found that within error, the fit parameter c_3 depends strongly on the choice of G_{110}.

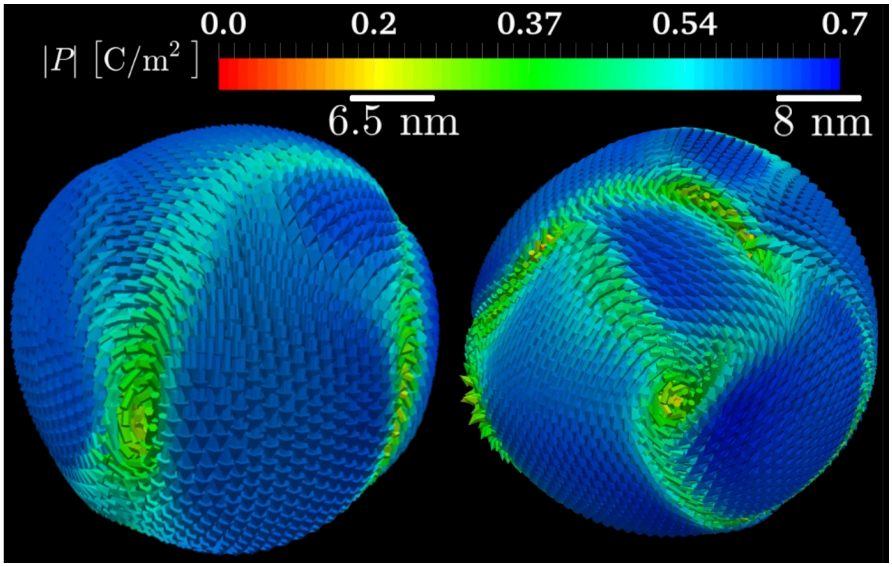

Fig. 5.9 A multidomain state found in a 24 nm (left) and 32 nm (right) $PbTiO_3$ particle.

in the near-surface region, which, in combination with remaining vorticity, results in finite saturation values of F_{wall} at large d.

The amount of vorticity present in the polarization field can be mathematically described by means of computing a Chern-Simons (CS) winding number density [76]. For the 3D polarization vector field in this study, the winding number density is

$$n_{\text{CS}} = (\nabla \times \mathbf{P}) \cdot \mathbf{P}. \tag{5.6}$$

This quantity must be close to zero in the monodomain state. However, for the vortex-like state, it should have an extremum. Due to the presence of numerous localized vortices in the multidomain state, this winding number density can also be (locally) nonzero in the particle. This quantity proves to be especially useful in identifying the presence of vortices during electric field poling, as described in the next section.

5.6 Hysteretic switching under an applied field

We have studied the electric-field induced topological changes for all of the polarization textures — monodomain, vortex-like and multidomain — that we observe in both PT and BT-based ferroelectric nanoparticles, thus probing their intrinsic response to applied fields. Such simulations are conducted with the help of a quasi-static approach, where the electric field is generated by applying a Dirichlet boundary condition in the form of an electrostatic potential difference $\Delta\Phi = \Phi_2 - \Phi_1$ on the opposing system boundary planes. This produces a (pre-poled) monodomain polarization distribution invariant of particle size probed (as expected, energetic contributions of $\mathbf{P}\cdot\mathbf{E}$ are minimized when $\mathbf{P}||\mathbf{E}$). After the minimum energy configuration of $\mathbf{P}$ is found, the solution is used as an initial condition in the following expression:

$$-\gamma\frac{\partial\mathbf{P}}{\partial t} = \frac{\delta}{\delta\mathbf{P}}\int_{\Omega} d^3\mathbf{x}\; f(\mathbf{P}) + \xi\cdot\hat{\mathbf{P}}, \tag{5.7}$$

where $\Delta\Phi = 0$ and ξ is the noise term[7]. The introduction of the noise term is helpful in ejecting the initial solution out of its original energy well. This quasi-static scheme has been used in similar numerical simulations of magnetic hysteresis experiments [38, 39]. A diagram of the poling procedure is presented in Fig. 5.10 for n field steps.

For the PT results presented in this section, the G_{ijkl} coefficients used are from set I [188]. For the monodomain particle (as demonstrated in Fig. 5.11, $d < d_v$), the shape of the poling loop is similar to that of a generic bulk ferroelectric, with abrupt switching of $\mathbf{P}$ between $-\hat{z}$ and $+\hat{z}$ orientations at a distinct value of coercive field E_c. We have also evaluated the dependence of the poling loop shape on the crystallographic orientation by aligning the easy-axis of the ferroelectric crystal along different directions with respect to the direction

[7] Depending on the choice of ξ, a minimum might not even exist. The noise term effectively introduces a small amount of energy into the system, which can be effectively related to the existence of thermal noise in a real experiment [128].

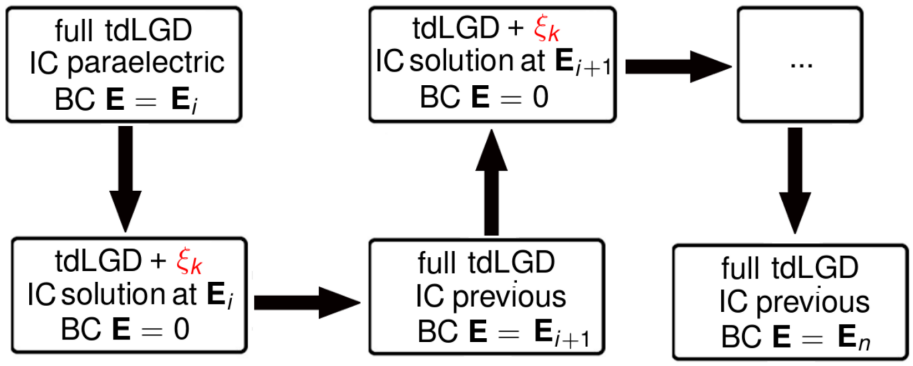

Fig. 5.10 Algorithmic procedure for the quasi-static electric field poling for n field steps. The term ξ_k represents random noise that is supposed to kick the polarization field out of its local-energy minimum configuration (and towards the lower energy minimum).

of the poling field **E**. Results of this particular investigation are presented in Fig. 5.11, with P being the average polarization along the field. The monodomain particle poling loop and winding number evolution, for the polarization easy axis parallel to the field are also shown in Fig. 5.12, case (i).

For particle diameters $d > d_v$, switching between $-\hat{z}$ and $+\hat{z}$ monodomain orientations proceeds in two stages, as presented in Fig. 5.12, case (ii). The initial monodomain configuration persists from $E_z = -E_{\max}$ to $E_z \simeq +E_c$, at which point it is replaced with a hybrid texture consisting of a monodomain core polarized along the $+\hat{z}$ direction combined with a vortex-like closure pattern in the near-surface region. This results in the response curve exhibiting a small plateau at $E_c < E_z < E_{\max}$ with roughly constant $\bar{P}_z$, originating from the polarized inclusion core, that is considerably smaller than the saturation polarization. As the field is increased further, the vortex-like texture is abruptly expelled from the near-surface region and the polarization aligns along the $+\hat{z}$ direction everywhere in the particle. Multistage switching processes similar to the one observed here have been reported before in some nanopatterned FE[105, 215] and ferromagnetic[38, 39] systems.

As the particle diameter increases further, the intermediate vortex-like texture occurring in the the near-surface region at $E_z \simeq +E_c$ is replaced with a multidomain texture, such as the

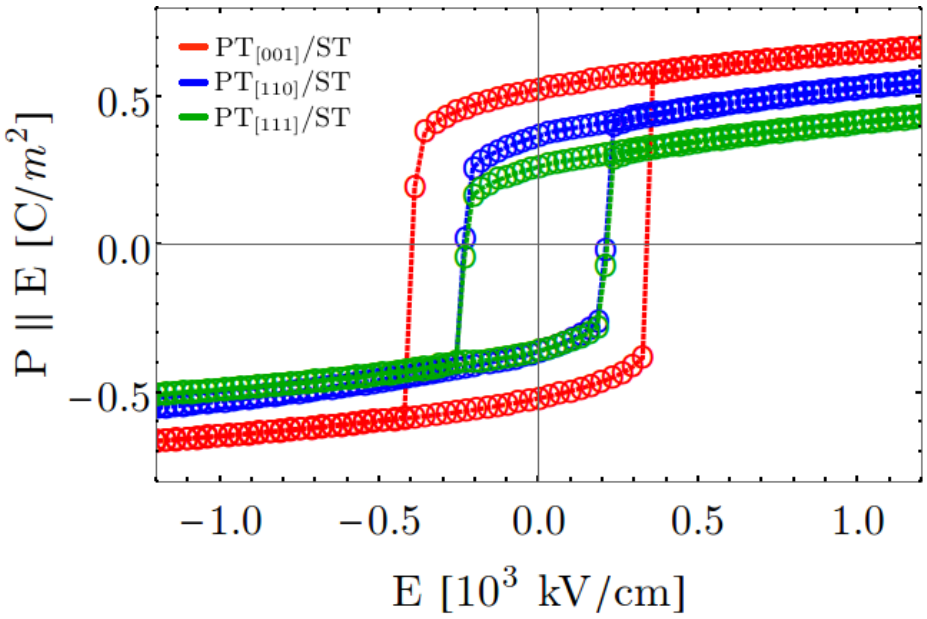

Fig. 5.11 Applied field-dependent polarization curves for a PT particle with $d < d_v$ embedded in the ST dielectric medium. The electric field is applied along the $\hat{z}$ direction, while different crystallographic orientations ([001], [110], [111]) of the PT unit cell are aligned with the field by rotating the particle. Note that [001] corresponds to the crystallographic $\hat{\mathbf{c}}$ axis along $\hat{\mathbf{z}}$. Adopted from Ref. [209] with permission from the publisher.

one shown as case (iii) in Fig. 5.12 **(c)**. Similar to the zero-field configurations, domains at the inclusion surface prefer to have tangential orientations of their **P** to minimize the electrostatic energy arising from q_S. As the magnitude of the field is increased, the transition into the monodomain state occurs by a gradual alignment of the surface domain polarizations along the $+\hat{z}$ direction. This switching mechanism produces multiple shoulders in the response curve, which merge together smoothly for larger particles that contain many surface domains [see, e.g., curve (iii) in Fig. 5.12 **(a)**].

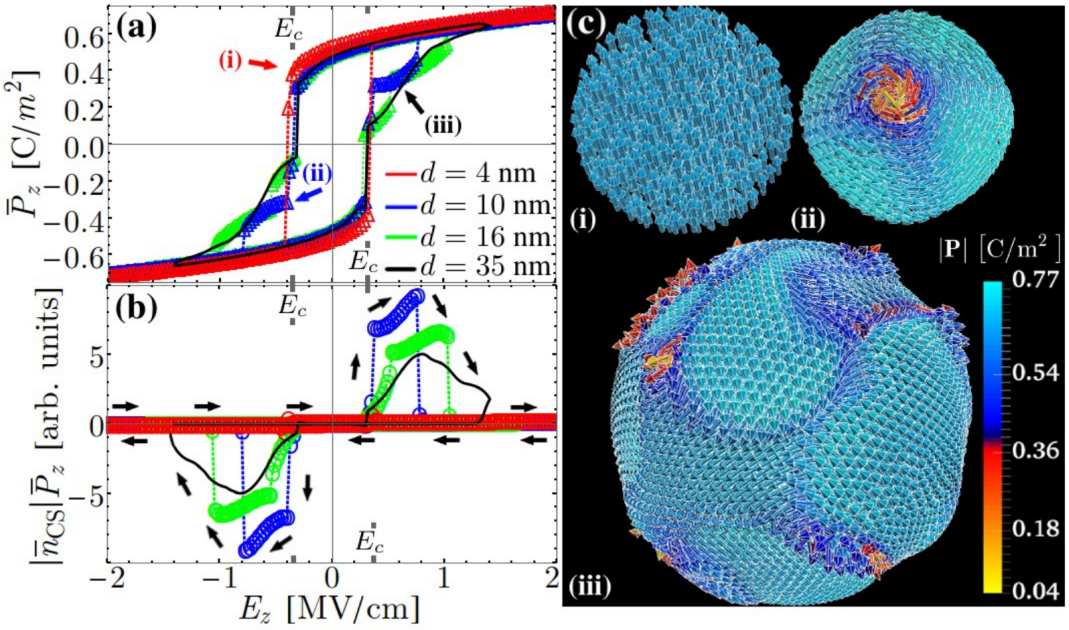

Fig. 5.12 **(a)** Average polarization $\bar{P}_z$ and **(b)** polarization-scaled winding number density $|\bar{n}_{CS}|\cdot\bar{P}_z$ as functions of applied electric field E_z in PT/ST systems of different sizes. Panel **(c)** shows polarization textures in (i) monodomain, $d = 4$ nm, (ii) vortex-like, $d = 10$ nm, and (iii) multidomain, $d = 35$ nm, systems corresponding to the markings in panel **(a)**.

In Fig. 5.12 **(b)** we present the changes in system vorticity under the changing electric field, which is represented by the sphere-averaged value of $|\bar{n}_{\mathrm{CS}}|$ weighted by the $\bar{P}_z$, for the same PT/ST structures as in Fig. 5.12 **(a)**. In case (i), monodomain texture at zero field, polarization switching occurs with $|\bar{n}_{\mathrm{CS}}| \equiv 0$ everywhere throughout the poling loop. For all the other cases at $d > d_v$, switching between monodomain states at $-E_{\max}\hat{z}$ and

$+E_{\max}\hat{z}$ happens through the formation of an intermediate vortex-like state, as indicated by the non-zero value of averaged n_{CS}. In case (ii), vortex-like texture at zero field, vorticity changes abruptly, but, as can be seen from comparison of the curves for $d = 16$ and 35 nm, this transition becomes progressively more diffuse for zero-field multidomain textures at increasing d. However, even for large nanoparticles containing many domains, such as in case (iii), $|\bar{n}_{\mathrm{CS}}|$ remains non-zero during the switching due to the presence of vortex-like twists of **P** along domain walls.

In Fig. 5.13 we show field-induced variations in polarization response [panel (a)] and vorticity [panel (b)] in the BT/ST systems with particle $d = 9$ to 30 nm. These curves look more slim, in comparison with the ones shown for PT/ST in Fig. 5.12 **(a)**, while the dependence of $|\bar{n}_{\mathrm{CS}}|$ on E_z suggests diffuse poling behavior in BT/ST proceeding through the formation of an intermediate state with non-zero vorticity at all of the considered inclusion sizes. Therefore, unlike in the PT/ST systems with $d_v < d < d_m$, where vortex-like texture in the near-surface region gets expelled abruptly upon transitioning into the monodomain state [see curve (ii) in Fig. 5.12(a-b)], in BT/ST this texture disappears gradually, as local polarization continuously rotates to align itself with the applied field and the core monodomain grows outward. A vector map of such an intermediate hybrid state, exhibiting both monodomain and vortex-like features, is shown in Fig. 5.13 **(c)**.

All these results suggest that a wide variety of different switching patterns and behaviors can be designed by controlling the size of the particle as well as the materials properties of the particle and the matrix. We note that the dielectric response of an aggregate system consisting of ferroelectric particles of varying sizes dispersed in a dielectric medium will depend strongly on the nature of the applied mechanical and electrical boundary conditions. For example, coherency (misfit) strains between the particle and the dielectric matrix, thermal and/or epitaxial stresses introduced into thin-film heterostructures during growth, specifics of the electric field application to the structure — such as usage of top-bottom or interdigitated

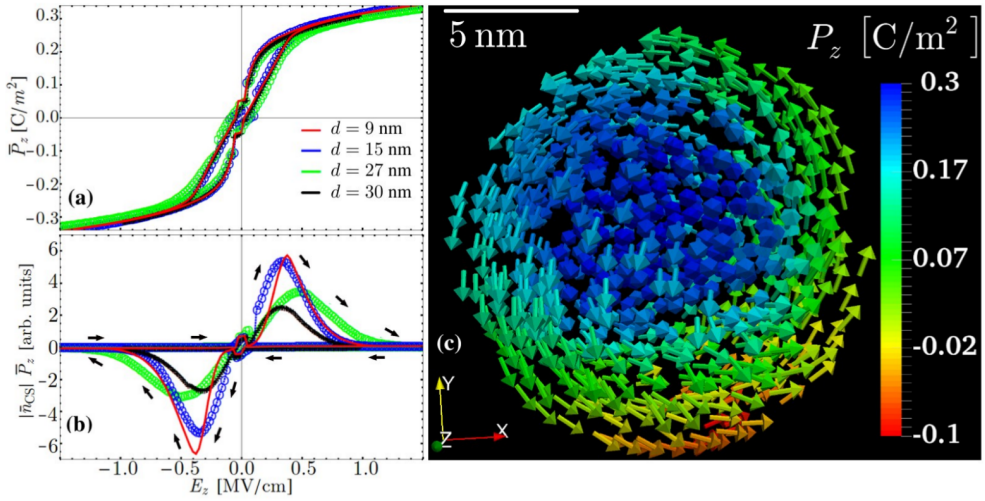

Fig. 5.13 **(a)** Average polarization $\bar{P}_z$ and **(b)** polarization-scaled winding number density $|\bar{n}_{\mathrm{CS}} \cdot \bar{P}_z$ as functions of applied electric field E_z in BT/ST structures of different sizes. Panel **(c)** shows a BT/ST system with a 15 nm inclusion that is in the process of nucleating a monodomain core (the blue region) as its polarization aligns with the external field. At zero applied field, this particle has a vortex-like **P** texture. In the near-surface region, **P** is curling around, which results in nonzero value of n_{CS}

electrodes, or an atomic-force microscope tip — will all have a significant effect on the overall dielectric response of the composite.

5.7 Conclusions

We have investigated the behavior of ferroelectric nanoparticles in dielectric media in a parametric space where different interactions, such as the electrostatics resulting from surface and bulk charges, as well as domain-wall and electrostrictive energies, are of similar magnitudes and compete. As a consequence, the observed ferroelectric behavior and response is complex and highly tunable by the selection of materials parameters and/or external fields. Our results show that a high-permittivity dielectric medium, that compensates charges on the inclusion surface, can stabilize non-zero polarization in PT particles as small as 2 nm in diameter.

In contrast, embedding in a low-permittivity medium results in large uncompensated surface charges that completely suppress polarization in particles smaller than d $\sim 3.4 - 3.6$ nm. Above that critical size, the ferroelectric state emerges as a vortex-like texture, which minimizes the electrostatic energy arising from the surface charges, while at even larger sizes, a multidomain texture is formed as a compromise between the electrostatic and polarization-gradient energy contributions. The electrostrictive coupling between the elastic and polar degrees of freedom softens sharp 90° domain walls, producing rounded vortex-like textures with cylindrical cores that can penetrate all the way through the spherical particle.

From an intricate dependence of the shape of the field vs polarization response loop on the particle size — an effect that cannot be directly reproduced in bulk ferroelectric materials — we also predict high intrinsic dielectric tunability of such ferroelectric nanoinclusions. This behavior is rooted in a multistage switching of the polarization through an intermediate state with non-zero winding number that can emerge/disperse gradually or abruptly, depending on a particular choice of material parameters and particle sizes. Field induced polarization response curves, such as the ones presented in Figs. 5.12 **(a)** and 5.13 **(a)**, can be obtained experimentally, e.g., using piezo-force microscopy. Therefore, it may be possible to utilize such measurements to explore the predicted rearrangements of polarization textures within the ferroelectric particles, as well as to evaluate the quality of the LGD G_{ijkl} -parameterizations for the gradient energy terms by observing and comparing the shapes of the response curves in samples with different particle sizes.

Chapter 6

Phason active caloric materials

In the previous Chapter, the discussion of a polar-elastic dielectric system was focused on applied electric field response, with no specific considerations of any thermal phenomena. In this Chapter, we investigate a different model system, where thermal and entropic degrees of freedom are explicitly coupled into the material description, with an emphasis on the electrocaloric effect. An original semi-analytic approach, utilizing an energy functional reconstructed from the results of a previous DFT-based study, is developed and applied for elucidating the details of electrothermal energy interconversion within the model, providing interesting insights into possible design of novel electrocaloric materials for solid state heating and cooling applications. It should be noted that (unlike in the previous Chapter), while polarization-field inhomogeneities are not included in the semi-analytic energy description presented here, we are currently working on expanding this description by fitting domain-wall energy terms from DFT. The expanded energy functional has already been added to the FERRET FEM-based module and is currently being tested.

6.1 Introduction

Caloric cooling processes involve adiabatic changes of temperature, ΔT, under a sweep of an electric, magnetic, or mechanical fields — characterizing an electro-, magneto-, or elastocaloric effects, respectively. These effects have been investigated in shape-memory alloy systems where large entropic changes can be achieved by using reversible mechanical deformations to drive a transition between ferroelastic twins [40, 205, 204]. However, defect formation at the twin (phase) boundaries can be problematic, causing the material to be more susceptible to fatigue [83].

A number of ferromagnetic systems have also been actively studied for magnetocaloric properties, with the induced ΔT observed to be $\simeq$ 10-20 K, when operating around room temperature [86, 231]. For these materials to be successfully integrated into devices at a large scale, the change in temperature must exceed this range to outperform conventional vapor-pump refrigeration schemes [83, 12, 294]. Ferroelectric materials can be a promising alternative if modest electric fields can be utilized for the electrocaloric energy interconversion, compared to large magnetic fields ($>$ 2 T) needed to drive the similar effects in their magnetic counterparts [12, 83].

Epstein *et al.* [79] suggested that if an electrocaloric material is patterned as a thin film and wedged between closed heat switches, the efficiency of that system could be higher than those of conventional refrigerators and thermoelectric devices. The movable heat-switch layer concept was exploited further [106] in order to employ a "chip scale" approach, where the moving-part friction and dielectric loss contributions to heating efficiency were shown to induce $\delta T \simeq 2$ K, with a prototype device exhibiting a total $\Delta T \simeq 6$ K during operation under moderate applied electric fields. This layering approach is particularly advantageous, as Wang *et al.* [308] showed that a device consisting of a ferroelectric ($BaTiO_3$) slab wedged between silicon layers can operate without fatigue for thousands of actuation cycles, which is an important requirement for practical implementation.

Therefore, comprehensive studies of the electrocaloric effect (ECE) in thin ferroelectric films are integral to improving and optimizing the performance of thermal energy interconversion devices. Thin films of $PbZr_{0.95}Ti_{0.05}O_3$ have been observed to generate large *positive* $\Delta T/\Delta E \simeq 0.5$ K/V[1] [226]. Also, thin films of a ferrelectric relaxor material $Pb_{0.8}Ba_{0.2}ZrO_3$ were shown to have $\Delta T \simeq 45$ K for a few hundred kV/cm of applied field [251]. This very large value was attributed to the coexistence of nanoscale regions of ferroelectric and antiferroelectric ordering within the material sample. Furthermore, ferroelectric polyvinylidene fluoride (PVDF)-based copolymer and terpolymer films were shown to exhibit $\Delta T \simeq 12$ K under $\Delta E \simeq 100$ kV/cm field change [179, 198]. Due to low-cost of synthesis, these polymer systems remain very attractive candidates for ECE applications.

The question of the influence of the polarization inhomogeneities (i.e., domain structure) on the ECE has been investigated by Karthik and Martin [149, 318]. In this study, it was found that thermal (and dielectric) susceptibilities of the domain-wall regions could be enhanced, producing secondary intrinsic contributions to the system pyroelectric response and thus improving the ECE temperature change. In another study [207], compositionally graded heterostructures [from $PbZr_{0.2}Ti_{0.8}O_3$ to $PbZr_{0.8}Ti_{0.2}O_3$] were shown to have lower the dielectric permittivity (due to built in electric fields), while retaining the magnitude of their pyroelectric response. This allows for better ECE performance with respect to single crystals of $LiNbO_3$ or $LaNbO_3$ [207]. Additionally, other researchers have investigated how the *size* of inhomogeneities can affect the overall ECE [313]. A coexistence of negative and positive ECE was seen in a single crystal $BaTiO_3$ due to the presence of inhomogeneous domains aligned noncollinear with the applied field direction.

Other materials, such as relaxors or antiferroelectrics have been shown to exhibit a *negative* (or anomalous) ECE, whose physical underpinnings are still unclear [258, 180, 97]. It is suggested that rotations of the polarization field could be responsible for the negative ECE response [258]. This understanding seems to be supported by a study done by Li

[1] This term, $\Delta T/\Delta E$, is called the associated electrocaloric strength after Ref. [313].

et al. [180] where two ferroelectric twin domains separated by a 180° domain wall were simulated under an applied electric field. These researchers showed that as an electric field is applied perpendicular to one of the 180° twins, the subsequent rotation of the polarization (to align with the electric field) generates an positive pyroelectric coefficient, which leads to a negative sign of the ECE induced ΔT – as shown in Eq. (2.112). So far, the largest (negative) values observed experimentally remain below $\Delta T = -10$ K for much smaller ΔE than in systems with $\Delta T > 0$.

In *conventional* ferroelectric materials, the magnitude of the (negative) field-dependent pyroelectric coefficient is maximum near T_C, which restricts their efficient operation to that specific temperature. The best values of ΔT induced by the conventional ECE in modern nanoengineered materials (which include ceramic, polymer, and liquid crystal systems) range from 20 to 45 K, for electric-field sweeps $\Delta E \leq 500$ kV/cm.

A $BaTiO_3$ thin film, as detailed in Chapter 2, was shown to have a weak dependence of the ΔT on the value of an applied epitaxial lattice-misfit strain. More importantly, this example demonstrates that the *location* of the ΔT peak along the T axis can be changed by the epitaxial strain, as it adjusts the location of the film T_C where the pyroelectric coefficient reaches its maximum. Still, we are left with the question of what other microscopic mechanisms may be responsible for the ECE, including its anomalous incarnation that produces *cooling*, rather than heating, as well as how these microscopic-level insights can be utilized to improve electrothermal device design? In this Chapter, we undertake a multiscale theoretical investigation of the ECE in an artificial layered-perovskite superlattice, that exhibits some unusual intrinsic properties, such as Goldstone-like (or *phason*) excitations of its polar degrees of freedom. Our methodological approach recycles data from a previous *ab initio* study of this material to construct a Landau-type energy functional for it. This DFT-based energy functional is then used to evaluate the caloric response of this material, elucidating the role of both polar amplitudon and phason excitations in the ECE.

6.2 Method

Using DFT simulations, Nakhmanson and Naumov [239] investigated the phonon-band structure of $PbSr_2Ti_2O_7$ (PSTO) layered perovskite-oxide superlattice. This artificial crystal belongs to the Ruddlesden-Popper (RP) compound series, $A_{n-1}A'_2B_nX_{3n+1}$, where A = Pb, A' = Sr , B = Ti, X = O, and $n = 2$ [267, 36]. Two types of the structure of this crystal are depicted in Fig. 6.1. RP phases can be imbued with a variety of interesting properties characteristic of their parent ABO_3 compounds, such as large magnetoresistance, superconductivity, and ferroelectricity, as well as, possibly, by more interesting functionalities that may be tunable by controlling the thickness of the perovskite slab (i.e., parameter n) [112].

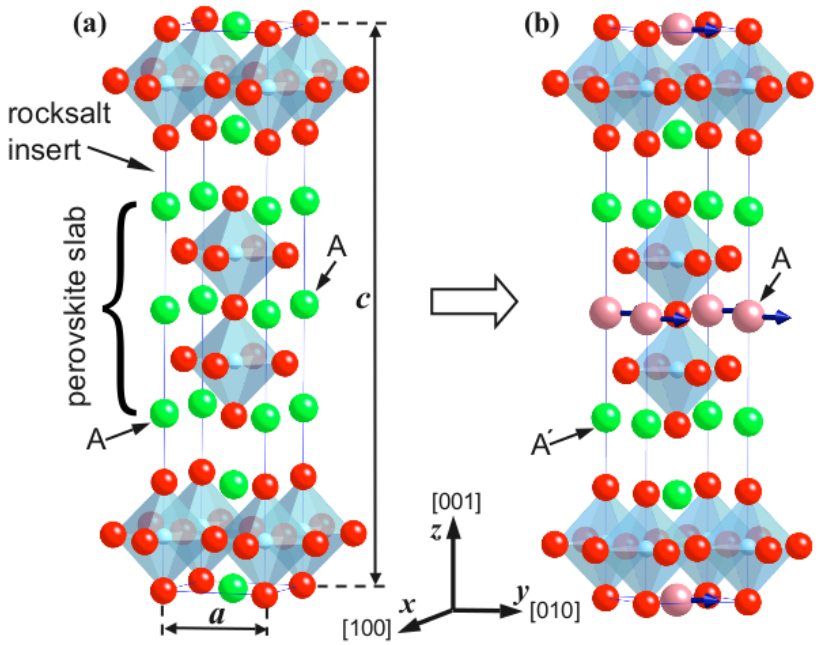

Fig. 6.1 Crystal structure of $n = 2$ RP compounds: (a) $Sr_3Ti_2O_7$; the lattice constants for the tetragonal cell are also shown. (b) $PbSr_2Ti_2O_7$ RP superlattice obtained from the structure (a) by assigning different A-site ions to the perovskite and rocksalt units. An in-plane ferroelectric distortion of the superlattice, consisting mostly of displacements of the lead atoms, is outlined by bold arrows. TiO_6 cages are represented by translucent octahedra, Sr atoms are shown in green (dark gray) and Pb atoms in pink (light gray). Figure and caption reproduced from Ref. [239] with permission from publisher.

For the DFT calculations, QUANTUM ESPRESSO plane-wave-basis package [98] was used, utilizing a local-density approximation in the Perdew-Zunger parametrization [252] and Vanderbilt ultrasoft pseudopotentials [301]. The ionic forces were relaxed to less than 0.2×10^{-5} Ry/bohr (0.5×10^{-4} eV/A) and the appropriate stress tensor components were converged to values below 0.2 kBar. The ionic Born effective charge tensors $Z^*_{i,\alpha\beta}$, with i the ion number, and the high-frequency dielectric permittivity tensor $\epsilon^{\infty}_{\alpha\beta}$ were calculated using the density-functional perturbation approach. The system polarization was evaluated with a linearized approximation, involving products of $Z^*_{i,\alpha\beta}$ and ionic displacements away from the centrosymmetric phase.

The phonon bands that were computed across the tetragonal Brillouin zone (BZ) revealed interesting behavior. It was shown that the rocksalt layers in PSTO effectively destroy any polar instabilities oriented along the c axis of the crystal. Instead, polar instabilities were found to be oriented within the basal plane of the structure, leading to polarization $|\mathbf{P}| = 0.22\,\mathrm{C/m^2}$ (comparable to that of bulk $BaTiO_3$) produced mostly by off-centering of the Pb ions in the PbO layers (shown by arrows in Fig. 6.1). The calculations also suggested that polar distortions in neighboring perovskite slabs are practically uncorrelated in their orientations (by the near-degeneracy phonon bands corresponding to antiferroelectric and ferroelectric distortions) and therefore this structure may be regarded as a collection of non-interacting quasi-two-dimensional polar sheets.

The system energy surfaces with respect to the amplitudes of the frozen-in polar distortions under changing epitaxial misfit elastic strain $\varepsilon_{xx} = \varepsilon_{yy} = \varepsilon$ were computed and are shown in Fig. 6.2 **(a)**-**(c)**. The epitaxial[2] thin-film constraint on a cubic (001)-oriented substrate was simulated by varying the in-plane lattice constant a of the tetragonal cell giving rise to ε and allowing the out-of-plane lattice constant c to relax (by converging the normal stress in this direction to a small value). This was performed while preserving the imposed

[2]The biaxial misfit strain ε is defined as $(a - a_0)/a_0$, where a_0 is the in-plane lattice parameter of the free standing structure.

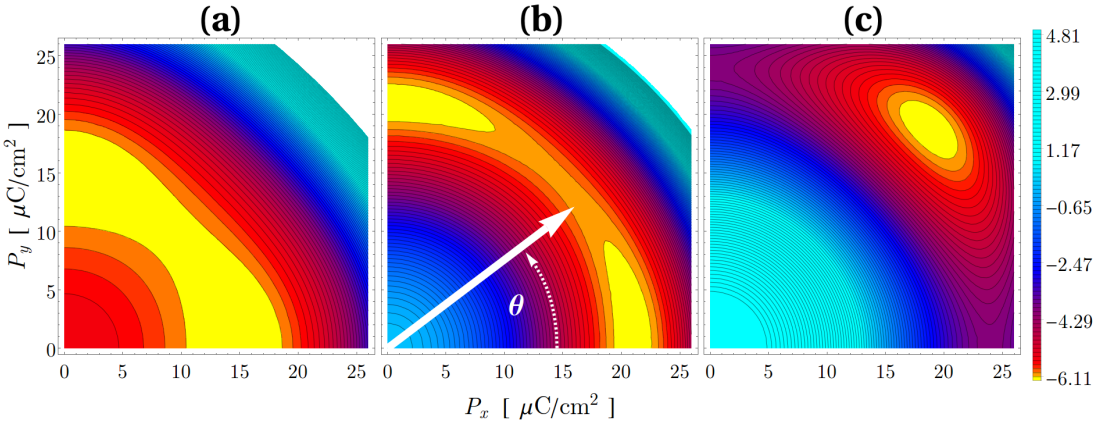

Fig. 6.2 Contour-map views of the system energy-density function (fitted from the DFT data of Ref. [239]) with respect to developing in-plane polarization $\mathbf{P} = (P_x, P_y)$ for the biaxial strain ε equal to **(a)** -1, **(b)** 0, and **(c)** +1 %. The energy of the paraelectric phase is taken as zero. The location of the polarization vector within the minimum-energy "groove" and its azimuthal angle θ are marked out in panel **(b)** for the shown $(P_x, P_y) > 0$ quadrant of the energy surface. The energy scale on the right is in meV/s.u. and applicable to panel **(b)**. The application of biaxial strain greatly influences the shape of the system energy surface, changing both the depth and the location of its minima (highlighted in yellow). Figure is adapted from Ref. [211] with permission from the publisher.

$P4/mmm$ unit-cell symmetry. Remarkably, the minima of the energy surface at $\varepsilon = 0\%$ were found to exhibit no specific preference for the polarization direction within the xy-plane, see Fig. 6.2 **(b)**, with energy barriers between the [100] and [110] oriented sets of minima being very small [on the order of only a few meV per structural unit (s.u.)]. Both sets of minima effectively merge into a circular 'groove' in the energy landscape, that takes on a sombrero-hat shape, which is indicative of a Goldstone-like mode being present in the system [100]. As the system is put under slight ($\varepsilon > 0.1\%$) to modest epitaxial tension, the polarization orients itself along the [110] or a symmetrically equivalent direction, again with a rather shallow energy barrier between these favored directions [see panel **(c)**], and the energy 'groove' state disappears. When the system is under compression, the 'groove' state persists, although with gradually diminishing value of equilibrium polarization, until at $\varepsilon < -1\%$ it collapses, with the system becoming stable with respect to in-plane polar distortions and its energy surface adopting a parabolic shape.

The celebrated Goldstone theorem [100] in its nonrelativistic form states that breaking of a continuous-symmetry element in a system gives rise to a massless excitation with frequency $\omega \to 0$ for a wave vector $\mathbf{k} \to 0$ that "on average" restores the lost continuous symmetry. Although a few examples of such Goldstone modes are known in isotropic solids, including Heisenberg ferromagnets [50], liquid crystals [235], and incommensurate structures [43], in regular crystals — such as ferroelectric oxides — which are usually highly anisotropic, such modes are extremely rare. In what follows, by 'Goldstone-like' we understand *light* [$\omega(\mathbf{k} = 0 \sim 0$], rather than strictly massless excitations. The existence of a state with an absence of the preferable direction for polarization, that is proposed for PSTO in Ref. [239], indicates that this material can easily adopt a vortex (or toroidal) dipole ordering when shaped into a nanodisk or other flat nanoparticle [172]. As already discussed in Chapter 2, such vortex patterns may be promising for nonvolatile memory applications due to a projected several orders of magnitude increase in storage density [240, 241].

We have used the data from the DFT calculations of Ref. [239] to fit a Landau-style energy functional for PSTO with respect to its quasi-two-dimensional polarization $\mathbf{P} = (P_x, P_y)$ and applied biaxial strain $\varepsilon \in (-2\%, +2\%)$. The polynomial expansion in powers of $\mathbf{P}$ and ε,

$$\begin{aligned} f =& \alpha_1(T - T_C)(P_x^2 + P_y^2) + \alpha_2(P_x^4 + P_y^4) \\ &+ \alpha_3 P_x^2 P_y^2 + \alpha_4(P_x^6 + P_y^6) + \alpha_5(P_x^4 P_y^2 + P_x^2 P_y^4) \\ &+ \left(\chi_1(P_x^2 + P_y^2) + \chi_2(P_x^4 + P_y^4) + \chi_3 P_x^2 P_y^2\right)\varepsilon \\ &+ \left(\chi_4(P_x^2 + P_y^2) + \chi_5(P_x^4 + P_y^4) + \chi_6 P_x^2 P_y^2\right)\varepsilon^2, \end{aligned} \tag{6.1}$$

is fitted with a nonlinear least-squares optimization algorithm. It should be noted that higher order strain terms, compared to a standard Landau-style coupled energy expansion (comparing to Eq. (2.107) from Ch. 2), were needed to reproduce the behavior of the PSTO

energy surface under changing applied strain, including the shift of the energy-minima sets from [100] to [110] orientations [3]. The fitting coefficients are listed in Table 6.1.[4] The value of the Curie temperature, T_C, was approximated by comparing the energy differences between the non-polar $I4/mmm$ and polarized $\mathbf{P}||[100]$ and $\mathbf{P}||[110]$ states:

$$T_C = \frac{E_{\text{I4mmm}} - E_{\text{symm}}}{k_B} = 120\,\text{K}, \tag{6.2}$$

with $k_B = 1.38063 \times 10^{-23}$ m^2 kgs^{-2} K^{-1} being the Boltzmann constant. This estimate allows for the temperature dependence to be introduced into the energy expression, in the first coefficient of the Landau expansion (same as for $PbTiO_3$). Such a dependence is essential for reproducing the parabolic $\rightarrow$ quartic phase transition in the system as the temperature is lowered below T_C.

α_j		unit	χ_j		unit
α_1	1.27×10^6	J/K m^{3}C^2	χ_1	-4.18×10^9	J/ m^{3}C^2
α_2	1.76×10^9	J/ m^{3}C^4	χ_2	-3.69×10^{10}	J/ m^{3}C^4
α_3	3.73×10^9	J/ m^{3}C^6	χ_3	-2.51×10^{11}	J/ m^{3}C^4
α_4	-5.91×10^8	J/ m^{3}C^6	χ_4	1.21×10^{11}	J/ m^{3}C^2
α_5	-6.51×10^8	J/ m^{3}C^6	χ_5	2.41×10^{12}	J/ m^{3}C^4
			χ_6	6.49×10^{12}	J/ m^{3}C^4

Table 6.1 Coefficients of the Landau expansion for the energy functional of the PSTO system. The fitting was performed in Wolfram Research's *Mathematica for Students* (version 10.3) [311]. Fit parameter errors are assembled in the Supplemental of Ref. [211]

[3] It is also automatically implied that symmetrically equivalent energy minima are obtained by C_4 rotations of the energy surface

[4] The fit was performed in *Wolfram Research Mathematica for Students* 3 (version 10.3)[311] using the `NonlinearModelFit[]` function. Options `Method`$\rightarrow$`NMinimize` with automatic `MaxIterations` were utilized. Test of the goodness of fit returned an R^2 value of 0.999304.

In order to find the thermodynamic equilibrium of the system, polarization values must obey the following partial differential equations

$$\frac{\partial f}{\partial P_x} = 0 \text{ and } \frac{\partial f}{\partial P_y} = 0. \tag{6.3}$$

Furthermore, the following constraints

$$P_x, P_y \geq 0,\ P_x, P_y \leq 1, \frac{\partial^2 f}{\partial P_x \partial P_y} > 0,$$

and

$$\det \begin{vmatrix} \frac{\partial^2 f}{\partial P_x^2} & \frac{\partial^2 f}{\partial P_x \partial P_y} \\ \frac{\partial^2 f}{\partial P_x \partial P_y} & \frac{\partial^2 f}{\partial P_y^2} \end{vmatrix} > 0,$$

should be included to find strict minima (forcing the numerical solver to toss out saddle points) on the energy surface $f = f(P_x, P_y)$. The solutions are found on a grid of variables T, ϵ, E_x, E_y with the `NSolve[]` function with `ParallelTable[]` to improve computational efficiency. The solutions, $\mathbf{P}^0 = (P_x^0, P_y^0)$, are then substituted back into the free energy-density expression, yielding an equilibrium free energy density,

$$f^0 = f(\mathbf{P}^0). \tag{6.4}$$

Using thermodynamic expressions discussed in Chapter 2, one can write the following for the transitional excess entropy and heat capacity [7]:

$$\begin{aligned} \Delta C^{\mathrm{XS}} &= T\left(\frac{\partial^2 f^0(\mathbf{P}^0)}{\partial T^2}\right)_{\mathbf{E},\varepsilon} \\ S^{\mathrm{XS}} &= -\left(\frac{\partial f^0(\mathbf{P}^0)}{\partial T}\right)_{\mathbf{E},\varepsilon}. \end{aligned} \tag{6.5}$$

At fixed $\mathbf{E}$, T, and ε, the pyroelectric coefficient (which here has x and y components, same as the system polarization), that is dual to the change in entropy with respect to the applied electric field, is

$$p_k = \left(\frac{\partial S}{\partial E_k}\right)_{\varepsilon,T} = \left(\frac{\partial P_k^0}{\partial T}\right)_{\varepsilon,\mathbf{E}}.$$

Consequently, then the temperature change due to the ECE, calculated from Eq. (2.112), can be simplified for the 2D material (no pyroelectricity along the $\hat{\mathbf{z}}$ due to no $\mathbf{P}$ along this direction) to

$$\Delta T = -T\sum_{k=x,y}\int_{E_{k,a}}^{E_{k,b}} dE_k \left(\frac{1}{C_V + \Delta C^{\mathrm{XS}}}\right)_{\mathbf{E},\varepsilon}\left(\frac{\partial P_k^0}{\partial T}\right)_{\mathbf{E},\varepsilon}, \tag{6.6}$$

where the changes in the electric field components are $E_{k,b} - E_{k,a} = \Delta E_k$ with $E_{k,a} \leq E_{k,b}$.

The variable C_V, denotes the heat capacity as a function of both temperature and applied strain, which can be computed with *ab initio* methods [212, 238]. The formal expression for

the heat capacity is

$$C(T) = 3R \int_0^{E_{\max}} \left(\frac{E}{k_B T}\right)^2 \frac{e^{E/k_B T}}{\left(e^{E/k_B T} - 1\right)^2} g(E) dE, \tag{6.7}$$

which can be discretized as

$$C_p = \frac{3nN_A\hbar^2}{k_B T^2} \sum_{\omega} \omega^2 \frac{\mathrm{VDOS}(\omega) e^{\frac{\hbar\omega}{k_B T}}}{\left(e^{\frac{\hbar\omega}{k_B T}} - 1\right)^2} \tag{6.8}$$

with vibrational density of states $\mathrm{VDOS}(\omega)$ normalized to unity, $k_B = 1.38 \times 10^{-23}$ J/K, $\hbar = 1.05 \times 10^{-24}$ J· s, $n = 24$ atoms, and $N_A = 6.022 \times 10^{23}$. The $\mathrm{VDOS}(\omega)$ is computed for the non-polar system configuration using QUANTUM ESPRESSO [98] and shown in Fig. 6.3 **(a)**, while the resulting $C_V(T)$ is presented in Fig. 6.3 **(b)**.

6.3 Results

Due to the fragility of the Goldstone-like state in PSTO (perceived through the shallowness of the associated energy minima), the behavior of the system and its equilibrium polarization $\mathbf{P}^0$ can be analyzed in two different regimes, depending on the strength of the applied electric fields. For applied electric fields $\Delta E_k \geq 40 - 50$ kV/cm (depending on the strain) the energy landscape – shown in Fig. 6.2 – can be perturbed away from its original sombrero-hat shape. I.e., at a strong applied field, the polar vector instantly locks into an energy minimum aligned with the field direction, which effectively destroys the Goldstone-like excitation. Then, subsequent poling fields ΔE_k preserve this locked state of $\mathbf{P}^0$. This *amplitudon* mode of operation is representative of the conventional ECE, which arises due to modulation of the magnitude of $\mathbf{P}^0$ around T_C. A plot of the polarization magnitude vs. temperature in this

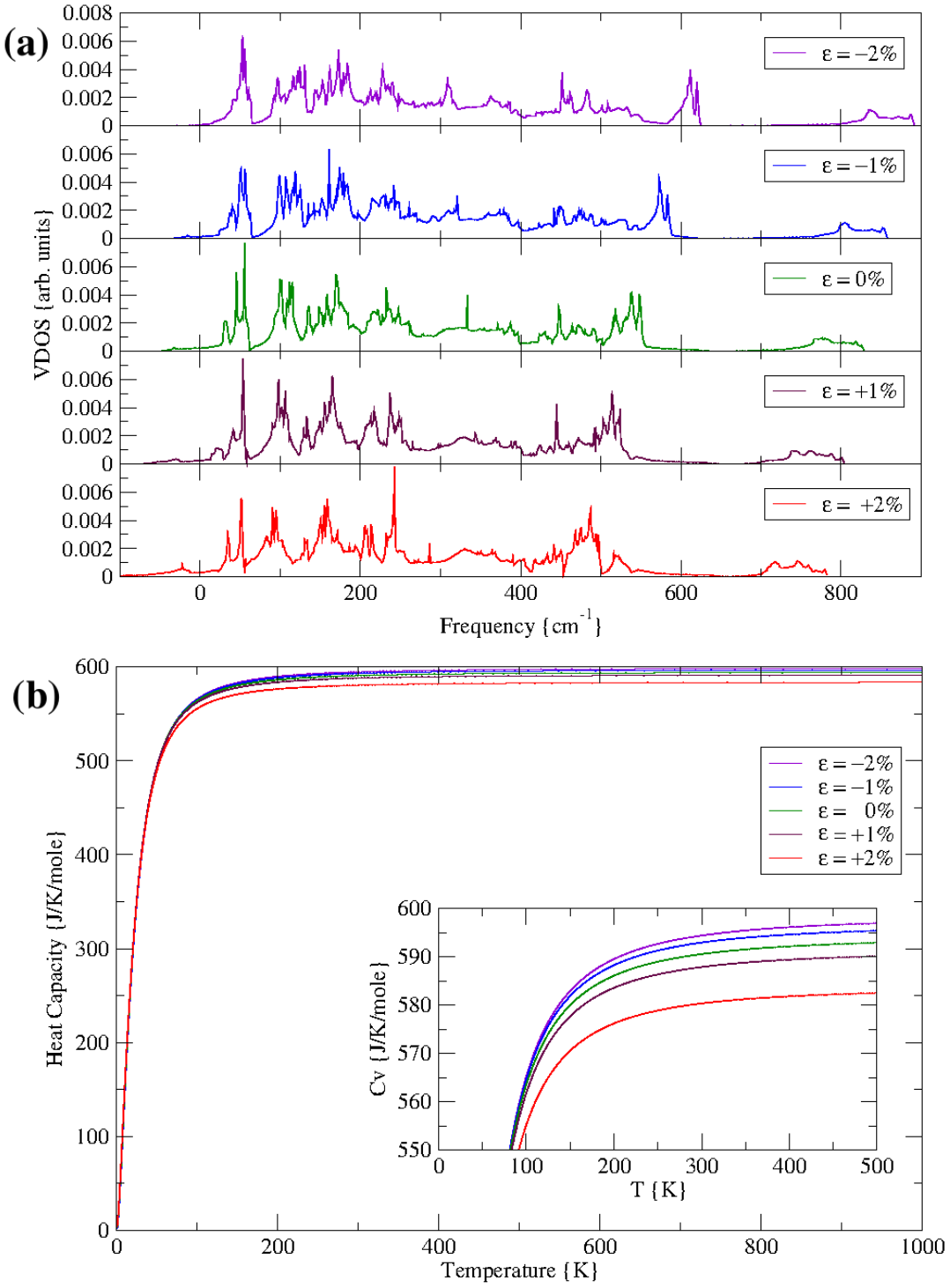

Fig. 6.3 **(a)** Normalized VDOS computed for PSTO (in the non-polar configuration, space group $I4/mmm$) with Quantum Espresso, for different strain states. **(b)** Heat capacity as a function of temperature. This figure is reprinted from the Supplemental of Ref. [211] with permission from the publisher.

regime, presented in Fig. 6.4 **(a)**, is similar to Fig. 2.13 from Chapter 2 and also shows a large change in the polarization magnitude (corresponding to the maximum of the conventional pyroelectric coefficient) near T_C.

The high-field poling regime pyroelectric coefficients for PSTO are shown in Fig. 6.4 **(b)**, reaching their maximum values in the vicinity of the ferroelectric-paraelectric phase transition. The transitional excess entropy [panel **(c)**] and heat capacity [panel **(d)**], calculated from Eq. (6.5), are shown as well. Once again, this behavior looks the same as the conventional ECEf in perovskite ferroelectrics [146]. The resulting high-field poling regime system ΔT is

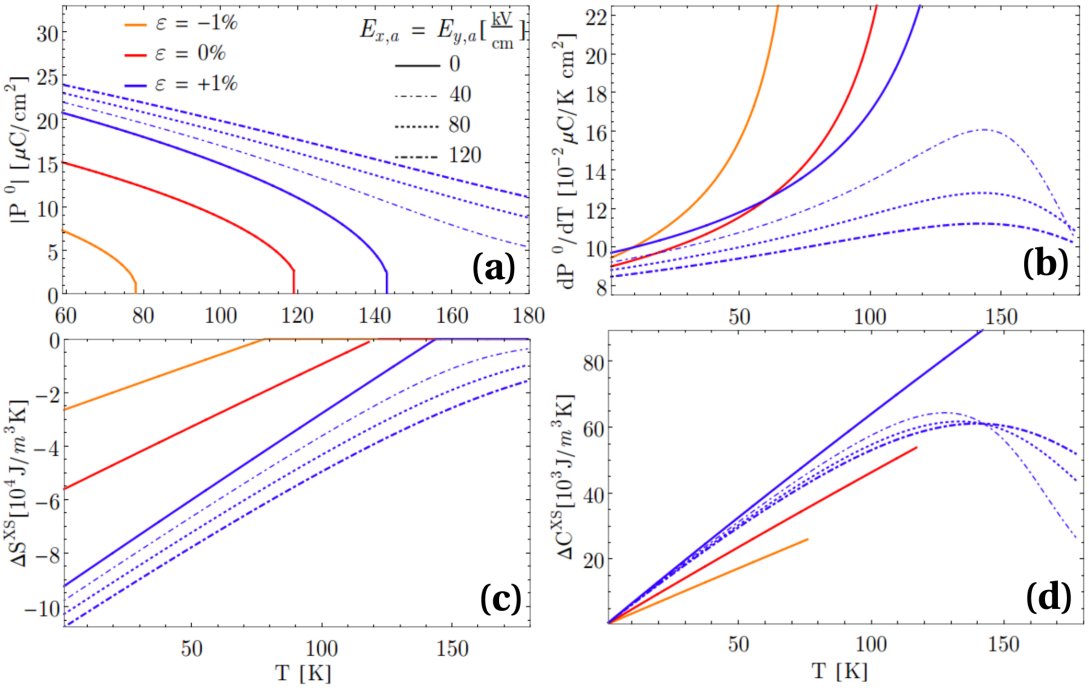

Fig. 6.4 Equilibrium polarization **(a)** as a function of temperature for the high-field poling regime at different applied strains and electric fields. The corresponding pyroelectric coefficient **(b)** and excess entropy **(c)** and heat capacity **(d)** calculated from Eq. (6.5) are shown as well.

shown in Fig. 6.5 for different choices of ε and $\Delta E_x = \Delta E_y = 180$ kV/cm.

A different operating regime is observed for low values of the applied electric field ($E_k \leq$ 40-50 kV/cm), when the sombrero-hat shaped energy surface is only *slightly* perturbed.

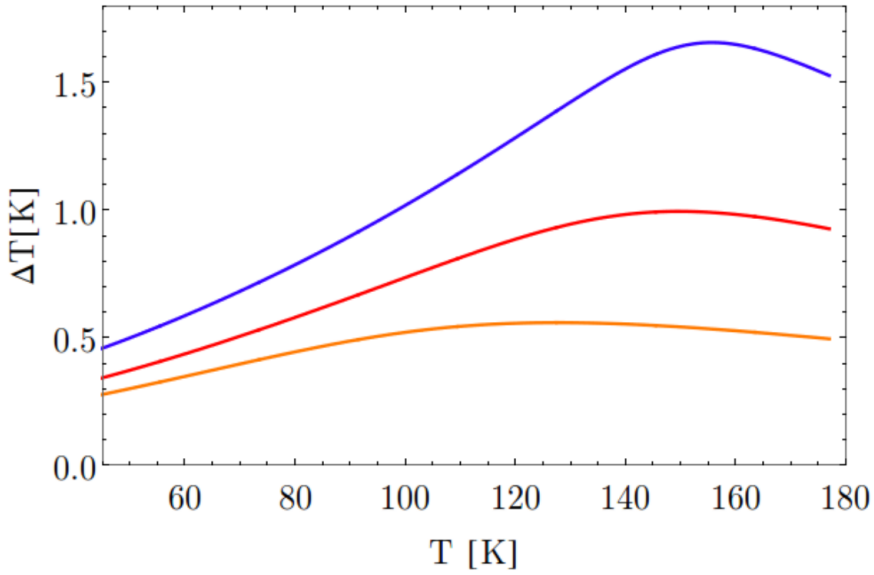

Fig. 6.5 ECE induced ΔT in the high-field poling regime for $\varepsilon = -1, 0, +1\%$ at $\Delta E_x = \Delta E_y = 180$ kV/cm. Color convention is the same as in Fig. 6.4 **(a)**. Reprinted from the Supplemental of Ref. [211] with permission from the publisher.

Before proceeding with the rest of the discussion, we need to define the azimuthal angle θ of the polarization vector, as shown in Fig. 6.2 **(b)**. Now, if the $\mathbf{P}||[100]$ state of Fig. 6.2 **(b)** is taken as a starting point, applying a noncollinear electric field induces a rotation of the polar vector along the minimum-energy 'groove' until $\mathbf{P}||\mathbf{E}$. During this rotation process, which we refer to as *phason* polarization switching, its azimuthal angle θ changes while its amplitude $|\mathbf{P}^0|$ remains approximately constant.

The $\theta(T)$ dependence for different configurations of applied electric fields is shown in Fig. 6.6 **(a)** and **(b)**. In panel **(a)**, a symmetric $E_x = E_y$ electric field is applied, while in panel **b** the applied electric field is asymmetric, i.e., $E_x \neq E_y$. Here, the polarization is initially pointing along $\theta = 0^\circ$ (the nearest [100] energy minimum), and the angle between **P** and the direction of applied **E** is less than 45°. For both scenarios, it is observed that **P** can align with **E** only if sufficient energy is supplied in the form of heat. For the symmetric case, the polarization vector locks with the field abruptly at some temperature T_{lock}, which can induce large pyroelectric coefficients. However, for asymmetrically applied electric fields,

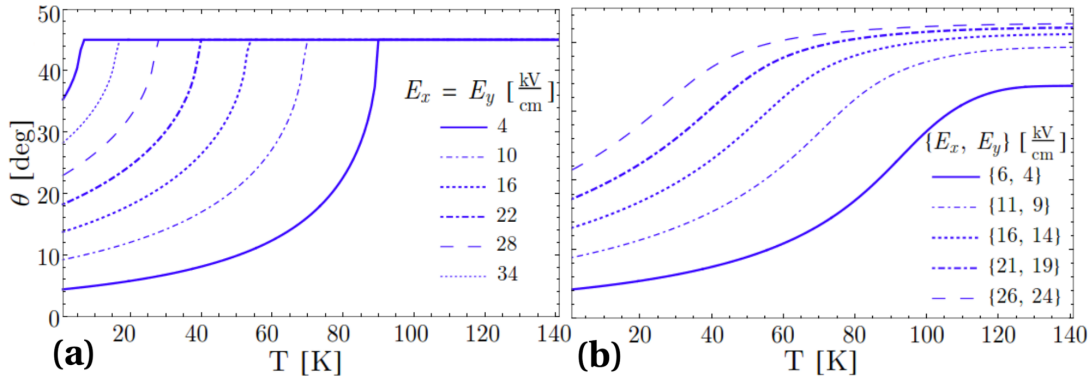

Fig. 6.6 Temperature dependence of the polarization azimuthal angle θ under **(a)** symmetrically, $E_{x,a} = E_{y,a}$, and asymmetrically $E_{x,a} \neq E_{y,a}$, applied static electric fields. In case **(a)**, the polarization vector locks with the field abruptly at some temperature T_{lock}, while in case **(b)** it smoothly aligns with the electric field. Figure is adapted from Ref. [211] with permission from the publisher.

the alignment of **P** with **E** always happens smoothly, as seen in Fig. 6.6 **(b)**. Since there is no abrupt locking, this does not produce large pyroelectric coefficients.

For the symmetric case, the large pyroelectric coefficients (from dP_x/dT and dP_y/dT) cancel each other out and the ΔT curve looks similar to those of Fig. 2.13 and Fig. 6.5 (albeit with a sharper peak). Components of **P** are shown in Fig. 6.7 **(a)** and **(b)**. The ΔT response for symmetric poling, where $E_x = E_y$ is kept *fixed* with $\Delta E = 40$ kV/cm is presented in Fig. 6.7 **(d)**.

From the $\theta(T)$ data shown in Fig. 6.7 **(c)**, we can see the value of T_{lock} can be adjusted by changing the magnitude of **E** throughout the whole temperature range up to T_C [see Fig. 6.8]. This behavior is similar to the previously considered case of the BTO thin film where T_C could be adjusted with applied strain, however doing the same with an applied electric field is much more convenient for device applications. The location of T_{lock} defines an upper-bound on the phason stability as no polarization rotations are allowed above T_{lock}. The inset of Fig. 6.8 shows the effect of compressive strains on the phason stability, with slight compression maximizing the value of T_{lock}.

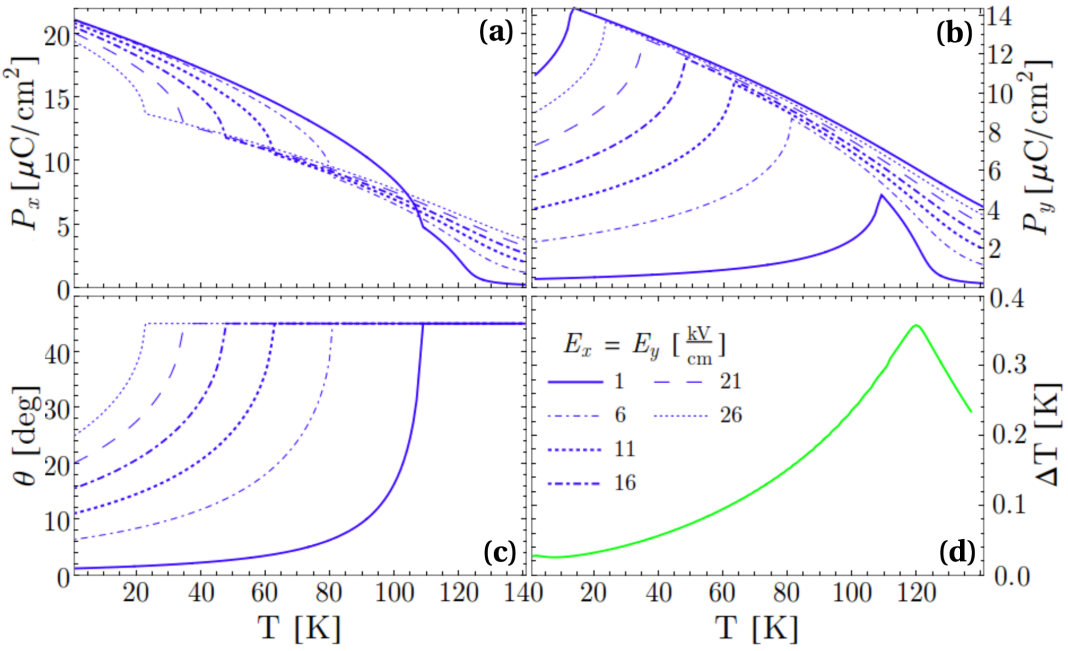

Fig. 6.7 Polarization vector components **(a)** P_x and **(b)** P_y for different static applied fields $E_{x,a} = E_{y,a}$ at zero strain. **(c)** Corresponding variation of $\theta(T)$ under the same conditions, emphasizing its abrupt locking along the field direction. ECE induced ΔT for the case of symmetric poling, where $E_x = E_y$ is kept *fixed* for $\Delta E = 40$ kV/cm. The pyroelectric coefficients from both P_x and P_y cancel each other out, and no contribution from the polar phason mode is observed in the shape of the ΔT curve. Reprinted from the Supplemental of Ref. [211] with permission from the publisher.

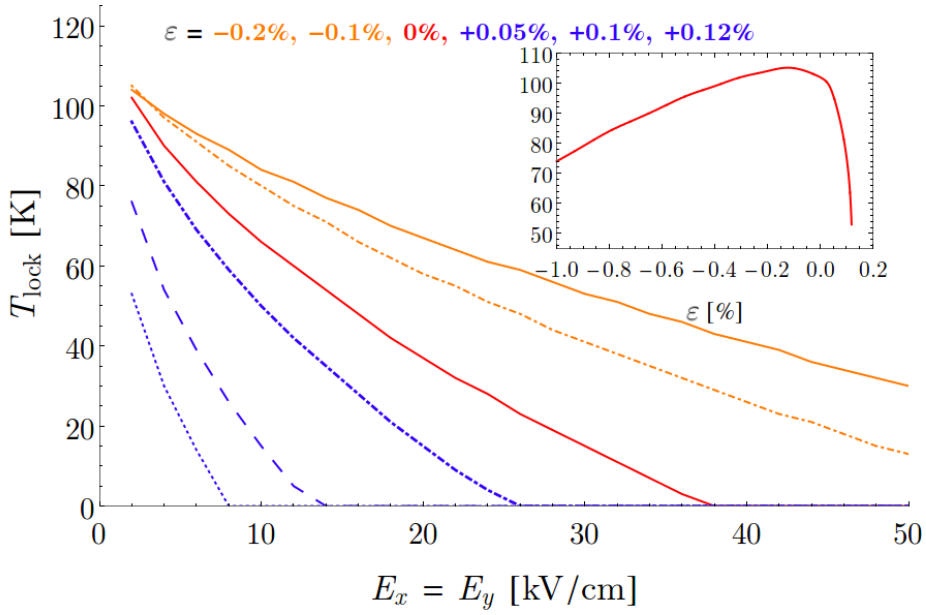

Fig. 6.8 The locking temperature T_{lock} as a function of the symmetric field strength $E_x = E_y$. The phason polarization rotations are only allowed when $T_{\text{lock}} \neq 0$. As shown in the insert depicting the $T_{\text{lock}}(\varepsilon)$ dependence, slight compressive strains can allow the phason mode to be more stable at higher applied fields. A peak in T_{lock} is observed at $\varepsilon \simeq 0.18\%$

By now we have shown that the passage of the polarization *through* the saddle point of the energy surface (e.g., located at 45° for $\varepsilon = 0$) is accompanied by an emergence of a large pyroelectric coefficient. Therefore, in order to utilize the largeness of the pyroelectric response for improving ΔT, we can propose the following switching scenario:

- The system is prepared with initial polarization in the the $\theta = 0°$ energy minima.
- A static electric field $E_x = \widetilde{E}$ is applied, with $\Delta E_x = 0$. This effectively eliminates one of the integrals in Eq. (2.112).
- A field along $\hat{\mathbf{y}}$ is applied, changing from $E_{y,a} < \widetilde{E}$ to $E_{y,b} > \widetilde{E}$.

This process is illustrated step-by-step in Fig. 6.9. The idea is to trigger a rotation of $\mathbf{P}$ from one energy equivalent minimum to another. For example, this may be a $\sim 90°$ from $\mathbf{P}||[100]$ across the [110] saddle point, and into the $\mathbf{P}||[110]$ minimum.

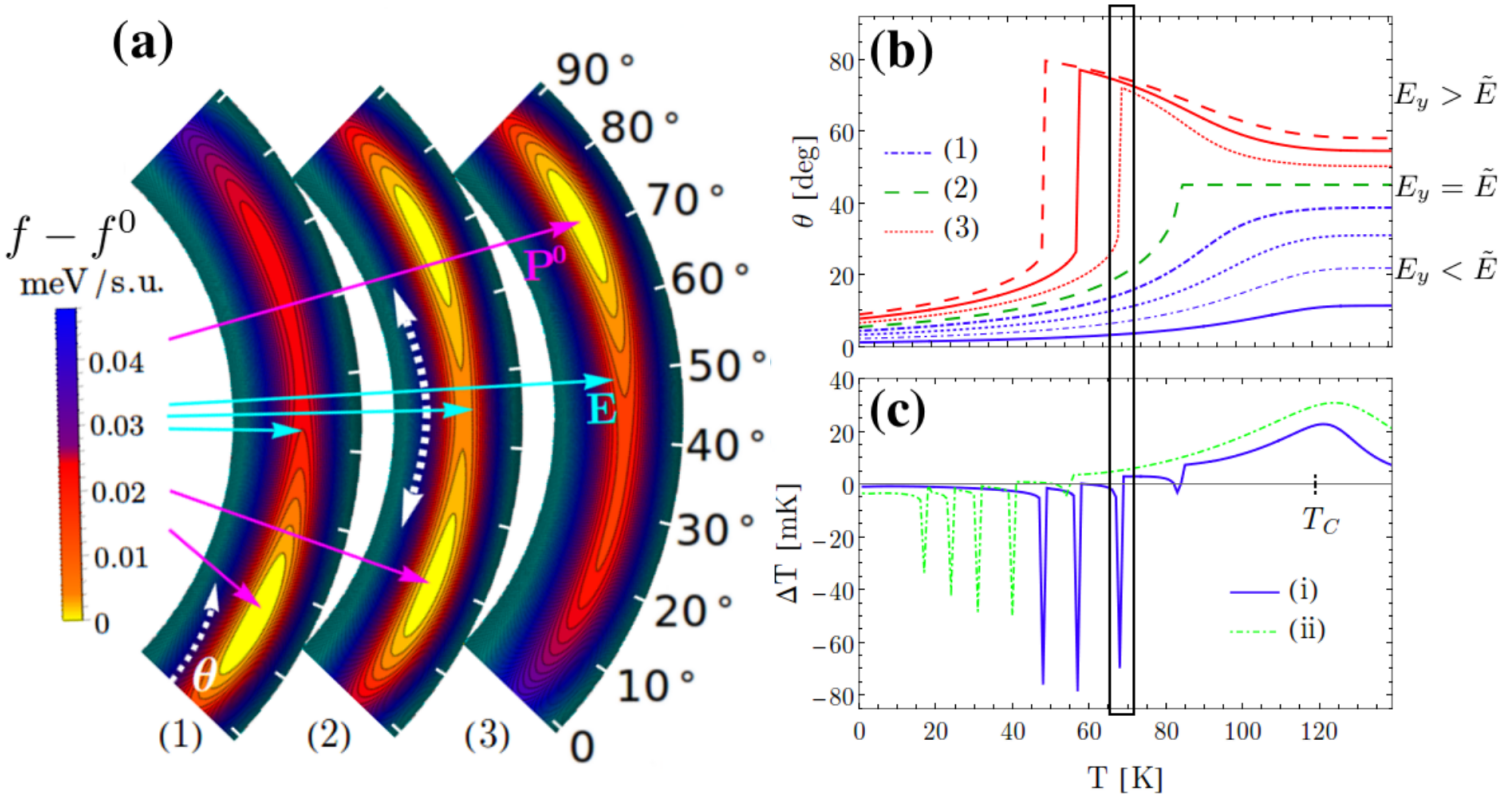

Fig. 6.9 **(a)** A step-by-step sketch of **P** rotation under poling $\widetilde{E} = 5$ kV/cm and $T = 68$ K for (1) **P** close to the [100] minimum with $E_y < \widetilde{E}$ and $\theta \sim 0°$, (2) **P** passing through the saddle point along [110] with $E_y \simeq \widetilde{E}$ and $\theta \simeq 45°$, (3) **P** switching to the neighboring minimum along [010] with $E_y > \widetilde{E}$ and $\theta \sim 90°$. Arrows represent approximate directions of polarization and electric field at steps (1) through (3). **(b)** $\theta(T)$ angular dependence at different static electric fields. **(c)** ΔT response for two scenarios (i) $\widetilde{E} = 5$ kV/cm, $\Delta E_y = 7$ kV/cm and (ii) $\widetilde{E} = 13$ kV/cm, $\Delta E_y = 17$ kV/cm. The connection between an abrupt change of θ and the produced ECE response is outlined by the rectangular selection spanning panels (b, c). Reprinted from Ref. [211] with permission from the publisher.

Fig. 6.9 **(b,c)** shows that abrupt changes in θ translate into large *negative* values of EC ΔT. As illustrated by the two different switching cases, the position of the phason ECE peak on the temperature axis, as well as its width, can both be controlled purely by means of applied electric field — specifically by setting the values of $\tilde{E}$, and ΔE_y, respectively. For example, changing $\tilde{E}$ from 5 to 13 kV/cm moves the center of the phason ECE peak down from 60 to 30 K. Such precise tuning of the shape and location of the phason-induced ECE response can be accomplished for all temperatures below T_C. Typical maximum entropy changes achieved in this poling scenario are 0.5–1 $\mathrm{J\,kg^{-1}\,K^{-1}}$, similar to values observed by others for low-field switching [86, 231].

The positive peaks on the ΔT curve shown in Fig. 6.9 **(c)** represent contributions from the amplitudon mode, at the operating temperature near T_C, while at temperatures below T_C the phason more induced contributions are negative and thus indicate cooling of the system. The negative sign of the phason-switching induced ΔT originates from the following consideration: as $T \to T_{\mathrm{lock}}$ and polarization rotation occurs, the $\widehat{\mathbf{P},\mathbf{E}}$ angle is always diminished. Naturally, polarization component $P_{\gamma,b}$ after the rotation is always larger than component $P_{\gamma,a}$ before the rotation, where γ is the direction along the field. Thus, the associated $p_\gamma \sim (P_{\gamma,b} - P_{\gamma,a})/(T_{\mathrm{lock}} - T)$ is positive, which results in negative ΔT according to Eq. (6.6).

As shown in Fig. 6.9 **(c)** , abrupt changes of θ, each occurring under a specific *fixed* value of $E_y > \tilde{E}$, result in an emergence of sharp bumps in the ECE induced ΔT response. Furthermore, by choosing the values of the stationary $\tilde{E}$ field and the bracketing ΔE_y poling interval, these peaks can be shifted to lower or higher temperatures on demand. When during the poling procedure E_y is swept continuously from $E_{y,a} < \tilde{E}$ to $E_{y,b} > \tilde{E}$, individual peaks in the ΔT curve merge into an envelope that is presented in Figs. 6.10 and 6.11 for different values of ε. Remarkably, the variation of ε by $\leq 1\%$ can result in the system ECE response

changing from cooling (phason contribution) to heating (amplitudon contribution) at the same operating temperature.

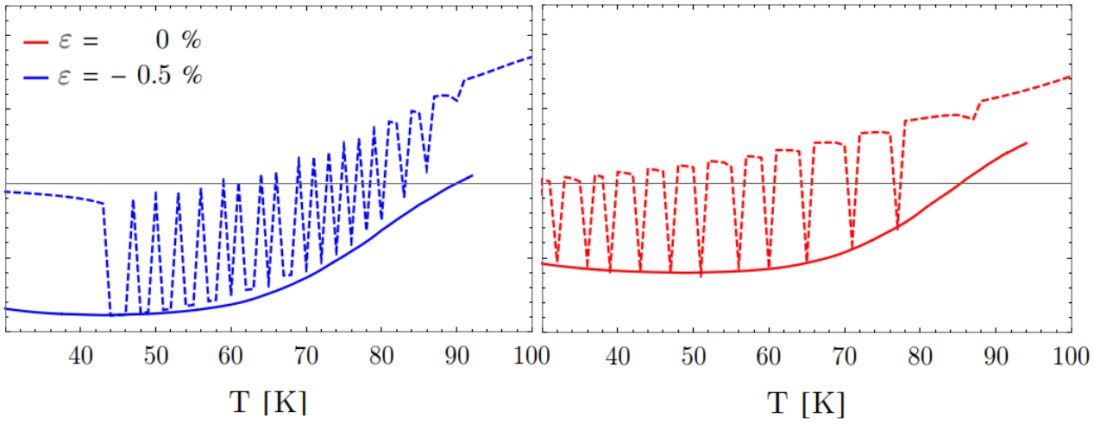

Fig. 6.10 Envelope estimation for the phason-induced contribution to the ECE response. The presented panels display an intermediate data-processing step leading to smooth envelope estimations for strains of $\varepsilon = -0.5\%$ and 0%. These evaluations were performed using Wolfram Research Mathematica for Students (version 10.3)[311] `EstimatedBackground[]` function with the statistics-sensitive nonlinear iterative peak clipping method. Reprinted from Ref. [211] with permission from the publisher.

It should be mentioned that integration (and subsequent envelope estimation) carried out in Eq. (2.112) is a rather delicate procedure. Instead of utilizing the Maxwell relations of Eq. (2.61), a number of other researchers have developed the co-called direct approaches for evaluating ECE that utilize effective Hamiltonian techniques, molecular dynamics, or Monte Carlo simulations [258, 202, 213]. These methods can handle first-order phase transitions and the associated entropy changes that may contain abrupt changes of the pyroelectric coefficient. Here, we have carefully investigated the convergence of the integration in Eq. (2.112) for the poling schemes presented in this Chapter. Variations of about 15%-20% in the resulting ΔT for phason-induced switching were found as long as the dE_k step of the numerical sweep was not too small (typical step values ranged from 0.5 to 0.05 kV/cm).

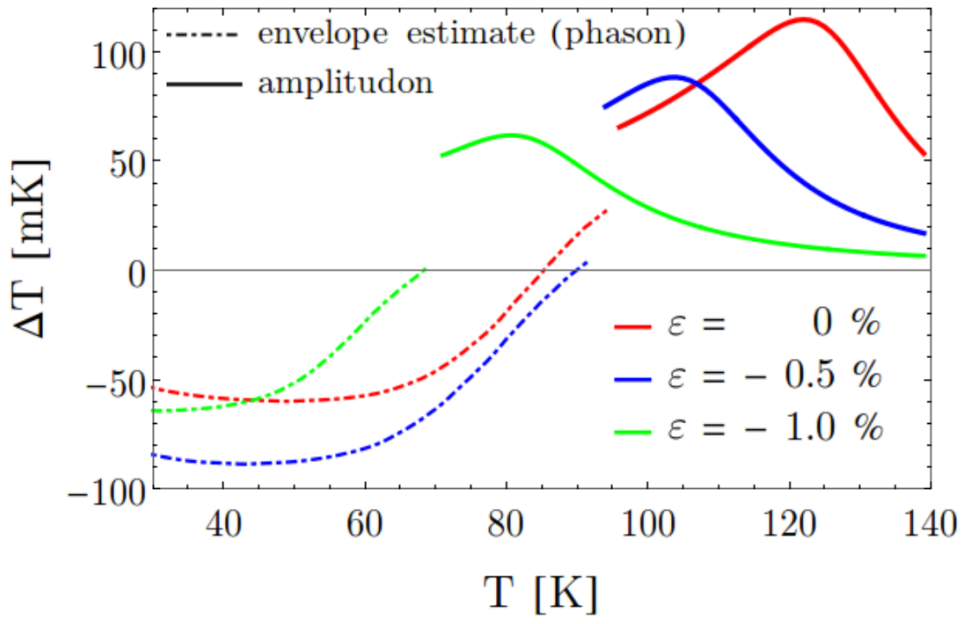

Fig. 6.11 Temperature changes ΔT computed with $\widetilde{E} = 5$ kV/cm and $\Delta E_y = 34$ kV/cm. For $T = 70$ K, it should be possible to flip the sign of the ECE response from cooling to heating or vice versa by tuning the value of T_C by applied strain.

6.4 Conclusions

In the high-field regime, individual slab polarizations are switched "all at once," being forcefully correlated by the applied field. I.e., the multi-slab system possesses only one entropy channel and the value of $\Delta T \simeq 1$–2 K quoted above for PSTO should represent its aggregate ECE response. In the low-field regime, applied fields are insufficient to correlate the directions of (disordered) polar vectors in different slabs and, therefore, polarization rotations under the cycling of the field should occur independently in each slab. In such a case, each slab acts as a separate entropy channel and the aggregate ECE response of the whole system should be proportional to the logarithm of the number of slabs [255, 12]. Then, even with individual slab contributions being low ($\sim$100 mK for PSTO), a system comprised of a large number of slabs should possess an aggregate ΔT that is at least comparable with other state-of-the-art *negative* ECE materials [181, 19, 254, 97].

In this work, the consideration of the ECE in PSTO did not take into account inhomogeneities of the elastic and polarization fields that are likely to be present realistic systems. For example, no estimates of polar domain-wall motion effects during the poling procedure, which could increase the aggregate ΔT, have been performed. Also, a variational solution approach to investigate possible polarization-closure patterns in PSTO nanostructures predicted [172] that these states are likely to form and their behavior sensitively depends on the applied strain, suggesting that multiple entropy channels may be created (or destroyed, if needed) in each slab by distorting its shape.

In summary, we have shown that layered polar systems with Goldstone-like instabilities should exhibit attractive ECE properties that are highly tunable by applying electric fields and elastic distortions over a wide range of operating temperatures below T_C, which may even include on-demand switching between cooling and heating. By virtue of operating at low electric fields, device applications of actual materials will require modest power consumption, compared to most other known ECE compounds, where fields of upwards of 500 kV/cm are needed for best performance. Furthermore, in such model systems the mechanisms behind the emergence of independent entropy channels can be clearly established allowing for an easy up- or down-scaling of the system entropy-flow and ECE characteristics by growing an appropriate number of layers.

Chapter 7

Conclusions and future outlook

The goal of this dissertation research thrust aimed at developing a mesoscale-level modeling approach for simulating the behavior of dielectric materials with coupled elastic, polar, and thermal degrees of freedom has produced a flexible, open-source computational tool that is currently being used by a number of researchers at the University of Connecticut and abroad. As the mathematical methodology and its numerical implementations were being developed, different test problems were solved: to both ensure the validity of our approach and apply it to a variety of systems with practical importance.

The first test problem involved an investigation of an influence of elastic distortions on the electronic band gaps of semiconducting core-shell nanoparticles. These particles are useful in a variety of biomedical and photocatalytic fields. In this study, it was shown that due to intrinsic surface tension and high surface-to-volume ratio produce residual stress fields in the particles. Using results fitted from *ab initio* calculations, changes to the electronic band gap as a function of these stress fields were probed with respect to varying size, shell/core microstructure, materials choice, and applied mechanical boundary conditions. This work resulted in a publication in *Physical Review Applied* in 2015 [210]. The same modeling strategies could be applied to other material systems, such as popular CdTe or anatase TiO_2, and alternative geometric configurations, such as nanowires or disks. Furthermore, the same

materials-by-design principles could be adapted to search for multimaterial combinations that have the greatest property tunability due to their geometry, elastic anisotropies, deformation potentials, and surface tensions.

The next test problem involved modeling of ferroelectric polarization behavior in polar-dielectric nanocomposites with elastic degrees of freedom. Specifically, polarization topology of spherical ferroelectric nanoparticles embedded in a dielectric matrix was probed as a function of particle size, material choice, and applied electrical boundary conditions. A tendency for the system to form a vortex-like state for a certain range particle diameters was revealed, along with other possible configurations, such as monodomain and multidomain. Under hysteretic field switching, large tunable dielectric responses were observed that indicate that ferroelectric nanoparticles could support a multibit-switching memory scheme. This work resulted in a publication in *Nanoscale* in early 2017 [209]. Currently, the dependence of polarization topology on the particle shape is being investigated, including octahedral, cubic and elliptic geometries, which have all been shown possible to be synthesized in experiments. This future direction is enabled by the capability of our approach to effectively process arbitrary and irregular computational domains — a capability that is unavailable in phase-field methods that rely on spectral or Fourier numerical techniques. Another ongoing investigation involves simulations of *multiple* ferroelectric particles interacting with each other through the dielectric matrix, which should bring us closer to understanding surprising collective behavior of ferroelectric/dielectric composites. Both of these studies should enable us to formulate specific design rules for optimization of interparticle spacing, concentration, size, shape, morphology and materials choice in order to improve and custom-tailor a variety of dielectric device properties.

Finally, a test problem involving investigation of thermal effects in a quasi-two-dimensional polar-elastic model dielectric was considered, with an emphasis on the electrocaloric effect (ECE). In that work, the ECE was studied in with a semi-analytic approach that did

not take into account inhomogeneous elastic and polarization fields that may be present in real ferroelectric systems. We found that two different polarization switching modes can be induced in this model system depending on the largeness of the applied electric field: low-field polar rotations below T_C, as well as a conventional ferroelectric-paraelectric transitions with changing polarization magnitude near T_C. The former operational mode, which we called a *phason* mode of electrocaloric energy interconversion, produces a highly tunable ECE temperature shift ΔT at low-voltage that is anomalous in its nature and results in system cooling instead of heating. Furthermore, in the low-field switching regime, each quasi-two-dimensional polar slab switches independently from its neighbors and thus can be regarded as an independent channel of entropic changes within the system. Individual contributions from multiple switching slabs should be additive, and the total ECE response of the system should depend on the number of slabs, which could lead to new paradigms in ECE device design. This study was published in *npj Computational Materials* in mid-2016 [211]. While not yet explicitly connecting this investigation to our computational methodologies, we are currently developing a Landau-type parameterization for this system that includes polarization and elastic field inhomogeneities, and that will be well-suited for use in the FEM-based modeling, as implemented in our computational module FERRET. Nonetheless, there are a number of remaining open questions that we intend to investigate in the future: How does the discovered *phason* induced switching influence the domain structure evolution in ferroelectric nanostructures? Could the ECE response be studied with our mesoscale method implementation where temperature is treated as an *inhomogeneous* field, allowing for thermal energy flow through the system?

It is the author's hope that these test projects highlight the versatility of the developed method and that it will be widely utilized by the scientific community to make transformative discoveries in materials modeling of dielectric and ferroic nanostructures.

References

[Cub] CUBIT meshing software is developed by Sandia National Laboratories and is available at https://cubit.sandia.gov/.

[vor] VORO++ is an open-source software package for performing Voronoi tessellations on user-defined geometries and is available at http://math.lbl.gov/voro++/.

[acm] Global Catalyst Market. http://www.acmite.com/market-reports/environmentals/global-catalyst-market.html. Accessed: 2017-06-05.

[4] (2015). Moose workshop slides. MOOSE developers Idaho National Laboratory.

[5] Ahluwalia, R., Tagantsev, A. K., Yudin, P., Setter, N., Ng, N., and Srolovitz, D. J. (2014). Influence of flexoelectric coupling on domain patterns in ferroelectrics. *Phys. Rev. B*, 89(174105).

[6] Aizu, K. (1965). Possible species of ferroelectrics. *Phys. Rev.*, 146(2).

[7] Akcay, G., Alpay, S. P., Rossetti, G. A., and Scott, J. F. (2008). Influence of mechanical boundary conditions on the electrocaloric properties of ferroelectric thin films. *J. Appl. Phys.*, 103(024104).

[8] Akdogan, E. K. and Safari, A. (2007a). Thermodynamic theory of intrinsic finite-size effects in $PbTiO_3$ nanocrystals. I. Nanoparticle size-dependent tetragonal phase stability. *J. Appl. Phys.*, 101(6):064114.

[9] Akdogan, E. K. and Safari, A. (2007b). Thermodynamic theory of intrinsic finite size effects in $PbTiO_3$ nanocrystals. II. Dielectric and piezoelectric properties. *J. Appl. Phys.*, 101(6):064115.

[10] Alda, J. and Rico-Garcia, J. M. and López, J. M. and Boreman, G. (2005). Optical antennas for nano-photonic applications. *Nanotechnology*, 16(5).

[11] Allen, S.-K. and Cahn, J. W. (1979). A macroscopic theory for antiphase boundary motion and its application to antiphase domain coarsening. *Ada. Metall.*, 27:1085–1095.

[12] Alpay, S. P., Mantese, J., Trolier-McKinstry, S., Zhang, Q., and Whatmore, R. W. (2014). Next-generation electrocaloric and pyroelectric materials for solid-state electrothermal energy interconversion. *MRS Bull.*, 39(12):1099–1111.

[13] Argyris, J. H. (1955). Energy theorems and structural analysis: A generalized discourse with applications on energy principles of structural analysis including the effects of temperature and nonlinear stress-strain relations Part I. General Theory. *Air. Engr. Aero. Tech.*, 27(2):85 – 97.

[14] Armero, F. and Callari, C. (1999). An analysis of strong discontinuities in a saturated poro-plastic solid. *Internat. J. Numer. Methods Eng.*, 46:1673–1698.

[15] Arnold, D. N., Brezzi, F., Cockburn, B., and Marini, L. D. (2002). Unified analysis of discontinuous Galerkin methods for elliptic problems. *SIAM J. Numer. Anal.*, 39(5):1749–1779.

[16] Artyukhov, V. I., Liu, M., and Yakobson, B. I. (2014). Mechanically induced metal–insulator transition in carbyne. *Nano. Lett.*, 14(8):4224–4229.

[17] Auciello, O., Scott, J. F., and Ramesh, R. (1998). The physics of ferroelectric memories. *Physics Today*, 51(7):22–27.

[18] Auciello, O. and Scott, J. F. and Ramesh, R. (1998). . *Phys. Today*, 51:22–27.

[19] Axelsson, A.-K., Le Goupil, F., Dunne, L. J., Manos, G., Valant, G., and Alford, N. M. (2013). Microscopic interpretation of sign reversal in the electrocaloric effect in a ferroelectric $PbMg_{1/3}Nb_{2/3}O_3$-$PbTiO_3$ single crystal. *Appl. Phys. Lett.*, 102(102902).

[20] Babuska, I. and Guo, B. Q. (1992). The h, p and h-p version of the finite element method: basis theory and applications. *Adv. Engr. Soft.*, 15(3).

[21] Bahadur, N. M., Furusawa, T., Sato, M., Kurayama, F., and Suzuki, N. (2010). Rapid synthesis, characterization and optical properties of TiO_2 coated ZnO nanocomposite particles by a novel microwave irradiation method. *Mater. Res. Bull.*, 45(10):1383 – 1388.

[22] Baker, G. (1977). Finite element methods for elliptic equations using nonconforming elements. *Math. Comp.*, 31(137):45–59.

[23] Balay, S., Abhyankar, S., Adams, M. F., Brown, J., Brune, P., Buschelman, K., Eijkhout, V., Gropp, W. D., Kaushik, D., Knepley, M. G., McInnes, L. C., Rupp, K., Smith, B. F., and Zhang, H. (2014). PETSc users manual. Technical Report ANL-95/11 - Revision 3.5, Argonne National Laboratory.

[24] Balke, N., Winchester, B., Ren, W., Chu, Y. H., Morozovska, A. N., Eliseev, E. A., Huijben, M., Vasudevan, R. K., Maksymovych, P., Britson, J., Jesse, S., Kornev, I., Ramesh, R., Bellaiche, L., Chen, L.-Q., and Kalinin, S. V. (2012). Enhanced electric conductivity at ferroelectric vortex cores in $BiFeO_3$. *Nature*, 8:1745–2473.

[25] Bardeen, J. and Shockley, W. (1950). Deformation potentials and mobilities in non-polar crystals. *Phys. Rev.*, 80(1).

[26] Baroni, S., Gironcoli, S., and Corso, A. D. (2001). Phonons and related crystal properties from density-functional perturbation theory. *Rev. Mod. Phys.*, 73:515.

[27] Barrett, J., Blowey, J. F., and Garcke, H. (1999). Finite element approximation of the Cahn-Hilliard equation with degenerate mobility. *SIAM J. Numer. Anal.*, 37(1):286 – 318.

[28] Bateman, T. B. (1962). Elastic moduli of single-crystal zinc oxide. *J. Appl. Phys.*, 33(1962):3309–3312.

[29] Bates, C. H. and Roy, R. (1962). New high-pressure polymorph of zinc oxide. *Science*, 137:993–993.

[30] Bathe, K.-J. (2014). *Finite Element Procedures, Second Edition*. Prentice-Hall, Pearson Education, Inc.

[31] Battye, R., Cooper, N. R., and Sutcliffe, P. M. (2002). Stable skyrmions in two-component Bose-Einstein condensates. *Phys. Rev. Lett.*, 88(8).

[32] Baudry, L., Luk'yanchuck, I. A., and Vinokur, V. M. (2017). Ferroelectric symmetry-protected multibit memory cell. *Sci. Rep.*, 7(42196).

[33] Becker, E., Carey, G. F., and Oden, J. T. (1981). *Finite Elements: An Introduction*. Prentice-Hall, Inc., New Jersey.

[34] Belytschko, T., Chen, H., Xu, J., and Zi, G. (2003). Dynamic crack propagation based on loss of hyperbolicity and a new discontinuous enrichment. *Int. J. Numer. Meth. Eng.*, 58:1873–1905.

[35] Bersuker, I. B. (1966). On the origin of ferroelectric in perovskite-type crystals. *Phys. Lett. A*, 20(6).

[36] Beznosikov, B. V. and Aleksandrov, K. S. (2000). Perovskite-like crystals of the Ruddlesden–Popper series. *Crystall. Rep.*, 45(5):792–798.

[37] Bianchi, F., Ferrigno, R., and Girault, H. H. (2000). Finite element simulation of an electroosmotic-driven flow division at a T-junction of microscale dimensions. *Anal. Chem.*, 72(9):1987–1993.

[38] Boardman, R. P., Fangohr, H., Cox, S. J., Goncharov, A. V., Zhukov, A. A., and de Groot, P. A. J. (2005a). Micromagnetic simulation of ferromagnetic part-spherical particles. *J. Appl. Phys.*, 95:11.

[39] Boardman, R. P., Zimmerman, J., Fangohr, H., Zhukov, A. A., and de Groot, P. A. J. (2005b). Micromagnetic simulation studies of ferromagnetic part spheres. *J. Appl. Phys.*, 97:10E305.

[40] Bonnot, E., Romero, R., Mañosa, L., Planes, A., Vives, E., and Planes, A. (2008). Elastocaloric effect associated with the martensitic transition in shape-memory alloys. *Phys. Rev. Lett.*, 100(125901).

[41] Bower, A. F. (2010). *Applied Mechanics of Solids*. CRC Press, Taylor Francis Group.

[42] Bowles, J. E. (1988). *Foundational Analysis and Design*. McGraw-Hill Book Company Limited.

[43] Bruce, A. D. and Cowley, R. A. (1981). *Structural phase transitions*. Taylor and Francis Ltd., London.

[44] Bruchez, M. J., Moronne, M., Gin, P., Weiss, S., and Alivisatos, A. P. (1998). Semiconductor nanocrystals as fluorescent biological labels. *Science*, 281:2013–2015.

[45] Bunge, H. (1993). *Texture Analysis in Materials Science: Mathematical Methods*. Cuvillier Verlag.

[46] Cao, W. (1994). Polarization gradient coefficients and the dispersion surface of the soft mode in perovskite ferroelectrics. *J. Phys. Soc. Jpn.*, 63:1156–1161.

[47] Cao, W. (2008). Constructing Landau-Ginzburg-Devonshire type models for ferroelectric systems based on symmetry. *Ferroelectrics*, 375:28–39.

[48] Cao, W. and Cross, L. E. (1991). Theory of tetragonal twin structures in ferroelectric perovskites with a first-order phase transition. *Phys. Rev. B.*, 44(1).

[49] Caruntu, D., Rostamzadeh, T., Costanzo, T., Parizi, S. S., and Caruntu, G. (2015). Solvethermal synthesis and controlled self-assembly of monodisperse titanium-based perovskite colloidal nanocrystals. *Nanoscale*, 7:12955.

[50] Chaikin, P. M. and Lubensky, T. C. (1995). *Principles of Condensed Matter Physics*. Cambridge University Press, Cambridge.

[51] Chan, J. M., Zhang, L., Yuet, K. P., Liao, G., Rhee, J.-W., Langer, R., and Farokhzad, O. C. (2009). PLGA-lecithin-PEG core-shell nanoparticles for controlled drug delivery. *Biomaterials*, 30:1627–1634.

[52] Chan, S.-K. (1977). Steady-state kinetics of diffusionless first order phase transformations. *J. Chem. Phys.*, 67:5755–5762.

[53] Chandrasekaran, A. a. (2016). Asymmetric structure of 90° domain walls and interactions with defects in $PbTiO_3$. *Phys. Rev. B*, 93(144102).

[54] Chaudhuri, R. G. and Paria, S. (2012). Core/shell nanoparticles: Classes, properties, synthesis mechanisms, characterization, and applications. *Chem. Rev.*, 112(4):2373–2433.

[55] Chen, L.-Q. (2002). Phase-field models for microstructure evolution. *Annu. Rev. Mater. Res.*, 32:113–140.

[56] Chen, T., Chiu, M.-S., and Weng, C.-N. (2006). Derivation of the generalized Young-Laplace equation of curved interfacts in nanoscaled solids. *J. Appl. Phys.*, 100(074308).

[57] Cho, K., Wang, X., Nie, S., Chen, Z., and Shin, D. M. (2008). Therapeutic Nanoparticles for Drug Delivery in Cancer. *Clin. Cancer Res.*, 14:1310–1316.

[58] Clough, R. W. and Woodward, R. J. (1967). Analysis of embankment stresses and deformations. *J. Soil. Mech. Found. Div.*, 93(4):529 – 549.

[59] Cochran, W. (1959). Crystal stability and the theory of ferroelectricity. *Phys. Rev.*, 3:412 – 414.

[60] Cockburn, B., Karniadakis, G. E., and Shu, C.-W. (2000). *Discontinuous Galerkin methods. Theory, computation and applications, Lecture Notes in Computational Science and Engineering*. Springer-Verlag, Berlin.

[61] Colli Franzone, P. and Franzone, L. (2004). A parallel solver for reaction–diffusion systems in computational electrocardiology. *Math. Models Meth. Appl. Sci.*, 14:883–911.

[62] Comes, R., Lambert, M., and Guinier, A. (1968). The chain structure of $BaTiO_3$ and $KNbO_3$. *Solid State Commun.*, 6(715).

[63] Courant, R. (1943). Variational methods for the solution of problems of equilibrium and vibrations. *Bull. Amer. Math. Soc.*, 49:1 – 23.

[64] Coussy, O. (2004). *Poromechanics*. John Wiley and Sons, Ltd.

[65] Curie, J. and Curie, P. (1880). Development, via compression, of electric polarization in hemihedral crystals with inclined faces. *Bulle. de la Societe de Miner. de France*, 3:90–93.

[66] Davis, M. E. (1984). *Numerical methods and modeling for chemical engineers*. John Wiley and Sons, Ltd.

[67] Dawber, M., Rabe, K. M., and Scott, J. F. (2005). Physics of thin-film ferroelectric oxides. *Rev. Mod. Phys.*, 77:4.

[68] de Jong, M., Chen, W., Angsten, T., Jain, A., Notestine, R., Gamst, A., Sluiter, M., Ande, C. K., van der Zwaag, S., Plata, J. J., Toher, C., Curtarolo, S., Ceder, G., Persson, K. A., and Asta, M. (2015). Charting the complete elastic properties of inorganic crystalline compounds. *Scientific Data 2*, 2::150009.

[69] Dennis, J. E. and Schnabel, R. B. (1996). *Numerical Methods for Unconstrained Optimization and Nonlinear Equations*. Prentice-Hall, Inc.

[70] DeSalvo, G. J. and Swanson, J. A. (1985). *ANSYS Engineering Analysis System User's Manual*. Swanson Analysis Systems.

[71] Desgreniers, S. (1998). High-density phases of ZnO: structural and compressive parameters. *Phys. Rev. B*, 58(14102).

[72] Devonshire, A. F. (1949). *The London, Edinburgh, and Dublin Philosophical Magazine and Journal of Science*, 40:1040.

[73] Devonshire, A. F. (1951). *The London, Edinburgh, and Dublin Philosophical Magazine and Journal of Science*, 42:1065.

[74] Diebold, U. (2003). The surface science of titanium dioxide. *Surf. Sci. Rep.*, 48(x):53–229.

[75] Duan, H., Wang, J., Huang, Z. P., and Karihaloo, B. L. (2005). Size-dependent effective elastic constants of solids containing nano-inhomogeneities with interface stress. *J. Mech. Phys. Solids*, 53:1574–1596.

[76] Dunne, G. V. (1999). Lecture notes on aspects of Chern-Simons theory.

[77] Dzyaloshinskii, I. E. (1958). A thermodynamic theory of "weak" ferromagnetism of antiferromagnetics. *J. Phys. Chem. Solids*, 4(241255).

[78] El-Batanouny, M. and Wooten, F. (2008). *Symmetry in Condensed Matter Physics: A Computational Approach*. Cambridge.

[79] Epstein, R. I. and Malloy, K. J. (2009). Electrocaloric devices based on thin-film heat switches. *J. Appl. Phys.*, 78(06509).

[80] Erdem, E. Semmelhack, H.-C., Böttcher, R., Rumpf, H., Banys, J., Matthes, A., Gl′asel, H.-J., Hirsch, D., and Hartmann, E. (2006). Study of the tetragonal-to-cubic phase transition in $PbTiO_3$ nanopowders. *J. Phys.: Cond. Matter.*, 18:3861–3874.

[81] Espinal, Y., Kesim, M. T., Misirlioglu, I. B., Trolier-McKinstry, S., Mantese, J. V., and Alpay, S. P. (2014). Pyroelectric and dielectric properties of ferroelectric films with interposed dielectric buffer layers. *Appl. Phys. Lett.*, 105(23):232905.

[82] Etier, M., Schmitz-Antoniak, C., Salamon, S., Trivedi, H., Gao, Y., Nazrabi, A., Landers, J., Gautam, D., Winterer, M., Schmitz, D., Wende, H., Shvartsman, V. V., and Lupascu, D. C. (2015). Magnetoelectric coupling on multiferroic cobalt ferrite–barium titanate ceramic composites with different connectivity schemes. *Acta Mater.*, 90:1–9.

[83] Fähler, S., Rößler, U. K., Kastner, O., Eckert, J., Eggeler, G., Emmerich, H., Entel, P., Müller, S., Quandt, E., and Albe, K. (2012). Caloric effects in ferroic materials: New concepts for cooling. *Adv. Engr. Mater.*, 14.

[84] Fedorov, F. (1968). *Theory of Elastic Waves in Crystals*. Plenum Press, New York.

[85] Fong, D. D. and Thompson, C. (2006). *In-situ* synchrotron x-ray studies of ferroelectric thin films. *Annu. Rev. Mater. Res.*, 36:431–465.

[86] Franco, V., Blázquez, J. S., Ingale, B., and Conde, A. (2012). The magnetocaloric effect and magnetic refridgeration near room temperature: materials and models. *Annu. Rev. Mater.*, 42:305–342.

[87] Fridkin, V. M. and Ducharme, S. (2001). General features of the intrinsic ferroelectric coercive field. *Phys. Solid State*, 43(7):1320 – 1324.

[88] Fried, E. and Gurtin, M. E. (1993). Continuum theory of thermally induced phase transitions based on an order parameter. *Physica D: Nonlinear phenomena*, 68:326–343.

[89] Fried, E. and Gurtin, M. E. (1994). Dynamic solid–solid transitions with phase characterized by an order parameter. *Physica D: Nonlinear phenomena*, 72:287–308.

[90] Fries, T. P. and Belytschko, T. (2006). The intrinsic XFEM: A method for arbitrary discontinuities without additional unknowns. *Int. J. Numer. Meth. Engr.*, 68:1358–1385.

[91] Frisch, M. J., Trucks, G. W., Schlegel, H. B., Scuseria, G. E., Robb, M. A., Cheeseman, J. R., Scalmani, G., Barone, V., Petersson, G. A., Nakatsuji, H., Li, X., Caricato, M., Marenich, A. V., Bloino, J., Janesko, B. G., Gomperts, R., Mennucci, B., Hratchian, H. P., Ortiz, J. V., Izmaylov, A. F., Sonnenberg, J. L., Williams-Young, D., Ding, F., Lipparini, F., Egidi, F., Goings, J., Peng, B., Petrone, A., Henderson, T., Ranasinghe, D., Zakrzewski, V. G., Gao, J., Rega, N., Zheng, G., Liang, W., Hada, M., Ehara, M., Toyota, K., Fukuda, R., Hasegawa, J., Ishida, M., Nakajima, T., Honda, Y., Kitao, O., Nakai, H.,

Vreven, T., Throssell, K., Montgomery, Jr., J. A., Peralta, J. E., Ogliaro, F., Bearpark, M. J., Heyd, J. J., Brothers, E. N., Kudin, K. N., Staroverov, V. N., Keith, T. A., Kobayashi, R., Normand, J., Raghavachari, K., Rendell, A. P., Burant, J. C., Iyengar, S. S., Tomasi, J., Cossi, M., Millam, J. M., Klene, M., Adamo, C., Cammi, R., Ochterski, J. W., Martin, R. L., Morokuma, K., Farkas, O., Foresman, J. B., and Fox, D. J. (2016). Gaussian~16 Revision A.03. Gaussian Inc. Wallingford CT.

[92] Fukuda, J. and Žumer, S. (2010). Quasi-two-dimensional Skyrmion lattices in a chiral nematic liquid crystal. *Nat. Commun.*, 2(246).

[93] Gao, P. X., Lao, C. S., Ding, Y., and Wang, Z. L. (2006). Metal/semiconductor core/shell nanodisks and nanotubes. *Adv. Funct. Mater.*, 16:53–62.

[94] Garaud, J., Carlstr$^{\acute{}}$om, J., Babaev, E., and Speight, M. (2013). Chiral $\mathbb{C}\mathbf{P}^2$ skyrmions in three-band superconductors. *Phys. Rev. B*, 87(014507).

[95] Gaston, D., Newman, C., Hansen, G., and Lebrun-Grandié, D. (2009). MOOSE: A parallel computational framework for coupled systems of nonlinear equations. *Nucl. Eng. Design*, 239:1768.

[96] Gelfand, I. M. and Fomin, S. V. (2000). *Calculus of Variations*. Dover Publications; Dover Books on Mathematics.

[97] Geng, W., Liu, Y., Meng, X., Bellaiche, L., Scott, J., Dkhil, B., and Jiang, A. (2015). Giant Negative Electrocaloric Effect in Antiferroelectric La-Doped Pb(ZrTi)O3 Thin Films Near Room Temperature. *Adv. Mater.*, 27:3165–3169.

[98] Giannozzi, P., Baroni, S., Bonini, N., Calandra, M., Car, R., Cavazzoni, C., Ceresoli, D., Chiarotti, G. L., Cococcioni, M., Dabo, I., Corso, A. D., de Gironcoli, S., Fabris, S., Fratesi, G., Gebauer, R., Gerstmann, U., Gougoussis, C., Kokalj, A., Lazzeri, M., Martin-Samos, L., Marzari, N., Mauri, F., Mazzarello, R., Paolini, S., Pasquarello, A., Paulatto, L., Sbraccia, C., Scandolo, S., Sclauzero, G., Seitsonen, A. P., Smogunov, A., Umari, P., and Wentzcovitch, R. M. (2009). QUANTUM ESPRESSO: a modular and open-source software project for quantum simulations of materials. *J. Phys. Cond. Matt.*, 21(39):395502.

[99] Ginzburg, V. (1949). *Zh. eksp. teor. Fiz.*, 19(36).

[100] Goldstone, J., Salam, A., and Weinberg, S. (1962). Broken symmetries. *Phys. Rev.*, 127(3):965–970.

[101] Goniakowski, J., Finocchi, F., and Noguera, C. (2008). Polarity of oxide surfaces and nanostructures. *Rep. Prog. Phys.*, 71(016501):1–50.

[102] Greene, L. E., Law, M., Yuhas, B. D., and Yang, P. (2007). ZnO-TiO_2 core-shell nanorod/P3HT solar cells. *J. Phys. Chem. C*, 111(50):18451–18456.

[103] Grindlay, J. (1970). *An introduction to the phenomenological theory of ferroelectricity*. Pergamon Press, Ltd.

[104] Grünebohm, A., Gruner, M. E., and Entel, P. (2012). Domain structure in the tetragonal phase of $BaTiO_3$ - from bulk to nanoparticles. *Ferroelectrics*, 426:21–30.

[105] Gruverman, A. Wu, D., Fan, H.-J., Vrejoiu, I., Alexe, M., Harrison, R. J., and Scott, J. F. (2008). Vortex ferroelectric domains. *J. Phys.: Condens. Matter*, 20:342201.

[106] Gu, H., Qian, X., Li, X., Craven, B., Zhu, W., Chen, A., Yao, S. C., and Zhang, Q. M. (2013). A chip scale electrocaloric effect based cooling device. *Appl. Phys. Lett*, 102(122904).

[107] Gu, Y., Li, M., Morozovska, A. N., Wang, Y., Eliseev, E. A., Gopalan, V., and Chen, L.-Q. (2014). Flexoelectricity and ferroelectric domain wall structures: Phase-field modeling and DFT calculations. *Phys. Rev. B.*, 89:174111.

[108] Guo, X., Deng, Y., Gu, D., Che, R., and Zhao, D. (2009). Synthesis and microwave absorption of uniform hematite nanoparticles and their core-shell mesoporous silica nanocomposites. *J. Mater. Chem.*, 19:6706–6712.

[109] Guo, Y., Afghah, S., Xiang, J., Lavrentovich, O. D., Selinger, R. L. B., and Wei, Q.-H. (2016). Cholesteric liquid crystals in rectangular microchannels: skyrmions and stripes. *Soft Mater.*, 12(6312).

[110] Gurtin, M. E. (1996). Generalized Ginzburg–Landau and Cahn–Hilliard equations based on a microforce balance. *Physica D: Nonlinear phenomena*, 92:178–192.

[111] Gurtin, M. E. and Ian Murdoch, A. (1975). A continuum theory of elastic material surfaces. *Arch. Ration. Mech. Anal.*, 57(4):291–323.

[112] Haeni, J. H., Theis, C. D., Schlom, D. G., Tian, W., Pan, X. Q., Chang, H., Takeuchi, I., and Xiang, X.-D. (2001). Epitaxial growth of the first five members of the $Sr_{n+1}Ti_nO_{3n+1}$ Ruddlesden–Popper homologous series. *Appl. Phys. Lett.*, 78(21):3292.

[113] Hafner, J. (2008). Ab-initio simulations of materials using VASP: Density-functional theory and beyond. *J. Comput. Chem.*, 29(13):2044–2078.

[114] Halperin, W. P. (1986). Quantum size effects in metal particles. *Rev. Mod. Phys.*, 58(3).

[115] Hao, Y., Wang, X., and Li, L. (2014). Highly dispersed $SrTiO_3$ nanocubes from a rapid sol-precipitation method. *Nanoscale*, 6(7940).

[116] Harada, J., Axe, J. D., and Shirane, G. (1971). Soft ferroelectric modes in lead titanate. *Phys. Rev. B*, 4(155).

[117] Heinonen, O. and Bozeman, S. P. (2006). Finite-element modeling and micromagnetic modeling of perpendicular writers. *J. Appl. Phys.*, 99(08S301).

[118] Herring, H. and Vogt, E. (1956). Transport and deformation-potential theory for many-valley semiconductors with anisotropic ccattering. *Phys. Rev.*, 105(1933).

[119] Hess, J. L. and Smith, A. M. O. (1967). Calculation of potential flow about arbitrary bodies. *Prog. Aero. Sci.*, 8:1–138.

[120] Hino, J., Yoshimura, T., and Konishi, K. (1984). A finite element method prediction of the vibration of a bridge subjected to a moving vehicle load. *J. Sound and Vibration*, 96(1):45–53.

[121] Hlinka, J. (2007). Mobility of ferroelastic domain walls in barium titanate. *Ferroelectrics*, 349:49 – 544.

[122] Hlinka, J. (2017). Manifestations of Bloch walls in perovskite ferroelectrics. Amer. Phys. Soc. (2017) March Meeting, New Orleans, LA.

[123] Hlinka, J. and Marton, P. (2006). Phenomenological model of a 90° domain wall in $BaTiO_3$-type ferroelectrics. *Phys. Rev. B.*, 74:104104.

[124] Hong, L. and Soh, A. K. (2011). Unique vortex and stripe domain structures in $PbTiO_3$ epitaxial nanodots. *Appl. Phys. Lett.*, 81:342–347.

[125] Hoshino, S., Mitsui, T., Jona, F., and Pepinsky, R. (1957). Dielectric and thermal study of tri-glycine sulfate and tri-glycine fluoberyllate. *Phys. Rev.*, 107(1255).

[126] Hsiao, I. L. and Huang, Y. J. (2011). Titanium oxide shell coatings decrease the cytotoxicity of ZnO nanoparticles. *Chem. Res. Toxicol.*, 24:303–313.

[127] Hu, D., Ma, H., Tanaka, Y., Zhao, L., and Feng, Q. (2015). Ferroelectric mesocrystalline $BaTiO_3/SrTiO_3$ nanocomposites with enhanced dielectric and piezoelectric properties. *Chem. Mater.*, 27:4983–4994.

[128] Hu, H.-L. and Chen, L.-Q. (1998). Three-dimensional computer simulations of ferroelectric domain formation. *J. Am. Ceram. Soc.*, 81(3):492–500.

[129] Hu, J. Q., Li, Q., Meng, X. M., Lee, C. S., and Lee, S. T. (2003). Thermal reduction route to the fabrication of coaxial Zn/ZnO nanocables and ZnO nanotubes. *Chem. Mater.*, 15:305–308.

[130] Huang, L., Jia, Z., Kymissis, I., and O'Brien, S. (2010). High K capacitors and OFET gate dielectrics from self-assembled $BaTiO_3$ and (Ba, Sr) TiO_3 nanocrystals in the superparaelectric limit. *Adv. Func. Mater.*, 20:554–560.

[131] Huber, J. E., Fleck, N. A., Landis, C. M., and McMeeking, R. M. (1999). A constitutive model for ferroelectric polycrystals. *J. Mec. Phys. Solids*, 47(8):1663–1697.

[132] Hubert, A. and Schäfer, R. (2000). *Magnetic Domains: The Analysis of Magnetic Microstructures*. Springer-Verlag Berlin Heidelberg.

[133] Hughes, T. J. R., Liu, W. K., and Brooks, A. (1979). Finite element analysis of incompressible viscous flows by the penalty function formulation. *J. Comp. Phys.*, 30(1):1–60.

[134] Ihlefeld, J. F., Harris, D. T., Keech, R., Jones, J. L., Maria, J.-P., and Trolier-McKinstry, S. (2016). Scaling effects in perovskite ferroelectrics: Fundamental limits and process-structure-property relations. *J. Am. Ceram. Soc.*, 99(8):2537–2557.

[135] Isaak, D. G., Carnes, J. D., Anderson, O. L., Cynn, H., and Hake, E. (1998). Elasticity of TiO 2 rutile to 1800 K. *Phys. Chem. Miner.*, 26(1):31–43.

[136] Jaafar, M., Yanes, R., Asenjo, A., Chubykalo-Fesenko, O., Vazquez, M., Gonzalez, E. M., and Vicent, J. L. (2008). Field induced vortex dynamics in magnetic Ni nanotriangles. *Nanotechnology*, 19.

[137] Jackson, J. D. (1998). *Classical Electrodynamics, 3rd Edition*. Wiley.

[138] Jain, A., Ong, S. P., Hautier, G., Chen, W., Richards, W. D., Dacek, S., Cholia, S., Gunter, D., Skinner, D., Ceder, G., and Persson, K. A. (2013). The materials project: A materials genome approach to accelerating materials innovation. *APL Materials*, 1(1)(011002).

[139] Jaiswal, J. K., Mattoussi, H., Mauro, J. M., and Simon, S. M. (2003). Long-term multiple color imaging of live cells using quantum dot bioconjugates. *Nat. Biotechnol.*, 21:47–51.

[140] Jia, L., Shu, D.-J., and Wang, M. (2012). Tuning the area percentage of reactive surface of TiO_2 by strain engineering. *Phys. Rev. Lett.*, 109(15):156104.

[141] Jiang, W., Upadhyaya, P., Zhang, W., Yu, G., Jungfleisch, M. B., Fradin, F. Y., Pearson, J. E., Tserkovnyak, Y., Wang, K. L., Heinonen, O., te Velthuis, S. G. E., and Hoffmann, A. (2015). Blowing magnetic skyrmion bubbles. *Science*, 349.

[142] Johann, F., Morelli, A., and Vrejoiu, I. (2012). Stability of 71° stripe domains in epitaxial $BiFeO_3$ films upon repeated electrical switching. *Phys. Status Solidi B*, 249(11):2278–2286.

[143] Jokisaari, A. (2016). *Multiphysics phase field modeling of hydrogen diffusion and δ-hydride precipitation in α-zirconium*. PhD dissertation, University of Michigan.

[144] Jokisaari, A. M. and Thornton, K. (2015). General method for incorporating CALPHAD free energies of mixing into phase field models: Application to the α-zirconium/δ-hydride system. *Calphad*, 51:334–343.

[145] Jokisaari, A. M., Voorhees, P. W., Guyer, J. E., Warren, J., and Heinonen, O. G. (2017). Benchmark problems for numerical implementations of phase field models. *Comp. Mater. Sci.*, 126:139–151.

[146] Jona, F. and Shirane, G. (1993). *Ferroelectric Crystals*. Dover Publications, Inc.

[147] Jou, D., Casas-Vázquez, and Lebon, G. (2001). *Extended Irreversible Thermodynamics*. Springer-Verlag Berlin Heidelberg.

[148] Kamat, P. V. and Shanghavi, B. (1997). Interparticle electron transfer in metal/semiconductor composites. Picosecond dynamics of CdS-capped gold nanoclusters. *J. Phys. Chem. B*, 101,39:7675–7679.

[149] Karthik, J. and Martin, L. W. (2011). Pyroelectric properties of polydomain epitaxial $Pb(Zr_{1-x}Ti_x)O_3$ thin films. *Phys. Rev. B*, 84(024102).

[150] Katzir, S. (2012). Who knew piezoelectricity? Rutherford and Langevin on submarine detection and the invention of sonar. *Notes Rec. R. Soc.*, (0035-9149).

[151] Kenway, G. K. W. and Martins, J. (2014). Multipoint high-fidelity aerostructural optimization of a transport aircraft configuration. *J. Aircraft*, 51(1):144–160.

[152] Kesim, M. T., Cole, M. W., Zhang, J., Misirlioglu, I. B., and Alpay, S. P. (2014). Tailoring dielectric properties of ferroelectric-dielectric multilayers. *Appl. Phys. Lett.*, 104(2):022901.

[153] Khassaf, H., Khakpash, N., Vijayan, S., Aindow, M., and Alpay, S. (2016). Electrostatically driven dielectric anomaly in mesoscopic ferroelectric-paraelectric bilayers. *Acta Mater.*, 105:68 – 74.

[154] Khawaja, U. and Stoof, H. (2001). Skyrmions in a ferromagnetic Bose-Einstein condensates. *Nature*, 411:918–920.

[155] Kim, H. W., Shim, S. H., and Lee, J. W. (2008). Variation of ZnO shell thickness and its effects on the characteristics of coaxial nanowires. *Nanotechnology*, 19:145601.

[156] Kim, Y., Kook, K., Hwang, S. K., Park, C., and Cho, J. (2014). Polymer/perovskite-type nanoparticle multilayers with multielectric properties prepared from ligand addition-induced layer-by-layer assembly. *ACS. Nano.*, 8(3):2419–2430.

[157] Kim, Y.-T., Provatas, N., Goldenfeld, N., and Dantzig, J. (1999). Universal dynamics of phase-field models for dendtritic growth. *Phys. Rev. E*, 59(3).

[158] Kirk, B. S., Peterson, J. W., Stogner, R. H., and Carey, G. F. (2006). libmesh: A c++ library for parallel adaptive mesh refinement/coarsening simulations. *Eng. with Comp.*, 22(3-4):237–254.

[159] Kittel, C. (1946). Theory of the structure of ferromagnetic domains in films and small particles. *Phys. Rev.*, 70:965–971.

[160] Knigavko, A. and Rosenstein, B. (1999). Magnetic skyrmion lattices in heavy-fermion superconductor UPt_3. *Phys. Rev. Lett.*, 82(1261).

[161] Knoll, D. A. and Keyes, D. E. (2010). Jacobian-free Newton-Krylov methods: a survey of approaches and applications. *J. Comp. Phys.*, 193:357–397.

[162] Kolodiazhnyi, T., Petric, A., Niewczas, M., Bridges, C., Safa-Sefat, A., and Greedan, J. E. (2003). Thermoelectric, Hall effect, and mobility of *n*-type $BaTiO_3$. *Phys. Rev. B*, 68.

[163] Kong, X. Y., Ding, Y., and Wang, Z. L. (2004). Metal/semiconductor Zn/ZnO core/shell nanobelts and nanotubes. *J. Phys. Chem. B*, 108(2):570–574.

[164] Kornev, I., Fu, H., and Bellaiche, L. (2004). Ultrathin films of ferroelectric solid solutions under a residual depolarizing field. *Phys. Rev. Lett.*, 93(19):196104.

[165] Krause, A. R., Neste, C. V., Senesac, T., Thundrat, T., and Finot, E. (2008). Trace explosive detection using photothermal deflection spectroscopy. *J. Appl. Phys.*, 103(094906).

[166] Landau, L. (1935). . *Phys. Z. Sowjetunion (in Russian)*, 8(153).

[167] Landau, L. and Khalatnikov, I. (1965). *On the theory of superconductivity*. Collected Papers of L.D. Landau, (ed. D. Ter Haar), Pergamon, Oxford.

[168] Landau, L. and Lifshitz, E. M. (1959). *Theory of Elasticity*. Pergamon Press, Inc.

[169] Lang, S. B. (1999). *Ferroelectrics*, 230:99–108.

[170] Law, M., Greene, L. E., Radenovic, A., Kuykendall, T., Liphardt, J., and Yang, P. (2006). ZnO-Al_2O_3 and ZnO-TiO_2 core-shell nanowire dye-sensitized solar cells. *J. Phys. Chem.*, 101:22652–22663.

[171] Ledbetter, H. M. (1977). Elastic properties of zinc: A compilation and a review. *J. Phys. Chem. Ref. Data*, 6(4):1181–1203.

[172] Lee, B., Nakhmanson, S. M., and Heinonen, O. (2014). Strain induced vortex-to-uniform polarization transitions in soft-ferroelectric nanoparticles. *Appl. Phys. Lett.*, 104(26):262906.

[173] Lee, D., Behera, R. K., Wu, P., Xu, H., Sinnott, S. B., Phillpot, S. R., Chen, L.-Q., and Gopalan, V. (2009). Mixed bloch-néel-ising character of 180° ferroelectric domain walls. *Phys. Rev. B*, 80(060102(R)).

[174] Lee, D., Yang, S. M., Kim, T. H., Jeon, B. C., Kim, Y. S., Yoon, J.-G., Lee, H. N., Baek, S. H., Eom, C. B., and Noh, T. W. (2012). Multilevel data storage memory using deterministic polarization control. *Adv. Mater.*, 24(3):402–406.

[175] Lee, D.-H. and Kane, C. L. (1990). Boson-vortex-Skyrmion duality, spin-singlet fractional quantum Hall effect and spin-1/2 anyon superconductivity. *Phys. Rev. Lett.*, 64(1313).

[176] Leslie, L. S., Hansen, A., Wright, K. C., Deustch, B. M., and Bigelow, N. P. (2009). Creation and detection of skyrmions in a Bose-Einstein condensate. *Phys. Rev. Lett.*, 103(250401).

[177] Levanyuk, A. P. and Blinc, R. (2013). Ferroelectric phase transitions in small particles and local regions. *Phys. Rev. Lett.*, 11:097601.

[178] Li, B., Habbal, F., and Ortiz, M. (2010a). Optimal transportation meshfree approximation schemes for fluid and plastic flows. *Int. J. Numer. Meth. Engr.*, 83(12):1541.

[179] Li, B., Ren, W. J., Wang, X. W., Meng, H., Liu, X. G., Wang, Z. J., and Zhang, Z. D. (2010b). Intrinsic electrocaloric effects in ferroelectric poly(vinylidene fluoride-trifluoroethylene) copolymers: Roles of order of phase transition and stresses. *Appl. Phys. Lett.*, 96.

[180] Li, B., Wang, J. B., Zhong, X. L., Wang, F., Zeng, Y. K., and Zhou, Y. C. (2013a). Giant electrocaloric effects in ferroelectric nanostructures with vortex domain structures. *RSC Adv.*, 3(21):7928.

[181] Li, B., Wang, J. B., Zhong, X. L., Wang, F., Zeng, Y. K., and Zhou, Y. C. (2013b). The coexistence of the negative and positive electrocaloric effect in ferroelectric thin films for solid-state refrigeration. *Europhys. Lett.*, 102(47004).

[182] Li, X., He, G., Xiao, G., Liu, H., and Wang, M. (2009). Synthesis and morphology control of ZnO nanostructures in microemulsions. *J. Colloid Interface Sci.*, 333:465–473.

[183] Li, X., Niitsoo, O., and Couzis, A. (2016). Electrostatically assisted fabrication of silver-dielectric core/shell nanoparticles thinfilm capacitor with uniform metal nanoparticle distribution and controlled spacing. *J. Coll. Interface Sci.*, 465:333–341.

[184] Li, Y., Hu, S., Liu, Z., and Chen, L. (2002a). Effect of substrate constraint on the stability and evolution of ferroelectric domain structures in thin films. *Acta Mater.*, 50(2):395 – 411.

[185] Li, Y. L. and Chen, L.-Q. (2006). Temperature-strain phase diagram for $BaTiO_3$ thin films. *Appl. Phys. Lett.*, 88.

[186] Li, Y. L., Choudhury, S., Haeni, J. H., and Chen, L.-Q. (2006). Phase transitions and domain structures in strained pseudocubic $(100)SrTiO_3$ thin films. *Phys. Rev. B.*, 73.

[187] Li, Y. L., Cross, L. E., and Chen, L.-Q. (2005). A phenomenological thermodynamic potential for $BaTiO_3$ single crystals. *J. Appl. Phys.*, 98(064101).

[188] Li, Y. L., Hu, S. Y., Liu, Z. K., and Chen, L.-Q. (2001). Phase-field model of domain structures in ferroelectric thin films. *Appl. Phys. Lett.*, 78:24.

[189] Li, Y. L., Hu, S. Y., Liu, Z. K., and Chen, L.-Q. (2002b). Effect of electrical boundary conditions on ferroelectric domain structures in thin films. *Appl. Phys. Lett.*, 81:3.

[190] Liao, D. L., Badour, C. a., and Liao, B. Q. (2008). Preparation of nanosized TiO_2/ZnO composite catalyst and its photocatalytic activity for degradation of methyl orange. *J. Photochem. Photobiol. A Chem.*, 194:11–19.

[191] Liao, M.-H., Hsu, C.-H., and Chen, D.-H. (2006). Preparation and properties of amorphous titania-coated zinc oxide nanoparticles. *J. Solid State Chem.*, 179:2020–2026.

[192] Lim, C. S. (2010). Processing research synthesis and characterization of TiO_2-ZnO nanocomposite by a two-step chemical method. *J. Ceram. Process. Res.*, 11(5):631–635.

[193] Lin, H., Huang, C. P., Li, W., Ni, C., Shah, S. I., and Tseng, Y. H. (2006). Size dependency of nanocrystalline TiO_2 on its optical property and photocatalytic reactivity exemplified by 2-chlorophenol. *Appl. Catal. B Environ.*, 68:1–11.

[194] Lin, Y.-H. and Trethewey, M. W. (1990). Finite element analysis of elastic beams subjected to moving dynamic loads. *J. Sound and Vibration*, 136(2):323–343.

[195] Lines, M. E. and Glass, A. M. (1977). *Principles and Applications of Ferroelectrics and Related Materials*. Clarendon Press Oxford.

[196] Liu, G. R. (2003). *Meshfree methods: moving beyond the finite element method*. CRC Press, LLC.

[197] Liu, H., Ding, Y., Somyazulu, M., Qian, J., Shu, J., Häusermann, D., and Mao, H. (2005). Rietveld refinement study of the pressure dependence of the internal structural parameter *u* in the wurtzite phase of ZnO. *Phys. Rev. B*, 71(212103).

[198] Lu, B., Li, P., Tang, Z., Yao, Y., Gao, X., Kleemann, W., and Lu, S.-G. (2011). Large electrocaloric effect in relaxor ferroelectric and antiferroelectric lanthanum doped lead zirconate titanate ceramics. *Sci. Rep.*, 7(45335).

[199] Lu, Y., Yin, Y., Li, Z.-Y., and Xia, Y. (2002). Synthesis and Self-Assembly of Au@SiO_2 Core-Shell Colloids. *Nano Lett.*, 2:785–788.

[200] Lupan, O., Chow, L., Chai, G., and Heinrich, H. (2008). Fabrication and characterization of Zn-ZnO core-shell microspheres from nanorods. *Chem. Phys. Lett.*, 465(4-6):249–253.

[201] Ma, Q., Xiong, R., Zhai, B., and Huang, Y. M. (2013). Core-shelled Zn/ZnO microspheres synthesized by ultrasonic irradiation for photocatalytic applications. *Micro and Nano Letters*, 8:491–495.

[202] Ma, Y.-B., Albe, K., and Xu, B.-X. (2015). Lattice-based Monte Carlo simulations of the electrocaloric effect in ferroelectrics and relaxor ferroelectrics. *Phys. Rev. B*, 91(184108).

[203] Ma, J. and Hu, J. and Li, Z. and Nan, C. W. (2011). Recent progress in multiferroic magnetoelectric composites: from bulk to thin films. *Adv. Mater.*, 23(9).

[204] Mañosa, L., González-Alonso, D., Planes, A., Bonnot, E., Barrio, M., Tamarit, J.-L., Aksoy, S., and Acet, M. (2010). Giant solid-state barocaloric effect in the Ni-Mn-In magnetic shape-memory alloy. *Nat. Mater.*, 9:478–481.

[205] Mañosa, L., Planes, A., Vives, E., Bonnot, E., and Romero, R. (2009). The use of shape-memory alloys for mechanical refrigeration. *Func. Mater. Lett.*, 2(2).

[206] Maksymovych, P., Morozovska, A. N., Yu, P., Eliseev, E. A., Chu, Y.-H., Ramesh, R., Baddorf, A. P., and Kalinin, S. V. (2012). Domain wall conductivity in La-doped $BiFeO_3$. *Nano. Lett.*, 12(1):209–213.

[207] Mangalam, R. V. K., Karthik, J., Damodaran, A. R., Agar, J. C., and Martin, L. W. (2013a). Improved pyroelectric figures of merit in compositionally graded $PbZr_{1-x}Ti_xO_3$ thin films. *ACS Appl. Mater. Interfaces*, 5:13235–13241.

[208] Mangalam, R. V. K., Karthik, J., Damodaran, A. R., Agar, J. C., and Martin, L. W. (2013b). Unexpected crystal and domain structures and properties in compositionally graded $PbZr_{1-x}Ti_xO_3$ thin films. *Adv. Mater.*, 25:1761–1767.

[209] Mangeri, J., Espinal, Y., Jokisaari, A., Alpay, S. P., Nakhmanson, S., and Heinonen, O. (2017). Topological phase transformations and intrinsic size effects in ferroelectric nanoparticles. *Nanoscale*, 9(4):1616–1624.

[210] Mangeri, J., Heinonen, O., Karpeyev, D., and Nakhmanson, S. (2015). Influence of elastic and surface strains on the optical properties of semiconducting core-shell nanoparticles. *Phys. Rev. Appl.*, 4:014001.

[211] Mangeri, J., Pitike, K. C., Alpay, S. P., and Nakhmanson, S. (2016). Amplitudon and phason modes of electrocaloric energy interconversion. *npj Comp. Mater.*, 2:16020.

[212] Maradudin, A. A. (1971). *Theory of Lattice Dynamics in the Harmonic Approximation*. Academic Press, New York.

[213] Marathe, M., Grünebohm, A., Nishimatsu, T., Entel, P., and Ederer, C. (2016). First-principles-based calculation of the electrocaloric effect in $BaTiO_3$: A comparison of direct and indirect methods. *Phys. Rev. B*, 93(054110).

[214] Marcì, G., Augugliaro, V., López-Muñoz, M. J., Martín, C., Palmisano, L., Rives, V., Schiavello, M., Tilley, R. J. D., and Venezia, A. M. (2001). Preparation characterization and photocatalytic activity of polycrystalline ZnO/TiO_2 systems. 2. Surface, bulk characterization, and 4-nitrophenol photodegradation in liquid/solid regime. *J. Phys. Chem. B*, 105(5):1033–1040.

[215] Martelli, P.-W., Mefire, S., and Luk'Yanchuk, I. A. (2015). Multidomain switching in ferroelectric nanodots. *Euro. Phys. Lett.*, 111:50001.

[216] Martin, L. and Rappe, A. M. (2016). Thin-film ferroelectric materials and their applications. *Nat. Rev. Mater.*, 1:16087.

[217] Marton, P., Klíč, A., Paściak, M., and Hlinka, J. (2017). First-principles based Landau-Devonshire potential for $BiFeO_3$. *ArXiv e-prints*.

[218] Matthias, B. T., Miller, C. E., and Remeika, J. P. (1956). Ferroelectricity of glycine sulfate. *Phys. Rev.*, 104(849).

[219] Maurya, D., Sun, F.-C., Alpay, S. P., and Priya, S. (2015). A new method for achieving enhanced dielectric response over a Wide temperature range. *Sci. Rep.*, 5:15144.

[220] McQuaid, R. G. P. and Gruverman, A. and Scott, J. F. and Gregg, J. M. (2014). Exploring vertex interactions in ferroelectric flux-closure domains. *Nanoletters*, 14:4230–4237.

[221] Meier, D., Seidel, J., Cano, A., Delaney, K., Kumagai, Y., Mostovoy, M., Spaldin, N. A., Ramesh, R., and Fiebig, M. (2012). Anisotropic conductance at improper ferroelectric domain walls. *Nat. Mater.*, 11:284–288.

[222] Melenk, J. M. (2002). *hp-Finite Element Methods for Singular Perturbations*. Springer.

[223] Meng, Q., Han, M.-G., Tao, J., Xu, G., Welch, D. O., and Zhu, Y. (2015). Velocity of domain-wall motion during polarization reversal in ferroelectric thin films: Beyond Merz's law. *Phys. Rev. B*, 91:054104.

[224] Merz, W. J. (1949). The electric and optical behavior of $BaTiO_3$, single-domain crystals. *Phys. Rev.*, 76(8).

[225] Michalet, X., Pinaud, F., Bentolila, L. A., Tsay, J. M., Doose, S., Li, J., Sundaresan, G., Wu, A. M., Gambhir, S. S., and Weiss, S. (2005). Quantum dots for live cells, in vivo imaging, and diagnostics. *Science*, 307:538–544.

[226] Mischenko, A. S., Zhang, Q., Scott, J. F., Whatmore, R. W., and Mathur, N. D. (2006). Giant electrocaloric effect in thin-film $PbZr_{0.95}Ti_{0.05}O_3$. *Science*, 311(5765):1270–1271.

[227] Mo$^{'}$es, N., Dolbow, J., and Belytschko, T. (1999). A finite element method for crack growth without remeshing. *Int. J. Numer. Meth. Engr.*, 46(1):131–150.

[228] Mohanty, D., Chaubey, G. S., Yourdkhani, A., Adireddy, S., and Caruntu, G. (2012). Synthesis and piezoelectric response of cubic and spherical $LiNbO_3$ nanocrystals. *RSC Advances*, 2:1913–1916.

[229] Mokrý, P. and Sluka, T. (2016). Identification of defect distribution at ferroelectric domain walls from evolution of nonlinear dielectric response during the aging process. *Phys. Rev. B.*, 93(064114).

[230] Moriya, T. (1960). Anisotropic superexchange interaction and weak ferromagnetism. *Phys. Rev.*, 120(9198).

[231] Moya, X., Kar-Narayan, S., and Mathur, N. (2014). Caloric materials near ferroic phase transitions. *Nat. Mater.*, 13:439–450.

[232] Mühlbauer, S., Binz, B., Jonietz, F., Pfleiderer, C., Rosch, A., Neubauer, A., Georgii, R., and B$^{'}$onil (2009). Skyrmion Lattice in a Chiral Magnet. *Science*, 323(5916):915–919.

[233] Müller, K. A. and Berlinger, W. (1986). Microscopic probing of order-disorder versus displacive behavior in $BaTi0_3$ by Fe^{3+} EPR. *Phys. Rev. B.*, 34.

[234] Müller, K. A. and Burkard, H. (1979). $SrTiO_3$: An intrinsic quantum paraelectric below 4 K. *Phys. Rev. B*, 19:7.

[235] Muševič, I., Blinc, R., and Žekš, B. (2000). *The Physics of Ferroelectric and Antiferroelectric Liquid Crystals*. World Scientific, Singapore.

[236] Nahas, Y., Prokhorenko, S., Louis, L., Gui, Z., Kornev, I., and Bellaiche, L. (2015). Discovery of stable skyrmionic state in ferroelectric nanocomposites. *Nature Comm.*, 6:8542.

[237] Nakahashi, K. and Deiwert, G. S. (1987). Self-adaptive-grid method with application to airfoil flow. *AIAA Journ.*, 25(4):513–520.

[238] Nakhmanson, S. and Drabold, D. A. (2000). Low-temperature anomalous specific heat without tunneling modes: A simulation for a-Si with voids. *Phys. Rev. B*, 61:5376–5380.

[239] Nakhmanson, S. M. and Naumov, I. (2010). Goldstone-like states in a layered perovskite with frustrated polarization: A first-principles Investigation of $PbSr_2Ti_2O_7$. *Phys. Rev. Lett.*, 104:097601.

[240] Naumov, I., Bellaiche, L., and Fu, H. (2004). Unusual phase transitions in ferroelectric nanodisks and nanorods. *Nature*, 432:737–740.

[241] Naumov, I. and Bratkovsky, A. M. (2008). Unusual polarization patterns in flat epitaxial ferroelectric nanoparticles. *Phys. Rev. Lett.*, 101:107601.

[242] Newnham, R. E. (2005). *Properties of Materials: Anisotropy, Symmetry, Structure*. Oxford University Press.

[243] Ng, N., Ahluwalia, R., and Srolovitz, D. J. (2012). Domain patterns in free-standing nanoferroelectrics. *Acta. Mater.*, 60:3632–3642.

[244] Niu, H., Dizhang, Meng, Z., and Cai, Y. (2012). Fast defluorination and removal of norfloxacin by alginate/Fe@Fe_3O_4 core/shell structured nanoparticles. *J. Hazard. Mater.*, 227-228:195–203.

[245] Nye, J. F. (1985). *Physical Properties of Crystals*. Oxford University Press Inc.

[246] O'Brien, S., Brus, L., and Murray, C. B. (2001). Synthesis of monodisperse nanoparticles of barium titanate: Toward a generalized strategy of oxide nanoparticle synthesis. *J. Am. Ceram. Soc.*, 123:12085–12086.

[247] Oganesyan, L. (1963). Numerical calculation of slabs. *Engr. Sol. Elec. Comp.*, 1:85–97.

[248] Ostfeld, A. E. and Arias, A. C. (2017). Flexible photovoltaic power systems: integration opportunities, challenges and advances. *Flex. and Printed Elect.*, 2(1):13001.

[249] Pabst, W. and Gregorova, E. (2013). Elastic properties of silica polymorphs – a review. *Ceramics*, 57:(3) 167–184.

[250] Paniagua, S. A., Kim, Y., Henry, K., Kumar, R., Perry, J. W., and Marder, S. R. (2014). Surface-initiated polymerization from barium titanate nanoparticles for hybrid dielectric capacitors. *ACS. Appl. Mater. Interfaces*, 6:3477–3482.

[251] Peng, B., Fan, H., and Zhang, Q. (2013). A giant electrocaloric effect in nanoscale antiferroelectric and ferroelectric phase coexisting in a relaxor $Pb_{0.8}Ba_{0.2}ZrO_3$ thin film at room temperature. *Adv. Mater.*, 23:2987–2992.

[252] Perdew, J. P. and Zunger, A. (1982). Self-interaction correction to density-functional approximations for many-electron sys- tems. *Phys. Rev. B.*, 23:5048–5079.

[253] Pertsev, N. A., Zembilgotov, A. G., and Tagantsev, A. K. (1998). Effect of mechanical boundary conditions on phase diagrams of epitaxial ferroelectric thin films. *Phys. Rev. Lett.*, 80:9.

[254] Pirc, R., Rožič, B., Koruza, J., Malic, B., and Kutnjak, Z. (2014). Negative electrocaloric effect in antiferroelectric PbZrO3. *Europhys. Lett.*, 107.

[255] Pirc, R., Zutnjak, Z., Blinc, R., and Zhang, Q. M. (2011). Upper bounds on the electrocaloric effect in polar solids. *Appl. Phys. Lett.*, 98.

[256] Plimpton, S. (1995). Fast parallel algorithms for short–range molecular dynamics. *J. Comp. Phys.*, 117:1–19.

[257] Polking, M. J., Han, M.-G., Yourdkhani, A., Petkov, V., Kisielowski, C. F., Volkov, V. V., Zhu, Y., Caruntu, G., Alivisatos, A. P., and Ramesh, R. (2012). Ferroelectric order in individual nanometre- scale crystals. *Nat. Mater.*, 11:700–709.

[258] Ponomareva, I. and Lisenkov, S. (2012). Bridging the macroscopic and atomistic descriptions of the electrocaloric effect. *Phys. Rev. Lett.*, 108(167604).

[259] Press, W. H., Teukolsky, S. A., Vetterling, W. T., and Flannery, B. P. (2007). *Numerical Recipes: The Art of Scientific Computing*. Cambridge University Press.

[260] Presser, V. and Dennison, C. R. and Campos, J. and Knehr, K. W. and Kumbur, E. C., and Gogotsi, Y. (2012). The electrochemical flow capacitor: a new concept for rapid energy storage and recovery. *Adv. Energy Mater.*, 2(7):895–902.

[261] Prosandeev, S. and Bellaiche, L. (2007). Influence of crystallographic steps on properties of ferroelectric ultrathin films: An *ab initio* study. *Appl. Phys. Lett.*, 91:072901.

[262] Pryor, R. W. (2009). *Multiphysics Modeling Using COMSOL: A First Principles Approach*. Jones and Bartlett Publishers, Inc.

[263] Puricea, A., Dinescua, G., Scarisoreanua, N., Verardib, P., Craciunc, F., and Galassid, C. (2006). Ferroelectric thin films obtained by pulsed laser deposition. *J. Euro. Ceram. Soc.*, 26(14):2937–2943.

[264] Qiu, Q. Y., Nagarajan, V., and Alpay, S. P. (2008). Film thickness versus misfit strain phase diagrams for epitaxial $PbTiO_3$ ultrathin ferroelectric films. *Phys. Rev. B*, 78(064117).

[265] Raabe, J., Quitmann, C., Back, C. H., Nolting, F., Johnson, S., and Buehler, C. (2005). Quantitative analysis of magnetic excitations in Landau flux-closure structures using synchrotron-radiation microscopy. *Phys. Rev. Lett.*, 94:217204.

[266] Ren, Y., Ascienzo, D., and Ouyang, J. (2017). Nonlinear optical detection of mixed phases in $Ba(Zr,Ti)O_3$ films. Amer. Phys. Soc. (2017) March Meeting, New Orleans, LA.

[267] Ruddlesden, S. N. and Popper, P. (1957). New compounds of the K_2NIF_4 type. *Acta Cryst.*, 10:538–539.

[268] Rüdiger, A., Schneller, T., Roelofs, A., Tiedke, S., Schmitz, T., and Waser, R. (2005). Nanosize ferroelectric oxides - tracking down the superparaelectric limit. *Appl. Phys. A.*, 80:1247–1255.

[269] Saad, Y. (2003). *Iterative Methods for Sparse Linear Systems, Second Edition*. Soc. Ind. Appl. Math.

[270] Saad, Y. and Schultz, M. (1986). GMRES: A generalized minimal residual algorithm for solving nonsymmetric linear systems. *J. Sci. Stat. Comp.*, 7:856–869.

[271] Saito, T., Adachi, H., Wada, T., and Adachi, H. (2005). Pulsed-Laser Deposition of Ferroelectric $NaNbO_3$ Thin Films. *Jap. J. Appl. Phys.*, 44(9B).

[272] Sandhu, R. S., Liu, H., and Singh, K. J. (1977). Numerical performance of some finite element schemes for analysis of seepage in porouos elastic media. *Internat. J. Anal. Methods Geomech.*, 1:177–194.

[273] Schlom, D. G., Chen, L.-Q., Eom, C.-B., Rabe, K. M., Streiffer, S. K., and Triscone, J.-M. (2007). Strain tuning of ferroelectric thin films. *Annu. Rev. Mater. Res.*, 37:589–626.

[274] Schmidt, A. (1996). Computation of three dimensional dendrites with finite elements. *J. Comp. Phys.*, 125(2):293 – 312.

[275] Scholz, W., Fidler, J., Schrefl, T., Suess, D., Dittrich, R., Forster, H., and Tsiantos, V. (2003). Scalable parallel micromagnetic solvers for magnetic nanostructures. *Comp. Mat. Sci.*, 28:366–383.

[276] Schwab, C. (1998). *p- and hp- Finite Element Methods: Theory and Applications in Solid and Fluid Mechanics*. Oxford University Press, 1998.

[277] Scott, J. F. (1974). Soft-mode spectroscopy. Experimental studies of structural phase transitions. *Rev. Mod. Phys.*, 46(1).

[278] Scott, J. F. and Paz de Araujo, C. A. (1989). Ferroelectric memories. *Science*, 246:1400–1405.

[279] Scrymgeour, D. A., Gopalan, V., Itagi, A., Saxena, A., and Swart, P. J. (2005). Phenomenological theory of a single domain wall in uniaxial trigonal ferroelectrics. *Phys. Rev. B*, 71(184110).

[280] Seidel, J., Maksymovych, P., Batra, Y., Katan, A., Yang, S.-Y., He, Q., Baddorf, P., Kalinin, S. V., Yang, C.-H., Yang, J.-C., Chu, Y.-H., Salje, E. K. H., Wormeester, H., Salmeron, M., and Ramesh, R. (2010). Domain wall conductivity in La-doped $BiFeO_3$. *Phys. Rev. Lett.*, 105(197603).

[281] Seidel, J., Martin, L. W., He, Q., Zhan, Q., Chu, Y. H., Rother, A., Hawkridge, M. E., Maksymovych, P., Yu, P., Gajek, M., Balke, N., Kalinin, S. V., Gemming, S., Wang, F., Catalan, G., Scott, J. F., Spaldin, N. A., Orenstein, J., and Ramesh, R. (2009). Conduction at domain Walls in oxide multiferroics. *Nat. Mater.*, 8(3):229–234.

[282] Shapiro, S. M., Axe, J. D., Shirane, G., and Riste, T. (1972). Critical neutron scattering in $SrTiO_3$ and $KMnF_3$. *Phys. Rev. B*, 6(11).

[283] Sharma, P., Ganti, S., and Bhate, N. (2003). Effect of surfaces on the size-dependent elastic state of nano-inhomogeneities. *Appl. Phys. Lett.*, 82(4).

[284] Shaw, T. M., Trolier-McKinstry, S., and McIntyre, P. C. (2000). The properties of ferroelectric films at small dimensions. *Annu. Rev. Mater. Sci.*, 30(1):263–298.

[285] Shen, J., Cong, J., Shang, D., Chai, Y., Shen, S., Zhai, K., and Sun, Y. (2016). A multilevel nonvolatile magnetoelectric memory. *Sci. Rep.*, 6(34473).

[286] Shirane, G. (1974). Neutron scattering studies of structural phase transitions at Brookhaven. *Rev. Mod. Phys.*, 46(3).

[287] Skulski, R. (1999). Superparaelectric behaviours of relaxor ferroelectrics. *Mater. Sci. Eng.*, B64:39–43.

[288] Slater, J. C. (1950). The Lorentz correction in barium titanate. *Phys. Rev.*, 78(748).

[289] Son, J. Y., Song, S., Lee, J.-H., and Jang, H. M. (2016). Anomalous domain periodicity observed in ferroelectric $PbTiO_3$ nanodots having 180° stripe domains. *Sci. Rep.*, 6(26644).

[290] South, J., Hafez, M., and Murman, E. (1979). Artificial compressibility methods for numerical solutions of transonic full potential equation. *AIAA Journ.*, 17(8):838–844.

[291] Stepkova, V. and Hlinka, J. (2017). On the possible internal structure of the ferroelectric Ising lines in BaTiO3. *Phase Trans.*, 90(1):1116.

[292] Su, Y. and Landis, C. (2007). Continuum thermodynamics of ferroelectric domain evolution: Theory, finite element implementation, and application to domain wall pinning. *J. Mec. Phys. Solids*, 55:280 – 305.

[293] Szilágyi, B. and Lindblom, L. and Scheel, M. A. (2009). Simulations of binary black hole mergers using spectral methods. *Phys. Rev. D*, 80.

[294] Takeuchi, I. and Sandeman, K. (2015). Solid-state cooling with caloric materials. *Physics Today*, 68.

[295] Tanaka, M., Hironaka, K., and Onodera, A. (2002). Thermal behavior of ferroelectric switching properties of SBT thin films. *Ferroelectrics*, 266(396):103–110.

[296] Tang, D.-M., Liu, G., Li, F., Tan, J., Liu, C., Lu, G. Q., and Cheng, H.-m. (2009). Synthesis and photoelectrochemical property of Urchin-like Zn/ZnO core/shell structures. *J. Phys. Chem. C*, 113:11035–11040.

[297] Tonks, M. R., Gaston, D., Millett, P. C., and Andrs, D. (2012). An object-oriented finite element framework for multiphysics phase field simulations. *Comp. Mater. Sci.*, 51:20–29.

[298] Truesdell, C. (1969). *Rational Thermodynamics*. McGraw-Hill Book Company.

[299] Vaidya, S., Patra, A., and Ganguli, A. K. (2010). Cds@TiO_2 and ZnS@TiO_2 core-shell nanocomposites: Synthesis and optical properties. *Colloids Surf., A*, 363:130–134.

[300] Valasek, J. (1922). Properties of Rochelle salt related to the piezo-electric effect. *Phys. Rev.*, 20:639 – 664.

[301] Vanderbilt, D. (1990). Soft self-consistent pseudopotentials in a generalized eigenvalue formalism. *Phys. Rev. B*, 41(11):7892–7895.

[302] Voight, W. (1910). *Lehrbuch der kristallphysik*. Verlag B.G. Teubner, Leipzig, Berlin.

[303] Völker, B., Marton, P., Elsässer, C., and Kamlah, M. (2011). A finite element method for crack growth without remeshing. *Continuum Mech. Thermodyn.*, 23:435–451.

[304] von Hippel, A., Breckenridge, R. G., Chesley, F. G., and Tisza, L. (1946). High dielectric constant ceramics. *Ind. Engr. Chem.*, 88(11).

[305] Waghmare, U. V. and Rabe, K. M. (1997). Ab initio statistical mechanics of the ferroelectric phase transition in $PbTiO_3$. *Phys. Rev. B*, 55.

[306] Wagner, M. R., Callsen, G., Reparaz, J. S., Kirste, R., Hoffmann, A., Rodina, A. V., Schleife, A., Bechstedt, F., and Phillips, M. R. (2013). Effects of strain on the valence band structure and exciton-polariton energies in ZnO. *Phys. Rev. B*, 88(23):235210.

[307] Wang, J., Shi, S.-Q., Chen, L.-Q., Li, Y., and Zhang, T.-Y. (2004). Phase field simulations of ferroelectric/ferroelastic polarization switching. *Acta Mater.*, 52:749–764.

[308] Wang, Y. D., Smullin, S. J., Sheridan, M. J., Wang, Q., Eldershaw, C., and Schwartza, D. E. (2015). A heat-switch-based electrocaloric cooler. *Appl. Phys. Lett*, 107(134103).

[309] Wei, S., Wang, Q., Zhu, J., Sun, L., Lin, H., and Guo, Z. (2011). Multifunctional composite core-shell nanoparticles. *Nanoscale*, 3(11):4474–4502.

[310] Williamson, R. L., Hales, J. D., Novascone, S. R., Tonks, M. R., Gaston, D. R., Permann, C. J., Andrs, D., and Martineau, R. C. (2012). Multidimensional multiphysics simulation of nuclear fuel behavior. *J. Nuc. Mater.*, 423:149–163.

[311] Wolfram Research, I. (2016). Mathematica, Version 10.3. Champaign, IL, 2016.

[312] Wu, A., Jia, J., and Luan, S. (2011). Amphiphilic PMMA/PEI core-shell nanoparticles as polymeric adsorbents to remove heavy metal pollutants. *Colloids Surf., A*, 384:180–185.

[313] Wu, H.-H., Zhu, J., and Zhang, T.-Y. (2015). Size-dependent ultrahigh electrocaloric effect near pseudo-first-order phase transition temperature in barium titanate nanoparticles. *RSC Adv.*, 5:37476–37484.

[314] Wu, J. J., Liu, S. C., Wu, C. T., Chen, K. H., and Chen, L. C. (2002). Heterostructures of ZnO-Zn coaxial nanocables and ZnO nanotubes. *Appl. Phys. Lett.*, 81(2002):1312–1314.

[315] Wul, B. M. and Goldman, I. M. (1945). Dielectric constants of titanates of metals of second group. *Compt. Rend. Acad. Sci., U.R.S.S.*, 46:139–142.

[316] Xing, Y. and Rao, J. (2008). Quantum dot bioconjugates for in vitro diagnostics & in vivo imaging. *Cancer Biomark.*, 4:307–319.

[317] Xing, Y. J., Xi, Z. H., Xue, Z. Q., Zhang, X. D., Song, J. H., Wang, R. M., Xu, J., Song, Y., Zhang, S. L., and Yu, D. P. (2003). Optical properties of the ZnO nanotubes synthesized via vapor phase growth. *Appl. Phys. Lett.*, 83(2003):1689–1691.

[318] Xu, R. and Karthik, J. and Damodaran, A. R. and Martin, L. W. (2014). Stationary domain wall contribution to enhanced ferroelectric susceptibility. *Adv. Energy Mater.*, 5(3120).

[319] Yadav, A. K., Nelson, C. T., Hsu, S. L., Hong, Z., Clarkson, J. D., Schlep̀utz, C. M., Damodaran, A. R., Shafer, P., Arenholz, E., Dedon, L. R., Chen, D., Vishwanath, A., Minor, A. M., Chen, L.-Q., Scott, J. F., Martin, L. W., and Ramesh, R. (2016). Observation of polar vortices in oxide superlattices. *Nature*, 530:198–201.

[320] Yin, W.-J., Chen, S., Yang, J.-H., Gong, X.-G., Yan, Y., and Wei, S.-H. (2010). Effective band gap narrowing of anatase TiO_2 by strain along a soft crystal direction. *Appl. Phys. Lett.*, 96(22):221901.

[321] Yoffe, A. D. (1993). Low-dimensional systems: quantum size effects and electronic properties of semiconductor microcrystallites (zero-dimensional systems) and some quasi-two dimensional systems. *Adv. in Phys.*, 51(2).

[322] Yu, X. Z., Onose, Y., Kanazawa, N., Park, J. H., Han, J. H., Matsui, Y., Nagaosa, N., and Tokura, Y. (2010). Real-space observation of a two-dimensional skyrmion crystal. *Nature*, 465:901–904.

[323] Yvonnet, J., Mitrushchenkov, A., Chambaud, G., He, Q.-C., and Gu, S.-T. (2012). Characterization of surface and nonlinear elasticity in wurtzite ZnO nanowires. *J. Appl. Phys.*, 111(12):124305.

[324] Zalar, B., Laguta, V. V., and Blinc, R. (2003). NMR evidence for the coexistence of order-disorder and displacive components in barium titanate. *Phys. Rev. Lett.*, 90.

[325] Zalar, B., Lebar, A., Seliger, J., Blinc, R., Laguta, V. V., and Itoh, M. (2005). NMR study of disorder in $BaTiO_3$ and $SrTiO_3$. *Phys. Rev. B*, 71.

[326] Zeches, R. J., Rossell, M., Zhang, J. X., Hatt, A. J., He, Q., Yang, C.-H., Kumar, A., Wang, C. H., Melville, A., Adamo, C., Sheng, G., Chu, Y.-H., Ihlefeld, J. F., Erni, R., Ederer, C., Gopalan, V., Chen, L.-Q., Schlom, D. G., Spaldin, N. A., Martin, L. W., and Ramesh, R. (2008). A strain-driven morphotropic phase boundary in $BiFeO_3$. *Science*, 326:977–980.

[327] Zeng, H., Cai, W., Cao, B., Hu, J., Li, Y., and Liu, P. (2006a). Surface optical phonon Raman scattering in Zn-ZnO core-shell structured nanoparticles. *Appl. Phys. Lett.*, 88(18).

[328] Zeng, H., Cai, W., Hu, J., Duan, G., Liu, P., and Li, Y. (2006b). Violet photoluminescence from shell layer of Zn-ZnO core-shell nanoparticles induced by laser ablation. *Appl. Phys. Lett.*, 88(17).

[329] Zeng, H., Li, Z., Cai, W., Cao, B., Liu, P., and Yang, S. (2007). Microstructure control of Zn/ZnO core/shell nanoparticles and their temperature-dependent blue emissions. *J. Phys. Chem. B*, 111:14311–14317.

[330] Zhai, Y., Zhai, J., Zhou, M., and Dong, S. (2009). Ordered magnetic core-manganese oxid shell nanostructures and their application in water treatment. *J. Mater. Chem.*, 19:7030–7035.

[331] Zhang, Q., Fan, W., and Gao, L. (2007). Anatase TiO_2 nanoparticles immobilized on ZnO tetrapods as a highly efficient and easily recyclable photocatalyst. *Appl. Catal. B Environ.*, 76:168–173.

[332] Zhang, X., Liu, X. H., Song, K. Z., and Lu, M. W. (2001). Least-square collocation meshless method. *Int. J. Numer. Meth. Engr.*, 51(9):1089–1100.

[333] Zheludev, I. S. (1971). *Physics of Crystalline Dielectrics: Volume 1 Crystallography and Spontaneous Polarization*. Springer.

[334] Zhong, W., Vanderbilt, D., and Rabe, K. M. (1995). First-principles theory of ferroelectric phase transitions for perovskites: The case of $BaTiO_3$. *Phys. Rev. B*, 52(6301).

[335] Zhou, Y., Iacocca, E., Awad, A. A., Dumas, K., Zhang, F. C., Braun, H. B., and Åkerman, J. (2015). Dynamically stabilized magnetic skyrmions. *Nature Comm.*, 6:8193.

[336] Zhu, J., Wei, S., Haldolaarachchige, N., Young, D. P., and Guo, Z. (2011). Electromagnetic field shielding polyurethane nanocomposites reinforced with core-shell Fe-silica nanoparticles. *J. Phys. Chem. C*, 115:15304–15310.